Dispersive analysis of charmed meson decays

Dissertation

zur

Erlangung des Doktorgrades (Dr. rer. nat.)

der

Mathematisch-Naturwissenschaftlichen Fakultät

der

Rheinischen Friedrich-Wilhelms-Universität Bonn

vorgelegt von

Franz Niecknig

aus

Bonn

Bonn, April 2016

Angefertigt mit Genehmigung der Mathematisch-Naturwissenschaftlichen Fakultät der Rheinischen Friedrich-Wilhelms-Universität Bonn

1. Gutachter: Professor Dr. Bastian Kubis

2. Gutachter: Professor Dr. Christoph Hanhart

Tag der Promotion: 04.07.2016

Erscheinungsjahr: 2016

Abstract

The Standard Model comprises most of today's knowledge of particle physics and is overall well tested and understood. However the dynamics of strong interactions, given by Quantum Chromodynamics (QCD), are still a challenge at low energies. The running coupling constant prevents a direct perturbative calculation of QCD at the hadronic scale and therefore other methods have to be employed.

In this thesis we apply dispersion theory to study strong final-state interactions in three-particle decays and investigate the $J/\psi \to \pi^0\gamma^*$ transition form factor.

In the first part of this thesis we introduce a dispersive framework for three-body decays, based on Khuri–Treiman equations, that satisfies analyticity, unitarity, and crossing symmetry by construction and includes crossed-channel rescattering effects. We explicitly display the derivation of the Khuri–Treiman equations on general vector-meson decays into three pions $V \to 3\pi$ with $V \in \{\omega, \phi, J/\psi\}$. These decays provide an ideal test case as the equations are of simple form. In this context we study the general dependence of the resulting amplitude on the vector-meson mass and investigate the employed iterative solution strategy and its convergence.

Building on the obtained $J/\psi \to 3\pi$ amplitude we study the J/ψ transition form factor. The transition form factors of light vector mesons have been of great interest over the last years because of their importance in the theoretical determination of the anomalous magnetic moment of the muon. However the available experimental data is difficult to understand theoretically. With the larger phase space available, the $J/\psi \to \pi^0\gamma^*$ transition may shed light onto the lighter vector-meson transition form factors.

In the second part we resume our study of three-particle decays on the Cabibbo-favored $D^+ \to K\pi\pi^+$ decays. Heavy-flavor three-body decays into light mesons provide a valuable source for Standard Model tests and beyond. They play an important role due to their richer kinematic structure compared to two-body decays which can be exploited e.g. in CP-violation studies. So far the Khuri–Treiman-type equations have been applied successfully to light meson decays but not to heavy-flavor decays. Thus the Cabibbo favored $D^+ \to K\pi\pi^+$ decays provide an ideal test to establish the framework in the open-charm sector. We introduce a new numerical method to solve the Khuri–Treiman-type equations, compare the obtained decay amplitudes to the data from the CLEO, FOCUS, and BES III collaboration as well as previous theoretical studies and discuss the impact of crossed-channel rescattering effects in these decays.

Parts of this thesis have been published in the following articles:

- F. Niecknig and B. Kubis, *Dispersion-theoretical analysis of the $D^+ \to K^-\pi^+\pi^+$ Dalitz plot*, JHEP **1510** 142 (2015)
- B. Kubis and F. Niecknig, *Analysis of the $J/\psi \to \pi^0\gamma^*$ transition form factor*, Phys. Rev. D **91**, no. 3, 036004 (2015).

Furthermore, the material presented in Chapter I generalizes results published in

- F. Niecknig, B. Kubis and S. P. Schneider, *Dispersive analysis of* $\omega \to 3\pi$ *and* $\phi \to 3\pi$ *decays*, Eur. Phys. J. C **72** 2014 (2012)
- S. P. Schneider, B. Kubis and F. Niecknig, *The* $\omega \to \pi^0\gamma^*$ *and* $\phi \to \pi^0\gamma^*$ *transition form factors in dispersion theory*, Phys. Rev. D **86** 054013 (2012)
- M. Hoferichter, B. Kubis, S. Leupold, F. Niecknig and S. P. Schneider, *Dispersive analysis of the pion transition form factor*, Eur. Phys. J. C **74**, 3180 (2014).

Contents

Chapter 1

Introduction

The understanding and prediction of natural phenomena has been at the heart of human desire since time immemorial—especially the strive to discover the smallest building blocks and how these form the world as we see it today.

At the center of today's knowledge of theoretical particle physics stands the Standard Model. The Standard Model, introduced in the 60s and 70s, see Refs. [1–4], is a local $SU(3) \times SU(2) \times U(1)$ gauge quantum field theory, which unifies the strong, the electromagnetic and the weak force, three of the four fundamental forces.

The constituents of the SM are the six quarks (u, d, c, s, t, b), the six leptons (ℓ, ν_ℓ with $\ell \in \{e, \mu, \tau\}$) and the force carriers, the vector bosons: eight gluons mediating the strong interaction, the $W^\pm$ and Z bosons responsible for the weak interaction and the photon γ for the electromagnetic interaction. Furthermore a scalar boson, the Higgs boson, was proposed to give the otherwise massless weak gauge bosons ($W^\pm$ and Z) and chiral fermions (quarks and leptons) a mass. The recent experimental confirmation, see Ref. [5, 6], caught world wide attention.

Over the last decades the Standard Model has withstood numerous challenges, experimental and theoretical, and is regarded as one of the best tested theories up to date. However the unification of the Standard Model with the gravitational force is still an ongoing endeavor and further caveats like the hierarchy problem, the dark matter and dark energy puzzle, matter-antimatter asymmetry in the universe to name a few, suggest that the Standard Model may be embedded in a more global yet to unravel theory.

Focusing on intrinsic issues, Standard Model calculations have historically relied heavily on the well developed and successful technique of perturbation theory, pioneered in Quantum Electrodynamics (QED), which spurred the progress in the energy regions where the perturbative expansion converges. However at low energies, strongly interacting processes do not permit perturbative calculations, since the running coupling constant of the strong interaction becomes too large. Therefore the strong dynamics at low energies are still not

adequately understood. The field of theoretical hadron physics is dedicated to this issue and alternative solution methods have been developed. Besides effective field theory and lattice QCD, dispersion theory is one of these alternatives. Based on the fundamental principles of unitarity, analyticity and crossing symmetry, the analytic structure of the process in question is exploited to obtain integral equations that are solved to obtain the amplitude in question.

In this thesis we will employ dispersion relations to investigate in particular three-body decays. Heavy-meson three-body decays have caught much attention in Standard model tests and beyond, for example in CP-violation studies. The more involved kinematic structure, compared to two-body decays, makes these decays a prime target to test our knowledge of low-energy QCD and Standard Model physics.

Not only from the theoretical side precision tools for low-energy strong processes are required, but also from the experimental side. Most experimental analyses are performed in the so-called isobar model where two-particle interactions are often expressed by pure resonance exchange in the form of Breit–Wigner parametrizations and additional background terms. Beside that some resonances are by no means of Breit–Wigner shape, these analyses often violate basic physical principles like unitarity and analyticity, see Ref. [7], and suffer from not taking interactions beyond two-particle interactions into account. Thus also from the experimental point of view there is a need for more rigorous approaches like the dispersion relations employed in this thesis.

The thesis is structured as follows: After a short introduction into the dynamics of strong interactions and non-perturbative approaches needed at low energies, we display the concept of dispersion theory and give a first application, the pion vector form factor. In part I the dispersive treatment of three-particle decays with Khuri–Treiman equations is introduced on the example of $V \to 3\pi$ decays. The Khuri–Treiman-type equations for these decays have a simple form and therefore serve as a test ground to study the dependence on the decaying mass and the convergence of the iterative solution strategy. We will explicitly study the $J/\psi \to 3\pi$ decay. Chapter 3 is devoted to the study of the $J/\psi \to \pi^0\gamma^*$ transition form factor taking the $J/\psi \to 3\pi$ decay amplitude obtained in Chapter 2 as input. In part II we extend the Khuri–Treiman formalism to decays of the open-charm sector, namely the $D^+ \to K\pi\pi^+$ decays, construct a new solution strategy, discuss the influence of crossed-channel rescattering effects and compare the obtained decay amplitudes to data and other theoretical approaches.

1.1 Strong interaction

The fundamental theory of strong interactions is QCD. It is a non-abelian quantum field theory with the underlying $SU(3)$ color symmetry group (Yang–Mills theory), stemming from the $SU(3)$ part of the Standard Model, see Ref. [1]. The QCD Lagrangian (omitting

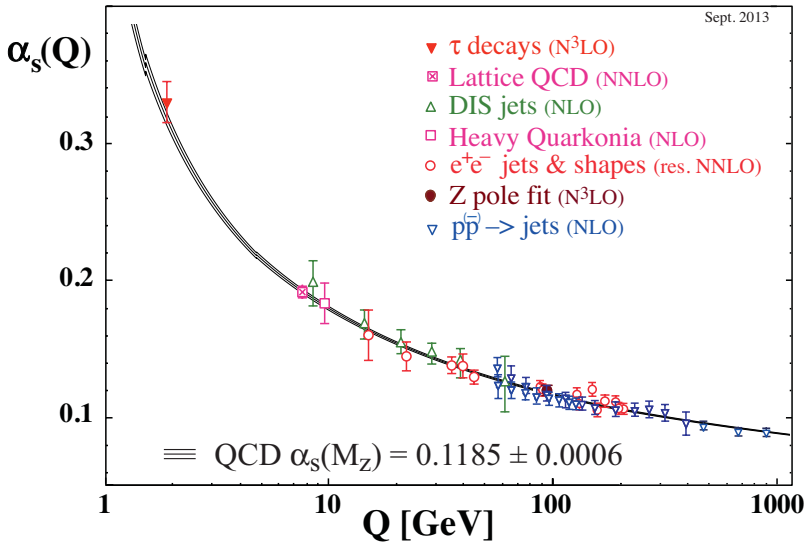

Figure 1.1: The graph, taken from Ref. [8], shows the summary of the measurements of the running coupling constant $\alpha_s(Q)$ with respect to the energy scale Q. The QCD perturbative order used in the extraction of the strong coupling constant is given in the brackets (NLO: next-to-leading order; NNLO: next-to-next-to-leading order; res. NNLO: NNLO matched with resummed next-to-leading logs; N^{3}LO: next-to-NNLO).

the Θ-term) is given by

$$\mathcal{L}_{QCD} = \bar{\psi}_f(iD_\mu\gamma^\mu - m_f)\psi_f - \frac{1}{4}F^i_{\mu\nu}F_i^{\mu\nu} \ , \tag{1.1}$$

with the quark fields ψ_f, which come in six flavors, $f \in \{u, d, c, s, t, b\}$ and $D_\mu = \partial_\mu - ig_s A^i_\mu t^i$ is the covariant derivative with the $SU(3)$ generators t^i and the eight corresponding gauge fields A^i being the gluons. The field strength tensor is defined by

$$F^i_{\mu\nu} = \partial_\mu A^i_\nu - \partial_\nu A^i_\mu + g_s f^{ijk} A^j_\mu A^k_\nu \ , \tag{1.2}$$

with the strong coupling constant g_s or $\alpha_s = g_s^2/(4\pi)$ and f^{ijk} the structure constants of the $SU(3)$ Lie algebra. The appearance of a connection $igA^i_\mu t^i$ and curvature $F^i_{\mu\nu}$ is the consequence of the local nature of the gauge symmetry. The non-abelian nature of this theory induces gluon-gluon interaction terms (the last term in Eq. (1.2)). These are also responsible for the peculiar nature of asymptotic freedom, see Ref. [9, 10], encoded in the β_{QCD}-function of the renormalization group equation of QCD. We state β_{QCD} to one loop

order

$$\beta_{QCD}(\alpha_s) \equiv Q^2 \frac{\mathrm{d}\alpha_s(Q^2)}{\mathrm{d}Q^2} = -\left(11 - \frac{2n_f}{3}\right)\frac{\alpha_s(Q^2)}{2\pi} + \mathcal{O}(\alpha_s^3)$$
$$\Rightarrow \alpha_s(Q^2) \approx \frac{\alpha_s(\mu^2)}{1 + (33 - 2n_f)/(12\pi)\ln\left(\frac{Q^2}{\mu^2}\right)}\ , \tag{1.3}$$

where Q denotes the momentum transfer, μ the reference scale, often taken to be the mass of the Z boson, and n_f the number of flavors. The minus sign in β_{QCD} gives rise to a small coupling at high-momentum transfer (asymptotic freedom), while for low momentum transfer a strong coupling is realized, see Fig. 1.1. As the strong coupling constant is the expansion parameter of perturbative QCD, other methods have to be devised in the low-energy region.

1.2 Non-perturbative QCD

We have seen above that the nature of the strong interaction admits to perturbative calculations at very high energies but not at low energies due to the nature of the running coupling constant. Thus the asymptotic freedom of QCD leads to the fact that other means than perturbative QCD have to be applied to study low-energy strong interactions. The major pillars of non-perturbative QCD calculations are lattice QCD, effective field theories, and dispersion theory.

The main idea of lattice QCD is to reformulate QCD on a discretized space-time lattice with finite extension. On this lattice correlation functions are calculated numerically via the path integral formalism and the obtained results are extrapolated back to continuous space-time. However these calculations come at a great expense of computational resources and have to be performed on supercomputers. Additionally, the signal-to-noise ratio as well as the sign problem can present issues which are difficult to overcome.

A second ansatz are effective field theories (EFTs). EFTs exploit the conjecture made by Weinberg [11], that any quantum field theory has no content besides unitarity, analyticity, cluster decomposition and symmetries: analyticity which stems from microcausality, unitarity which ensures probability conservation, cluster decomposition, meaning that distant experiments are uncorrelated, and the symmetries which are the characteristic features of the underlying theory directly linked to its conservation laws.

The effective Lagrangian for the relevant degrees of freedom at the considered length scale is thus given by the most general Lagrangian which inherits the symmetries of the underlying theory. To obtain a meaningful and powerful effective theory it is imperative that we have a large scale separation between the considered low-energy scale and the integrated out high-energy scale. The ratio of the two scales, the expansion parameter, provides an

ordering scheme (power counting) of the operators in the Lagrangian. Operators with higher order in the expansion parameter are suppressed compared to low order operators. Thus we have a systematic ordering of the operators by their contribution strength. Every term in the Lagrangian comes with a prefactor a priori not known, called low-energy constants (LECs). These have to be determined either from experiment or from the underlying theory and incorporate higher-energy effects. Having a small expansion parameter renders the theory more predictive since less terms in the Lagrangian and therefore less LECs have to be considered.

In the following we will briefly discuss the low-energy effective field theory of QCD, namely chiral perturbation theory (ChPT), before introducing dispersion theory in more detail in the ensuing section. To construct the low-energy effective theory of QCD we have to first specify the relevant degrees of freedom. Since the fundamental degrees of freedom of QCD, the quarks and gluons, are confined to color neutral composites at the hadronic scale (mesons, baryons, ...) it is not directly apparent how the fundamental and hadronic degrees of freedom are connected. The connection is the approximate chiral symmetry of QCD for the lightest quark flavors at the hadronic scale. With the quark fields decomposed in its chiral left- and right-handed spinors

$$\psi_{R/L} \equiv \frac{1 \pm \gamma_5}{2} \psi_f \ , \tag{1.4}$$

we obtain for the QCD Lagrangian Eq. (1.1)

$$\mathcal{L}_{QCD} = i\bar{\psi}_R D_\mu \gamma^\mu \psi_R + i\bar{\psi}_L D_\mu \gamma^\mu \psi_L - \bar{\psi}_R m_f \psi_L - \bar{\psi}_L m_f \psi_R - \frac{1}{4} F^i_{\mu\nu} F_i^{\mu\nu} \ . \tag{1.5}$$

The left- and right-handed field equations decouple if the quark mass term is neglected. In this scenario the QCD Lagrangian gains the additional symmetry

$$U_R(n_f) \times U_L(n_f) = SU_L(n_f) \times SU_R(n_f) \times U_V(1) \times U_A(1) \ , \tag{1.6}$$

with $V = L + R$ (vector) and $A = L - R$ (axial). The $U_V(1)$ symmetry corresponds to the baryon number conservation and $U_A(1)$ is anomalously broken, meaning that this symmetry does not survive quantization. Considering only the lightest quarks u, d and s, their masses are much smaller than the typical hadronic scale ($\approx 1\,\text{GeV}$). We can therefore expect that the remaining $SU_L(3) \times SU_R(3)$ symmetry is approximately realized in the hadronic spectrum. In principle there are two realizations of a symmetry in the particle spectrum: the Wigner–Weyl mode, where the symmetry is realized in degenerate particle multiplets, or the Goldstone mode, in which the symmetry is spontaneously broken. In the Wigner-Weyl realization we should observe degenerate states of opposite parity since left- and right-handed operators have opposite parity. This is not observed. Also the vacuum expectation value of the axial- and vector current should be equal. This again is

not observed in experiments. What one observes is that the $SU_L(3) \times SU_R(3)$ symmetry is spontaneously broken to an $SU_V(3)$ symmetry where the arising Goldstone bosons are interpreted as the pseudoscalar ground-state mesons. These include the pion triplet, the four kaons and the eta-meson. We could have restricted ourselves to a pure pionic theory considering only u and d quarks, such that the $SU(3)$ symmetries reduce to $SU(2)$. Since the pion masses are much smaller than the kaon and eta-meson masses, the systematic error of $SU(2)$ ChPT is smaller than that of $SU(3)$ ChPT.

We choose the one-parameter subgroup exponentiation representation of the Goldstone bosons octet given by

$$U = \exp\left(\frac{i\phi}{f}\right) \quad \text{with} \quad \phi \equiv \sum_{i=1}^{8} \phi^i t^i = \begin{pmatrix} \pi^0 + \frac{1}{\sqrt{3}}\eta & \sqrt{2}\pi^+ & \sqrt{2}K^+ \\ \sqrt{2}\pi^- & -\pi^0 + \frac{1}{\sqrt{3}}\eta & \sqrt{2}K^0 \\ \sqrt{2}K^- & \sqrt{2}\bar{K}^0 & -\frac{2}{\sqrt{3}}\eta \end{pmatrix} , \tag{1.7}$$

where t^j, $j \in \{1, 2, \ldots, 8\}$, are the 8 generators of the $[SU_L(3) \times SU_R(3)]/SU_V(3) \simeq SU(3)$ quotient space in the Gell-Mann representation, f can be identified with the meson octet decay constant in the chiral limit. As we work in the low-energy region the number of small momenta p, small compared to a yet to determine scale Λ_χ, or equivalently the number of derivatives, give us a natural power counting scheme of the importance of operators. The general ChPT Lagrangian is thus ordered via

$$\mathcal{L} = \mathcal{L}^{(2)} + \mathcal{L}^{(4)} + \mathcal{L}^{(6)} + \ldots , \tag{1.8}$$

where the upper index denotes the number of derivatives. Note that odd numbers of derivatives are forbidden by Lorentz invariance and the $\mathcal{L}^0$ term amounts to an irrelevant constant. We know that chiral symmetry is an approximate symmetry and that the mass term explicitly breaks the symmetry. To account for non-zero quark and meson masses one introduces an explicit symmetry-breaking mass term that breaks the chiral symmetry exactly as the QCD mass term does. The leading order Lagrangian $\mathcal{L}^{(2)}$ consistent with the imposed symmetry, mass term and Eq. (1.7) reads

$$\mathcal{L}^{(2)} = \frac{f_\pi^2}{4}\left\langle \partial_\mu U \partial^\mu U + 2B_0(\mathcal{M}^\dagger U + U^\dagger \mathcal{M})\right\rangle , \quad \mathcal{M} \equiv \begin{pmatrix} m_u & 0 & 0 \\ 0 & m_d & 0 \\ 0 & 0 & m_s \end{pmatrix} . \tag{1.9}$$

with $\langle\rangle$ denoting the $SU(3)$ trace and the quark masses count like $\mathcal{O}(p^2)$, due to the Gell–Mann–Oakes-Renner relation. The validity range of ChPT, as discussed above, is given by the breaking scale Λ_χ, which is estimated by the mass of the lightest resonance ($\rho(770)$-resonance) or by next-to-leading order considerations

$$M_\rho \approx 0.775\,\text{GeV} \leq \Lambda_\chi \leq 4\pi f_\pi \approx 1.2\,\text{GeV} . \tag{1.10}$$

For a deeper introduction into ChPT we refer the reader to Refs. [12, 13].

1.3 The S-matrix

This section is dedicated to the exploration of the analytic properties of the S-matrix and a successive introduction into dispersion relations. Let us consider an initial multi-particle state $|i\rangle$ scatter or decay. The probability of measuring a state $|f\rangle$ as a final state is given by the squared modulus of the S-matrix element

$$|\langle f|S|i\rangle|^2 \ . \tag{1.11}$$

For a consistent definition, the S-matrix has to comply with the following properties, see Ref. [14]:

1. *short-range character of the force*

   Demanding a short-range character of the force is necessary in order to have asymptotically free initial and final states.

2. *superposition principle of quantum theory*

   The superposition principle is fundamental to describe quantum phenomena and renders the S-matrix linear.

3. *requirement of special relativity*

   It is clear that the S-matrix has to abide to the laws of special relativity. Lorentz invariance dictates that $\langle f|S|i\rangle = \langle Lf|S|Li\rangle$ with L a proper Lorentz transformation.

4. *probability conservation*

   The requirement of probability conservation is mandatory for the probability interpretation of Eq. (1.11). Summing over all possible measured final states we should always retain unity. This directly translates into the unitarity of the S-matrix $SS^\dagger = 1$.

5. *causality*

   Causality states that signals can not be received before transmission. This property has severe impact on the analytic properties and the pole structure of the S-matrix.

We note that the link between perturbation theory and the S-matrix is given by the LSZ reduction formula, see Ref. [15]. The S-matrix can be decomposed further into a non-interacting part and an interacting part, the T-matrix

$$S = \mathbb{1} + iT \ . \tag{1.12}$$

In the following we will study the analytic structure of the S-matrix.

1.3.1 Unitarity relation and analyticity

For simplicity we will consider in the following a two-particle scattering process with spinless and identical particles of mass M

$$A(p_1)B(p_2) \to C(k_1)D(k_2) \ , \tag{1.13}$$

with the four-momenta p_1, p_2, k_1, k_2. The Lorentz invariance of the S-matrix infers that the S-matrix element $\langle k_1, k_2|S|p_1, p_2\rangle$ can only depend on scalar products of the four momenta. With the Lorentz scalar Mandelstam variables defined as follows

$$s = (p_1 + p_2)^2, \quad t = (p_1 - k_1)^2, \quad u = (p_1 - k_2)^2 \ , \quad \text{and} \quad s + t + u = 4M^2 \ , \tag{1.14}$$

the scattering amplitude $\mathcal{M}(s, t, u)$ is defined via

$$\mathcal{M}(s, t, u) \equiv (2\pi)^4 \delta^4\big(p_1 + p_2 - k_1 - k_2\big)\big\langle k_1, k_2|T|p_1, p_2\big\rangle \ , \tag{1.15}$$

where the δ-distribution imposes energy and momentum conservation. To investigate the analytic structure of the scattering amplitude we study the implications of the unitarity of the S-matrix. With Eq. (1.12) we have

$$T^\dagger T = i\left(T^\dagger - T\right) \ . \tag{1.16}$$

Inserting the orthogonal projection we obtain

$$\begin{aligned} &\sum_m \langle f|T^\dagger|m\rangle\langle m|T|i\rangle = i\langle f|(T^\dagger - T)|i\rangle \\ &\Rightarrow T_{if} - T^*_{fi} = i\sum_m (2\pi)^4 \delta(p_m - p_f) T^*_{mf} T_{mi} \ , \end{aligned} \tag{1.17}$$

with $T_{if} \equiv \langle f|T|i\rangle$ and $\sum\limits_m$ denoting the sum and phase-space integral over all possible intermediate states m. In the case $T_{if} = T_{fi}$ holds, true for elastic two-particle scattering, we can identify the left-hand side of Eq. (1.17) with $2\,\mathrm{Im}\,T_{if}$. More generally causality dictates that the physical scattering amplitude is given by

$$\lim_{\epsilon\to 0} \mathcal{M}(s + i\epsilon, t, u) = \delta^4(p_i - p_f)\, T_{if} \ , \tag{1.18}$$

and due to hermitian analyticity, see Ref. [16],

$$\lim_{\epsilon\to 0} \mathcal{M}(s - i\epsilon, t, u) = \delta^4(p_i - p_f)\, T^*_{fi} \ . \tag{1.19}$$

We thus obtain

$$\mathrm{disc}\,\mathcal{M}(s, t, u) \equiv \mathcal{M}(s + i\epsilon, t, u) - \mathcal{M}(s - i\epsilon, t, u) = i\sum_m (2\pi)^4 \delta(p_m - p_f) T^*_{mf} T_{mi} \ . \tag{1.20}$$

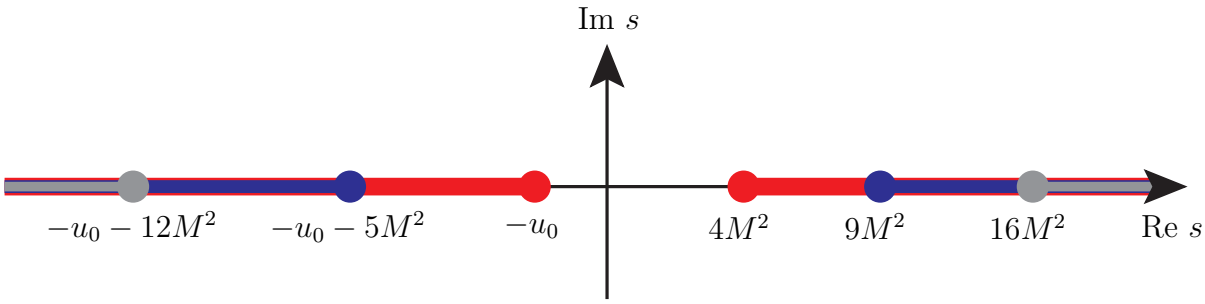

Figure 1.2: Analytic structure of the identical particle scattering amplitude for fixed $u = u_0$ in the complex s-plane. The colored lines indicate the right- and left-hand branch cuts starting at the corresponding multi-particle thresholds: two-particle (red), three-particle (blue) and four-particle (gray).

This relation is known as the unitarity relation. Whenever an intermediate state can go on-shell we obtain a contribution to the discontinuity and thus a branch cut opens with corresponding additional Riemann sheets. The first branch cut thus opens at the elastic threshold ($s = 4M^2$) followed by the three-particle threshold ($s = 9M^2$) spanning to infinity. These cuts are called right-hand cuts. Moreover, intermediate bound states can exist, which would give singular points on the real axis below the elastic threshold. However, there are more non-analytic structures present. Due to crossing symmetry, or in other words due to analytic continuation in the Mandelstam variables, the scattering amplitude also covers the crossed scattering processes

$$\begin{aligned} A(p_1)\bar{C}(-k_1) &\to \bar{B}(-p_2)D(k_2) \quad t\text{-channel process} \\ A(p_1)\bar{D}(-k_2) &\to \bar{B}(-p_2)C(k_1) \quad u\text{-channel process} , \end{aligned} \tag{1.21}$$

where $\bar{A}$ denotes the antiparticle of particle A and similarly for B,C, and D. These crossed processes exhibit branch cuts for $t \geq 4M^2$ (t-channel) and $u \geq 4M^2$ (u-channel), stemming from the corresponding unitarity relations. Note that, due to CPT symmetry (charge conjugation, parity and time reversal) combined with crossing symmetry, we have six processes described by the same scattering amplitude $\mathcal{M}(s,t,u)$. In the case of additional PT symmetry, we have twelve. The branch cuts of the t- and u-channel are connected to the s-channel through the relation $s + t + u = 4M^2$, see Eq. (1.14). For example fixing $u = u_0$, the first t-channel branch cut ($t \geq 4M^2$) begins at $s = -u_0$ and spans to $s \to -\infty$, see Fig. 1.2. These branch cuts in the complex s-plane stemming from the crossed t- and u-channels are called left-hand cuts.

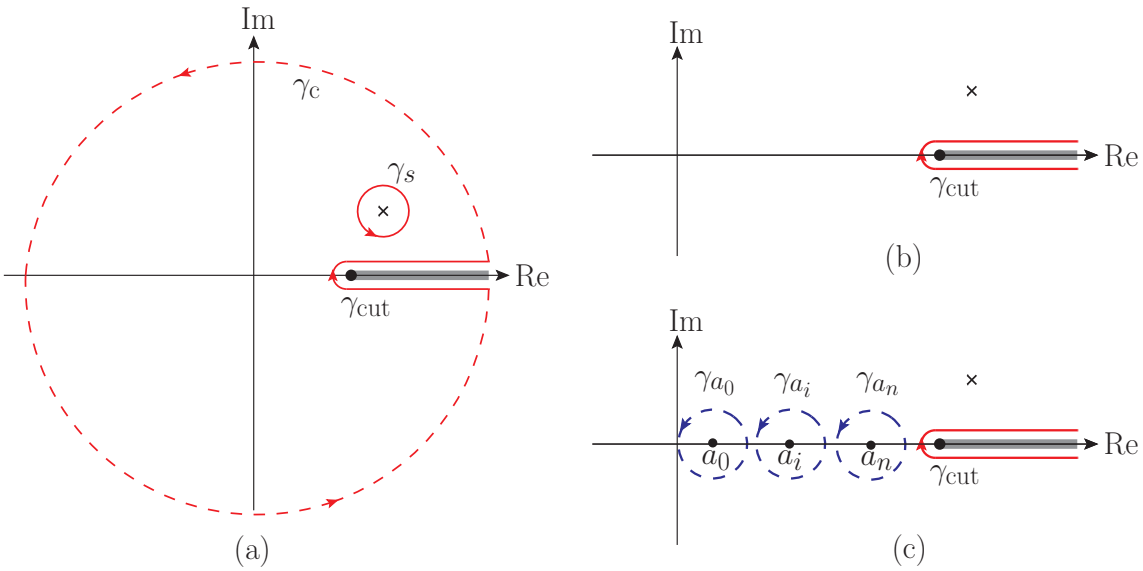

Figure 1.3: The complex plane with the branch cut (gray) starting at the elastic threshold (x_{th}) and different integration contours. Figure (a) depicts the closed circular contour γ_s of Cauchy's integral formula around point s, see Eq. (1.22), and the enlargement to $\gamma_c+\gamma_{\text{cut}}$. Figure (b) depicts the resulting integration contour taking the radius of contour γ_c to infinity and (c) the additional contributions from the subtraction points a_i if subtractions are introduced.

1.3.2 Dispersion relations

Dispersion relations exploit the analytic structure of the physical amplitude in question. They provide a model-independent tool based on the fundamental principles of any meaningful quantum field theory: micro causality (analyticity), probability conservation (unitarity of the S-matrix) and crossing symmetry. The construction of dispersion relations relies on basic complex analysis theorems.

Let us assume that the only non-analytic structure of a complex function $f(s)$ on the physical sheet stems from the discontinuity given by the unitarity relation (maximal analyticity) and no crossed-channel contributes. In other words, $f(s)$ is analytic on the open set $\mathbb{C} \setminus \{x | x \geq x_{\text{th}},\ x \in \mathbb{R}\}$, with the branch point x_{th}. Cauchy's integral formula states that on this open set we can rewrite $f(s)$ by

$$f(s) = \frac{1}{2\pi i} \oint_{\gamma_s} \frac{f(x)}{x - s} \mathrm{d}x \ , \tag{1.22}$$

where the integration path γ_s is depicted in Fig. 1.3 encircling the point s. We can enlarge the closed contour γ_s by Cauchy's theorem to $\gamma_c + \gamma_{\text{cut}}$ provided that in the swept area the

function is analytic. Assuming that the function $f(s)$ vanishes fast enough approaching complex infinity the radius of the contour can be taken to infinity such that the integral over γ_c vanishes. Thus only the integral over γ_{cut} remains, see Fig 1.3 b),

$$f(s) = \frac{1}{2\pi i}\int_{\gamma_{\text{cut}}} \frac{f(x)}{x-s}\mathrm{d}x = \frac{1}{2\pi i}\int_{x_{\text{th}}}^{\infty} \frac{\operatorname{disc} f(x)}{x-s}\mathrm{d}x \ . \tag{1.23}$$

Since we have information on the right-hand-cut discontinuity of $f(s)$ from the unitarity relation we can reconstruct the function $f(s)$ in the whole complex plane with this localized information. Thus the function satisfies the unitarity relation and the imposed analytic constraints by construction. In the case where $f(s)$ does not fall off fast enough in the complex infinity limit, subtractions are introduced: $f(s)$ is divided by a polynomial such that the resulting function vanishes sufficiently fast approaching complex infinity. However this introduces further singularities which result in unknown subtraction constants which have to be determined beyond the scope of dispersion theory either by theoretical considerations or experimental data. We define

$$g(s) \equiv \frac{f(s)}{\sum_{i=0}^{n} c_i (x-a_i)^i} \ , \tag{1.24}$$

where a_i are called the subtraction points. Starting again with Cauchy's theorem we have enlarging the circular integration contour, see Fig. 1.3 c),

$$g(s) = \frac{1}{2\pi i}\int_{\gamma_{\text{cut}}} \frac{g(x)}{(x-s)}\mathrm{d}x + \sum_{i=0}^{n} \frac{1}{2\pi i}\int_{\gamma_{a_i}} \frac{g(x)}{(x-s)}\mathrm{d}x \ . \tag{1.25}$$

We determine the sum of integrals encircling the subtraction points a_i via the residue theorem,

$$\begin{aligned}\frac{1}{2\pi i}\int_{\gamma_{a_i}} \frac{g(x)}{(x-s)}\mathrm{d}x &= \frac{1}{2\pi i}\mathrm{Res}\left(\frac{g(x)}{x-s}, a_i\right) = \lim_{x\to a_i}\left[(x-a_i)\frac{g(x)}{x-s}\right] \\ &= \frac{f(a_i)}{(a_i-s)\sum\limits_{j=0,\, j\neq i}^{n} c_j (a_i-a_j)^j} \ .\end{aligned} \tag{1.26}$$

We therefore obtain from Eq. (1.25)

$$f(s) = h_{n-1}(s) + \frac{p_n(s)}{2\pi i}\int_{x_{\text{th}}}^{\infty} \frac{\operatorname{disc} f(x)}{p_n(x)(x-s)}\mathrm{d}x \ , \tag{1.27}$$

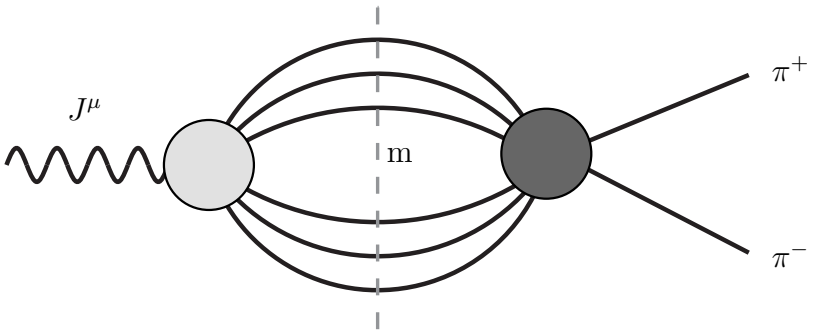

Figure 1.4: The diagrammatic contribution to the discontinuity of the pion vector form factor. The gray circle denotes the $J^\mu \to m$ transition amplitude and the black circle stands for the $m \to \pi^+\pi^-$ amplitude, where m denotes the possible intermediate states. In the elastic case they correspond to the pion vector form factor and $\pi^+\pi^- \to \pi^+\pi^-$ amplitude respectively. The dashed gray line shows the Cutkosky cuts.

with the polynomials $p_n(s) = \sum_{i=0}^{n} c_i(s-a_i)^i$ being of order n and

$$h_{n-1}(s) = p_n(s) \sum_{i=0}^{n} \frac{f(a_i)}{(a_i - s) \sum\limits_{j=0,\, j\neq i}^{n} c_j (a_i - a_j)^j} \ , \tag{1.28}$$

being of order $n-1$. In the following we will always subtract at the origin $a_i = 0$ and $c_i = 1$ without any loss of generality

$$f(s) = \tilde{h}_{n-1}(s) + \frac{s^n}{2\pi i} \int_{x_{\rm th}}^{\infty} \frac{\operatorname{disc} f(x)}{x^n (x-s)} \mathrm{d}x \ , \tag{1.29}$$

where the subtraction polynomial $\tilde{h}_{n-1}(s)$ is of order $n-1$.

1.4 Pion vector form factor and Omnès problem

The first physical application we want to discuss is the pion vector form factor at low energies ($\lesssim 1\,\mathrm{GeV}$) defined by the following matrix element,

$$\langle \pi^+(p')\pi^-(p)|J_\mu(0)|0\rangle = (p'-p)_\mu F_V(q^2) \ , \tag{1.30}$$

with $q = p' + p$ and J_μ the electromagnetic current. The dispersive representation of the pion vector form factor is a good pedagogic advent towards the study of three-particle

decays in a dispersive framework and the challenges in the description of non-perturbative QCD at low energies. The dispersive analysis of the pion vector form factor will also serve as input in the following studies. The pion vector form factor is a key subprocess in many hadronic reactions also providing the biggest hadronic contribution to the anomalous magnetic moment of the muon. Experimentally the form factor is directly accessible via the processes $e^+e^- \to \pi^+\pi^-$ or via $\tau^- \to \pi^-\pi^0\nu_\tau$ if we assume isospin symmetry. Large isospin violating corrections explicitly include the $\rho - \omega$ mixing, which is only present in the neutral current.

Although ChPT provides an effective theory for low energy QCD dynamics it does include only the lowest pseudoscalar mesons as dynamical degrees of freedom. Therefore the applicability range of ChPT in the vector channel with the prominent broad $\rho(770)$ resonance is reduced to well below the $\rho(770)$ resonance. A natural procedure is the extension of ChPT to include higher resonances, like the vector-meson octet, in a suitable manner (e.g. Refs. [17–21]). However these theories suffer from an unclear scale separation and are therefore not as rigorous or precise as ChPT.

This calls for a precision tool that respects the fundamental principles of relativistic quantum phenomena. The precision tool we will employ is dispersion theory and in the following we will explicitly treat the pion vector form factor in a dispersive setting known as the Omnès problem. The Omnès problem is a classic subject, first discussed in Refs. [22,23] and widely utilized in pion vector form factor studies, see e.g. Refs. [24–27]. Let us first note that due to Bose symmetry the $\pi\pi$ system has isovector quantum numbers as it couples to the vector current and is therefore in a pure P-wave state. The inaugural step to employ dispersion relations lies in the study of the analytic structure of the amplitude in question. In this respect the pion vector form factor is a simple example having only a right-hand cut (see Fig. 1.4), due to lacking crossed channels. The unitarity relation thus reads

$$(p' - p)_\mu \operatorname{disc} \mathcal{F}_V(q^2) = \frac{i}{2} \sum_m (2\pi)^4 \delta^4(p_m - q) \left\langle \pi^+(p')\pi^-(p)|T|m\right\rangle \left\langle m|J_\mu(0)|0\right\rangle \,, \qquad (1.31)$$

where the sum runs over all possible intermediate states m with overall four momentum p_m. At low energies the discontinuity relation is saturated by low-lying intermediate states. In the following we will assume elastic unitarity, so only the $\pi\pi$ intermediate state is considered. This is a legitimate approximation in the energy region in question. The next higher inelastic contribution would be induced by 4π intermediate states, strictly contributing at $s \geq 16M_\pi^2$, but phenomenologically found to set in noticeable around the $\omega\pi$ threshold. As we consider a P-wave, the inset of inelasticities is mild and we can conclude that up to the region of 1 GeV the elastic description gives a good approximation. Beyond, a treatment of inelastic channels is certainly required. For further information and a thorough inclusion of inelastic effects in a multi-channel approach we refer the reader to Ref. [27] and references therein.

We will now consider the elastic unitarity relation, Eq. (1.31) with only $\pi\pi$ intermediate states

$$(p'-p)_\mu \,\mathrm{disc}\,\mathcal{F}_V(q^2) = \frac{i}{2}\int \frac{\mathrm{d}k^4}{(2\pi)^2}\,\delta((q-k)^2-M_\pi^2)\delta(k^2-M_\pi^2)T_{\pi\pi}(q,k)\,(q-2k)_\mu\,\mathcal{F}_V(q^2)\ , \tag{1.32}$$

with $T_{\pi\pi}(q,k) \equiv \big\langle \pi^+(p')\pi^-(p)|T|\pi^+(q-k)\pi^-(k)\big\rangle$. The partial-wave decomposition for the $\pi\pi$ scattering amplitude $\big\langle \pi^+(p')\pi^-(p)|T|\pi^+(k-q)\pi^-(k)\big\rangle$ is given by

$$T_{\pi\pi}(s,z_s) = 32\pi\sum_L (2L+1)h_L^1(s)P_L(z_s)\ , \tag{1.33}$$

where $h_L^1(s)$ denotes the partial wave of angular momentum L and isospin $I=1$, $P_L(z_s)$ the Legendre polynomials and z_s the cosine of the scattering angle. We obtain with the above partial-wave decomposition and the orthogonality relation for the Legendre polynomials

$$\mathrm{disc}\,\mathcal{F}_V(s) = 2i\sigma_\pi(s)\,\mathcal{F}_V(s)h_1^{1\,*}(s)\Theta\big(s-4M_\pi^2\big)\ , \tag{1.34}$$

with $\sigma_\pi(s) \equiv \sqrt{1-4M_\pi^2/s}$. Rewriting $h_1^1(s)$, in the elastic approximation, in favor of the vector-isovector scattering phase shift $\delta_1^1(s)$,

$$h_1^1(s) = \frac{\sin\delta_1^1(s)e^{i\delta_1^1(s)}}{\sigma_\pi(s)}\ , \tag{1.35}$$

we finally obtain the following discontinuity equation for $\mathcal{F}_V(s)$ solely depending on the phase shift $\delta_1^1(s)$,

$$\frac{1}{2i}\mathrm{disc}\,\mathcal{F}_V(s) = \mathrm{Im}\mathcal{F}_V(s) = \mathcal{F}_V(s)\sin\delta_1^1(s)e^{-i\delta_1^1(s)}\Theta\big(s-4M_\pi^2\big)\ . \tag{1.36}$$

The first equality relating the discontinuity to the imaginary part holds as the form factor satisfies the Schwarz reflection principle $F_V(s^*) = F_V^*(s)$. Note that since $\mathrm{Im}F_V(s)$ is real the right-hand side of Eq. (1.36) has to be also real. Therefore in the elastic region the phase of the pion vector form factor agrees with the $\pi\pi$ phase shift. This is known as Watson's final-state theorem [28]. Recasting Eq. (1.36) into an homogeneous Hilbert-type equation,

$$\mathcal{F}_V(s+)e^{-2i\delta_1^1(s)} - \mathcal{F}_V(s-) = 0 \quad \text{with} \quad F_V(s\pm) \equiv \lim_{\epsilon\to 0} F_V(s\pm\epsilon)\ , \tag{1.37}$$

we arrive at the classical Muskhelishvili–Omnès problem studied in Refs. [22,23]. Note that multiplying any solution with an arbitrary entire function yields also a solution. So we can define equivalence classes on the solution space

$$A(s)\sim B(s) \text{ if } \exists\ f(s)\in C^\infty(\mathbb{C}) \text{ with } A(s) = f(s)B(s) \vee B(s) = f(s)A(s)\ , \tag{1.38}$$

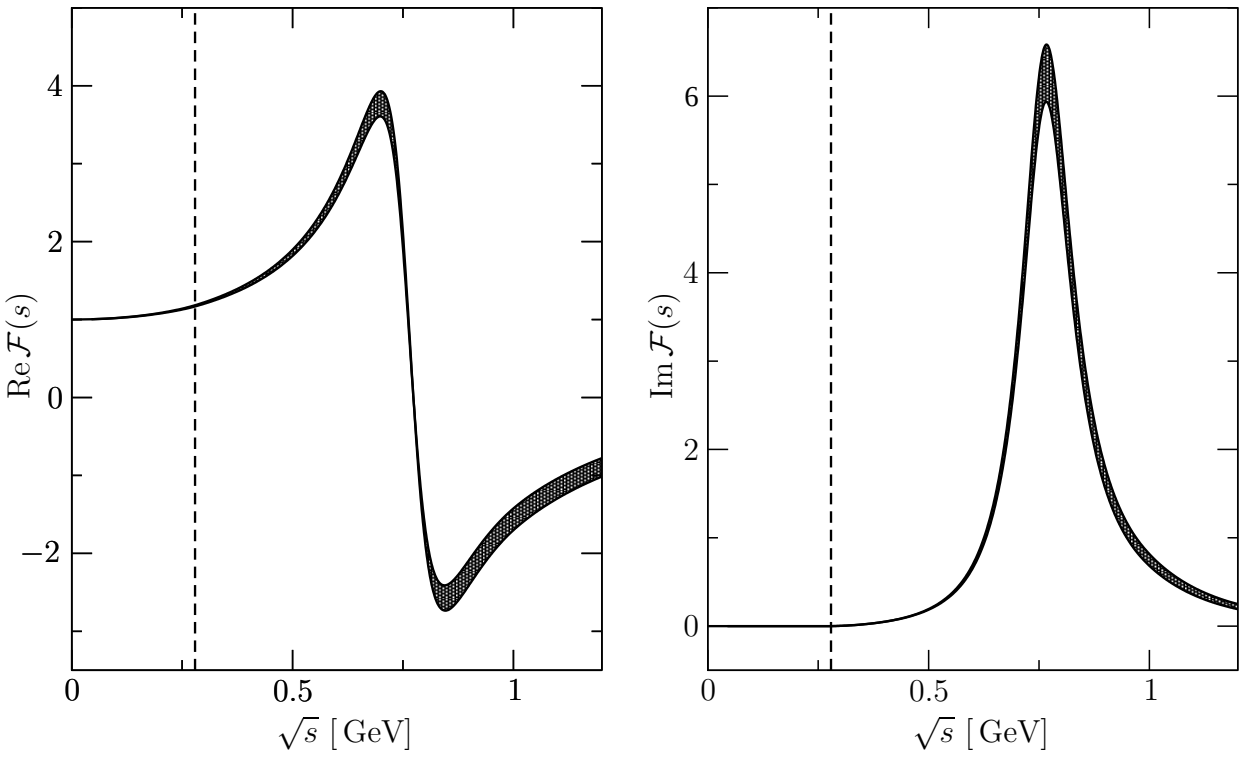

Figure 1.5: Real and imaginary part of the Omnès function given in Eq. (1.40). The error bands stem from the different phase inputs. The dashed line denotes the $\pi\pi$ threshold.

Without loss of generality we assume that the form factor has no zeros and take the logarithm of Eq. (1.37),

$$\ln\big(\mathcal{F}_V(s+)\big) - \ln\big(\mathcal{F}_V(s-)\big) = 2i\,\delta_1^1(s)\,\Theta\big(s-4M_\pi^2\big)\;,$$
$$\mathrm{Im}\ln\big(\mathcal{F}_V(s)\big) = \delta_1^1(s)\,\Theta\big(s-4M_\pi^2\big)\;.$$

Rewriting $\ln\big(\mathcal{F}_V(s)\big)$ into a once subtracted dispersion relation yields

$$\ln(\mathcal{F}_V(s)) = a + \frac{s}{\pi}\int_{4M_\pi^2}^{\infty}\frac{\delta_1^1(s')}{s'(s'-s-i\epsilon)}\mathrm{d}s'\;. \tag{1.39}$$

The solution is given via exponentiating Eq. (1.39) by the so-called Omnès function $\Omega_1^1(s)$ [22, 23], times an entire function $P_1^1(s)$

$$\mathcal{F}_V(s) = P_1^1(s)\Omega_1^1(s)\,,\quad \Omega_1^1(s) = \exp\left\{\frac{s}{\pi}\int_{4M_\pi^2}^{\infty}\mathrm{d}s'\frac{\delta_1^1(s')}{s'(s'-s)}\right\}. \tag{1.40}$$

The subtraction constant a is absorbed in the overall normalization condition $\mathcal{F}_V(0)=1$ dictated by gauge invariance. The solution is thus only dependent on the phase input

$\delta_1^1(s)$ and an entire function $P_1^1(s)$, which we can approximate by a polynomial in the energy region in question. The phase-shift input is taken from the dispersive analysis of $\pi\pi$ scattering using Roy equations in Refs. [29–31] (Bern phase) and Ref. [32] (Madrid-Krakow phase). The resulting Omnès function is depicted in Fig. 1.5, with the different phase inputs taken as an estimate of the inherent uncertainty.

Part I

$V \to 3\pi$ decays and the $J/\psi \to \pi^0\gamma^*$ transition form factor

Chapter 2

Dispersive analysis of $V \to 3\pi$ decays

2.1 Introduction

In this part of the thesis we introduce the dispersive treatment of three-body decays, based on Khuri–Treiman equations, while studying the decay of a vector-meson into three pions $V \to 3\pi$. The cases $V = \{\omega, \phi\}$ have already been studied in Refs. [33, 34]. Apart from the interest in these decays themselves, with ongoing experimental and theoretical activities, they are important ingredients in a scheme to pin down the light-by-light scattering contribution to the muon anomalous magnetic moment, see Refs. [35, 36]. They serve as input to the studies of the vector-meson transition form factors, with $\omega/\phi \to \pi^0\gamma^*$ studied in Ref. [37] and $J/\psi \to \pi^0\gamma^*$ studied in the next chapter of this thesis, or, extended to model the process $\gamma^* \to 3\pi$, to the pion transition form factor $\pi^0 \to e^+e^-\gamma$ in Ref. [38].

The theoretical framework we base our analysis on are Khuri–Treiman equations [39]. The dispersive framework adapted to study three-body decays was originally introduced for the decay $K \to 3\pi$ [39], and subsequently further developed [40–44]. The formalism has been resurrected in a modern form in Refs. [45, 46]. The Khuri–Treiman equations are based on elastic two-body unitarity respecting maximal analyticity and crossing symmetry and explicitly generate crossed-channel rescattering between the three final-state particles. The equations are constructed by setting up dispersion relations for the crossed scattering processes, with a subsequent analytic continuation back into the decay region. This continuation is performed along the lines of the continuation of the perturbative triangle graph and is extensively discussed in Ref. [40].

The explicit $V \to 3\pi$ Khuri–Treiman equations and the numerics have been studied and developed in Refs. [33,34] on $\omega/\phi \to 3\pi$. The process is maximal symmetric interchanging s- t- and u-channel and due to Bose symmetry only odd partial waves contribute. Restricting to the partial P-wave and neglecting contributions to the discontinuity from higher partial waves, the decay amplitude depends only on the input of the $\pi\pi$ P-wave phase shift which

we take from Roy equation analysis of Refs. [29–32]. The equations employed are thus simple in structure and ideal cases to introduce and study the concept of Khuri–Treiman equations.

We will explicitly study the $J/\psi \to 3\pi$ decay, the dependence of crossed-channel rescattering contributions on the decaying vector-meson mass and the convergence of the standard iterative solution strategy used to solve the Khuri–Treiman equations. Studying the $J/\psi \to 3\pi$ decay stretches the elastic two-body unitarity assumption beyond its validity. We justify it by the observation that the Dalitz plot is dominated by the quasi elastic $\pi\pi$ $\rho(770)$ resonance and no further inelastic resonance like the $\rho(1450)$ or $\rho(1700)$ resonance is observed, see Ref. [48]. However, the result should not be understood as a precision study of the $J/\psi \to 3\pi$ Dalitz plot, but as an input to the later study of the J/ψ transition form factor, for which the accuracy of the thus obtained $J/\psi \to 3\pi$ amplitude is more than satisfactory considering the available experimental data.

2.2 Kinematics and decay amplitude

We begin with kinematic definitions concerning the decay

$$V(p_V) \to \pi^+(p_+)\pi^-(p_-)\pi^0(p_0) \ , \tag{2.1}$$

and define the Mandelstam variables as follows,

$$\begin{aligned} s &= (p_+ + p_-)^2 = (p_V - p_0)^2 \ , \\ t &= (p_- + p_0)^2 = (p_V - p_+)^2 \ , \\ u &= (p_+ + p_0)^2 = (p_V - p_-)^2 \ , \end{aligned} \tag{2.2}$$

which satisfy the usual identity $s + t + u = M_V^2 + 3M_\pi^2 \equiv 3s_0$. We further define the crossed-channel scattering angles Θ by

$$\begin{aligned} \cos\Theta_s &= \angle(\vec{p}_+, \vec{p}_0) = \frac{t-u}{\kappa(s)} \ , \qquad & \cos\Theta_t &= \angle(\vec{p}_+, \vec{p}_-) = \frac{s-u}{\kappa(t)} \ , \\ \cos\Theta_u &= \angle(\vec{p}_-, \vec{p}_0) = \frac{t-s}{\kappa(u)} \ , \end{aligned} \tag{2.3}$$

with $\kappa(x)$ defined by

$$\kappa(s) = \sqrt{1 - \frac{4M_\pi^2}{s}}\lambda^{1/2}(s, M_V^2, M_\pi^2) \ , \tag{2.4}$$

with the Källén function $\lambda(x,y,z) = x^2+y^2+z^2-2(xy+xz+yz)$. The $V \to \pi^+\pi^-\pi^0$ decay is of odd intrinsic parity; we have an odd number of pseudoscalars (pions) contributing and

thus the decay is driven by the following term, which gives the only possible kinematic structure of odd intrinsic parity,

$$\propto \mathrm{Tr}\left\{\epsilon^{\mu\nu\alpha\beta}V_\mu\partial_\nu\pi^+\partial_\alpha\pi^-\partial_\beta\pi^0\right\} , \tag{2.5}$$

where V_μ is the vector-meson field. We can therefore decompose the decay amplitude $\mathcal{M}(s,t,u)$ as follows,

$$\mathcal{M}(s,t,u) = \epsilon^{\mu\nu\alpha\beta}n_\mu p^+_\nu p^-_\alpha p^0_\beta \mathcal{F}(s,t,u) , \tag{2.6}$$

where n_μ is the polarization vector of the vector meson and $\mathcal{F}(s,t,u)$ is a scalar amplitude independent of the polarization vector. With this decomposition we obtain

$$|\mathcal{M}(s,t,u)|^2 = \frac{s}{16}\kappa^2(s)\sin^2(\Theta_s)\,|\mathcal{F}(s,t,u)|^2 , \tag{2.7}$$

where we have summed over all possible polarizations. Therefore the cross section of the crossed scattering processes $V\pi \to \pi\pi$ is given by

$$\sigma(s) = \frac{1}{3072\pi^2 s}(s-4M_\pi^2)^{\frac{3}{2}}\int |\mathcal{F}(s,t,u)\sin(\Theta_s)|^2\,d\Omega . \tag{2.8}$$

We choose to investigate the scalar amplitude $\mathcal{F}(s,t,u)$ in the helicity basis. The helicity formalism is favorable, since we do not have to investigate the orbital angular momentum and spin structure separately. The helicity is invariant under rotations such that states of definite angular momentum and helicity can be constructed. This is fundamental to obtain a consistent partial-wave description in the helicity formalism. The following considerations and notations are taken from Ref. [50].

Instead of using the standard spin-quantization axis (conventionally the z-axis), we use the particle trajectory as the spin-projection axis. This projection is called helicity λ. We choose the helicity plane wave state $\psi_{p\lambda}$ to have momentum p and helicity λ in the z-direction. Arbitrary directions can be obtained by rotation,

$$\mathcal{R}_{\alpha\beta\gamma} = e^{-i\alpha J_z}e^{-i\beta J_y}e^{-i\gamma J_z} , \tag{2.9}$$

where J_x are the angular momentum operators. We define the rotated state by

$$|p;\Theta,\phi;\lambda\rangle \equiv \mathcal{R}_{\phi\Theta-\phi}\psi_{p\lambda} . \tag{2.10}$$

This formalism can be extended naturally to a two-particle state and simplified in the center-of-mass system

$$\psi_{p\lambda_1\lambda_2} \equiv \psi_{p\lambda_1}\otimes\chi_{p\lambda_2} , \tag{2.11}$$

where the momentum of $\chi_{p\lambda_2}$ is orientated in the negative z-direction, p being the relative momentum and the overall helicity $\lambda = \lambda_1 - \lambda_2$ being invariant under rotations. An arbitrary direction of this two-particle state is then obtained by applying Eq. (2.9). Thus by switching to a common eigenbasis $|p; J, M; \lambda_1, \lambda_2\rangle$ we get a (unitary) irreducible representation of rotations,

$$D^j_{m'm}(\alpha, \beta, \gamma) = \langle jm'|\mathcal{R}_{\alpha\beta\gamma}|jm\rangle = e^{-im'\alpha} d^j_{m'm}(\beta) e^{-im\gamma} \ . \tag{2.12}$$

$D^j_{m'm}(\alpha, \beta, \gamma)$ are the Wigner D-matrices and $d^j_{m'm}(\beta)$ are called small Wigner d-matrices.

In the following we are mainly interested in the partial-wave projection of $\mathcal{F}(s, t, u)$. The plan is to deduce from the cross section and partial-wave decomposition of $\mathcal{M}(s, t, u)$ the form of the partial-wave decomposition of the scalar amplitude. We implement the following agenda with the explicit derivation given in Appendix B:

1. Derive the transition matrix from plane wave states $|p; \Theta, \phi; \lambda_1, \lambda_2\rangle$ to helicity states with definite angular momenta and z-component $|p; J, M; \lambda_1, \lambda_2, \rangle$.

2. Rewrite the S-matrix elements in this basis and deduce the partial-wave decomposition of $\mathcal{M}(s, t, u)$.

3. Calculate the form of the cross section in the helicity formalism and compare with the cross section of Eq. (2.8) to obtain the partial-wave decomposition of $\mathcal{F}(s, t, u)$.

In the helicity basis we obtain for the cross section

$$\sigma = \int \left| \frac{1}{2\sqrt{s}} \sum_J \frac{2J+1}{\sqrt{J(J+1)}} \langle 0, 0|T^J(s)|1, 0\rangle \, P'_J(\cos\Theta) \right|^2 \sin^2(\Theta) \, \mathrm{d}\Omega \ . \tag{2.13}$$

A comparison of Eq. (2.8) with Eq. (2.13) yields for the partial-wave decomposition

$$\mathcal{F}(s, t, u) = \sum_J f_J(s) P'_J(\cos\Theta_s) \ . \tag{2.14}$$

Additionally, bose symmetry dictates that only odd partial waves contribute; considering the scattering process $V\pi \to \pi\pi$ the final-state two-pion system has to have isospin one. To obtain a symmetric two-pion wave function the angular momentum of the two pions has to be odd. Applying the orthogonality relation of the differentiated Legendre polynomials,

$$\frac{1}{2} \int_{-1}^{1} P'_j(z)(P_{l-1}(z) - P_{l+1}(z)) \mathrm{d}z = \delta_{lj} \ , \tag{2.15}$$

we obtain for the P-wave projection of $\mathcal{F}(s, t, u)$

$$f_1(s) = \frac{3}{8\pi} \int \mathcal{F}(s, t, u) \sin^2(\Theta) \, \mathrm{d}\Omega \ . \tag{2.16}$$

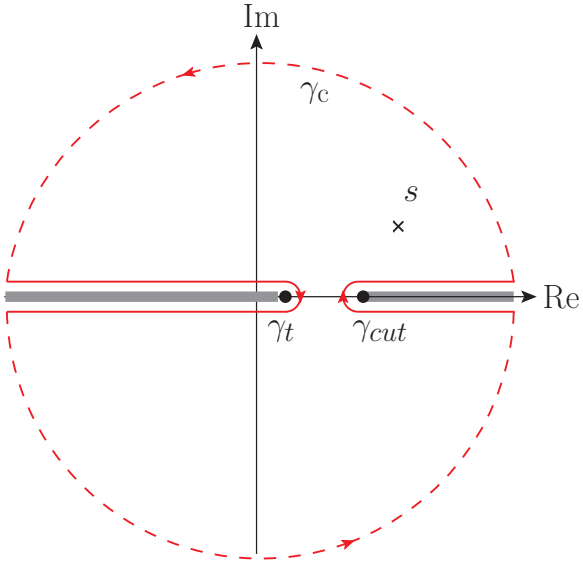

Figure 2.1: The analytic structure and dispersive integration path of the fixed-u dispersion relation fixed at u_0. γ_{cut} denotes the integration path around the right-hand cut, which starts at the two-particle threshold (here $s \geq 4M_\pi^2$) and γ_t gives the integration contour around the left-hand cut which originates from the t-channel discontinuity $t > 4M_\pi^2$ and translates into the s-channel to give $s < M_V^2 - M_\pi^2 - u_0$.

The P-wave projection is in accordance with Ref. [51]. The next higher contributing partial wave would be the F-wave. It was extensively argued in Appendix A of Ref. [34] that contributions are negligible for the ω/ϕ decays. For the J/ψ decay we again refer to the phenomenological findings of Ref. [48] that no F-wave resonances, e.g. the $\rho_3(1690)$ resonance, or higher partial-wave resonances are observed. Note also that only the P-wave is of importance for the transition form factor study. In the next section we will introduce and develop the dispersive framework for three-body decays.

2.3 Dispersive treatment of three-body decays

In this section we will introduce the dispersive description of three-particle decays built on Khuri–Treiman equations. Once more, the inaugural step is the study of the analytic structure of the decay amplitude in question. The scalar decay amplitude $\mathcal{F}(s,t,u)$ as such depends on two kinematical variables and therefore exhibits an elaborate analytic structure. Setting up a dispersion relation directly is thus not easy. To simplify the task we employ a decomposition of the decay amplitude into amplitudes depending on one single

kinematical variable only (single-variable amplitudes) known as reconstruction theorem, see Refs. [46, 52–56].

We start our considerations with the crossed-channel scattering processes of the $V \to 3\pi$ decay, namely $V\pi \to \pi\pi$. Furthermore, we restrict ourselves to vector-meson masses of $M_V < 3M_\pi$ such that the vector-meson decay into three pions is kinematically forbidden. This is mandatory since the left- and right-hand cuts would otherwise overlap. In this scenario the scalar amplitude $\mathcal{F}(s,t,u)$ has a much simpler analytic structure. We can set up a fixed-x dispersion relation in a particular crossed-channel, where x is the placeholder for Mandelstam s, t, or u. Fixed-x dispersion relations are dispersion relations with the Mandelstam variable x fixed to a constant. Additionally, we utilize a partial-wave expansion, which directly leads to a decomposition of the scalar amplitude in single-variable amplitudes. This has to be performed generally for all three channels (s-, t-, and u-channel), however, the $V \to 3\pi$ amplitude is fully symmetric in the s-, t-, and u-channel assuming isospin symmetry. Thus we only have to study one of these fixed dispersion relations. The full amplitude is then given by symmetrization.

Explicitly we study the s-channel process by fixing the Mandelstam variable $u = u_0$ with u_0 arbitrary but fixed. The resulting analytic structure in the s-plane is depicted in Fig. 2.1 with the right-hand cut ($s \geq 4M_\pi^2$) and the left-hand cut stemming from the t-channel discontinuity ($t \geq 4M_\pi^2$). The fixed-u dispersion relation thus reads

$$\begin{aligned}\mathcal{F}(s,t,u_0) =& P^{n-1}(s,t,u_0) + \frac{s^n}{2i\pi}\int_{4M_\pi^2}^{\infty} \frac{\operatorname{disc}\mathcal{F}(s',t'(s'),u_0)}{s'^n(s'-s)}\mathrm{d}s' \\ &+ \frac{t^n}{2i\pi}\int_{4M_\pi^2}^{\infty} \frac{\operatorname{disc}\,\mathcal{F}(s'(t'),t',u_0)}{t'^n(t'-t)}\mathrm{d}t' \ , \end{aligned} \tag{2.17}$$

with the number of subtractions n not fixed yet. We decompose the amplitude $\mathcal{F}(s,t,u_0)$ in s- and t-channel partial waves following Eq. (2.14),

$$\begin{aligned} &s\text{-channel:} && \mathcal{F}(s,t(s),u_0) = \sum_{\text{odd } l} f_l^1(s) P_l'(z_s) \ , \\ &t\text{-channel:} && \mathcal{F}(s(t),t,u_0) = \sum_{\text{odd } l} f_l^1(t) P_l'(z_t) \ , \end{aligned} \tag{2.18}$$

where again we only consider the P-wave and neglect higher partial waves. We thus have

$$\mathcal{F}(s,t,u_0) = P^{n-1}(s,t,u_0) + \frac{s^n}{2i\pi}\int_{4M_\pi^2}^{\infty} \frac{\operatorname{disc} f_1^1(s')}{s'^n(s'-s)}\mathrm{d}s' + \frac{t^n}{2i\pi}\int_{4M_\pi^2}^{\infty} \frac{\operatorname{disc} f_1^1(t')}{t'^n(t'-t)}\mathrm{d}t' \ , \tag{2.19}$$

and similar results for fixed-t and fixed-s dispersion relations. The symmetrization of all

fixed dispersion relations is thus trivial and we obtain

$$\begin{aligned}\mathcal{F}(s,t,u) =& P^{n-1}(s,t,u) + \frac{s^n}{2i\pi}\int_{4M_\pi^2}^{\infty}\frac{\operatorname{disc} f_1^1}{s'^n(s'-s)}\mathrm{d}s' + \frac{t^n}{2i\pi}\int_{4M_\pi^2}^{\infty}\frac{\operatorname{disc} f_1^1}{t'^n(t'-t)}\mathrm{d}t' \\ &+ \frac{u^n}{2i\pi}\int_{4M_\pi^2}^{\infty}\frac{\operatorname{disc} f_1^1(u')}{u'^n(u'-t)}\mathrm{d}u' \ . \end{aligned} \tag{2.20}$$

The number of subtractions as explained in Section 1.3.2 depends on the assumed asymptotic behavior of the decay amplitude and is chosen such that the dispersion integrals converge. We loosely base our assumption on the asymptotic behavior upon the Froissart bound [57]. The Froissart bound gives an asymptotic bound on the absolute value of elastic scattering amplitudes; the absolute value of the crossed scattering amplitude $V\pi \to \pi\pi$ is therefore bounded asymptotically by $s\,\ln^2(s)$. The phase-space factor of Eq. (2.6) scales like p^3 and thus $\mathcal{F}(s,t,u)$ and also $f_1^1(s)$ are asymptotically of order $s^{-1/2}\ln^2(s)$ or smaller. To obtain convergent integrals in Eq. (2.20) we thus need at least one subtraction. The full decay amplitude is hence decomposed into

$$\mathcal{F}(s,t,u) = \mathcal{F}(s) + \mathcal{F}(t) + \mathcal{F}(u) \ , \tag{2.21}$$

with

$$\mathcal{F}(s) = c_0 + \frac{s}{2i\pi}\int_{4M_\pi^2}^{\infty}\frac{\operatorname{disc}\mathcal{F}(s',t'(s'),u_0)}{s'(s'-s)}\mathrm{d}s' \ , \tag{2.22}$$

with an arbitrary subtraction constant c_0 such that $P^{n-1}(s,t,u) = 3c_0$. To this end Eq. (2.22) gives the corresponding crossed-channel scattering amplitudes $V\pi \to \pi\pi$ for $M_V < 3\pi$. The description of the decay channel thus necessitates an analytic continuation to physical vector-meson masses as well as into the decay region. However, it is not directly apparent how this continuation can be performed. Worst of all the solutions to dispersion relations of the form of Eq. (2.22) are generally not unique, see Ref. [45]. Therefore they are not suited to treat three-particle decay processes.

In the following, we will rectify this caveat and introduce Khuri–Treiman-type dispersion relations. Again we choose the mass of the vector particle such that the decay into three pions is kinematically forbidden, $M_V < 3M_\pi$. From here on, we will work in the helicity basis introduced in Section 2.2. To clarify the angular dependencies we first write the unitarity relation Eq. (1.20) with explicit helicity states defined in Section 2.2, following Ref. [47]. The reference frame is chosen such that the overall amplitude depends only on one angle and the CMS energy. As noted in Appendix B it suffices to study the helicity $\lambda = 1$ initial state. The unitarity relation in the s-channel ($V\pi^0 \to \pi^-\pi^+$) reads

$$\operatorname{disc}\mathcal{M}_{fi}(s,\Theta) = i\sum_{m,\mu}(2\pi)^4\,\delta^4(p_m - p_i)\mathcal{M}^*_{fm}(s,\mu,\Omega_m,\Theta)\mathcal{M}_{mi}(s,\mu,\Omega_m) \ , \tag{2.23}$$

where the sum runs over all possible intermediate states m with helicity settings μ, Ω_m denotes the solid angle between initial and intermediate states, Θ stands for the scattering angle, and the amplitudes expressed in the helicity basis

$$\begin{aligned}
\mathcal{M}_{fi}(s,\Theta) &\equiv \langle p_f; J_f, M_f; 0,0|T(s)|p_i, J_i, M_i; 1,0\rangle \ , \\
\mathcal{M}^*_{fm}(s,\mu,\Omega_m,\Theta) &\equiv \langle p_f; J_f, M_f; 0,0|T^*(s)|p_m; J_m, M_m; \lambda_A, \lambda_B\rangle \ , \\
\mathcal{M}_{mi}(s,\mu,\Omega_m) &\equiv \langle p_m; J_m, M_m; \lambda_A, \lambda_B|T(s)|p_i; J_i, M_i; 1,0\rangle \ .
\end{aligned} \tag{2.24}$$

Restricting to the elastic case we obtain

$$\begin{aligned}
\operatorname{disc}\mathcal{M}_{fi}(s,\Theta) =& \frac{i}{(2\pi)^2}\sum_\mu \int \frac{\mathrm{d}^3p_-\mathrm{d}^3p_+}{4E_1E_2}\,\delta^4\left(p_- + p_+ - p_i\right)\mathcal{M}^*_{ff'}(s,\mu,\Omega_m,\Theta)\mathcal{M}_{f'i}(s,\mu,\Omega_m) \\
=& \frac{i}{4(2\pi)^2}\sqrt{\frac{s-4M_\pi^2}{s}}\sum_\mu \int \mathrm{d}\Omega_m\,\mathcal{M}^*_{ff'}(s,\mu,\Omega_m,\Theta)\mathcal{M}_{f'i}(s,\mu,\Omega_m) \ .
\end{aligned} \tag{2.25}$$

The partial-wave decompositions read, following Appendix B Eq. (B.7),

$$\begin{aligned}
\mathcal{M}_{f'i}(s,\mu,\Omega) &= \sum_{\text{odd l}} f_l^1(s) D^l_{\mu 1}(\Omega) \ , \\
\mathcal{M}_{ff'}(s,\mu,\Omega) &= \sum_{\text{odd j}} h_j^1(s) D^j_{\mu 0}(\Omega) \ ,
\end{aligned} \tag{2.26}$$

where f_L^1 and h_L^1 denote the partial waves with isospin $I=1$ and angular momentum L and $D^l_{\mu 1}(\Omega)$ the Wigner D-matrices. Using the addition theorems for Wigner D-matrices

$$\sum_{\mu=-J}^{+J} D^J_{\mu 0}(\alpha,\beta,\gamma)\left(D^J_{\mu 1}(\psi,\Theta,\phi)\right)^\dagger = \left(D^J_{01}(\psi',\Theta',\phi')\right)^\dagger \ , \tag{2.27}$$

together with the Wigner–Eckart theorem

$$\langle p_f; J_f, M_f; \lambda_c\lambda_d|T(s)|p_i; J_i, M_i; \lambda_a\lambda_b\rangle = \langle \lambda_c, \lambda_d|T_J(s)|\lambda_a,\lambda_b\rangle \delta^J_{J_i}\delta^{M_f}_{M_i}\delta^J_{J_f} \ , \tag{2.28}$$

we obtain from Eq. (2.25) with the partial-wave decompositions Eq. (2.26)

$$\sum_l D^l_{01}(\Omega)\operatorname{disc} f_l^1(s) = \frac{i}{4\pi}\sqrt{\frac{s-4M_\pi^2}{s}}\sum_l g_l^1(s)^* f_l^1(s)\, D^l_{01}(\Omega)\,\Theta\big(s-4M_\pi^2\big) \ . \tag{2.29}$$

The unitarity relation for the P-wave reads

$$\operatorname{Im} f_1^1(s) = \frac{1}{8\pi}\sqrt{\frac{s-4M_\pi^2}{s}} g_1^1(s)^* f_1^1(s)\,\Theta\big(s-4M_\pi^2\big) \ . \tag{2.30}$$

We can deduce that the partial wave $f_1^1(s)$ has to have the same phase as the $\pi\pi$ scattering partial wave g_1^1 since the right-hand side of Eq. (2.30) has to be real. This is known by Watson's final state theorem [28]. Similarly we construct the unitary relation for elastic $\pi\pi$ P-wave scattering,

$$\operatorname{Im} g_1^1(s) = \frac{1}{8\pi}\sqrt{\frac{s-4M_\pi^2}{s}}|g_1^1(s)|^2\,\Theta\big(s-4M_\pi^2\big)\ . \tag{2.31}$$

Combining Eq. (2.30) and Eq. (2.31) the unitarity relation for the partial wave $f_1^1(s)$ reads

$$\operatorname{Im}\ f_1^1(s) = f_1^1(s)e^{-i\delta_{ff'}(s)}\sin\delta_{ff'}(s)\ , \tag{2.32}$$

which depends only on the $\pi\pi$-P-wave scattering phase shift. In order to rewrite Eq. (2.32) in terms of the single-variable amplitude $\mathcal{F}(s)$ we apply the Sokhotsky–Weierstrass theorem to Eq. (2.22) and read off

$$\begin{aligned}&\operatorname{Im} f_1^1(s) = \operatorname{Im}\mathcal{F}(s)\\ &\Rightarrow f_1^1(s) = \mathcal{F}(s)+\hat{\mathcal{F}}(s)\ ,\end{aligned} \tag{2.33}$$

with a yet unknown function $\hat{\mathcal{F}}(s)$, called inhomogeneity, that is real on the right-hand cut. Rewriting Eq. (2.32) with respect to the single-variable amplitude $\mathcal{F}(s)$ using Eq. (2.33) we finally obtain

$$\operatorname{disc}\mathcal{F}(s) = 2i\big(\mathcal{F}(s)+\hat{\mathcal{F}}(s)\big)e^{-i\delta_{ff'}(s)}\sin\delta_{ff'}(s)\,\Theta\big(s-4M_\pi^2\big)\ . \tag{2.34}$$

This unitarity relation looks similar to the one of the pion vector form factor Eq. (1.36) except that we have the additional inhomogeneous term $\hat{\mathcal{F}}(s)$. We will see in the following that the inhomogeneity is related to left-hand-cut contributions and will correspond in the decay region to crossed-channel rescattering (see Fig. 2.2).

Inhomogeneous solution

In this section we want to solve Eq. (2.34) for $\mathcal{F}(s)$. The homogeneous case ($\hat{\mathcal{F}}(s)=0$) has been solved in Section 1.4 and is given by the Omnès function. We use a product ansatz to obtain the inhomogeneous solution, very similar to solving inhomogeneous ordinary differential equations,

$$\mathcal{F}(s) = \Omega_1^1(s)\Phi(s)\ , \tag{2.35}$$

with the Omnès function $\Omega_1^1(s)$ satisfying the homogeneous equation Eq. (1.36). Thus we get from Eq. (2.34) a discontinuity equation for $\Phi(s)$,

$$\begin{aligned}\exp\big[-2i\delta_1^1(x)\big]\mathcal{F}(s+)-\mathcal{F}(s-) &= 2i\hat{\mathcal{F}}(s)e^{-i\delta_1^1(s)}\sin\delta_1^1(s)\ \Theta\big(s-4M_\pi^2\big)\\ \Leftrightarrow\ \big[\Phi(s+)-\Phi(s-)\big]\Omega(s-) &= 2i\hat{\mathcal{F}}(s)e^{-i\delta_1^1(s)}\sin\delta_1^1(s)\ \Theta\big(s-4M_\pi^2\big)\\ \Leftrightarrow\ \operatorname{disc}\Phi(s) &= 2i\frac{\hat{\mathcal{F}}(s)\sin\delta(s)}{|\Omega(s)|}\ \Theta\big(s-4M_\pi^2\big)\ ,\end{aligned} \tag{2.36}$$

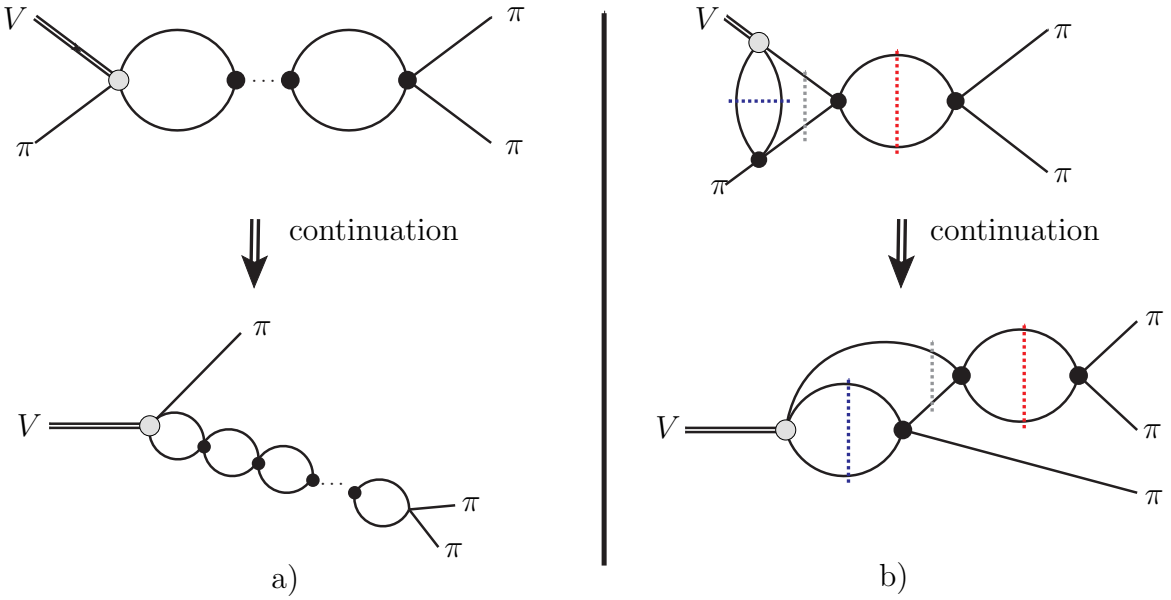

Figure 2.2: Figure a) depicts the diagrammatic two-particle rescattering contributions of the Omnès function and the corresponding continuation into the decay region with the third pion as spectator. Figure b) shows the additional crossed-channel rescattering topology (triangle graph) and its continuation into the decay region. The blue and gray dashed lines denote the additional contributions to the unitarity relation on top of the pure two-particle contribution denoted by the red dashed line.

which enables us to write $\Phi(s)$ in the following dispersion relation,

$$\Phi(s) = P_{n-1}(s) + \frac{s^n}{\pi} \int_{4M_\pi^2}^{\infty} \frac{\mathrm{d}s'}{s'^n} \frac{\sin \delta_1^1(s') \hat{\mathcal{F}}(s')}{|\Omega(s')|(s'-s)} \,, \tag{2.37}$$

with n subtractions chosen such that the convergence of the dispersion integral is guaranteed and $P_{n-1}(s)$ is the subtraction polynomial of order $n-1$.

Again the number of subtractions needs to be determined by the high-energy behavior of the integrand. We assume that the $\pi\pi$ scattering phase asymptotically reaches π and according to Appendix A.1 the Omnès function thus asymptotically behaves like $1/s$. This is motivated by the naive high energy behavior of the pion vector form factor $F_\pi^V(s)$, which is dominated by the one-gluon exchange,

$$F_\pi^V(s) \propto \frac{\alpha(s)}{s} \to \frac{1}{s} \,, \tag{2.38}$$

up to logarithmic corrections. The inhomogeneity $\hat{\mathcal{F}}(s)$ is asymptotically like $\mathcal{F}(s)$ of order $s^{-1/2} \ln^2(s)$ or lower, see Eq. (2.33). Therefore, we need again one subtraction to obtain a

convergent dispersion integral

$$\mathcal{F}(s) = \Omega(s)\left\{c_0 + \frac{s}{\pi}\int_{4M_\pi^2}^{\infty}\frac{\mathrm{d}s'}{s'}\frac{\sin\delta_1^1(s')\hat{\mathcal{F}}(s')}{|\Omega_1^1(s')|(s'-s)}\right\} . \tag{2.39}$$

To obtain an integral equation for $\mathcal{F}(s)$ we have to rewrite the inhomogeneity $\hat{\mathcal{F}}(s)$ in terms of $\mathcal{F}(s)$. With $\hat{\mathcal{F}}(s)$ defined by Eq. (2.33) we have

$$\begin{aligned}\hat{\mathcal{F}}(s) = f_1^1(s) - \mathcal{F}(s) &= \frac{3}{8\pi}\int \sin^2(\Theta)\left[\mathcal{F}(s) + \mathcal{F}\big(t(s,\Theta)\big) + \mathcal{F}\big(u(s,\Theta)\big)\right]\mathrm{d}\Omega - \mathcal{F}(s)\\ &= \frac{3}{4}\int \sin^3(\Theta)\left[\mathcal{F}\big(t(s,\Theta)\big) + \mathcal{F}\big(u(s,\Theta)\big)\right]\mathrm{d}\Theta \qquad (2.40)\\ &= 3\langle(1-z^2)\mathcal{F}\rangle , \qquad (2.41)\end{aligned}$$

with the angular average $\langle z^n\mathcal{F}\rangle$ defined by

$$\left\langle z^n\mathcal{F}\right\rangle \equiv \frac{1}{2}\int_{-1}^{1} z^n\mathcal{F}\left(\frac{3s_0 - s + z\kappa(s)}{2}\right)\mathrm{d}z , \tag{2.42}$$

and $z = \cos\Theta_s$. The inhomogeneities thus give the contributions from the crossed channels, see Eq. (2.40), or in other words the left-hand-cut contributions to the partial wave. While the homogeneous Omnès solutions give the two-body final-state rescattering, the dispersive integrals over the inhomogeneities produce crossed-channel three-particle rescattering among the final states, see Fig. 2.2. Finally we need to continue Eq. (2.39) to physical decay masses and into the decay region. This is extensively explained in Appendix B of Ref. [34]. However, the continuation is not straight forward. Performing the z-integration in Eq. (2.42) naively can lead to crossing the branch cut when M_V is continued beyond $3M_\pi$. This is a feature of the arising three-particle cut, which becomes physically accessible, and thus a integration path deformation is mandatory.

The analytic continuation is performed along the lines of the continuation of the perturbative triangle graph into the decay region and is extensively discussed in Ref. [40]. We have seen above in Fig. 2.2 that these triangle topologies are exactly the ones the dispersion integral over the inhomogeneities produces. To obtain the correct analytic behavior, consistent with the triangle topology continuation, we need to give the squared vector-meson mass an infinitesimal positive imaginary part, $M_V^2 + i\epsilon$. The continuation into the decay region is then trivial. The only M_V-dependent pieces we have to carefully analytically continue are the angular-average integrations Eq. (2.42). We rewriting the angular integral as follows,

$$\frac{1}{2}\int_{-1}^{1} z^n F\left(\frac{3s_0 - s + z\kappa(s)}{2}\right)\mathrm{d}z = \frac{1}{\kappa(s)}\int_{s_-(s)}^{s_+(s)}\mathrm{d}s'\left(\frac{2s' - 3s_0 + s}{\kappa(s)}\right)^n\mathcal{F}(s') , \tag{2.43}$$

where we have substituted $s' = 3s_0 - s + z\kappa(s)$ and the integration points are thus given by

$$s_\pm = \frac{1}{2}(3s_0 - s \pm \kappa(s)) \ . \tag{2.44}$$

The critical M_V dependence resides now only in the integration limits $s_\pm(s)$. Employing the $M_V^2 + i\epsilon$ description yields

$$s_\pm(s, M_V^2 + i\epsilon) = s_\pm(s, M_V^2) + i\epsilon \frac{\partial s_\pm(s, M_V^2)}{\partial M_V^2} \ . \tag{2.45}$$

Explicitly we thus obtain

$$\begin{aligned}
2s_+(s) &= \begin{cases} 3s_0 - s + |\kappa(s)| + i\epsilon \,, & s \in [4M_\pi^2, a] \,, \\ 3s_0 - s + i|\kappa(s)| \,, & s \in [a, b] \,, \\ 3s_0 - s - |\kappa(s)| \,, & s \in [b, \infty] \,, \end{cases} \\
2s_-(s) &= \begin{cases} 3s_0 - s - |\kappa(s)| + i\epsilon \,, & s \in \left[4M_\pi^2, \frac{M_V^2 - M_\pi^2}{2}\right] \,, \\ 3s_0 - s - |\kappa(s)| - i\epsilon \,, & s \in \left[\frac{M_V^2 - M_\pi^2}{2}, a\right] \,, \\ 3s_0 - s - i|\kappa(s)| \,, & s \in [a, b] \,, \\ 3s_0 - s + |\kappa(s)| \,, & s \in [b, \infty] \,, \end{cases}
\end{aligned} \tag{2.46}$$

where $a \equiv (M_V - M_\pi)^2$ and $b \equiv (M_V + M_\pi)^2$. The angular integration limits thus avoid the branch cut and the integration has to be performed such that the branch cut is not crossed. All further details are given in Ref. [34] and references therein.

2.4 Solution strategy and numerical implementation

With the Khuri–Treiman-type equations Eq. (2.39) constructed we come to the numerical solution strategy of these integral equations. We follow the numerical strategies employed for example in Refs. [45,46]. The equation is linear in the single-variable amplitude $\mathcal{F}(s)$ and also in the subtraction constants. Denoting the number of subtraction constants by n, we therefore have an n-dimensional solution space. The basis functions that span this solution space can be obtained by choosing a maximal set of linearly independent subtraction-constant configurations and solve the integral equations for each configuration. Thus the general solution can be written as a linear combination

$$\mathcal{F}(s, t, u) = \sum_i^n c_i \mathcal{F}_i(s, t, u) \ , \tag{2.47}$$

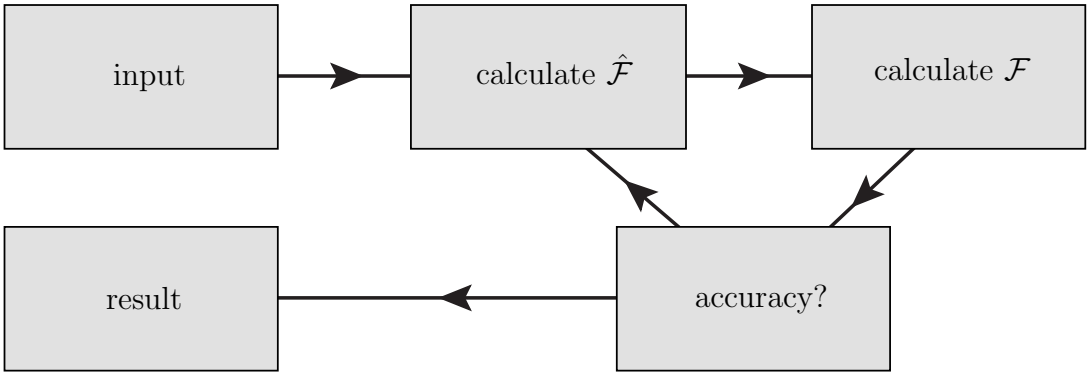

Figure 2.3: The standard numerical iteration scheme to solve the Khuri–Treiman equations is shown. Starting with an arbitrary input for the single-variable amplitudes, most efficiently the Omnès function, the inhomogeneities are calculated. With these a new set of single-variable amplitudes is calculated. The procedure is resumed until satisfactory convergence is achieved.

where the $\mathcal{F}_i(s,t,u)$ are the basis functions, the solutions to the subtraction-constant configuration, for example $c_j = \delta_{ij},\ j \in \{0,1,..,n-1\}$. In our explicit $V \to 3\pi$ case, given by Eq. (2.39), we have only one subtraction and thus only one basis function. The subtraction constant can be seen as just an overall normalization such that the obtained energy dependence of the calculated decay amplitude is a pure prediction.

Generally, the integral equations, for a fixed subtraction configuration, are solved by an iterative solution procedure depicted in Fig. 2.3. It is the standard method used to solve these equations, being numerically simple and fast. Starting with an arbitrary input for the single-variable amplitudes, the inhomogeneities are evaluated. With these the dispersion integrals are determined to obtain a new set of single-variable amplitudes. This cycle is repeated until satisfactory convergence is reached. In the case of convergence the solution is unique as we will see later in Section 4.4 when we review and develop a new solution strategy. However, it is not guaranteed that the iteration does converge to a solution and we will show numerically that under some circumstances the iteration procedure indeed breaks down.

The numerical implementation of the iterative procedure has been described in many previous works. We will display the most common implementation method performed in Refs. [33, 46, 58], to name a few. The dispersion relation we have to solve is given by Eq. (2.39)

$$\mathcal{F}(s) = \Omega(s)\left\{c_0 + \frac{s}{\pi}\int_{4M_\pi^2}^{\infty}\frac{\mathrm{d}s'}{s'}\frac{\sin\delta_1^1(s')\tilde{\mathcal{F}}(s')}{|\Omega_1^1(s')|\kappa^3(s')(s'-s)}\right\}\,. \tag{2.48}$$

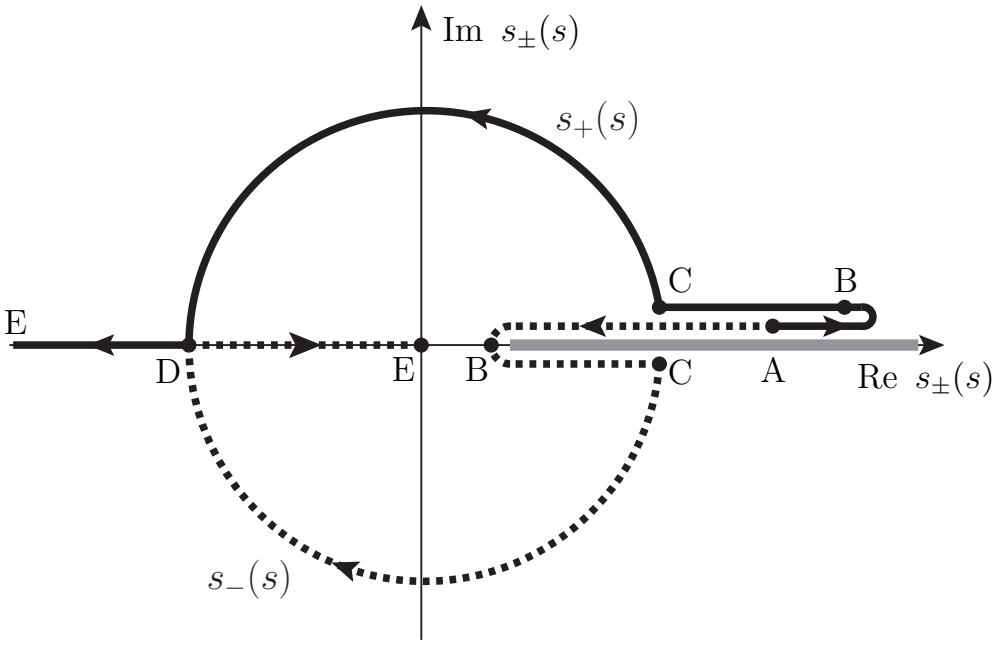

Figure 2.4: The contours of the integration end points $s_\pm(s)$ of Eq. (2.46). The contours start at the same point A $\left(s_\pm(4M_\pi^2)\right)$ above the branch cut. At point B $\left(s_\pm((M_V^2-M_\pi^2)/2)\right)$ the s_- contour reaches $4M_\pi^2$ and moves below the cut. From point C $(s_\pm(a))$ onwards to point D $\left(s_\pm(b)\right)$, s_- and s_+ have the same real part but opposite imaginary part. The contours finally meet at point D. From point D onwards both contours are purely real with s_- moving towards zero and s_+ to minus infinity.

where we have expressed the inhomogeneity by a singularity-free function $\tilde{\mathcal{F}}$ divided by κ^3 ,

$$\tilde{\mathcal{F}}(s) \equiv \kappa^3(s)\hat{\mathcal{F}} = 3\int_{s_-(s)}^{s_+(s)} ds' \left(\kappa^2(s) - (2s' - 3s_0 + s)^2\right)\mathcal{F}(s') \ . \tag{2.49}$$

This decomposition enables us to carefully investigate the singularity structure later on.

Following the iteration scheme in Fig. 2.3 the first step is the determination of the inhomogeneity or equivalently $\tilde{\mathcal{F}}(s)$, Eq. (2.49), from the input function. The integrand of Eq. (2.49) is well-behaving and poses no numerical problem, however the integration contour does. As discussed above the direct line integration from $s_-(s)$ to $s_+(s)$ can cross the branch cut and therefore the integration contour needs to be deformed. Explicitly the contours of the integration end points Eq. (2.46) are sketched in Fig. 2.4. The issue of integrating across the branch cut arises after point B where $s_-(s)$ moves below the branch cut while $s_+(s)$ stays above. Additionally, we can exploit the contours of the integration end points and take these as integration path. This has the advantage that the integrand needs

to be evaluated only on these integration end point contours. As we want to interpolate the integrand to save computation time this hugely simplifies the task to a one-dimensional interpolation rather than interpolating a two-dimensional grid. We will now discuss in more detail how the angular integration is performed. For $s < (M_V^2 - M_\pi^2)/2$ both integration end points are above the branch cut and the integral can be performed directly. This changes for the interval $(M_V^2 - M_\pi^2)/2 < s < a$. We choose the following integration contour: starting below the cut we integrate from $s_-(s)$ to $4M_\pi^2 - i\epsilon$ and then move above the cut and integrate from $4M_\pi^2 + i\epsilon$ to $s_+(s)$. This translates to

$$\begin{aligned}\tilde{\mathcal{F}}(s) =& 3\int_{s_-(s)}^{4M_\pi^2 - i\epsilon} ds' \left(\kappa^2(s) - (2s' - 3s_0 + s)^2\right)\mathcal{F}(s') \\ &+ 3\int_{4M_\pi^2 + i\epsilon}^{s_+(s)} ds' \left(\kappa^2(s) - (2s' - 3s_0 + s)^2\right)\mathcal{F}(s') \ . \end{aligned} \tag{2.50}$$

In the interval $a \leq s \leq b$ we want to exploit the fact that $s_+(b) = s_-(b)$ and parametrize the integration contours via $s_\pm(s)$. Unfortunately this parametrization has a singular Jacobian at the roots of $\kappa(s)$, namely $s = a$ and $s = b$. To bypass this issue we further substitute in Eq. (2.49)

$$y_s(s') = \begin{cases} \sqrt{\frac{\sqrt{s'}+(M_V-M_\pi)}{2}} - \sqrt{\frac{\sqrt{s'}-(M_V-M_\pi)}{2}}, & \text{for } s' \in \left[a, \frac{a+b}{2}\right] \\ \sqrt{\frac{(M_V+M_\pi)+\sqrt{s'}}{2}} - \sqrt{\frac{(M_V+M_\pi)-\sqrt{s'}}{2}}, & \text{for } s' \in \left]\frac{a+b}{2}, b\right] \end{cases} , \tag{2.51}$$

to obtain a non-singular Jacobian. The integration in the interval $a \leq s \leq b$ is performed as follows. We start by integrating from $s_-(s)$ to $s_-(b)$ (point D in Fig. 2.4), where the $s_-(s)$ and $s_+(s)$ contours meet, change to the $s_+(s)$ parametrization and integrate similarly to $s_+(s)$. Expressed in formulas this gives

$$\begin{aligned}\tilde{\mathcal{F}}(s) =& 3\left[\int_{y_s(s_-(s))}^{y_s(s_-(b))} \left[\mathcal{F}(s'(y_s))\kappa^2(s) - (2s'(y_s) - 3s_0 + s)^2\mathcal{F}(s'(y_s))\right]\frac{\mathrm{d}s'}{\mathrm{d}y_s}\mathrm{d}y_s \right. \\ &\left. + \int_{y_s(s_+(b))}^{y_s(s_+(s))} \left[\mathcal{F}(s'(y_s))\kappa^2(s) - (2s'(y_s) - 3s_0 + s)^2\mathcal{F}(s'(y_s))\right]\frac{\mathrm{d}s'}{\mathrm{d}y_s}\mathrm{d}y_s\right] \ . \end{aligned} \tag{2.52}$$

The angular integrals evaluated for $s > b$ again can be directly performed.

With the inhomogeneity calculated we have to perform the dispersive integral to obtain the single-variable amplitude, see iteration scheme Fig. 2.3. The dispersion integrand in Eq. (2.48) has in addition to the Cauchy kernel three characteristic points, the roots of $\kappa(s)$: the threshold ($4M_\pi^2$), the pseudothreshold (a) and the scattering threshold (b). The threshold point is well under control since not only $\tilde{\mathcal{F}}(s)$ vanishes but the P-wave phase

shift behaves like $\sim \left(1-4M_\pi^2/s\right)^{3/2}$ near the threshold and thus cancels the $\kappa^3(s)$ root such that the singularity is removed. In the following we will split up the integration in different parts such that the characteristic points together with the Cauchy kernel can be treated separately. The mathematical framework of the following numerical implementation comes from the field of hypersingular integrals and Hadamard finite part integration, which is often referred to as the generalization of Cauchy's principle value. We refer the reader to Refs. [59–61] and references therein for further detail.

First of all we will introduce a cutoff Λ^2 to the dispersion integral. Strictly the integral has to be performed up to infinity but the contributions of higher energies are suppressed and for the sake of numerical simplification we will neglect contributions higher than the cutoff energy. Varying the cutoff will become one source of the error estimation. Furthermore, we split the integral

$$\int_{4M_\pi^2}^{\Lambda^2} = \int_{4M_\pi^2}^{b} + \int_{b}^{\Lambda^2} \ , \tag{2.53}$$

and define for further convenience

$$\mathcal{G}(s) \equiv \frac{\tilde{\mathcal{F}}(s)\sin\delta_1^1(s)}{s\left(\sqrt{\frac{s-4M_\pi^2}{s}}\sqrt{b-s}\right)^3|\Omega_1^1(s)|} \ , \quad H(s) \equiv \frac{s\mathcal{G}(s)}{(a-s)^{\frac{3}{2}}} \ . \tag{2.54}$$

Let us assume $s \in [4M_\pi^2, a[$ first. Thus we have two singularites that we need to treat separately; the Cauchy singularity and a. To separate these two singularities we define $p = (a+s)/2$ and obtain

$$\begin{aligned}
&\int_{4M_\pi^2}^{\Lambda^2} \frac{\mathcal{G}(s')}{(a-s')^{\frac{3}{2}}(s'-s-i\epsilon)}\,\mathrm{d}s' = \int_{4M_\pi^2}^{p} \frac{H(s')-H(s)}{s'(s'-s-i\epsilon)}\,\mathrm{d}s' \\
&+ \int_{p}^{b} \frac{\mathcal{G}(s')-\mathcal{G}(a)-(a-s')\mathcal{G}'(a)}{(a-s')^{\frac{3}{2}}(s'-s-i\epsilon)}\,\mathrm{d}s' + \int_{b}^{\Lambda^2} \frac{\mathcal{G}(s')}{(a-s')^{\frac{3}{2}}(s'-s-i\epsilon)}\,\mathrm{d}s' \\
&+ H(s)\int_{4M_\pi^2}^{p} \frac{1}{s'(s'-s-i\epsilon)}\,\mathrm{d}s' + \int_{p}^{b} \frac{\mathcal{G}(a)+\mathcal{G}'(a)(a-s')}{(a-s')^{\frac{3}{2}}(s'-s-i\epsilon)}\,\mathrm{d}s' \ ,
\end{aligned} \tag{2.55}$$

where the first three integrals can be evaluated straightforwardly numerically and the second integral given by

$$\int_{p}^{b} \frac{\mathcal{G}(s')-\mathcal{G}(a)-(a-s')\mathcal{G}'(a)}{(a-s')^{\frac{3}{2}}(s'-s-i\epsilon)}\,\mathrm{d}s' = \int_{p}^{b} \mathrm{d}s' \begin{cases} \frac{a_2+(a-s')^{\frac{1}{2}}a_3+(a-s')a_4}{(s'-s-i\epsilon)}\,\mathrm{d}s' & |x-a|<2h \\ \frac{\mathcal{G}(s')-\mathcal{G}(a)-(a-s')\mathcal{G}'(a)}{(a-s')^{\frac{3}{2}}(s'-s-i\epsilon)}\,\mathrm{d}s' & |x-a|>2h \end{cases} \ , \tag{2.56}$$

with an appropriate small value for h and the expansion

$$\mathcal{G}(s) = \mathcal{G}(a) + (a-s)\mathcal{G}'(a) + (a-s)^{\frac{3}{2}}a_2 + (a-s)^2 a_3 + (a-s)^{\frac{5}{2}}a_4 \ . \tag{2.57}$$

The last two integrals of Eq. (2.55) can be calculated analytically in the spirit of hypersingular integrals. The first simply gives

$$\int_{4M_\pi^2}^{p} \frac{1}{s'(s'-s-i\epsilon)}\,\mathrm{d}s' = \frac{1}{s+i\epsilon}\log\left(\frac{4M_\pi^2(p-s-i\epsilon)}{p(4M_\pi^2-s-i\epsilon)}\right) , \tag{2.58}$$

and for the second integral we find

$$\int_p^b \frac{1}{(a-s')^{\frac{n}{2}}(s'-s-i\epsilon)}\mathrm{d}s' \tag{2.59}$$

$$= \begin{cases} \frac{2}{(a-s-i\epsilon)^{1/2}}\left(\operatorname{arctanh}\frac{\sqrt{a-p}}{\sqrt{a-s-i\epsilon}} - \operatorname{arctanh}\frac{\sqrt{a-b}}{\sqrt{a-s-i\epsilon}}\right) , & n=1 \ , \\ \frac{2}{(a-s-i\epsilon)}\left(\frac{1}{\sqrt{a-b}} - \frac{1}{\sqrt{a-p}}\right) + \frac{2}{(a-s-i\epsilon)^{3/2}}\left(\operatorname{arctanh}\frac{\sqrt{a-p}}{\sqrt{a-s-i\epsilon}} - \operatorname{arctanh}\frac{\sqrt{a-b}}{\sqrt{a-s-i\epsilon}}\right) , & n=3 \ , \end{cases} \tag{2.60}$$

Note that to obtain the correct branches it is sometimes advisable to give a an infinitesimal positive imaginary part analogously to the prescription $M_V^2 + i\epsilon$.

For $s \in]a,b]$ the procedure works similarly only that the integration is split differently to separate the integration over a and the Cauchy singularity s,

$$\begin{aligned} &\int_{4M_\pi^2}^{\Lambda^2} \frac{\mathcal{G}(s')}{(a-s')^{\frac{3}{2}}(s'-s-i\epsilon)}\,\mathrm{d}s' = \int_{4M_\pi^2}^{p} \frac{\mathcal{G}(s')-\mathcal{G}(a)-(a-s')\mathcal{G}'(a)}{(a-s')^{\frac{3}{2}}(s'-s-i\epsilon)}\,\mathrm{d}s' \\ &+ \int_p^b \frac{H(s')-H(s)}{s'(s'-s-i\epsilon)}\,\mathrm{d}s' + \int_b^{\Lambda^2} \frac{\mathcal{G}(s')}{(a-s')^{\frac{3}{2}}(s'-s-i\epsilon)}\,\mathrm{d}s' \\ &+ H(s)\int_p^b \frac{1}{s'(s'-s-i\epsilon)}\,\mathrm{d}s' + \int_{4M_\pi^2}^{p} \frac{\mathcal{G}(a)+\mathcal{G}'(a)(a-s')}{(a-s')^{\frac{3}{2}}(s'-s-i\epsilon)}\,\mathrm{d}s' \end{aligned} \tag{2.61}$$

For $s > b$ the Cauchy singularity is already well separated by Eq. (2.53) and thus we have

$$\begin{aligned} &\int_{4M_\pi^2}^{\Lambda^2} \frac{\mathcal{G}(s')}{(a-s')^{\frac{3}{2}}(s'-s-i\epsilon)}\,\mathrm{d}s' = \int_{4M_\pi^2}^{b} \frac{\mathcal{G}(s')-\mathcal{G}(a)-(a-s')\mathcal{G}'(a)}{(a-s')^{\frac{3}{2}}(s'-s-i\epsilon)}\,\mathrm{d}s' \\ &+ \int_b^{\Lambda^2} \frac{H(s')-H(s)}{s'(s'-s-i\epsilon)}\,\mathrm{d}s' + \int_{4M_\pi^2}^{b} \frac{\mathcal{G}(a)+\mathcal{G}'(a)(a-s')}{(a-s')^{\frac{3}{2}}(s'-s-i\epsilon)}\,\mathrm{d}s' \\ &+ H(s)\int_b^{\Lambda^2} \frac{1}{s'(s'-s-i\epsilon)}\,\mathrm{d}s' \ , \end{aligned} \tag{2.62}$$

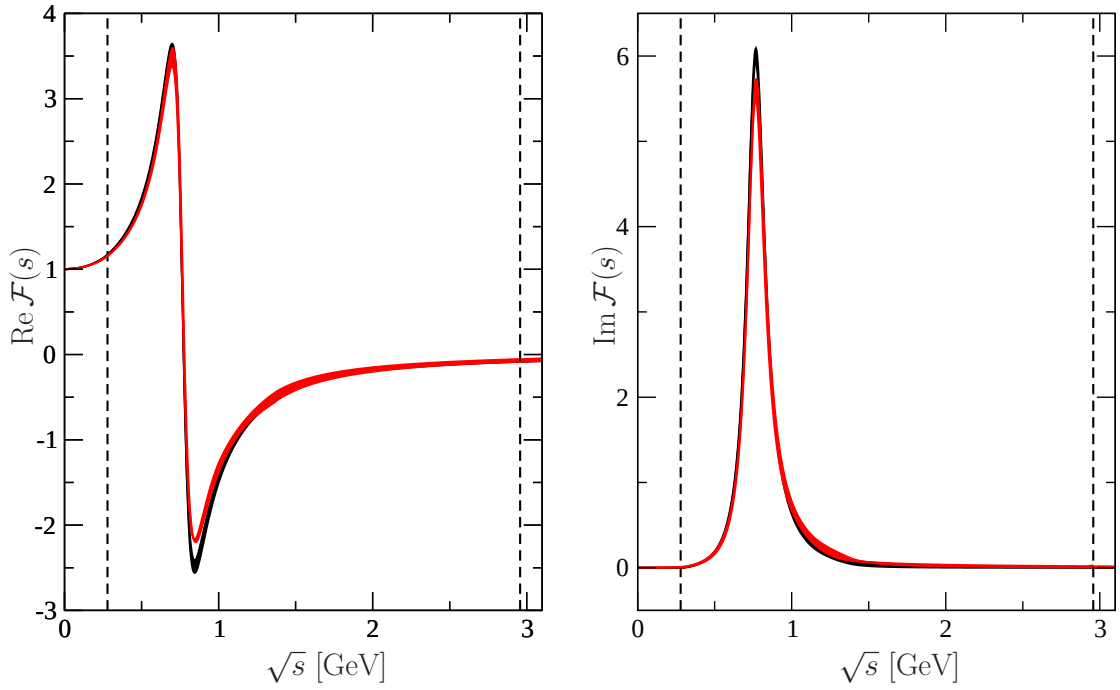

Figure 2.5: Results for the real part (left panel) and imaginary part (right panel) of the single-variable amplitude $\mathcal{F}(s)$ with the subtraction constant $c_0 = 1$. The black line denotes the Omnès solution and the red line the full dispersive solution. The error band stems from the different phase inputs. The vertical dashed lines denote the boundaries of the decay phase space ($4M_\pi^2$ and a)

where the first two integrals can be calculated numerically and the third and fourth analytically. The integration for $s < 4M_\pi^2$ or complex s is simpler as the Cauchy singularity is not present and we only have to treat the pseudothreshold a

$$\int_{4M_\pi^2}^{\Lambda^2} \frac{\mathcal{G}(s')}{(a-s')^{\frac{3}{2}}(s'-s-i\epsilon)}\,\mathrm{d}s' = \int_{4M_\pi^2}^{b} \frac{\mathcal{G}(s')-\mathcal{G}(a)-(a-s')\mathcal{G}'(a)}{(a-s')^{\frac{3}{2}}(s'-s-i\epsilon)}\,\mathrm{d}s' + \int_{b}^{\Lambda^2} \frac{\mathcal{G}(s')}{(a-s')^{\frac{3}{2}}(s'-s-i\epsilon)}\,\mathrm{d}s' + \int_{4M_\pi^2}^{b} \frac{\mathcal{G}(a)+\mathcal{G}'(a)(a-s')}{(a-s')^{\frac{3}{2}}(s'-s-i\epsilon)}\,\mathrm{d}s' \,. \tag{2.63}$$

Certainly the implementation displayed above is not the one and only way. We could have introduced integration kernels similar to Ref. [62] or discretized the integrals and sought a way to calculate the integrals following the $i\epsilon$ prescription in a more analytic way. Later in this thesis we will devise a discretization method and convert the integral equation into a matrix equation to solve D-meson three-particle decays.

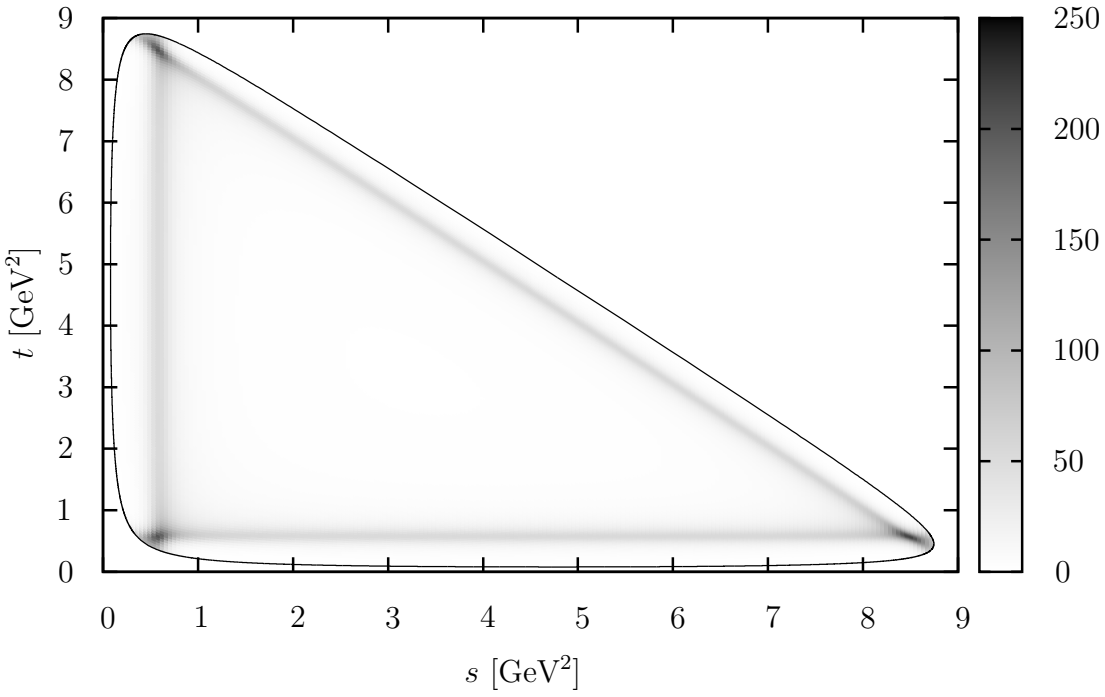

Figure 2.6: The figure shows the calculated $J/\psi \to 3\pi$ Dalitz plot normalized to one in the center of the Dalitz plot ($|\mathcal{F}(s_0, s_0, s_0)|^2 = 1$ with $s_0 = (M_V^2 + 3M_\pi^2)/3$).

2.5 Results

In this section we present the calculated $J/\psi \to 3\pi$ decay amplitude and Dalitz plot. We will further discuss the dependence of $\mathcal{F}(s)$ on the decaying vector-meson mass and study the convergence of the iteration procedure.

Following the iterative procedure we obtain the solution for the single-variable amplitude $\mathcal{F}(s)$ of Eq. (2.39). The resulting single-variable amplitude together with the Omnès function, which serves as our input function, is depicted in Fig. 2.5, with the subtraction constant taken to be $c_0 = 1$. We have noted above that, due to the linearity of the integral equation with respect to the subtraction constant, the subtraction constant serves as an overall normalization. The $J/\psi \to 3\pi$ Dalitz plot depicted in Fig. 2.6 is thus a pure prediction based only on the $\pi\pi$ P-wave phase-shift input and the masses of the involved particles. The difference between the Omnès function and $\mathcal{F}(s)$ is a measure of the importance of crossed-channel rescattering effects. We clearly see that compared to the $\omega/\phi \to 3\pi$ results in Ref. [34] the crossed-channel rescattering effects are considerably smaller. This raises the question of how these effects depend on the decaying vector-meson mass.

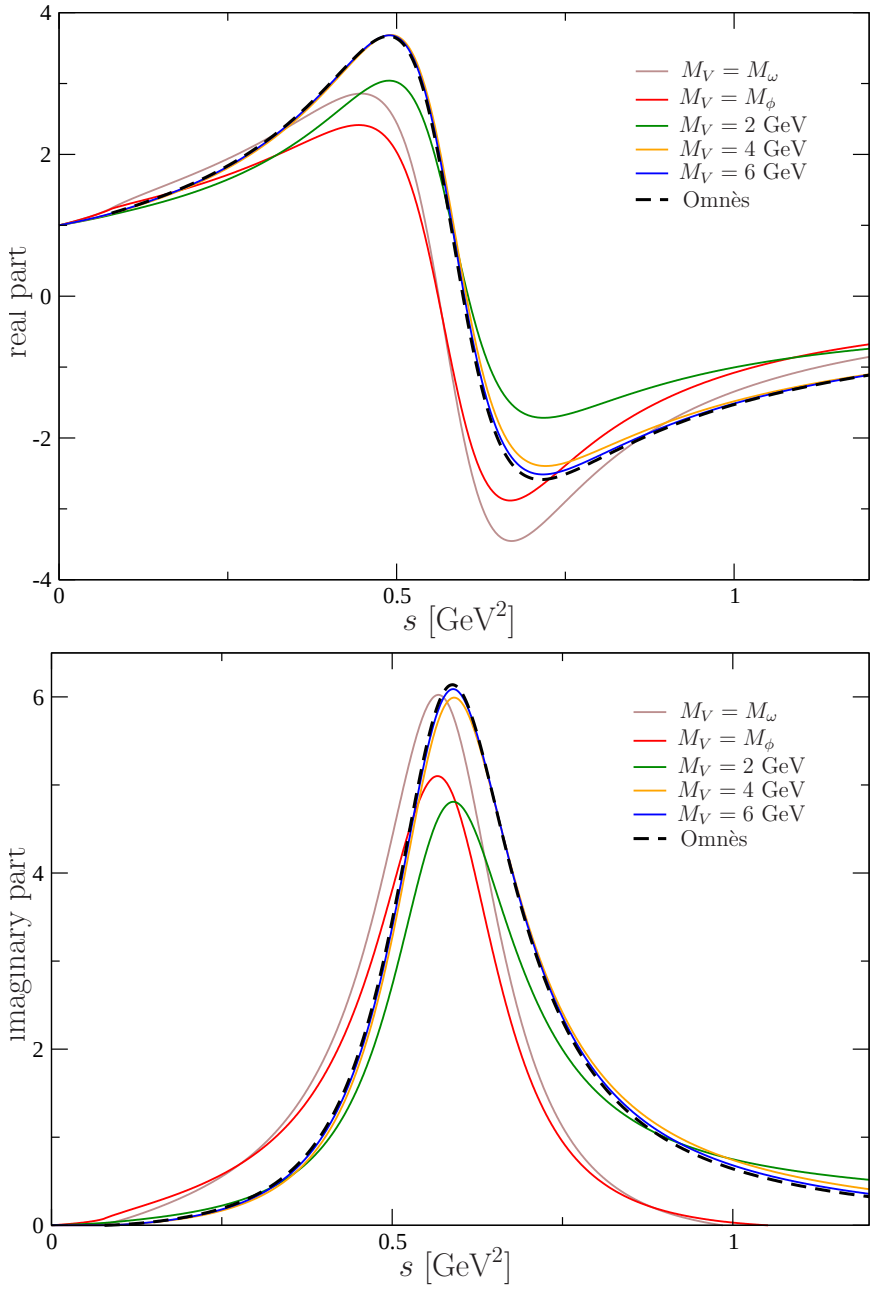

Figure 2.7: Real (top graph) and imaginary part (bottom graph) of the single-variable amplitude $\mathcal{F}(s)$ for different vector-meson masses M_V are shown. Additionally, the real and imaginary the part of the Omnès function are plotted. We note that for $M_V > 6\,\text{GeV}$ the single-variable amplitudes are already indistinguishable from the Omnès function and therefore refrain from showing them.

2.5.1 Basis functions in the $\mathcal{M}_V \to \infty$ limit

Intuition suggests, as we also see when going from the ω and ϕ mass to the J/ψ mass, that the crossed-channel rescattering effects become less important for higher decaying masses relative to two-particle rescattering. The third particle at fixed two-particle energies is more energetic and therefore has less time to rescatter with the two-particle system. To investigate this matter further, we solve the single-variable amplitude $\mathcal{F}(s)$ for different decaying masses. Figure 2.7 shows the resulting single-variable amplitudes. Up to $M_V = 2$ GeV we observe a significant impact of crossed-channel rescattering effects which also induce minor shifts of the $\rho(770)$-peak position. For decaying masses $M_V > 2$ GeV the crossed-channel rescattering effects become smaller and for $M_V > 6\,\text{GeV}$ the single-variable amplitudes are indistinguishable from the Omnès function input. Thus the intuitive picture is confirmed. However, we want to stress again that for higher decaying masses inelastic effects play a major role. Therefore the resulting higher mass single-variable amplitudes depicted in Fig. 2.7 serve as entities to investigate the nature of the Khuri–Treiman equations. They should not be taken as precise physical amplitudes.

Additionally, we note that the number of iterations needed to reach convergence changes when going to higher masses. This brings us directly to the question of convergence of the iteration procedure which we will investigate in the following section.

2.5.2 Convergence of the iteration procedure

With the input phase fixed, the convergence of the iteration procedure depends on two parameters: the mass of the decaying vector meson and the number of subtractions. We have strong existence and uniqueness statements for well-behaving integral equations, e.g. the Banach fixed-point theorem, Schauder fixed-point theorem to name a few. Unfortunately a rigorous purely analytic investigation of the convergence issue of these Khuri–Treiman-type equations is not known to us. The Banach fixed-point theorem for example comes with an explicit iterative strategy to determine the fixed point, which in the case of first order differential equations (Picard-Lindelöf theorem) is analogous to our iteration scheme. However, due to the singular structure of the Khuri–Treiman integrand and explicitly at the pseudothreshold a such theorems are not directly applicable.

In the following we therefore investigate the dependence of the convergence on the vector-meson mass and the number of subtractions numerically. To test the uniform convergence we take 50 evenly distributed points in the interval $[0\,\text{GeV}, 1\,\text{GeV}]$ and define the convergence of the iteration procedure as follows: the iteration is converged if an additional iteration step does not change the value of the single-variable amplitude at these points

more than $\pm 1\%$. Generally, for n subtractions the single-variable amplitude is given by

$$\mathcal{F}(s) = \Omega(s)\left\{ \sum_{j=0}^{n-1} c_j s^j + \frac{s^n}{\pi} \int_{4M_\pi^2}^{\infty} \frac{\mathrm{d}s'}{s'^n} \frac{\sin\delta_1^1(s')\hat{\mathcal{F}}(s')}{|\Omega_1^1(s')|(s'-s)} \right\} , \tag{2.64}$$

with the subtraction constants c_j. For each order of subtraction we investigate all basis functions. The ith order basis function of subtraction order m is obtained by solving Eq. (2.64) for $n = m$ and the subtraction constant set $c_j = \delta_{ij},\ j \in \{0, 1, .., n-1\}$.

The results are shown in Fig. 2.8 and Fig. 2.9. The plots show the zeroth and the first basis functions (Fig. 2.8) and the second and third basis functions (Fig. 2.9). We observe that the convergence behavior with varying vector-meson mass depends heavily on the the number of subtractions chosen. Up to two subtractions no convergence problems are observed, yet more iterations are needed for the twice-subtracted dispersion relation compared to the once-subtracted. The iteration procedure breaks down for three and four subtractions in the region of $M_V \approx 0.95\,\mathrm{GeV}$ and $M_V \approx 0.85\,\mathrm{GeV}$, respectively. This suggests that higher subtractions paired with higher decaying masses can induce a failure of the iteration procedure. This will become important in the following, when we want to investigate decays in the charm sector. Within the chosen subtraction the convergence is almost independent of the basis function investigated.

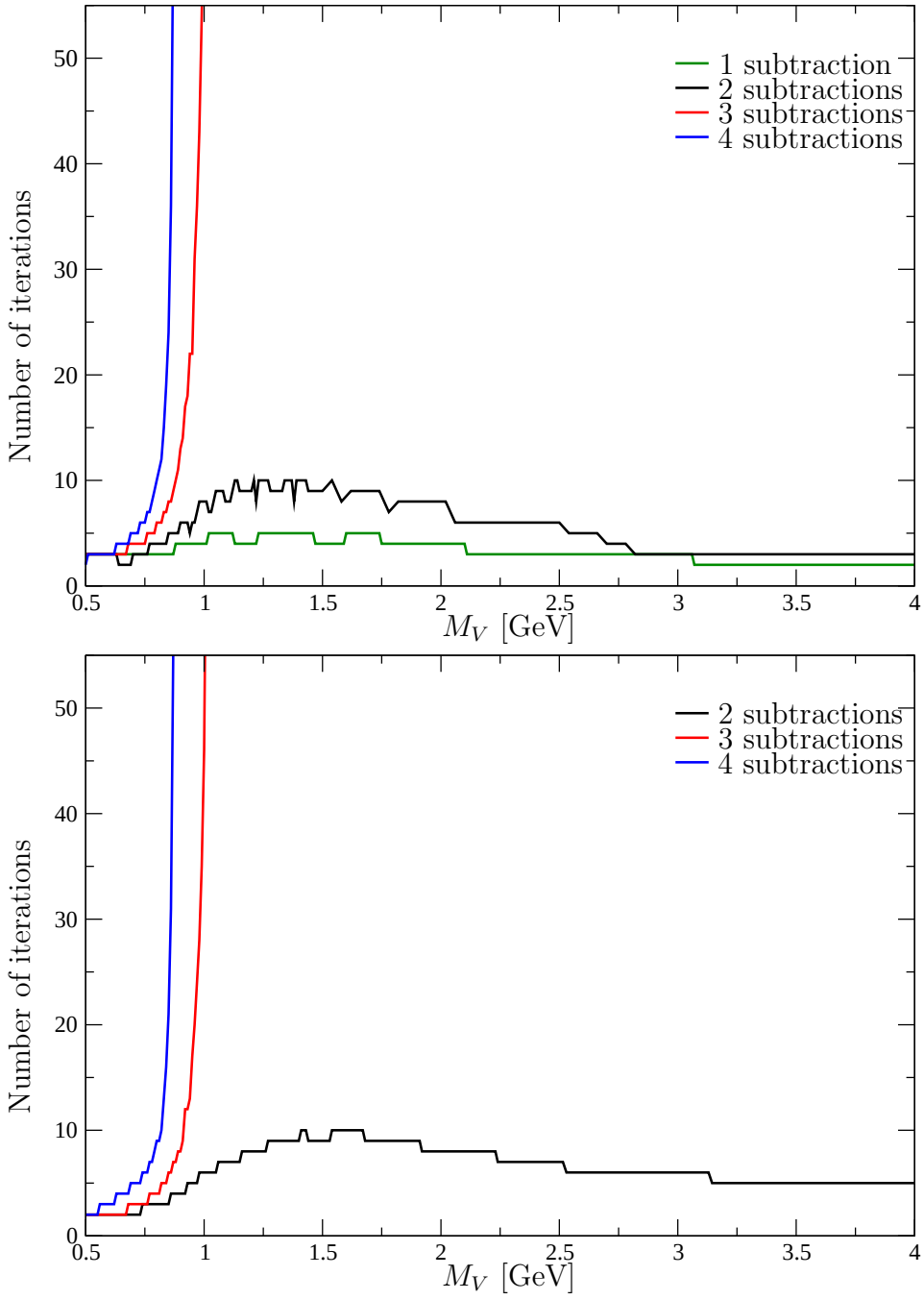

Figure 2.8: *Upper plot:* the zeroth basis functions are shown for the once, twice, three times, and four times subtracted dispersion integral. *Lower plot:* the first basis functions are depicted for the twice, three times, and four times subtracted dispersion integrals.

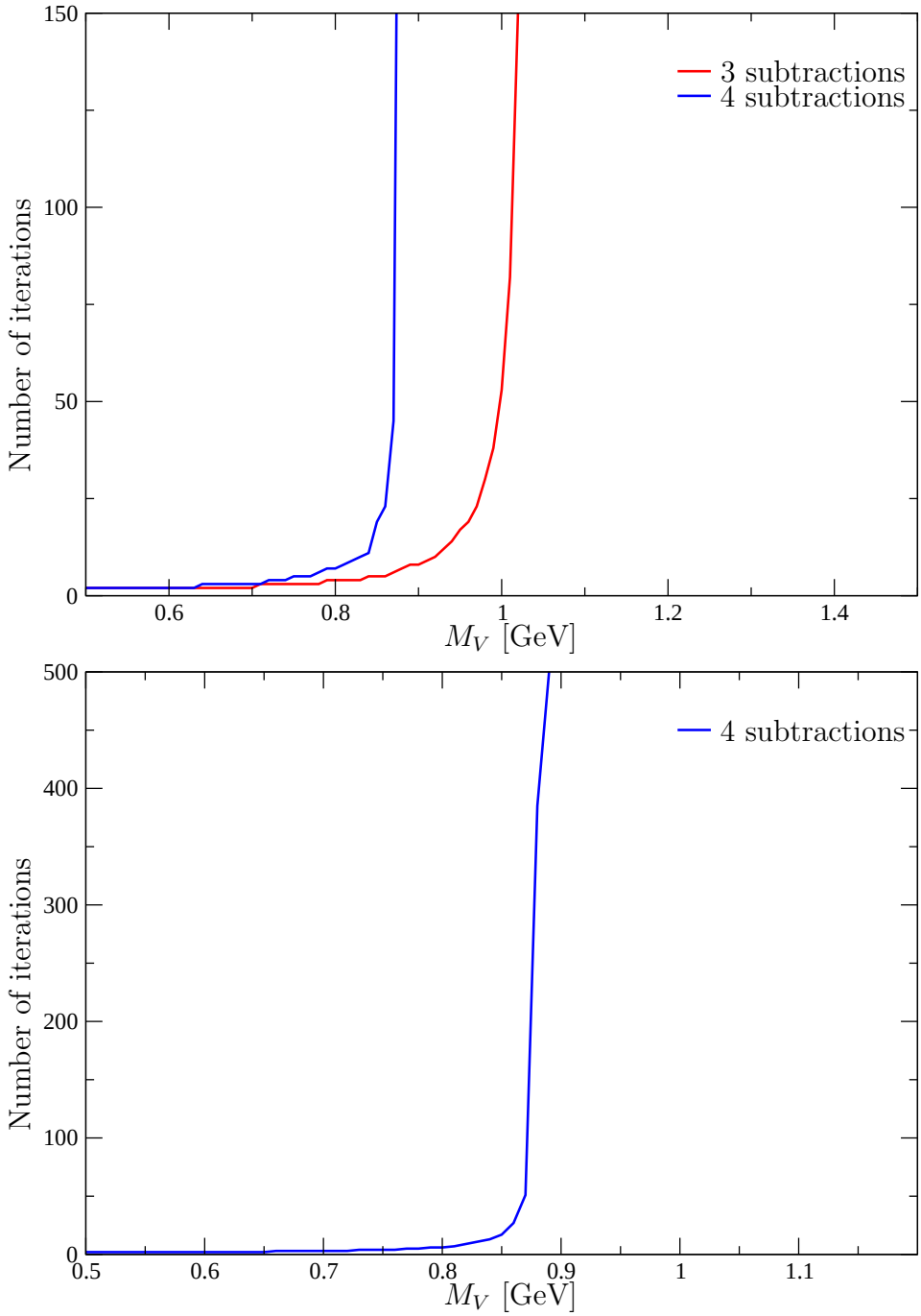

Figure 2.9: *Upper plot:* the second basis functions are shown for the three times and four times subtracted dispersion integral. *Lower plot:* the third basis function is depicted for the four times subtracted dispersion integrals.

Chapter 3

The $J/\psi \to \pi^0\gamma^*$ transition form factor[1]

3.1 Introduction

The transition form factors of light vector mesons (ω and ϕ in particular) have garnered increased interest in the last few years due to their impact on the transition form factors of the lightest pseudoscalars [38, 64], and hence on hadronic light-by-light scattering [36]. While e.g. the transition $\phi \to \eta e^+e^-$ [65] seems compatible with a vector-meson dominance picture [66], other experimental results, in particular for $\omega \to \pi^0\mu^+\mu^-$ and $\phi \to \pi^0 e^+e^-$, seem to indicate strong deviations [67–69], which are hard to understand theoretically [70].

Recently the first measurements of the analogous transition form factors from charmonium into light pseudoscalars have been reported by the BES III collaboration [71], which has determined the branching fractions for $J/\psi \to Pe^+e^-$, $P = \pi^0, \eta, \eta'$, and the transition form factor for the η' final state. The latter was parametrized in a simple monopole form [72], with the scale found in the characteristic charmonium mass region. On the other hand, in Ref. [72], such monopole form factors were assumed for all three final-state pseudoscalars, and the corresponding branching fractions were estimated; interestingly enough, experiment agrees well with these predictions for η and η', while there seems to be a tension for the π^0: the experimental determination arrives at $\mathcal{B}(J/\psi \to \pi^0 e^+e^-) = (7.56 \pm 1.32 \pm 0.50) \times 10^{-7}$ [71], while the theory prediction was $\mathcal{B}(J/\psi \to \pi^0 e^+e^-) = \left(3.89^{+0.37}_{-0.33}\right) \times 10^{-7}$ [72].

The assumption that the q^2-dependence of the $J/\psi \to \pi^0\gamma^*$ form factor should be determined by the charmonium mass scale seems implausible, given that this would imply an isospin-breaking transition, while the decay can proceed in an isospin-conserving manner,

[1] This part has been published in Ref. [63].

with the (virtual) photon being an isovector state, hence dominated by light-quark degrees of freedom. Indeed, it was pointed out by Chen *et al.* [73] very recently, in an effective-Lagrangian-based analysis, that the contributions of light vector mesons ought to be very sizable in this decay.

In this part, we consider the $J/\psi \to \pi^0\gamma^*$ transition form factor, defined in Section 3.2, in dispersion theory. Using the formalism employed previously for the analogous decays of the light isoscalar ω and ϕ mesons [74], we show in Section 3.3 that it is dominated by the lightest, $\pi\pi$, intermediate state, although not quite to the extent this dominance was found for ω and ϕ. We give rough estimates of possible further light contributions beyond two pions, as well as from charmonium states. While these induce a sizable uncertainty in the form factor, our results in Section 3.4 show that the experimentally observable decay spectra for $J/\psi \to \pi^0\ell^+\ell^-$, $\ell = e$, μ, as well as the integrated branching fractions are rather stable, as they are dominated by the low-energy region. We close with a summary.

3.2 Definitions, kinematics

The $J/\psi \to \pi^0\gamma^*$ transition form factor is defined according to

$$\langle \psi(p_V,\lambda)|j_\mu(0)|\pi^0(p)\rangle = -i\epsilon_{\mu\nu\alpha\beta}\epsilon^{\nu *}(p_V,\lambda)p^\alpha q^\beta f_{\psi\pi^0}(s), \tag{3.1}$$

where j_μ denotes the electromagnetic current, λ the polarization of the J/ψ with $\epsilon^\nu(p_V,\lambda)$ the corresponding polarization vector, $q = p_V - p$, and $s = q^2$. The form factor $f_{\psi\pi^0}(s)$ defined in this way has dimension GeV^{-1}. Sometimes also the corresponding normalized form factor is used, denoted by $F_{\psi\pi^0}(s) = f_{\psi\pi^0}(s)/f_{\psi\pi^0}(0)$. The differential cross section for the decay $J/\psi \to \pi^0\ell^+\ell^-$, normalized to the real-photon width, is given by

$$\frac{\mathrm{d}\Gamma_{\psi\to\pi^0\ell^+\ell^-}}{\Gamma_{\psi\to\pi^0\gamma}\,\mathrm{d}s} = \frac{16\alpha}{3\pi}\left(1+\frac{2m_\ell^2}{s}\right)\frac{q_\ell(s)q_{\psi\pi^0}^3(s)}{(M_\psi^2 - M_{\pi^0}^2)^3}|F_{\psi\pi^0}(s)|^2, \tag{3.2}$$

where α is the fine-structure constant, the real-photon width is determined by

$$\Gamma_{\psi\to\pi^0\gamma} = \frac{\alpha(M_\psi^2 - M_{\pi^0}^2)^3}{24M_\psi^3}|f_{\psi\pi^0}(0)|^2, \tag{3.3}$$

and the kinematical variables are

$$q_\ell(s) = \frac{1}{2}\sqrt{s-4m_\ell^2}, \quad q_{AB}(s) = \frac{\lambda^{1/2}(M_A^2, M_B^2, s)}{2\sqrt{s}}, \tag{3.4}$$

where $\lambda(a,b,c) = a^2+b^2+c^2-2(ab+ac+bc)$ is the usual Källén function. The universal (QED) radiative corrections to Eq. (3.2) have been calculated in Ref. [75].

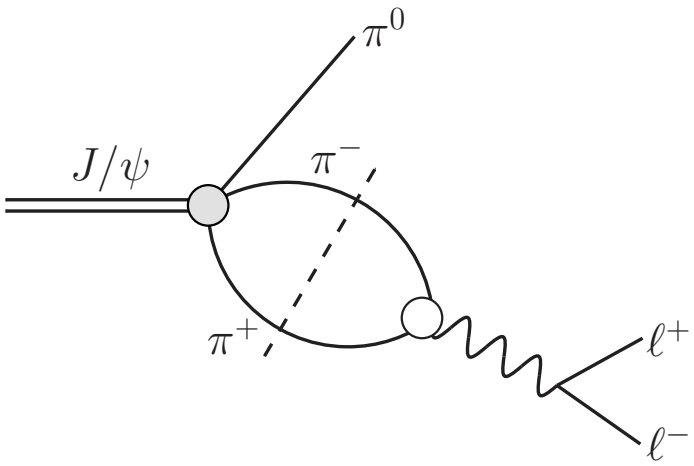

Figure 3.1: Two-pion contribution to the discontinuity of the $J/\psi \to \pi^0\ell^+\ell^-$ transition form factor. The gray circle denotes the $J/\psi \to 3\pi$ P-wave amplitude, whereas the white circle represents the pion vector form factor.

3.3 Dispersive analysis

Dispersion theory attempts to reconstruct form factors from the corresponding discontinuity across the cut along the positive real axis. In principle, one would expect an unsubtracted dispersion relation to work for the $J/\psi \to \pi^0\gamma^*$ form factor, i.e.

$$f_{\psi\pi^0}(s) = \frac{1}{2\pi i}\int_{4M_\pi}^{\infty} \mathrm{d}x \frac{\mathrm{disc}\, f_{\psi\pi^0}(x)}{x-s}, \tag{3.5}$$

where contributions to the discontinuity are given by multiparticle intermediate states as well as single-particle pole contributions. The lower limit of the integral is given by the lightest possible intermediate state, $\pi^+\pi^-$, that we will discuss in the following section.

3.3.1 $\pi\pi$ intermediate states

The contribution of the two-pion intermediate state to the discontinuity of the $J/\psi \to \pi^0\gamma^*$ transition form factor, see Fig. 3.1, is given by [74, 76]

$$\mathrm{disc}\, f^{\pi\pi}_{\psi\pi^0}(s) = \frac{i\, q^3_{\pi\pi}(s)}{6\pi\sqrt{s}} F_\pi^{V*}(s) f_1(s)\, \theta\big(s-4M_\pi\big), \tag{3.6}$$

where $F_\pi^V(s)$ is the pion vector form factor. $f_1(s)$ is the projection of the $J/\psi \to 3\pi$ decay amplitude onto the P partial wave determined in the previous Chapter 2 of this thesis:

with the amplitude $\mathcal{M}_{3\pi} = \mathcal{M}(\psi \to \pi^+(p_+)\pi^-(p_-)\pi^0(p_0))$ decomposed according to

$$\mathcal{M}_{3\pi} = i\epsilon_{\mu\nu\alpha\beta}\epsilon^{*\mu}p_+^\nu p_-^\alpha p_0^\beta \mathcal{F}(s,t,u), \tag{3.7}$$

it is given by

$$f_1(s) = \frac{3}{4}\int_{-1}^{1} \mathrm{d}z\big(1-z^2\big)\,\mathcal{F}(s,t,u), \tag{3.8}$$

where $z = (t-u)/(4q_{\pi\pi}(s)q_{\psi\pi^0}(s))$, and $s = (p_+ + p_-)^2$, $t = (p_- + p_0)^2$, $u = (p_+ + p_0)^2$.

To describe the $J/\psi \to 3\pi$ amplitude, we rely on the phenomenological observation that the Dalitz plot for this decay is entirely dominated by $\pi\rho$ intermediate states, i.e. by the lowest resonance in the $\pi\pi$ P-wave; neither higher resonances, nor resonant higher partial waves are observed [48]. We do not attempt to explain this suppression of additional structures [77], but just take it as the starting point for a generalized partial-wave decomposition that stops at P-wave contributions only [34, 78],

$$\mathcal{F}(s,t,u) = \mathcal{F}(s) + \mathcal{F}(t) + \mathcal{F}(u)\ . \tag{3.9}$$

Final-state interactions between all three pions are implemented in a Khuri–Treiman-type formalism [39], leading to [34] (compare also Ref. [79])

$$\begin{aligned}\mathcal{F}(s) &= a\,\Omega(s)\left\{1 + \frac{s}{\pi}\int_{4M_\pi}^{\infty}\frac{\mathrm{d}x}{x}\frac{\sin\delta(x)\hat{\mathcal{F}}(x)}{|\Omega(x)|(x-s)}\right\},\\ \hat{\mathcal{F}}(s) &= 3\langle(1-z^2)\mathcal{F}\rangle(s),\end{aligned} \tag{3.10}$$

where $\delta(s) \doteq \delta_1^1(s)$ is the isospin 1 $\pi\pi$ P-wave phase shift taken from Refs. [80, 81] and $\langle . \rangle$ denotes angular averaging. $\Omega(s)$ is the Omnès function calculated from the phase shift $\delta(s)$,

$$\Omega(s) = \exp\left\{\frac{s}{\pi}\int_{4M_\pi}^{\infty}\mathrm{d}x\frac{\delta(x)}{x(x-s)}\right\}. \tag{3.11}$$

The function $\hat{\mathcal{F}}$ denotes the partial-wave projection of the crossed-channel contributions, which are fed into the dispersive solution for $\mathcal{F}$. The partial wave $f_1(s)$ is related to both by $f_1(s) = \mathcal{F}(s) + \hat{\mathcal{F}}(s)$. The single subtraction constant a only affects the overall normalization of the amplitude and can be fixed, up to a phase, from the total $J/\psi \to 3\pi$ branching fraction. For the pion vector form factor $F_\pi^V(s)$, we also employ a representation based on the Omnès function Eq. (3.11); see Ref. [74] for details. This fully determines Eq. (3.6).

In particular, we can calculate the two-pion contribution to the *real*-photon transition $J/\psi \to \pi^0\gamma$ in the form of a sum rule [74]:

$$f_{\psi\pi^0}^{\pi\pi}(0) = \frac{1}{12\pi^2}\int_{4M_\pi}^{\infty}\mathrm{d}x\frac{q_{\pi\pi}^3(x)}{x^{3/2}}F_\pi^{V*}(x)f_1(x). \tag{3.12}$$

As the partial wave $f_1(s)$ depends on an unknown overall normalization constant a, the cleanest prediction following from Eq. (3.12) is in principle the ratio $\mathcal{B}(J/\psi \to \pi^0\gamma)/\mathcal{B}(J/\psi \to 3\pi)$ [74], which is determined by the phase shift $\delta(s)$ alone.

The experimental branching fraction for $J/\psi \to \pi^0\gamma$ [82], together with Eq. (3.3), leads to $|f_{\psi\pi^0}(0)| = (6.0 \pm 0.3) \times 10^{-4}\,\text{GeV}^{-1}$, whereas the sum rule Eq. (3.12) results in

$$|f^{\pi\pi}_{\psi\pi^0}(0)| = (4.8 \pm 0.2) \times 10^{-4}\,\text{GeV}^{-1}, \tag{3.13}$$

where the uncertainty is a combination of the experimental uncertainties in $\mathcal{B}(J/\psi \to 3\pi)$ and the width of the J/ψ, as well as the one in the dispersive integral. We therefore conclude that the two-pion intermediate state alone saturates the sum rule for the transition form factor normalization to about 80%. Note that this presents a very significant enhancement over a simple vector-meson dominance estimate based on the decay chain $J/\psi \to \rho^0\pi^0$, $\rho^0 \to \gamma$ (see e.g. Ref. [73]), which would rather result in $|f^{\rho}_{\psi\pi^0}(0)| \approx 3.3 \times 10^{-4}\,\text{GeV}^{-1}$.

This result is to be compared to similar sum rules for the decays $\omega \to \pi^0\gamma$ and $\phi \to \pi^0\gamma$, which were observed to be saturated to more than 90% accuracy [74]. The difference looks rather plausible, as the branching fractions of the J/ψ into more than three pions are actually *larger*: $\mathcal{B}(J/\psi \to 3\pi) = (2.11 \pm 0.07)\%$, $\mathcal{B}(J/\psi \to 5\pi) = (4.1 \pm 0.5)\%$, $\mathcal{B}(J/\psi \to 7\pi) = (2.9 \pm 0.6)\%$ [82]. It would therefore not come as a surprise if the inelastic contributions to the $J/\psi \to \pi^0\gamma^*$ transition form factor, coming from the discontinuities due to four and more pions, played a much more significant role than e.g. for the $\omega \to \pi^0\gamma^*$ transition. However, the information on the branching fractions alone does not lend itself easily to an improvement of the radiative decay/the transition form factor before more differential information in the form of a partial-wave analysis becomes available. From data on $e^+e^- \to [\text{hadrons}]_{I=1}$, the most important inelastic intermediate state of isospin $I = 1$ ought to be 4π, which couples strongly to the $\rho'(1450)$ resonance. In a very simplistic model approach, we therefore add a $\rho'(1450)$ resonance to the $J/\psi \to \pi^0\gamma^*$ transition form factor as an approximation to the possible effects of multipion intermediate states, which we allow to contribute between 10% and 30% of the dominant $\pi\pi$ channel to the sum rule for $f_{\psi\pi^0}(0)$. Note that in a more complete/realistic description the dispersive contributions from $\pi\pi$ and inelastic states would have to be treated as coupled channels; see e.g. Ref. [27] for a corresponding analysis of the pion vector form factor. We reconstruct the $\rho'(1450)$ propagator dispersively from the imaginary part of an energy-dependent Breit–Wigner function,

$$\begin{aligned}
\text{disc}\, f^{\rho'}_{\psi\pi^0}(s) &= \frac{2i\sqrt{s}M^2_{\rho'}\Gamma_{\rho'}(s)}{(M^2_{\rho'} - s)^2 + s\,\Gamma^2_{\rho'}(s)}, \\
\Gamma_{\rho'}(s) &= \left(\frac{M^2_{\rho'}}{s}\right)^2 \left[\frac{s - 16M_\pi}{M^2_{\rho'} - 16M_\pi}\right]^{7/2} \Gamma_{\rho'}\big(M^2_{\rho'}\big)\,\theta\big(s - 16M_\pi\big),
\end{aligned} \tag{3.14}$$

thus maintaining a reasonable analytic behavior. $\Gamma_{\rho'}(s)$ reproduces the near-threshold behavior of four-pion phase space [27]. With $M_{\rho'} = 1.6\,\text{GeV}$, $\Gamma(M_{\rho'}^2) = 0.6\,\text{GeV}$, the dispersive integral over Eq. (3.14) results in a function of which the peak position and width agree with the Particle Data Group Breit–Wigner parameters [82].

3.3.2 Light isoscalar contributions to $J/\psi \to \eta, \eta'\gamma^*$

Given the strong impact of light-quark degrees of freedom on the $J/\psi \to \pi^0\gamma^*$ transition, to what extent may something similar be true for the decays $J/\psi \to \eta, \eta'\gamma^*$? In the limit of isospin conservation, here only the light *isoscalar* vector mesons ω and ϕ can contribute, which in the context of this study we consider as sufficiently narrow that we can approximate their contribution to the discontinuity by δ-functions,

$$\text{disc}\, f_{\psi P}^V(s) = 2\pi i \sum_{V=\omega,\phi} c_{PV} F_V M_V \delta(s - M_V^2), \tag{3.15}$$

where $P = \eta$, η'. Here, F_V denote the vector-meson decay constants, determined from the corresponding electron–positron decay rates by

$$\Gamma_{V\to e^+e^-} = \frac{4\pi\alpha^2}{3}\frac{F_V^2}{M_V} \tag{3.16}$$

(neglecting the mass of the electron), while the effective coupling constants c_{PV} are fixed from the decay rates $J/\psi \to PV$ by

$$\Gamma_{J/\psi\to PV} = \frac{|c_{PV}|^2}{96\pi M_\psi^3}\lambda^{3/2}\big(M_\psi^2, M_V^2, M_P^2\big). \tag{3.17}$$

We do not attempt a symmetry-based analysis of the couplings c_{PV} here (compare Refs. [73, 83, 84] and references therein), but just estimate them individually from data; we note that SU(3) symmetry suggests constructive interference of ω and ϕ contributions for the η final state, but destructive interference for the η'. Individually, the estimated contributions of ω and ϕ to the transition form factors at the real-photon point, given simply by $f_{\psi P}^V(0) = c_{PV}F_V/M_V$, amount to

$$\begin{aligned} \big|f_{\psi\eta}^{\{\omega,\phi\}}(0)\big| &\approx \{0.9,\, 0.8\} \times 10^{-4}\,\text{GeV}^{-1}, \\ \big|f_{\psi\eta'}^{\{\omega,\phi\}}(0)\big| &\approx \{0.3,\, 0.7\} \times 10^{-4}\,\text{GeV}^{-1}, \end{aligned} \tag{3.18}$$

whereas the decay rates for $J/\psi \to \eta, \eta'\gamma$ [82] suggest $|f_{\psi\eta}(0)| = (35 \pm 1) \times 10^{-4}\,\text{GeV}^{-1}$, $|f_{\psi\eta'}(0)| = (85 \pm 3) \times 10^{-4}\,\text{GeV}^{-1}$. We conclude, in accordance with Ref. [73], that for the isoscalar transition form factors, light-quark resonances contribute only at the percent level, so the corresponding spectral functions are entirely dominated by charmonium intermediate states, in the loose sense of both $c\bar{c}$ resonances and open charm–anticharm continuum contributions.

3.3.3 Estimate of charmonium contributions

Given the vast dominance of charmonium in the transition form factors for η and η', we may wonder if such effects cannot also be sizable for $J/\psi \to \pi^0\gamma^*$, even though in that case, they break isospin symmetry. Indeed, in the same narrow-width approximation employed in the previous section, we can determine the contribution specifically of the $\psi(2S)$, using experimental information on the branching fractions for $\psi(2S) \to J/\psi\pi^0$ and $\psi(2S) \to e^+e^-$ [82] and analogous relations to Eq. (3.16) and Eq. (3.17) to determine the decay constant $F_{\psi(2S)}$ and an effective coupling $c_{\pi^0\psi(2S)}$. Surprisingly, one finds

$$|f_{\psi\pi^0}^{\psi(2S)}(0)| = (5.3 \pm 0.1) \times 10^{-4}\,\text{GeV}^{-1}, \tag{3.19}$$

which is larger than the two-pion contribution, see Eq. (3.13). However, the comparison to the $J/\psi \to \eta\gamma^*$ transition form factor demonstrates that this observation is too simplistic. Here, branching fractions into $J/\psi\eta$ (and e^+e^-) are known for the excited charmonium resonances $\psi(2S)$, $\psi(3770)$, and $\psi(4040)$, so we can determine their contributions to the sum rule for $f_{\psi\eta}(0)$. Their moduli turn out to be $(117 \pm 2) \times 10^{-4}\,\text{GeV}^{-1}$, $(25 \pm 6) \times 10^{-4}\,\text{GeV}^{-1}$, and $(70 \pm 7) \times 10^{-4}\,\text{GeV}^{-1}$, respectively, compared to the total $|f_{\psi\eta}(0)| = (35 \pm 1) \times 10^{-4}\,\text{GeV}^{-1}$. We conclude that there need to be strong cancellation effects between different charmonium resonances (as well as, probably, open-charm continuum channels) in the $J/\psi \to \eta\gamma^*$ form factor spectral function in order to explain the observed rate for $J/\psi \to \eta\gamma$.

To estimate the total charmonium contribution to $J/\psi \to \pi^0\gamma$, $|f_{\psi\pi^0}^{c\bar{c}}(s)|$, we therefore assume that the ratio of $\psi(2S)$ contributions to the transitions into π^0 and η gives a useful indication of the ratio of overall $c\bar{c}$ effects:

$$0.01 \lesssim \frac{|f_{\psi\pi^0}^{c\bar{c}}(0)|}{|f_{\psi\eta}^{c\bar{c}}(0)|} \lesssim \frac{|f_{\psi\pi^0}^{\psi(2S)}(0)|}{|f_{\psi\eta}^{\psi(2S)}(0)|} \approx 0.045. \tag{3.20}$$

We assume this to be an upper limit due to the observation that the $\psi(2S) \to J/\psi\pi^0$ decay rate is somewhat enhanced relative to $\psi(2S) \to J/\psi\eta$ due to charmed-meson loop effects [85]. The lower limit of 1% is the size of a typical, nonenhanced isospin-breaking effect, which requires cancellation of individual charmonium resonances by no more than one order of magnitude. We therefore estimate (with $|f_{\psi\eta}^{c\bar{c}}(0)| \approx |f_{\psi\eta}(0)|$)

$$0.3 \times 10^{-4}\,\text{GeV}^{-1} \lesssim |f_{\psi\pi^0}^{c\bar{c}}(0)| \lesssim 1.6 \times 10^{-4}\,\text{GeV}^{-1}. \tag{3.21}$$

For the s-dependence of this contribution, we adopt the simple monopole ansatz [72],

$$f_{\psi\pi^0}^{c\bar{c}}(s) = \frac{f_{\psi\pi^0}^{c\bar{c}}(0)}{1 - s/\Lambda^2}, \tag{3.22}$$

and vary the effective scale Λ between the mass of the J/ψ and the mass of the $\psi(2S)$.

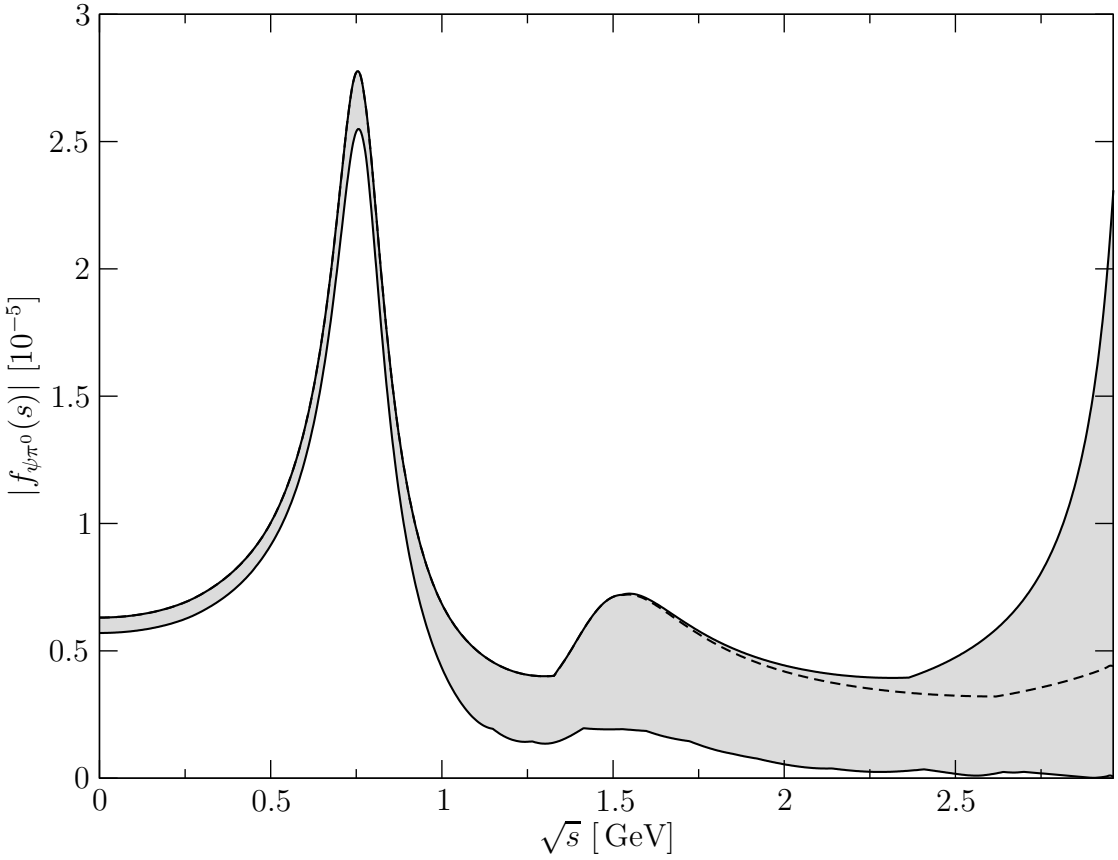

Figure 3.2: Modulus of the transition form factor $|f_{\psi\pi^0}(s)|$. See the main text for the discussion of the uncertainty band. The dashed curve denotes the upper limit of the band in the case that the scale Λ for the charmonium contribution is fixed to the $\psi(2S)$ mass.

3.4 Results and discussion

In Fig. 3.2, we show the modulus of our total form factor

$$f_{\psi\pi^0}(s) = f^{\pi\pi}_{\psi\pi^0}(s) + f^{\rho'}_{\psi\pi^0}(s) + f^{c\bar{c}}_{\psi\pi^0}(s). \tag{3.23}$$

While $f^{\pi\pi}_{\psi\pi^0}(s)$ is fixed within its (rather narrow) uncertainty, we vary the effective ρ' and charmonium contributions within the rather generous error bands discussed in the previous sections, with unknown relative signs, but subject to the constraint that the $J/\psi \to \pi^0\gamma$ sum rule be fulfilled within experimental uncertainties, $|f_{\psi\pi^0}(0)| = (6.0 \pm 0.3) \times 10^{-4}\,\mathrm{GeV}^{-1}$. This variation in the normalization determines the error band in the form factor at low energies, while the theoretical variation within our rather crude estimates of the ρ' and $c\bar{c}$ contributions dominates the uncertainty above $\sqrt{s} \gtrsim 1\,\mathrm{GeV}$. While all the light-quark

resonance contributions drop like $1/s$ above their respective characteristic scales (the masses of ρ and ρ'), $f_{\psi\pi^0}^{c\bar{c}}(s)$ rises close to the upper limit of the accessible decay phase space and dominates the total form factor there. In particular, if the characteristic scale Λ is set to the J/ψ mass, $f_{\psi\pi^0}^{c\bar{c}}(s)$ is enhanced by roughly a factor $M_\psi/(2M_{\pi^0}) \approx 11.5$ at $\sqrt{s} = M_\psi - M_{\pi^0}$. Figure 3.2 also shows the upper form factor limit using $\Lambda = M_{\psi(2S)}$ only, which limits the rise significantly. In addition, Fig. 3.3 shows the resulting differential decay rates for $J/\psi \to \pi^0 e^+ e^-$ and $J/\psi \to \pi^0 \mu^+ \mu^-$. For comparison, we also display the distributions obtained by setting $f_{\psi\pi^0}(s) \equiv f_{\psi\pi^0}(0)$. For both final states, the clear enhancement due to the ρ resonance in the $\pi\pi$ intermediate state is the dominating form factor feature, while $\mathrm{d}\Gamma_{\psi\to\pi^0 e^+e^-}/\mathrm{d}s$ rises strongly near $\sqrt{s} = 0$. The sizable form factor uncertainty at large energies occurs in a region where phase space already suppresses the decay distributions strongly; in particular, a potential strong rise in the form factor due to J/ψ pole contributions is probably not experimentally observable.

Integrating over the respective spectra, we can calculate the branching fractions for the two dilepton final states. We find

$$\begin{aligned} \mathcal{B}(J/\psi \to \pi^0 e^+ e^-) &= (5.5 \ldots 6.4) \times 10^{-7}, \\ \mathcal{B}(J/\psi \to \pi^0 \mu^+ \mu^-) &= (2.7 \ldots 3.3) \times 10^{-7}. \end{aligned} \tag{3.24}$$

This can be compared to the numbers obtained from QED spectra with a constant form factor, $\mathcal{B}(J/\psi \to \pi^0 e^+ e^-) = (3.7 \pm 0.4) \times 10^{-7}$, $\mathcal{B}(J/\psi \to \pi^0 e^+ e^-) = (0.9 \pm 0.1) \times 10^{-7}$. A monopole form factor as in Eq. (3.22), with the scale given by the mass of the $\psi(2S)$ [72], magnifies these by a few percent only. Our dispersive result therefore enhances the branching fractions very considerably, almost by a factor of 3 for the muon final state. Note that the dispersive prediction Eq. (3.24) is remarkably stable due to the dominance of the low-energy region in the integrated rate.

It is rather unclear how to compare Eq. (3.24) to the experimental result $\mathcal{B}(J/\psi \to \pi^0 e^+ e^-) = (7.56 \pm 1.32 \pm 0.50) \times 10^{-7}$ [71], as this has purportedly been obtained subtracting the ρ contribution to the form factor. Our analysis above demonstrates that such an attempt does not make sense: there is no theoretically sound way to separate the ρ resonance from the nonresonant $\pi\pi$ background, and we have demonstrated that the $\pi\pi$ contribution to the form factor normalization is actually dominant. In particular also the energy region below the ρ mass would have to be heavily affected by such a subtraction, leading to a form factor normalization that is in stark contradiction with the $J/\psi \to \pi^0\gamma$ decay rate. This is obviously quantitatively different from removing the isoscalar ω and ϕ resonances from $J/\psi \to \eta, \eta'\gamma^*$ transition form factors due to the overall smallness of their contribution.

It would be interesting and most desirable to experimentally extract the full, unchanged, transition form factor without any parts subtracted, given that it is precisely the interplay between three energy regions of the $J/\psi \to \pi^0\gamma^*$ form factor that is most challenging theoretically: low energies below 1 GeV with the dominance of the ρ; potentially sizable

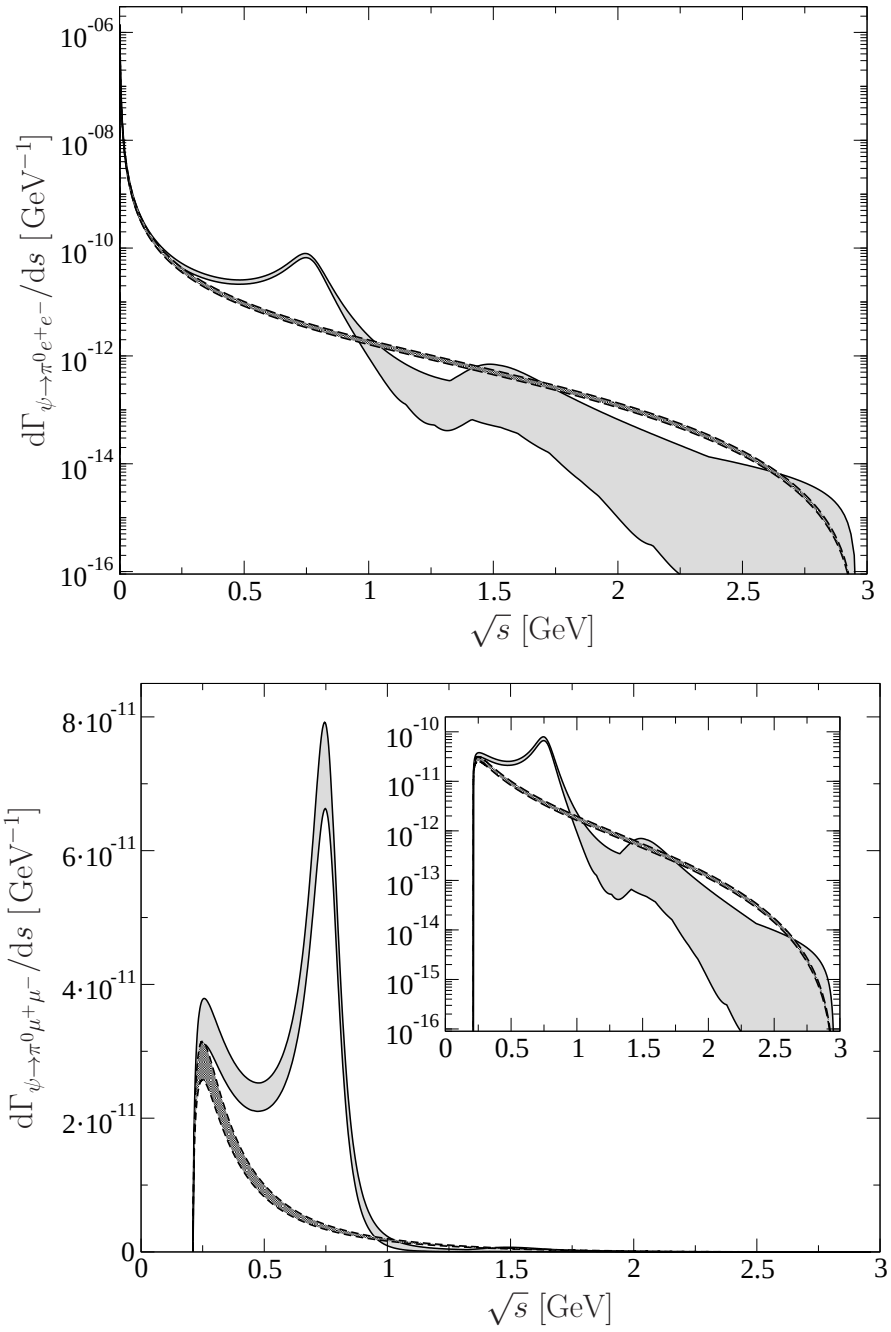

Figure 3.3: Differential decay rates $\mathrm{d}\Gamma/\mathrm{d}s$ for $J/\psi \to \pi^0 e^+e^-$ (left) and $J/\psi \to \pi^0\mu^+\mu^-$ (right); the insert in the right panel displays the same distribution on a logarithmic scale. The full gray bands correspond to our form factor prediction, while the dashed bands show the QED distributions for comparison, i.e. with the form factor set to a constant.

contributions of excited light ρ' resonances between 1 and 2 GeV; and the contribution from charmonium in the spectral function most visible near the upper limit of the decay region.

3.5 Summary

To summarize, we have analyzed the $J/\psi \to \pi^0\gamma^*$ transition form factor using dispersion theory. We have shown that the corresponding spectral function is dominated by the $\pi^+\pi^-$ intermediate state, of which the contribution can be calculated using the $J/\psi \to 3\pi$ P-wave decay amplitude as well as the pion vector form factor. A sum rule for the form factor normalization, which determines the decay rate $J/\psi \to \pi^0\gamma$, is saturated to about 80% by the $\pi\pi$ contribution only, showing that this transition form factor is dominated by light-quark dynamics. We have given rough estimates for the contributions of four pions, approximated by an effective $\rho'(1450)$ resonance, and charmonium states, comparing to the latter's (dominant) effect on the $J/\psi \to \eta$, $\eta'\gamma^*$ transitions.

For the differential decay rates $J/\psi \to \pi^0\ell^+\ell^-$, the ρ resonance in the $\pi\pi$ spectrum is the dominating feature, leading to very stable values for the integrated branching fractions despite large form factor uncertainties at high energies. An experimental confirmation of the decay spectra predicted here, as well as a determination of the branching fractions taking the full, unmodified form factor into account, would be highly desirable.

Part II

Dispersive analysis of the $D^+ \to K\pi\pi^+$ Dalitz plots[2]

[2]Parts of this part have been published in Ref. [86].

Chapter 4

The dispersion-theoretical decay amplitudes

4.1 Introduction

Heavy-flavor three-body decays into light mesons provide a valuable source for Standard Model tests and beyond. While they are driven, at short distances, by the weak interactions, their rich kinematic structure accessible in Dalitz plot distributions makes them a prime example for the application of modern tools of amplitude analysis [87]. A major motivation for the investigation of heavy-flavor decays is the study of CP violation, which manifests itself in the appearance of (weak) phases and requires the interference of different amplitudes with, at the same time, different phases in the strong final-state interactions (see, e.g., Ref. [88] for an in-depth overview). In contrast to (quasi-)two-body decays occurring at fixed total energies, three-body decays offer a resonance-rich environment with rapidly varying strong phases throughout the phase space available, which may strongly magnify the effects of CP violation in certain parts of the Dalitz plot.

Obviously, in order to turn the search for potentially very small CP-violating phases in such complicated hadronic environments into a precision instrument, it is inevitable to control the strong dynamics in the final state as accurately as possible, in a model-independent fashion that, however, incorporates a maximum of theoretical and phenomenological constraints. The traditional approach to model Dalitz plots in terms of isobars, i.e. a series of subsequent two-body decays, and describe the relevant line shapes in terms of Breit–Wigner (or Flatté) functions, has clear limitations: it fails to describe in particular the phase motion of the broad S-wave resonances such as the $f_0(500)$ in pion–pion or the $K_0^*(800)$ in pion–kaon scattering (see e.g. Refs. [89, 90] in the context of heavy-flavor decays), and neglects corrections beyond two-body rescattering in an unquantified manner.

It has therefore been advocated to employ the framework of dispersion theory for ampli-

tude analyses [87], which is built on unitarity, maximal analyticity, and crossing symmetry. The dispersion framework we will utilize is once more based on Khuri–Treiman dispersion relations.

Khuri–Treiman equations have been successfully applied to various low-energy meson decays, like e.g. $\eta \to 3\pi$ [45, 46, 91, 92], $\eta' \to \eta\pi\pi$ [58] or $\omega/\phi \to 3\pi$ [34, 93] and general $V \to 3\pi$ decays in the previous part of this thesis. In this part, we extend this formalism to three-body decays of open-charm mesons, analyzing the Cabibbo-favored decays $D^+ \to K^-\pi^+\pi^+/\bar{K}^0\pi^0\pi^+$. As input we solely rely on $\pi\pi$ and πK phase-shift input. While these are not yet decay channels of major interest to study CP violation, the final-state interactions are going to be similar for others that are, such as the Cabibbo-suppressed decays $D \to 3\pi/\pi K\bar{K}$. For the decays at hand, inelastic effects are small in large regions of the Dalitz plots, and therefore elastic unitarity provides a good approximation: the $\pi\pi$ channel allows for isospin 1 and 2 only, but no isoscalar components, which would necessitate a coupled-channel treatment, as a strong coupling to $K\bar{K}$ occurs. The major inelasticities in the πK channel are found to set in at the $\eta' K$ threshold [94–96].

Thus with the high-statistics experimental data available [97–100], these decays provide a good test case to establish this dispersive framework in higher energy regions and set the path to Cabibbo-suppressed decays where traces of physics beyond the Standard Model may be searched for. Besides, it allows for a further test of low-energy πK and $\pi\pi$ dynamics as well as the importance of crossed-channel rescattering effects in three-body decays. It may also provide an insight into scattering phase shifts at higher energies in the future.

The decays under consideration has been the subject of a number of previous theoretical publications, focusing on different issues raised by the experimental results. One challenge is the proper treatment of the isospin 1/2 S-wave with the very broad, non-Breit–Wigner-shaped $K_0^*(800)$ (or κ) resonance [101], and the inclusion of two scalar resonances $K_0^*(800)$ and $K_0^*(1430)$ in a way that conserves unitarity. Furthermore, the width of the $K_0^*(1430)$ extracted from the experimental analyses in Refs. [97, 98] is found to be inconsistent with PDG values [82]. In addition, the explicit comparison of the πK partial-wave phases extracted from these decays [99, 102] with πK scattering results [103] seems to indicate deviations from Watson's final-state theorem.

Ref. [104] focuses on the isospin 1/2 S-wave final-state interactions, based on coupled-channel partial waves for $K\pi$, $K\eta$, and $K\eta'$ constructed dispersively in Ref. [94]. Decay and scattering data could be reconciled, although no three-body rescattering effects, isospin 3/2 components, or $\pi\pi$ channel were included. Ref. [105] similarly observes mutual consistency of πK scattering and the D-meson decay, using related input to take two-body final-state interactions in the πK isospin 1/2 S- and P-wave into account in terms of the corresponding scalar and vector form factors. Furthermore, the short-distance weak interactions are described with the help of an effective Hamiltonian based on a factorization ansatz. Again, weak repulsive partial waves (of isospin 3/2 and in the $\pi\pi$ system) as well as crossed-channel rescattering are neglected. We mention that similar approaches, using dis-

persively constructed form factors for two-body rescattering, but neglecting third-particle interactions, have also been applied to $B \to K\pi\pi$ decays [106, 107].

In Ref. [108], a Faddeev-like equation is solved that builds up three-particle rescattering effects. The underlying two-particle πK amplitudes are obtained form unitarized chiral perturbation theory fitted to experimental data. The decay amplitude is simplified to include only the isospin 1/2 S-wave, aiming mainly at a study of the importance of rescattering effects and the reproduction of the experimental S-wave phases [99,102]. The model for the weak vertex has subsequently been improved [109]. Ref. [110] applies a similar approach with the addition of the isospin 3/2 πK S-wave, but is still restricted to S-waves only. The only theoretical analysis known to us with all relevant partial waves, three-particle rescattering effects, and effects of the intermediate state $\bar{K}^0\pi^0\pi^+$ included, is Ref. [111]. The author performs a full Dalitz plot analysis on pseudo data, which we will later compare to.

4.2 Kinematics

The Mandelstam variables of the D-meson decay

$$D^+(p_D) \to \bar{K}(p_K)\pi(p_1)\pi^+(p_2) \tag{4.1}$$

are given by $s = (p_D - p_1)^2$, $t = (p_D - p_2)^2$, and $u = (p_D - p_K)^2$. The corresponding scattering angles θ in the (crossed) scattering processes are given by

$$\begin{aligned} z_s \equiv \cos\theta_s = \frac{s(t-u)-\Delta}{\kappa_s(s)}\,, \quad z_t \equiv \cos\theta_t = \frac{t(s-u)-\Delta}{\kappa_t(t)}\,, \quad z_u \equiv \cos\theta_u = \frac{t-s}{\kappa_u(u)}\,, \\ \kappa_{s/t}(x) = \lambda^{1/2}(x, M_K^2, M_\pi^2)\lambda^{1/2}(x, M_D^2, M_\pi^2)\,, \quad \kappa_u(u) = \lambda^{1/2}(u, M_D^2, M_K^2)\sqrt{1-\frac{4M_\pi^2}{u}}\,, \end{aligned} \tag{4.2}$$

with $\Delta = \left(M_D^2 - M_\pi^2\right)\left(M_K^2 - M_\pi^2\right)$. Furthermore, we can express the Mandelstam variables in the x-channel by x and the cosine of scattering angle z_x which we will need in the following.

1. s-channel

$$t = \frac{1}{2}\left(\Sigma_0 - s + \frac{\Delta}{s} + \frac{\kappa_s(s)}{s}z_s\right)\,, \quad u = \frac{1}{2}\left(\Sigma_0 - s - \frac{\Delta}{s} - \frac{\kappa_s(s)}{s}z_s\right)\,. \tag{4.3}$$

2. t-channel

$$s = \frac{1}{2}\left(\Sigma_0 - t + \frac{\Delta}{t} + \frac{\kappa_t(t)}{t}z_t\right)\,, \quad u = \frac{1}{2}\left(\Sigma_0 - t - \frac{\Delta}{t} - \frac{\kappa_t(t)}{t}z_t\right)\,. \tag{4.4}$$

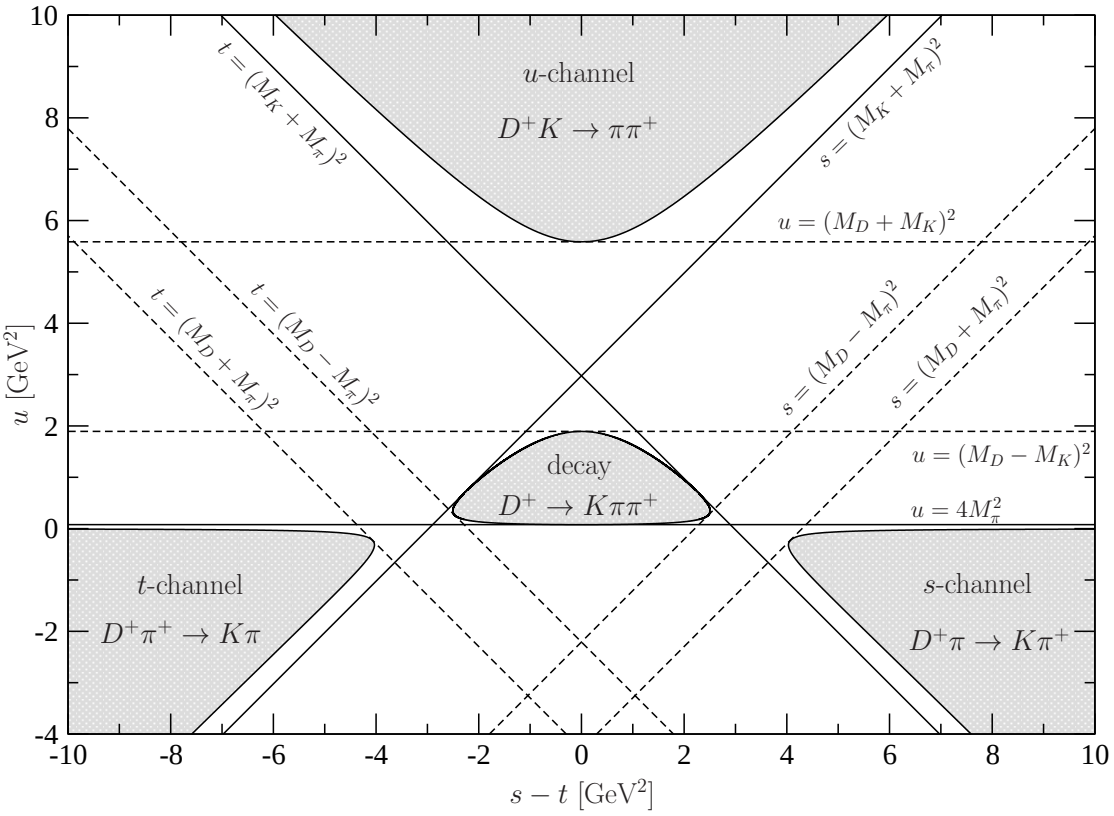

Figure 4.1: The Mandelstam plane with Mandelstam u plotted against $s - t$. The gray shaded areas are the decay region (Dalitz plot) and the s-, t-, and u-channel scattering regions respectively. The white area is the unphysical region.

3. u-channel

$$t = \frac{1}{2}\left(\Sigma_0 - u + \kappa_u(u) z_u\right) \ , \quad s = \frac{1}{2}\left(\Sigma_0 - u - \kappa_u(u) z_u\right) \ . \tag{4.5}$$

The different kinematical regions (decay and scattering) are depicted in Fig. 4.1.

4.3 Dispersive treatment

In this section we will derive the Khuri–Treiman dispersive integral equations analogously to the $V \to 3\pi$ analysis previously. Since here the three final-state particles are not identical the structure will be more evolved. We again start out decomposing the decay amplitude into functions of one variable via the reconstruction theorem, rewrite these in terms of

Khuri–Treiman-type equations, determine the number of subtraction constants needed, and solve the equations.

4.3.1 Reconstruction theorem

We start the dispersive endeavor with the reconstruction theorem introduced in Section 2.3. Opposed to the symmetric 3π state with maximal symmetry in s, t, and u, in the $K^-\pi^+\pi^+$ final state we have only an $s \leftrightarrow t$ symmetry, corresponding to the interchange of the two final-state pions. For the $\bar{K}^0\pi^0\pi^+$ state no such symmetry is present and we have to study all fixed-s, fixed-t, and fixed-u dispersion relations. We will start with the $K^-\pi^+\pi^+$ final state without πK D-wave amplitudes. The inclusion of πK D-waves is discussed in Appendix C.2.1 as well as the reconstruction of the $\bar{K}^0\pi^0\pi^+$ final state in Appendix C.2.2. Starting with the fixed-u dispersion relation (fixing Mandelstam $u = u_0$) we obtain

$$\begin{aligned}\mathcal{M}_{-++}(s,t,u_0) =& p_{n-1}(s,t,u_0) + \frac{t^n}{\pi}\int_{t_\text{th}}^{\infty} \frac{\operatorname{Im}\mathcal{M}_{-++}(s'(t'),t',u_0)}{t'^n(t'-t)}\mathrm{d}t' \\ &+ \frac{s^n}{\pi}\int_{s_\text{th}}^{\infty} \frac{\operatorname{Im}\mathcal{M}_{-++}(s',t'(s'),u_0)}{s'^n(s'-s)}\mathrm{d}s' \ , \end{aligned} \tag{4.6}$$

where $p_{n-1}(s,t,u)$ denotes a polynomial of order $n-1$ in s, t, and u and the thresholds $s_\text{th}/t_\text{th} = \big(M_K + M_\pi\big)^2$. The partial-wave decomposition of the s- and t-channel amplitudes read

$$\mathcal{M}_{-++}(s(t),t,u_0) = \sum_L f_L(t)P_L(z_t) \ , \qquad \mathcal{M}_{-++}(s,t(s),u_0) = \sum_L f_L(s)P_L(z_s) \ . \tag{4.7}$$

As the decay amplitude is symmetric interchanging the two final-state pions the decomposition yields the same partial waves. Inserting the partial-wave decomposition Eq. (4.7) into Eq (4.6) we find with $L < 2$

$$\begin{aligned}\mathcal{M}_{-++}(s,t,u_0) =& \ p_{n-1}(s,t,u_0) + \frac{t^n}{\pi}\int_{t_\text{th}}^{\infty} \frac{\operatorname{Im} f_0(t')}{t'^n(t'-t)}\mathrm{d}t' \\ &+ \frac{t^n}{\pi}\int_{t_\text{th}}^{\infty} \frac{\big(t'(s'(t')-u_0)-\Delta\big)\operatorname{Im} f_1(t')}{\kappa_t(t')t'^n(t'-t)}\mathrm{d}t' + (t \leftrightarrow s) \ . \end{aligned} \tag{4.8}$$

The first dispersion integral, the S-wave contribution in the t-channel, can be written directly as a function depending on one variable, while the other terms require further transformations. With $s'(t') = \Sigma - u_0 - t'$ and $\Sigma = s + t + u_0$ we have

$$t'(s'(t') - u_0) = t'(t - t' - u_0 + s) \ , \tag{4.9}$$

and therefore we obtain for the second term in Eq. (4.8)

$$\begin{aligned}
&\frac{t^n}{\pi}\int_{t_{\rm th}}^{\infty}\frac{\big(t'(s'(t')-u_0)-\Delta\big)\mathrm{Im}\,f_1(t')}{\kappa_t(t')t'^n(t'-t)}\mathrm{d}t' = \frac{t^n}{\pi}\int_{t_{\rm th}}^{\infty}\frac{t'(s-u_0)\mathrm{Im}\,f_1(t')}{\kappa_t(t')t'^n(t'-t)}\mathrm{d}t' \\
&-\Delta\frac{t^n}{\pi}\int_{t_{\rm th}}^{\infty}\frac{\mathrm{Im}\,f_1(t')}{\kappa_t(t')t'^n(t'-t)}\mathrm{d}t' + \frac{t^n}{\pi}\int_{t_{\rm th}}^{\infty}\frac{t'(t-t')\mathrm{Im}\,f_1(t')}{\kappa_t(t')t'^n(t'-t)}\mathrm{d}t' \\
&= p_n(s,t,u_0) + \big(t(s-u_0)-\Delta\big)\frac{t^{n-1}}{\pi}\int_{t_{\rm th}}^{\infty}\frac{\mathrm{Im}\,f_1(t')}{\kappa_t(t')t'^{n-1}(t'-t)}\mathrm{d}t' \ . \qquad (4.10)
\end{aligned}$$

This results in

$$\begin{aligned}
\mathcal{M}_{-++}(s,t,u_0) = p_n(s,t,u_0) &+ \frac{t^{n+1}}{\pi}\int_{t_{\rm th}}^{\infty}\frac{\mathrm{Im}\,f_0(t')}{t'^{n+1}(t'-t)}\mathrm{d}t' \\
&+ \big(t(s-u_0)-\Delta\big)\frac{t^{n-1}}{\pi}\int_{t_{\rm th}}^{\infty}\frac{\mathrm{Im}\,f_1(t')}{\kappa_t(t')t'^{n-1}(t'-t)}\mathrm{d}t' + (t\leftrightarrow s)\ , \qquad (4.11)
\end{aligned}$$

where we have subtracted the S-wave one time further. Similarly we obtain for the fixed-t dispersion relation ($t=t_0$)

$$\begin{aligned}
\mathcal{M}_{-++}(s,t_0,u) =& p_{n-1}(s,t_0,u) + \frac{u^n}{\pi}\int_{u_{\rm th}}^{\infty}\frac{\mathrm{Im}\,\mathcal{M}_{-++}(s'(u'),t_0,u')}{u'^n(u'-u)}\mathrm{d}t' \\
&+ \frac{s^n}{\pi}\int_{s_{\rm th}}^{\infty}\frac{\mathrm{Im}\,\mathcal{M}_{-++}(s',t_0,u'(s'))}{s'^n(s'-s)}\mathrm{d}s' \ . \qquad (4.12)
\end{aligned}$$

With the partial-wave decomposition

$$\mathcal{M}_{-++}(s(u),t_0,u) = \sum_L h_L(u)P_L(z_u), \quad \mathcal{M}_{-++}(s,t_0,u(s)) = \sum_L f_L(s)P_L(z_s)\ , \qquad (4.13)$$

the s-channel contributions follow as above. In the u-channel we retain only the S-wave contribution as due to Bose symmetry only even angular momenta are allowed in the $\pi^+\pi^+$-system and we truncate at $L<2$,

$$\begin{aligned}
\mathcal{M}_{-++}(s,t_0,u) = p_n(s,t_0,u) &+ \frac{u^n}{\pi}\int_{u_{\rm th}}^{\infty}\frac{\mathrm{Im}\,h_0(u')}{u'^n(u'-u)}\mathrm{d}u' + \frac{s^{n+1}}{\pi}\int_{s_{\rm th}}^{\infty}\frac{\mathrm{Im}\,f_0(s')}{s'^{n+1}(s'-s)}\mathrm{d}s' \\
&+ \big(s(t_0-u)-\Delta\big)\frac{s^{n-1}}{\pi}\int_{s_{\rm th}}^{\infty}\frac{\mathrm{Im}\,f_1(s')}{\kappa_s(s')s'^{n-1}(s'-s)}\mathrm{d}t' \ . \qquad (4.14)
\end{aligned}$$

The fixed-s dispersion relation is symmetric to the fixed t-dispersion relation since $\mathcal{M}_{-++}(s,t,u)=\mathcal{M}_{-++}(t,s,u)$.The symmetrization of the three fixed dispersion relations

to obtain the full decay amplitude yields

$$\begin{aligned}\mathcal{M}_{-++}(s,t,u) = p_n(s,t,u) &+ \frac{u^n}{\pi}\int_{u_\text{th}}^{\infty}\frac{\operatorname{Im} h_0(u')}{u'^n(u'-u)}\mathrm{d}u' + \frac{s^{n+1}}{\pi}\int_{s_\text{th}}^{\infty}\frac{\operatorname{Im} f_0(s')}{s'^{n+1}(s'-s)}\mathrm{d}s' \\ &+ \frac{t^{n+1}}{\pi}\int_{t_\text{th}}^{\infty}\frac{\operatorname{Im} f_0(t')}{t'^{n+1}(t'-t)}\mathrm{d}t' \\ &+ \big(s(t-u)-\Delta\big)\frac{s^{n-1}}{\pi}\int_{s_\text{th}}^{\infty}\frac{\operatorname{Im} f_1(s')}{\kappa_s(s')s'^{n-1}(s'-s)}\mathrm{d}s' \\ &+ \big(t(s-u)-\Delta\big)\frac{t^{n-1}}{\pi}\int_{t_\text{th}}^{\infty}\frac{\operatorname{Im} f_1(t')}{\kappa_t(t')t'^{n-1}(t'-t)}\mathrm{d}t' \,. \end{aligned} \tag{4.15}$$

Additionally, we would like to decompose the single-variable amplitudes further into definite isospin states. We associate the isospin structure of the strong final-state current in Fig. 4.2 with the D^+ meson. Since one $\bar{u}u/\bar{d}d$ pair is strongly produced, the associated isospin of the D meson is given by $I = 3/2$, $I_z = 3/2$. Thus the isospin decomposition of the respective (crossed) scattering processes reads

s/t-channel		u-channel	
$\mathcal{M}_{D^+\pi^0\to\bar{K}^0\pi^+}$	$= \sqrt{\frac{3}{5}}\mathcal{F}^{3/2}\,,$	$\mathcal{M}_{D^+K^0\to\pi^0\pi^+}$	$= \frac{1}{2\sqrt{2}}\big(\mathcal{F}^2-\sqrt{3}\mathcal{F}^1\big)\,,$
$\mathcal{M}_{D^+\pi^-\to K^-\pi^+}$	$= \sqrt{\frac{2}{15}}\mathcal{F}^{3/2}-\frac{1}{\sqrt{3}}\mathcal{F}^{1/2}\,,$	$\mathcal{M}_{D^+K^0\to\pi^+\pi^0}$	$= \frac{1}{2\sqrt{2}}\big(\mathcal{F}^2+\sqrt{3}\mathcal{F}^1\big)\,,$
$\mathcal{M}_{D^+\pi^-\to\bar{K}^0\pi^0}$	$= \frac{2}{\sqrt{15}}\mathcal{F}^{3/2}+\frac{1}{\sqrt{6}}\mathcal{F}^{1/2}\,,$	$\mathcal{M}_{D^+K^+\to\pi^+\pi^+}$	$= \mathcal{F}^2\,.$

(4.16)

With the phase condition employed in Appendix C.1 we obtain

$$\begin{aligned}\mathcal{M}_{-++}(s,t,u) =& p_n(s,t,u) + \frac{u^n}{\pi}\int_{u_\text{th}}^{\infty}\frac{\operatorname{Im} h_0^2(u')}{u'^n(u'-u)}\mathrm{d}u' \\ &+ \Bigg\{\frac{1}{\sqrt{3}}\frac{s^{n+1}}{\pi}\int_{s_\text{th}}^{\infty}\frac{\operatorname{Im} f_0^{1/2}(s')}{s'^{n+1}(s'-s)}\mathrm{d}s' - \sqrt{\frac{2}{15}}\frac{s^{n+1}}{\pi}\int_{s_\text{th}}^{\infty}\frac{\operatorname{Im} f_0^{3/2}(s')}{s'^{n+1}(s'-s)}\mathrm{d}s' \\ &+ \frac{1}{\sqrt{3}}\big(s(t-u)-\Delta\big)\frac{s^{n-1}}{\pi}\int_{s_\text{th}}^{\infty}\frac{\operatorname{Im} f_1^{1/2}(s')}{\kappa_s(s')s'^{n-1}(s'-s)}\mathrm{d}s' \\ &- \sqrt{\frac{2}{15}}\big(s(t-u)-\Delta\big)\frac{s^{n-1}}{\pi}\int_{s_\text{th}}^{\infty}\frac{\operatorname{Im} f_1^{3/2}(s')}{\kappa_s(s')s'^{n-1}(s'-s)}\mathrm{d}s' + (s\leftrightarrow t)\Bigg\}\,, \end{aligned} \tag{4.17}$$

where the $f_L^I(s)$ and $h_L^I(u)$ denote the partial waves of angular momentum L and isospin I. Thus all dispersion integrals are functions of one variable with corresponding angular

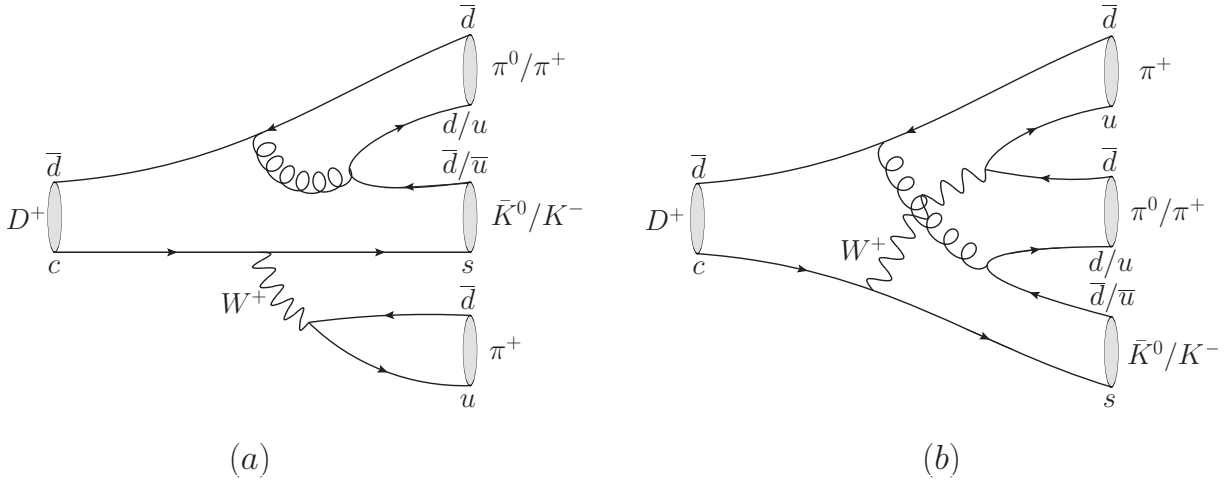

Figure 4.2: Quark line diagrams of the $D^+ \to K^-\pi^+\pi^+/\bar{K}^0\pi^0\pi^+$ decays: W^+ as a spectator (a) and internal W^+ conversion (b).

momentum polynomials in front. The only piece not fitting into the decomposition yet is the subtraction polynomial, which as a last hurdle needs to be incorporated as subtraction constants of the single dispersion integrals. As a last step we need to specify the number of subtractions and distribute the components of the subtraction polynomial p_n. With no loss of generality we take $n = 2$ in Eq. (4.15) and together with the $(s \leftrightarrow t)$ symmetry we obtain the general polynomial

$$p_2(s,t,u) = a_0 + a_1(s+t) + a_2(s^2+t^2) + b_1\big(s(t-u) + t(s-u)\big) \ . \tag{4.18}$$

The a_i can be interpreted as S-wave subtraction constants and b_1 as the P-wave subtraction constants of order 0 (tuned by a_i). Thus we obtain the following decomposition into single-variable amplitudes,

$$\begin{aligned}\mathcal{M}_{-++}(s,t,u) = \mathcal{F}_0^2(u) + \Bigg\{ &\frac{1}{\sqrt{3}}\mathcal{F}_0^{1/2}(s) - \sqrt{\frac{2}{15}}\mathcal{F}_0^{3/2}(s) \\ &+ \big[s(t-u) - \Delta\big]\left(\frac{1}{\sqrt{3}}\mathcal{F}_1^{1/2}(s) - \sqrt{\frac{2}{15}}\mathcal{F}_1^{3/2}(s)\right) + (s \leftrightarrow t)\Bigg\} \ , \end{aligned} \tag{4.19}$$

where the amplitudes $\mathcal{F}_L^I(x)$ of definite angular momentum L and isospin I in the x-channel are given by

$$\mathcal{F}_0^0(u) \equiv \frac{u^2}{\pi}\int_{u_{\rm th}}^{\infty} \frac{\operatorname{Im} h_0^0(u')}{u'^2(u'-u)}\mathrm{d}u' \ , \quad \mathcal{F}_0^{1/2}(s) \equiv d_0 + d_1 s + d_2 s^2 + \frac{s^3}{\pi}\int_{s_{\rm th}}^{\infty} \frac{\operatorname{Im}{}^{1/2} f_0(s')}{s'^3(s'-s)}\mathrm{d}s' \ ,$$

$$\mathcal{F}_0^{3/2}(s) \equiv \frac{s^3}{\pi}\int_{s_\text{th}}^{\infty}\frac{\operatorname{Im} f_0^{3/2}(s')}{s'^3(s'-s)}\mathrm{d}s' \ , \quad \mathcal{F}_1^{1/2}(s) \equiv d_3 + \frac{s}{\pi}\int_{s_\text{th}}^{\infty}\frac{\operatorname{Im} f_1^{1/2}(s')}{\kappa_s(s')s'(s'-s)}\mathrm{d}s' \ ,$$
$$\mathcal{F}_1^{3/2}(s) \equiv \frac{s}{\pi}\int_{s_\text{th}}^{\infty}\frac{\operatorname{Im} f_1^{3/2}(s')}{\kappa_s(s')s'(s'-s)}\mathrm{d}s' \ . \tag{4.20}$$

Note that assigning the subtraction constants to certain single-variable amplitudes can be ambiguous. In particular the subtraction constants of $\mathcal{F}_0^{1/2}$ can be shifted freely to $\mathcal{F}_0^{3/2}$ and back.

Likewise, the reconstruction procedure is applied to the $\mathcal{M}_{\bar{0}0+}(s,t,u)$ decay amplitude in Appendix C.2.2 resulting in

$$\begin{aligned}\mathcal{M}_{\bar{0}0+}(s,t,u) = {}& \frac{1}{2\sqrt{2}}\big(-\mathcal{F}_0^2(u) + \sqrt{3}(t-s)\,\mathcal{F}_1^1(u)\big) + \sqrt{\frac{3}{5}}\mathcal{F}_0^{3/2}(s) \\ & + \sqrt{\frac{3}{5}}\big[s(t-u)-\Delta\big]\,\mathcal{F}_1^{3/2}(s) + \frac{\sqrt{3}}{2\sqrt{5}}\big[3\big(s(t-u)-\Delta\big)^2 - \kappa_s^2(s)\big]\,\mathcal{F}_2^{3/2}(s) \\ & - \left(\frac{2}{\sqrt{15}}\mathcal{F}_0^{3/2}(t) + \frac{1}{\sqrt{6}}\mathcal{F}_0^{1/2}(t)\right) \\ & - \big[t(s-u)-\Delta\big]\left(\frac{2}{\sqrt{15}}\mathcal{F}_1^{3/2}(t) + \frac{1}{\sqrt{6}}\mathcal{F}_1^{1/2}(t)\right) \ ,\end{aligned} \tag{4.21}$$

The $\mathcal{M}_{\bar{0}0+}(s,t,u)$ amplitude exhibits an explicit contribution from the $\pi\pi$ P-wave single-variable amplitude $\mathcal{F}_1^1(u)$ not present in the $\mathcal{M}_{-++}(s,t,u)$ decay amplitude. The inclusion of D-waves is discussed in Appendix C.2.1. In order to rigorously prove the symmetrized decomposition including the D-waves in the spirit of the reconstruction theorem, one needs to include a subtraction polynomial of higher order (i.e., a larger number of unknown parameters) than what we have allowed for above and will allow for below. Otherwise the number of subtraction constants that have to be fixed by other means, experimental or theory beyond the dispersive treatment, will become too large. We mainly want to retain the πK D-wave to test the effect of the $K_2^*(1430)$ resonance, which is kinematically accessible in the decay phase space. The way we implement this approximately will be discussed in Section 4.3.5. The inclusion of the πK D-wave is thus heuristic and the decomposition including the D-wave reads

$$\begin{aligned}\mathcal{M}_{-++}(s,t,u) = {}& \mathcal{F}_0^2(u) + \left\{\frac{1}{\sqrt{3}}\mathcal{F}_0^{1/2}(s) - \sqrt{\frac{2}{15}}\mathcal{F}_0^{3/2}(s)\right. \\ & + \big[s(t-u)-\Delta\big]\left(\frac{1}{\sqrt{3}}\mathcal{F}_1^{1/2}(s) - \sqrt{\frac{2}{15}}\mathcal{F}_1^{3/2}(s)\right) \\ & \left. + \frac{1}{2}\big[3\big(s(t-u)-\Delta\big)^2 - \kappa_s^2(s)\big]\left(\frac{1}{\sqrt{3}}\mathcal{F}_2^{1/2}(s) - \sqrt{\frac{2}{15}}\mathcal{F}_2^{3/2}(s)\right) + (s\leftrightarrow t)\right\},\end{aligned}$$

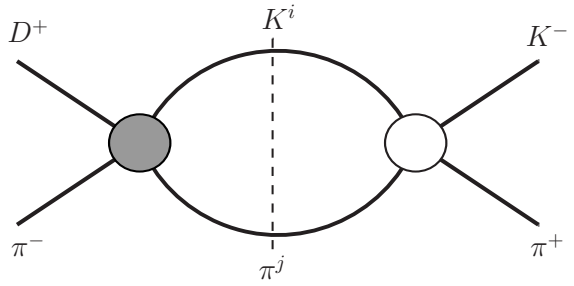

Figure 4.3: The associated s-channel scattering diagram $D^+\pi^- \to K^-\pi^+$ via the intermediate states $K^i\pi^j$. The gray vertex stands for the crossed decay amplitude $D^+\pi^- \to K^i\pi^j$ denoted by $\mathcal{M}_{ij+}$ and the white vertex the $K^i\pi^j \to K^-\pi^+$ scattering amplitude denoted by $T^{ij,-+}$. The dashed line gives the contribution to the discontinuity [112]. The other channels follow analogously.

$$\begin{aligned}\mathcal{M}_{\bar{0}0+}(s,t,u) = \frac{1}{2\sqrt{2}}\big(-\mathcal{F}_0^2(u) + \sqrt{3}(t-s)\,\mathcal{F}_1^1(u)\big) + \sqrt{\frac{3}{5}}\mathcal{F}_0^{3/2}(s) \\ + \sqrt{\frac{3}{5}}\big[s(t-u)-\Delta\big]\,\mathcal{F}_1^{3/2}(s) + \frac{\sqrt{3}}{2\sqrt{5}}\big[3\big(s(t-u)-\Delta\big)^2 - \kappa_s^2(s)\big]\,\mathcal{F}_2^{3/2}(s) \\ - \left(\frac{2}{\sqrt{15}}\mathcal{F}_0^{3/2}(t) + \frac{1}{\sqrt{6}}\mathcal{F}_0^{1/2}(t)\right) \\ - \big[t(s-u)-\Delta\big]\left(\frac{2}{\sqrt{15}}\mathcal{F}_1^{3/2}(t) + \frac{1}{\sqrt{6}}\mathcal{F}_1^{1/2}(t)\right) \\ - \frac{1}{2}\big[3\big(t(s-u)-\Delta\big)^2 - \kappa_t^2(t)\big]\left(\frac{2}{\sqrt{15}}\mathcal{F}_2^{3/2}(t) + \frac{1}{\sqrt{6}}\mathcal{F}_2^{1/2}(t)\right),\end{aligned} \tag{4.22}$$

with the additional πK D-waves given by (see Eq. (C.16))

$$\mathcal{F}_2^{1/2}(s) \equiv \frac{1}{\pi}\int_{s_{\rm th}}^{\infty}\frac{\mathrm{Im}\,f_2^{1/2}(s')}{\kappa_s^2(s')(s'-s)}\mathrm{d}s'\,, \qquad \mathcal{F}_2^{3/2}(s) \equiv \frac{1}{\pi}\int_{s_{\rm th}}^{\infty}\frac{\mathrm{Im}\,f_2^{3/2}(s')}{\kappa_s^2(s')(s'-s)}\mathrm{d}s'\,. \tag{4.23}$$

4.3.2 Unitarity and Khuri–Treiman equations

In this section we will derive the coupled Khuri–Treiman dispersive integral equations for the $D^+ \to K\pi\pi^+$ decays, which we solve for the single-variable amplitudes following Section 2.3. We begin with the dispersive treatment of the associated scattering processes linked to the decay by crossing symmetry, $D^+\bar{\pi} \to K\pi$ and $D^+\bar{K} \to \pi\pi$, where $\bar{A}$ denotes the antiparticle of particle A with mometum of opposite sign. The D-meson mass is artificially set to $M_D < M_K + 2M_\pi$ such that the corresponding decay is kinematically forbidden. The simpler

analytic structure of these scattering processes can be exploited to construct dispersion relations for the single-variable amplitudes valid for $s,t > (M_D+M_\pi)^2$ and $u > (M_D+M_K)^2$, respectively. The analytic continuation back to the physical D-meson mass as well as into the kinematic region $(M_K + M_\pi)^2 < (s,t) < (M_D - M_\pi)^2$, $4M_\pi^2 < u < (M_D - M_K)^2$ yields the anticipated decay amplitudes [40].

We demonstrate the framework for the example of the s-channel processes; the t- and u-channel amplitudes are constructed analogously. Elastic unitarity gives for the discontinuity (see Fig. 4.3 for $\mathcal{M}_{-++}$)

$$\begin{aligned}
\operatorname{disc}\mathcal{M}_{-++}(s,z_s) &= i\int\frac{\mathrm{d}^4 l}{(2\pi)^2}\sum_{(i,j)}\mathcal{M}_{ij+}(s,z_s')\mathcal{T}^{ij,-+*}(s,z_s'')\delta\big(l^2-M_i^2\big)\,\delta\big((q-l)^2-M_j^2\big)\,,\\
\operatorname{disc}\mathcal{M}_{\bar{0}0+}(s,z_s) &= i\int\frac{\mathrm{d}^4 l}{(2\pi)^2}\sum_{(i,j)}\mathcal{M}_{ij+}(s,z_s')\mathcal{T}^{ij,\bar{0}0*}(s,z_s'')\delta\big(l^2-M_i^2\big)\,\delta\big((q-l)^2-M_j^2\big)\,,
\end{aligned} \tag{4.24}$$

where $\mathcal{T}^{ij,-+}(x,z_x)$ ($K^i\pi^j \to K^-\pi^+$) and $\mathcal{T}^{ij,\bar{0}0}(x,z_x)$ ($K^i\pi^j \to \bar{K}^0\pi^0$) are the intermediate-to-final-state scattering amplitudes. $q = p_K + p_2 = (\sqrt{s},\vec{0})$ defines the center-of-mass frame, in which $z_s' = \cos\theta_s'$, the cosine of the angle between initial and intermediate states, and $z_s'' = \cos\theta_s''$, the cosine of the angle between intermediate and final state, are evaluated. The intermediate-state summation runs over the tuple $(i,j) \in \{(-,+),(\bar{0},0)\}$. The partial-wave decompositions for the πK ($\pi\pi$) amplitudes $\mathcal{T}^{ij,kl}$ and full decay amplitudes $\mathcal{M}_{ijk}$ read

$$\begin{aligned}
\mathcal{T}^{ij,kl}(s,z_s) &= \sum_{I,L} a_{I,L}^{ij,kl}\,P_L(z_s)\,t_L^I(s)\,,\\
\mathcal{M}_{ijk}(s,z_s) &= \sum_{I,L} a_{I,L}^{ijk}\,P_L(z_s)\,f_L^I(s)\,,
\end{aligned} \tag{4.25}$$

where the sum runs over isospin and angular momentum components I and L. Furthermore, we use the Clebsch–Gordan coefficients $a_{I,L}$, the Legendre polynomials $P_L(z)$, and the corresponding partial waves $t_L^I(s)$ and $f_L^I(s)$.[1] Exploiting the unitarity relation for elastic πK and $\pi\pi$ scattering we obtain the following partial-wave unitarity relations,

$$\operatorname{disc} f_L^I(s) = 2i\,f_L^I(s)\sin\delta_L^I(s)e^{-i\delta_L^I(s)}\theta\big(s-s_{\mathrm{th}}\big)\,, \tag{4.26}$$

where $\delta_L^I(s)$ denotes the elastic final-state scattering phase shift. The thresholds in the different channels are $s_{\mathrm{th}} = t_{\mathrm{th}} = (M_K+M_\pi)^2$ for πK and $u_{\mathrm{th}} = 4M_\pi^2$ for $\pi\pi$ scattering,

[1] Note that in contrast to the definition of the single-variable amplitudes in Eq. (4.22), we have not defined the partial waves in Eq. (4.25) to be free of kinematical zeros. This is independent of the singularities these partial waves display at the corresponding pseudo-thresholds or upper limits of the physical decay region, $s = (M_D - M_\pi)^2$ or $u = (M_D - M_K)^2$, which are well understood, see e.g. Ref. [34] or the discussion in Ref. [113] in a perturbative context.

respectively. Since the discontinuity of f_L^I and the according single-variable amplitude $\kappa_s^L \mathcal{F}_L^I$ coincide on the right-hand cut, we have

$$\begin{aligned} &\operatorname{disc} f_L^I(s) = \kappa_s^L(s) \operatorname{disc} \mathcal{F}_L^I(s) \\ \Rightarrow \quad &f_L^I(s) = \kappa_s^L(s) \left(\mathcal{F}_L^I(s) + \hat{\mathcal{F}}_L^I(s) \right), \end{aligned} \tag{4.27}$$

where we have introduced the inhomogeneities $\hat{\mathcal{F}}_L^I(s)$ that are free of discontinuities on the right-hand cut by construction. They incorporate the left-hand cut contributions and will be further discussed in Section 4.3.3. From Eqs. (4.26) and(4.27) we obtain

$$\operatorname{disc} \mathcal{F}_L^I(s) = 2i \left(\mathcal{F}_L^I(s) + \hat{\mathcal{F}}_L^I(s) \right) \theta(s - s_{\text{th}}) \sin \delta_L^I(s) e^{-i\delta_L^I(s)}, \tag{4.28}$$

which has again the form of an inhomogeneous Hilbert-type equation already encountered in Section 2.3. The homogeneous solution $\hat{\mathcal{F}}_L^I(s) = 0$ is given by the Omnès function $\Omega_L^I(s)$ [23] times an analytic function $P_L^I(s)$ (see Section. 1.4),

$$\mathcal{F}_L^I(s) = P_L^I(s) \Omega_L^I(s), \quad \Omega_L^I(s) = \exp\left\{ \frac{s}{\pi} \int_{s_{\text{th}}}^{\infty} \mathrm{d}s' \frac{\delta_L^I(s')}{s'(s' - s)} \right\}. \tag{4.29}$$

The inhomogeneous solution is obtained by a product ansatz, see Section 2.3, and gives

$$\mathcal{F}_L^I(s) = \Omega_L^I(s) \left\{ P_L^I(s) + \frac{s^n}{\pi} \int_{s_{\text{th}}}^{\infty} \frac{\mathrm{d}s'}{s'^n} \frac{\sin \delta_L^I(s') \hat{\mathcal{F}}_L^I(s')}{|\Omega_L^I(s')|(s' - s)} \right\}, \tag{4.30}$$

where $P_L^I(s)$ is now a polynomial of order $n-1$, and the number of subtractions n is chosen such that the convergence of the dispersion integral is guaranteed.

As our approach relies on elastic unitarity (see Ref. [114] for a generalization of the Khuri–Treiman formalism to coupled channels), the formalism breaks down when inelastic channels become important. We assume that Watson's theorem [28] is a good approximation up to the $\eta' K$ threshold in the πK channel. Inelastic effects in the prominent πK S-wave systems are found to become sizable above the $\eta' K$ threshold [94–96]. The main inelastic contributions in the isospin 1/2 P-wave come from the πK^* and ρK channels, which become noticeable in the energy region where they couple to $K^*(1410)$ and $K^*(1690)$ [96]. In all exotic partial waves, i.e. the isospin 2 $\pi\pi$ system as well as $I = 3/2$ πK partial waves, inelastic effects are assumed to be negligible.

4.3.3 Inhomogeneities

With the scattering phase shifts given as fixed input, the only quantities left in the dispersion integrals Eqs. (4.30) are the inhomogeneities $\hat{\mathcal{F}}_L^I$, which are determined as the projections of the crossed-channel amplitudes onto the considered channel. They can be

re-expressed in terms of the single-variable amplitudes $\mathcal{F}_L^I(x)$, such that we obtain integral equations that can be solved for the $\mathcal{F}_L^I(x)$. With the aid of Eq. (4.27) we find

$$f_L^I(x) = \frac{2L+1}{2a_{I,L}^{ijk}} \int \mathrm{d}z_x \mathcal{M}_{ijk}^{I_x}(x,z_x) P_L(z_x) = \kappa_x^L(x)\big(\mathcal{F}_L^I(x) + \hat{\mathcal{F}}_L^I(x)\big)$$

$$\Rightarrow \quad \hat{\mathcal{F}}_L^I(x) = \frac{2L+1}{2a_{I,L}^{ijk}\,\kappa_x^L(x)} \int_{-1}^{1} \mathrm{d}z_x \mathcal{M}_{ijk}^{I_x}(x,z_x) P_L(z_x) - \mathcal{F}_L^I(x)\,, \tag{4.31}$$

where $\mathcal{M}_{ijk}^{I_x}(x,z_x)$ denotes the projection of the full decay amplitude $\mathcal{M}_{ijk}(x,z_x)$ onto isospin I_x eigenfunctions in the x-channel. One term of the projection integral over $\mathcal{M}_{ijk}^{I_x}(x,z_x)$ is always $\mathcal{F}_L^I(x)$, such that the right-hand-cut discontinuity is canceled. The inhomogeneities are then indeed free of discontinuities on the right-hand cut as anticipated. The resulting inhomogeneities are given in Appendix C.3.

The interpretation of Eq. (4.31) as an angular integration is valid in the scattering region and needs to be analytically continued into the unphysical and decay regions as was done in Section 2.3 Performing the angular integration naively in the decay region results in crossing the unitarity cut. The prescription on how to perform the continuation has been extensively discussed in Ref. [40], motivated by the continuation of the (perturbative) triangle graph into the decay region. It ultimately leads to the prescription $M_D^2 \to M_D^2 + i\epsilon$, which allows one to derive an integration path that avoids the unitarity cut.

4.3.4 Angular integration

In this section we will display the continuation of the angular integrals following the $M_D^2 \to M_D^2 + i\epsilon$ prescription similar to what has been done in Section 2.3. Here we have six angular integrals corresponding to the three channels projected onto each other

$$\begin{aligned}
\langle z^n \mathcal{M}\rangle_{u_s} &\equiv \frac{1}{2}\int_{-1}^{1} dz_s\, z_s^n \mathcal{M}(u), & \langle z^n \mathcal{M}\rangle_{t_s} &\equiv \frac{1}{2}\int_{-1}^{1} dz_s\, z_s^n \mathcal{M}(t)\,, \\
\langle z^n \mathcal{M}\rangle_{s_t} &\equiv \frac{1}{2}\int_{-1}^{1} dz_t\, z_t^n \mathcal{M}(s), & \langle z^n \mathcal{M}\rangle_{u_t} &\equiv \frac{1}{2}\int_{-1}^{1} dz_t\, z_t^n \mathcal{M}(u)\,, \\
\langle z^n \mathcal{M}\rangle_{s_u} &\equiv \frac{1}{2}\int_{-1}^{1} dz_u\, z_u^n \mathcal{M}(s), & \langle z^n \mathcal{M}\rangle_{t_u} &\equiv \frac{1}{2}\int_{-1}^{1} dz_u\, z_u^n \mathcal{M}(t)\,,
\end{aligned} \tag{4.32}$$

where $\langle\rangle_{x_y}$ denotes the angular z_y integral of single-variable amplitudes depending on Mandelstam $x(y,z_y)$. Furthermore, with the kinematic relations of Eqs. (4.3), (4.4), and (4.5) we can relate three of the above angular average integrals to obtain three independent angular integrations,

$$\langle z^n \mathcal{M}\rangle_{u_s} = \langle z^n \mathcal{M}\rangle_{u_t},\ \langle z^n \mathcal{M}\rangle_{t_s} = \langle z^n \mathcal{M}\rangle_{s_t},\ \text{and} \langle z^n \mathcal{M}\rangle_{t_u} = (-1)^n \langle z^n \mathcal{M}\rangle_{s_u}\,. \tag{4.33}$$

Starting with the $\langle\rangle_{u_s}$ angular integration we have

$$\langle z^n \mathcal{M}\rangle_{u_s} \equiv \frac{1}{2}\int_{-1}^{1} dz_s\, z_s^n \mathcal{M}(u) = (-1)^n \frac{s}{\kappa_s(s)} \int_{s_-(s)}^{s_+(s)} ds' \left(\frac{2s's - 3s_0 s + s^2 + \Delta}{\kappa_s(s)}\right)^n \mathcal{M}(s') \,, \tag{4.34}$$

where we used the substitution $2s' = 3s_0 - s - \frac{\Delta}{s} - \frac{\kappa_s(s)}{s} z_s$. The integration end points $s_\pm(s)$ are the only non-trivial M_D dependend piece in Eq. (4.34) and the continuation following the $M_D^2 \to M_D^2 + i\epsilon$ prescription gives

$$2s\, s_+(s) = \begin{cases} 3s_0 s - s^2 - \Delta + |\kappa_s(s)| + i\epsilon \,, & s \in [(M_K + M_\pi)^2, a_{t/u}] \,, \\ 3s_0 s - s^2 - \Delta + i|\kappa_s(s)| \,, & s \in [a_{s/t}, b_{s/t}] \,, \\ 3s_0 s - s^2 - \Delta - |\kappa_s(s)| \,, & s \in [b_{s/t}, \infty] \,, \end{cases}$$

$$2s\, s_-(s) = \begin{cases} 3s_0 s - s^2 - \Delta - |\kappa_s(s)| + i\epsilon \,, & s \in \Big[(M_K + M_\pi)^2, c_s\Big] \,, \\ 3s_0 s - s^2 - \Delta - |\kappa_s(s)| - i\epsilon \,, & s \in \Big[c_s, a_{s/t}\Big] \,, \\ 3s_0 s - s^2 - \Delta - i|\kappa_s(s)| \,, & s \in [a_{s/t}, b_{s/t}] \,, \\ 3s_0 s - s^2 - \Delta + |\kappa_s(s)| \,, & s \in [b_{s/t}, \infty] \,, \end{cases} \tag{4.35}$$

with

$$a_{s/t} \equiv (M_D - M_\pi)^2 \,, \quad b_{s/t} \equiv (M_D + M_\pi)^2 \,, \quad \text{and} \quad c_s \equiv \frac{1}{2}\left(M_D^2 + M_K^2 - 2M_\pi^2\right) \,. \tag{4.36}$$

The trajectories of the integration end points $s_\pm(s)$ are depicted in Fig. 4.4. Point A denotes the starting point of the trajectories $s_+(s_{\rm th}) = s_-(s_{\rm th}) = c_u + i\epsilon$ above the branch cut. The integration point $s_+(s)$ moves up the branch cut until it reaches its maximal real part at B $\big(s_+(s_{\rm max}) = a_u + i\epsilon$ with $s_{\rm max} = M_D M_K + M_\pi^2\big)$. From point B the upper integration limit moves to point D $\big(s_+(a_s)\big)$. On the other hand, the lower integration limit $s_-(s)$ starts from point A and moves down the cut until it reaches the threshold at point C $\big(s_-(c_s) = s_{\rm th}\big)$. Then the lower integration limit moves below the cut and reaches point D $\big(s_-(a_s) = s_+^*(a_s)\big)$. From point D onwards to point E, $s_\pm(s)$ are related by complex conjugation and both trajectories obtain a sizable imaginary part. After point E, $\big(s_\pm(b_s) = -u_{\rm max} \equiv -(M_D^2 - M_K^2)M_\pi/(M_D - M_K)\big)$ both trajectories are purely real with $s_+(s)$ moving to negative infinity.

Similarly we have for the $\langle\rangle_{t_u}$ angular integration

$$\langle z^n \mathcal{M}\rangle_{t_u} \equiv \frac{1}{2}\int_{-1}^{1} dz_u\, z_u^n \mathcal{M}(t) = \frac{1}{\kappa_u(u)} \int_{u_-(u)}^{u_+(u)} \left(\frac{2u' - 3s_0 + u}{\kappa_u(u)}\right)^n \mathcal{M}(u') du' \,, \tag{4.37}$$

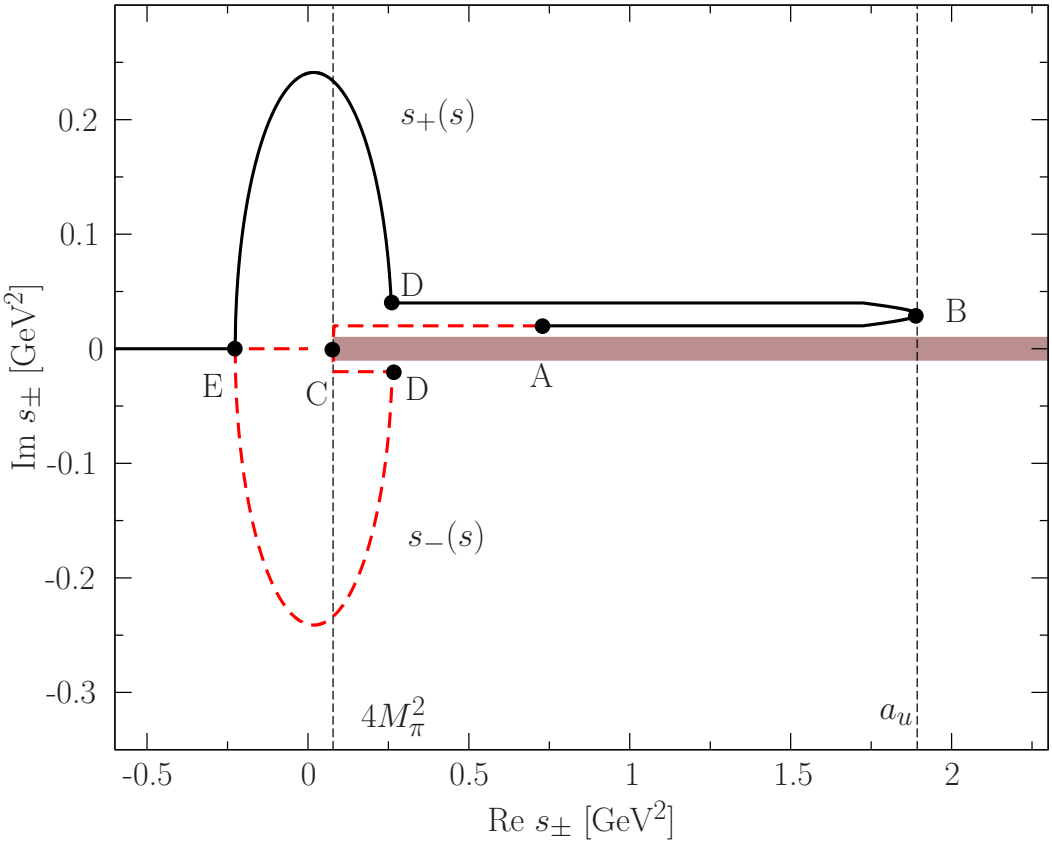

Figure 4.4: Plot of the $s_\pm(s)$ trajectories in the complex plane according to Eq. (4.35). From point A to D we have exaggerated the infinitesimal imaginary parts to visualize the trajectories better. The values of the characteristic points A to E are explained in the text. The thick brown line symbolizes the right-hand cut.

with the integration limits

$$
\begin{aligned}
2u_+(u) &= \begin{cases} 3s_0 - u + |\kappa_u(u)| + i\epsilon\,, & u \in [4M_\pi^2, a_u]\,, \\ 3s_0 - u + i|\kappa_u(u)|\,, & u \in [a_u, b_u]\,, \\ 3s_0 - u - |\kappa_u(u)|\,, & u \in [b_u, \infty]\,, \end{cases} \\
2u_-(u) &= \begin{cases} 3s_0 - u - |\kappa_u(u)| + i\epsilon\,, & u \in \left[4M_\pi^2, c_u\right]\,, \\ 3s_0 - u - |\kappa_u(u)| - i\epsilon\,, & u \in \left[c_u, a_u\right]\,, \\ 3s_0 - u - i|\kappa_u(u)|\,, & s \in [a_u, b_u]\,, \\ 3s_0 - u + |\kappa_u(u)|\,, & u \in [b_u, \infty]\,, \end{cases}
\end{aligned}
\tag{4.38}
$$

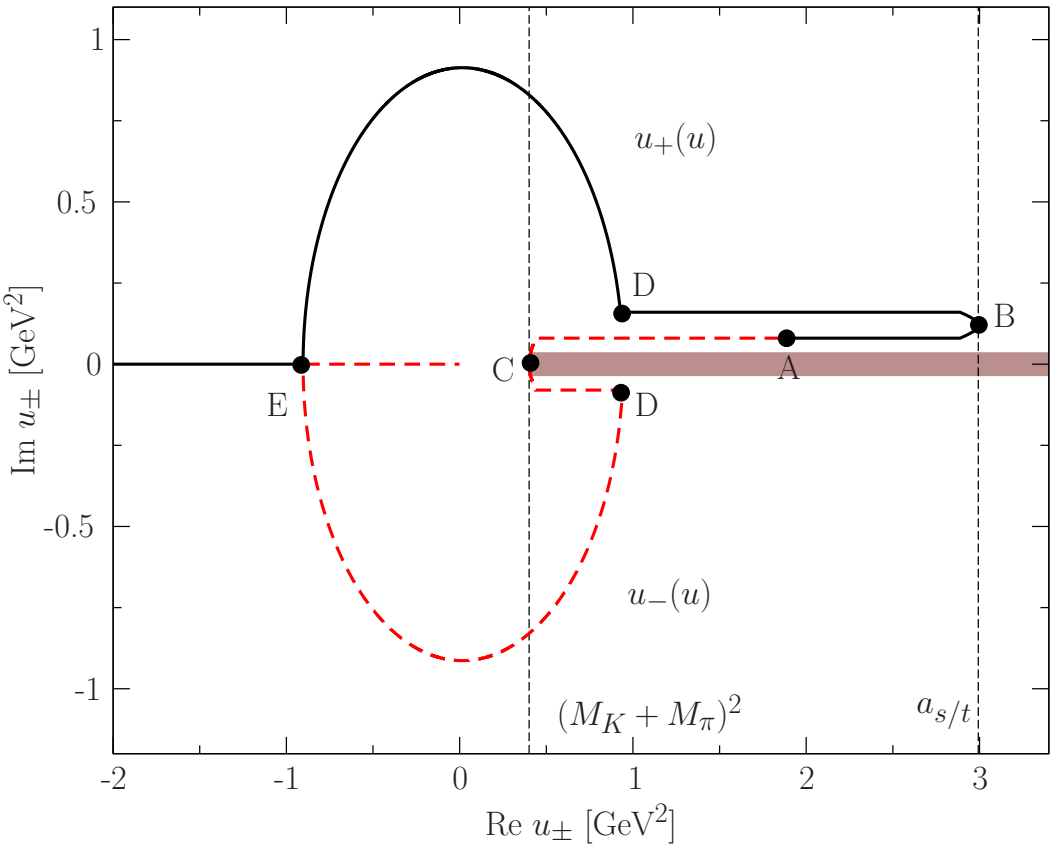

Figure 4.5: Plot of the $u_\pm(s)$ trajectories in the complex plane according to Eq. (4.38). From point A to D we have exaggerated the infinitesimal imaginary parts to visualize the trajectories better. The values of the characteristic points A to E are explained in the text. The thick brown line symbolizes the right-hand cut.

where

$$a_u \equiv (M_D - M_K)^2\,, \quad b_u \equiv (M_D + M_K)^2\,, \quad \text{and} \quad c_u \equiv \frac{(M_D^2 - M_K^2)M_\pi}{M_K + M_\pi}\,. \tag{4.39}$$

The trajectories of the integration end points $u_\pm(u)$ are shown in Fig. 4.5. Akin to above, the trajectories start at A $\big(u_\pm(4M_\pi^2) = c_s + i\epsilon\big)$. The upper integration limit moves first to B $\big(u_+(u_{\max}) = a_{s/t} + i\epsilon$ with $u_{\max} = (M_D^2 - M_K^2)M_\pi/(M_D - M_K)\big)$ and turns around to move to point D $(u_+(a_u) = s_{\max} + i\epsilon)$. The lower integration limit moves down to C $\big(s_-(c_s) = 4M_\pi^2\big)$ and below the cut to D $\big(u_-(a_u) = s_{\max} - i\epsilon\big)$. From D onwards to E, $\big(u_\pm(b_u) = M_\pi^2 - M_D M_K\big)$ the integration limits are related by complex conjugation. After point E, $u_+(u)$ moves to minus infinity.

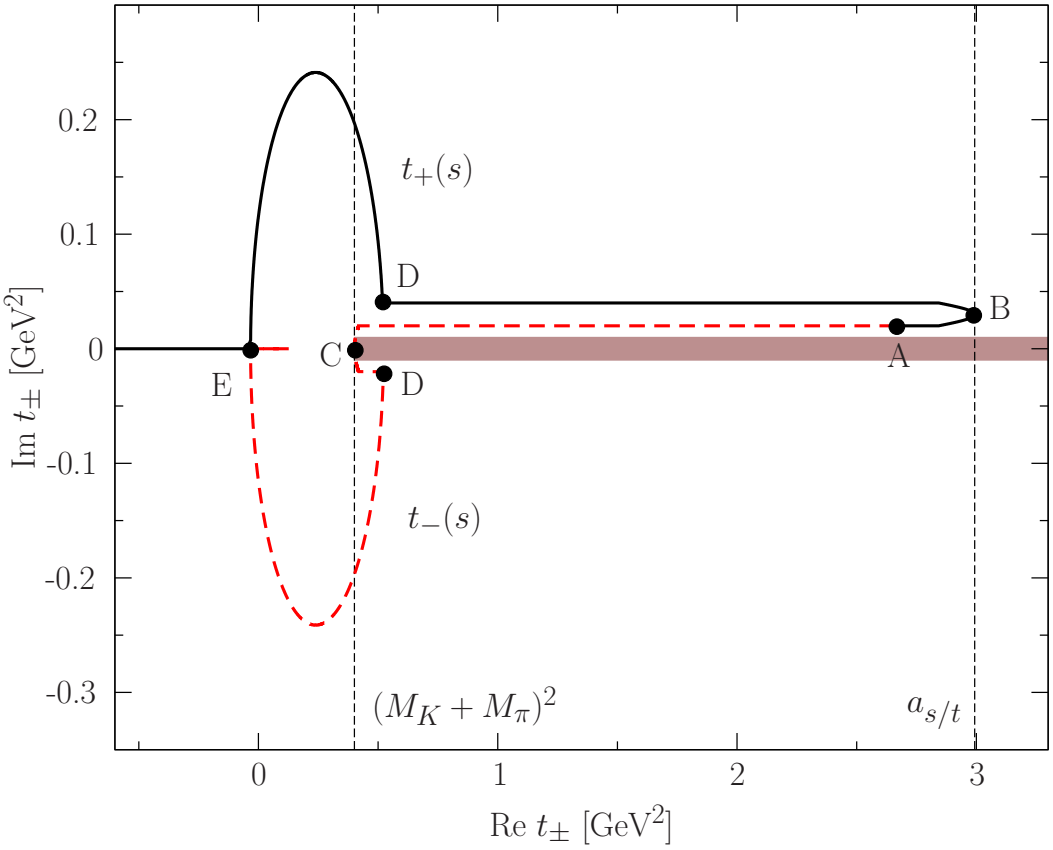

Figure 4.6: Plot of the $t_\pm(s)$ trajectories in the complex plane according to Eq. (4.41). From point A to D we have exaggerated the infinitesimal imaginary parts to visualize the trajectories better. The values of the characteristic points A to E are explained in the text. The thick brown line symbolizes the right-hand cut.

For the $\langle\rangle_{s_t}$ angular integration we obtain

$$\langle z^n \mathcal{M} \rangle_{s_t} \equiv \frac{1}{2} \int_{-1}^{1} dz_t \, z_t^n \mathcal{M}(s) = \frac{t}{\kappa_t(t)} \int_{t_-(t)}^{t_+(t)} dt' \left(\frac{2t't - 3s_0 t + t^2 - \Delta}{\kappa_t(t)} \right)^n \mathcal{M}(t') \,, \quad (4.40)$$

with the integration limits given by

$$2t\, t_+(t) = \begin{cases} 3s_0 t - t^2 + \Delta + |\kappa_t(t)| + i\epsilon \,, & u \in [(M_K + M_\pi)^2, a_{s/t}] \,, \\ 3s_0 t - t^2 + \Delta + i|\kappa_t(t)| \,, & u \in [a_{s/t}, b_{t/u}] \,, \\ 3s_0 t - t^2 + \Delta - |\kappa_t(t)| \,, & u \in [b_{t/u}, \infty] \,, \end{cases}$$

$$2t\,t_-(u) = \begin{cases} 3s_0t - t^2 + \Delta - |\kappa_t(t)| + i\epsilon\,, & t \in \Big[(M_K + M_\pi)^2, c_t\Big]\,, \\ 3s_0t - t^2 + \Delta - |\kappa_t(t)| - i\epsilon\,, & t \in \Big[c_t, a_{s/t}\Big]\,, \\ 3s_0t - t^2 + \Delta - i|\kappa_t(t)|\,, & t \in [a_{s/t}, b_{s/t}]\,, \\ 3s_0t - t^2 + \Delta + |\kappa_t(t)|\,, & t \in [b_{s/t}, \infty]\,, \end{cases} \tag{4.41}$$

and

$$c_t \equiv \frac{M_D^2 M_K + M_\pi^3}{M_K + M_\pi} - M_K M_\pi\ . \tag{4.42}$$

The contours of the integration end points $t_\pm(t)$ are depicted in Fig. 4.6. The trajectories start at A $\big(t_\pm(t_{\rm th}) = c_t + i\epsilon\big)$. The upper integration limit moves to B $\big(t_+(t_{\rm max}) = a_{s/t} + i\epsilon$ with $t_{\rm max} = (M_D^2 M_\pi - M_\pi^3 + M_D(M_K^2 - M_\pi^2))/(M_D - M_\pi)\big)$ and turns around to move down to point D $\big(t_+(a_t) = t_{\rm max} + i\epsilon\big)$. The lower integration limit moves down to C $\big(t_-(c_t) = t_{\rm th}\big)$ and below the cut to D $\big(t_-(a_u) = t_{\rm max} - i\epsilon\big)$. From D onwards to E, $\big(t_\pm(b_t) = \big(M_D(M_K^2 - M_\pi^2) + M_\pi^3 - M_D^2 M_\pi\big)/(M_D + M_\pi)\big)$ the integration limits are related by complex conjugation. After point E, $t_+(t)$ moves to minus infinity.

4.3.5 Number of subtraction constants

The minimal number of subtractions needed is dictated by the asymptotic behavior of the integrands in Eqs. (4.30). The decay amplitude and thus the inhomogeneities are assumed to grow at most linearly asymptotically, loosely based on the Froissart bound [57]. Assuming the phase shifts to approach constant values $\delta_L^I(\infty)$ for large energies, the Omnès functions $\Omega_L^I(x)$ behave like $\propto x^{-\delta_L^I(\infty)/\pi}$ asymptotically. The phase shift inputs are taken from Roy equation analyses of $\pi\pi$ scattering (Refs. [29–32]) and πK scattering (Ref. [115]) . With the following assumption for the phase shifts δ_L^I at high energies:

$$\begin{aligned} &\lim_{x\to\infty} \delta_0^{1/2}(x) = 2\pi\,, && \lim_{x\to\infty} \delta_1^{1/2}(x) = \pi\,, && \lim_{x\to\infty} \delta_2^{1/2}(x) = \pi\,, \\ &\lim_{x\to\infty} \delta_0^{3/2}(x) = 0\,, && \lim_{x\to\infty} \delta_1^{3/2}(x) = 0\,, && \lim_{x\to\infty} \delta_2^{3/2}(x) = 0\,, \\ &\lim_{x\to\infty} \delta_0^{2}(x) = 0\,, && \lim_{x\to\infty} \delta_1^{1}(x) = \pi\,, \end{aligned} \tag{4.43}$$

we need two subtractions for $\mathcal{F}_0^2$, $\mathcal{F}_1^1$, and $\mathcal{F}_0^{3/2}$, four subtractions for $\mathcal{F}_0^{1/2}$, and one subtraction for $\mathcal{F}_1^{1/2}$ to obtain convergent dispersion integrals. Note that the difference in the number of subtractions for $\mathcal{F}_1^1$ and $\mathcal{F}_1^{1/2}$, despite identical phase asymptotics, is due to the different kinematic prefactors for P-waves with equal and unequal masses, see Eq. (4.22). $\mathcal{F}_1^{3/2}$ needs no subtraction, but as the πK isospin 3/2 P-wave phase shift is very small and assumed to vanish at high energies, we neglect it altogether. Similarly, also the $I = 3/2$ D-wave is put to zero.

The inclusion of the D-wave $\mathcal{F}_2^{1/2}$ is delicate. Formally it requires no subtractions, but the kinematical pre-function corresponding to the $L = 2$ Legendre polynomial, multiplied with the required momentum factors to make it free of kinematical singularities, see Eq. (4.22), violates the assumed high-energy behavior of the decay amplitude and thus of all inhomogeneities. Therefore we will follow a "hybrid approach" for the D-wave: we will only consider the projections of S- and P-waves of other channels in order to generate the D-wave inhomogeneity, but will exclude D-wave projections, thus eschewing the need for further subtractions. This is loosely motivated by analogous observations in low-energy processes calculated in chiral perturbation theory, where higher partial waves are dominated by crossed-channel loop diagrams that correspond to low partial waves in those crossed channels.

In total we have eleven subtraction constants. However, the resulting representations of the decay amplitudes Eq. (4.22) are not unique due to the linear dependence of the Mandelstam variables s, t, and u: one can construct polynomial contributions to the single-variable amplitudes that leave the complete decay amplitudes $\mathcal{M}_{-++}(s,t,u)$ and $\mathcal{M}_{\bar{0}0+}(s,t,u)$ invariant; this is obvious in a standard dispersive representation, however slightly less trivial to demonstrate in the Omnès representations discussed above [116]. The polynomial coefficients can be tuned such that a maximal number of subtraction constants is eliminated to obtain a linearly independent set. These polynomials span the so-called invariance group of the decay amplitudes. Details are discussed in Appendix C.4. We choose to eliminate the subtraction constants in the non-resonant $I = 3/2\ \pi K$ and $I = 2\ \pi\pi$ S-waves, the rationale being solely to retain them in presumably large, resonant partial waves. This leaves seven linearly independent complex subtraction constants,

$$
\begin{aligned}
\mathcal{F}_0^2(u) &= \Omega_0^2(u)\frac{u^2}{\pi}\int_{u_\text{th}}^\infty \frac{\mathrm{d}u'}{u'^2}\frac{\hat{\mathcal{F}}_0^2(u')\sin\delta_0^2(u')}{\left|\Omega_0^2(u')\right|(u'-u)}\,,\\
\mathcal{F}_1^1(u) &= \Omega_1^1(u)\left\{c_0 + c_1 u + \frac{u^2}{\pi}\int_{u_\text{th}}^\infty \frac{\mathrm{d}u'}{u'^2}\frac{\hat{\mathcal{F}}_1^1(u')\sin\delta_1^1(u')}{\left|\Omega_1^1(u')\right|(u'-u)}\right\},\\
\mathcal{F}_0^{1/2}(s) &= \Omega_0^{1/2}(s)\left\{c_2 + c_3 s + c_4 s^2 + c_5 s^3 + \frac{s^4}{\pi}\int_{s_\text{th}}^\infty \frac{\mathrm{d}s'}{s'^4}\frac{\hat{\mathcal{F}}_0^{1/2}(s')\sin\delta_0^{1/2}(s')}{\left|\Omega_0^{1/2}(s')\right|(s'-s)}\right\},\\
\mathcal{F}_0^{3/2}(s) &= \Omega_0^{3/2}(s)\left\{\frac{s^2}{\pi}\int_{s_\text{th}}^\infty \frac{\mathrm{d}s'}{s'^2}\frac{\hat{\mathcal{F}}_0^{3/2}(s')\sin\delta_0^{3/2}(s')}{\left|\Omega_0^{3/2}(s')\right|(s'-s)}\right\},\\
\mathcal{F}_1^{1/2}(s) &= \Omega_1^{1/2}(s)\left\{c_6 + \frac{s}{\pi}\int_{s_\text{th}}^\infty \frac{\mathrm{d}s'}{s'}\frac{\hat{\mathcal{F}}_1^{1/2}(s')\sin\delta_1^{1/2}(s')}{\left|\Omega_1^{1/2}(s')\right|(s'-s)}\right\},\\
\mathcal{F}_2^{1/2}(s) &= \Omega_2^{1/2}(s)\frac{1}{\pi}\int_{s_\text{th}}^\infty \mathrm{d}s'\frac{\hat{\mathcal{F}}_2^{1/2}(s')\sin\delta_2^{1/2}(s')}{\left|\Omega_2^{1/2}(s')\right|(s'-s)}\,.
\end{aligned}
\tag{4.44}
$$

The subtraction constants cannot be determined in the framework of dispersion theory and have to be obtained either by matching to a more fundamental dynamical theory, or, as in this work, by a fit to experimental data. The solution space of the coupled system Eq. (4.44) has thus dimension seven, corresponding to the seven complex subtraction constants. We employ again the concept of basis functions explained in Section 2.4. In particular, we choose for the ith basis function $\mathcal{M}_i(s,t,u)$ the set of subtraction constants $c_j = \delta_{ij}$ with $i,j = 0\ldots6$. The full solution $\mathcal{M}(s,t,u)$ is then obtained by

$$\mathcal{M}(s,t,u) = \sum_i c_i \mathcal{M}_i(s,t,u)\,. \tag{4.45}$$

The basis functions are entirely determined by the phase shift input as well as the masses of all particles involved (taken from Ref. [82]).

4.4 Solution strategy

In this section we discuss different solution strategies of the Khuri–Treiman-type equations Eq. (4.44), their issues, and present our new solution strategy.

The standard solution strategy for the linear coupled double integral equations (4.44) has been an iteration procedure as performed for example in Refs. [34,58,91] and described in Section 2.4 or with the introduction of integral kernels in Ref. [62]. Unfortunately, the convergence of this iterative procedure is not always guaranteed, depending on the mass of the decaying particle and the number of subtractions as seen in Section 2.5.2. For larger decay masses and more subtractions applied, the corrections in each iteration step can be too large to reach the fixed-point solution. We find this to be the case in the D-meson decays considered here.

This necessitates a different solution strategy. Since the set of integral equations is linear in the single-variable amplitudes it is convenient to set it up in the form of a matrix equation instead. Provided that the matrix is invertible a unique solution exists. One such inversion strategy is known as the Pasquier inversion [43, 44] (see Ref. [117] for a recent comparison of Pasquier inversion and iterative solution), where a method to reduce the double integral equation to a single integral equation is introduced. The procedure involves the deformation of the integral contours of both integrals, allowing one to interchange the order of integrations such that a unique kernel function is obtained. The coupled single integral equations thus obtained do allow for a direct solution via matrix inversion.

We will follow a slightly modified strategy, constructing a matrix equation without performing a Pasquier inversion. In this context it is beneficial to solve for the inhomogeneities instead of the single-variable amplitudes, the advantage being that the inhomogeneities need to be evaluated only on the right-hand cuts and not also on the complex angular integration paths (Figs. 4.4, 4.5 and 4.6). The single-variable amplitudes themselves can be obtained in

the whole complex plane in a straightforward manner by performing the dispersion integral over the determined inhomogeneities once. We have tested this new solution strategy on the $V \to 3\pi$ system displayed in part 2 and found agreement with the standard iterative solution procedure, that is applicable in for these decays.

To illustrate the solution strategy we limit ourselves to one hypothetical inhomogeneity equation without any loss of generality,

$$\hat{\mathcal{F}}_L(s) = \frac{1}{2}\int_{-1}^{1} \mathrm{d}z_s\, z_s^m\, \mathcal{F}\big(t(s,z_s)\big)\,, \tag{4.46}$$

and focus on the functions $\tilde{\mathcal{F}}(s) \equiv \hat{\mathcal{F}}_L(s)\kappa_s^{2L+1}(s)$ that are free of singularities at the pseudo-threshold or upper limit of the kinematically accessible decay region (which is a zero in $\kappa_s(s)$). Inserting Eq. (4.30) into Eq. (4.46) yields

$$\begin{aligned}\tilde{\mathcal{F}}(s) &= \frac{\kappa_s^{2L+1}(s)}{2}\int_{-1}^{1} \mathrm{d}z_s\, z_s^m\, \Omega\big(t(s,z_s)\big)\Big\{P\big(t(s,z_s)\big) \\ &\quad + \frac{t(s,z_s)^n}{\pi}\int_{s_\mathrm{th}}^{\infty}\frac{\mathrm{d}x}{x^n}\frac{\tilde{\mathcal{F}}(x)\sin\delta(x)}{|\Omega(x)|\kappa_s^{2L+1}(x)\big(x-t(s,z_s)\big)}\Big\} \\ &\equiv A(s) + \frac{1}{\pi}\int_{s_\mathrm{th}}^{\infty}\tilde{\mathcal{F}}(x)K(s,x)\mathrm{d}x\,.\end{aligned} \tag{4.47}$$

The function $A(s)$ contains the dependence on the subtraction polynomial, while the integration kernel $K(s,x)$ is independent of any subtraction constants,

$$\begin{aligned}A(s) &= \frac{\kappa_s^{2L+1}(s)}{2}\int_{-1}^{1} \mathrm{d}z_s\, z_s^m\, P\big(t(s,z_s)\big)\,\Omega\big(t(s,z_s)\big)\,, \\ K(s,x) &= \kappa_s^{2L+1}(s)\frac{\sin\delta(x)}{x^n|\Omega(x)|\kappa_s^{2L+1}(x)}\int_{-1}^{1}\mathrm{d}z_s\frac{t(s,z_s)^n}{2}\frac{z_s^m\Omega\big(t(s,z_s)\big)}{x-t(s,z_s)}\,.\end{aligned} \tag{4.48}$$

Eq. (4.47) is thus a linear integral equation for $\tilde{\mathcal{F}}(s)$, to be solved for a given set of subtraction constants. Discretizing Eq. (4.47) yields

$$A(s_i) = \sum_j \left(\delta_{ij} - \int_{s_j}^{s_{j+1}} K(s_i,x)\,\mathrm{d}x\right)\tilde{\mathcal{F}}(s_j)\,, \tag{4.49}$$

where $\tilde{\mathcal{F}}(x)$ is factorized out of the integral since it is approximately constant over the considered integration intervals $[s_j, s_{j+1}]$. Equation (4.49) is solved by matrix inversion. The explicit implementation is unfolded in the next section.

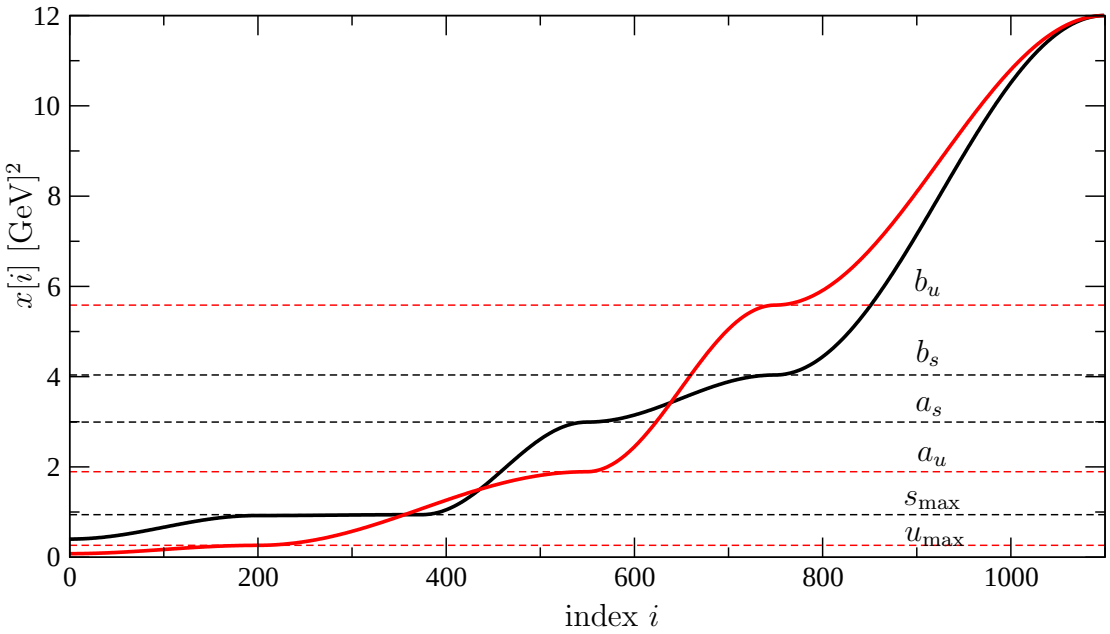

Figure 4.7: The distribution of the integration points $s[i]$ (black curve) and $u[i]$ (red curve). The characteristic points (a_s, b_s, s_{max}, and a_u, b_u, u_{max}) are visualized by the dotted lines.

4.5 Numerical implementation

After the short introduction into the new solution strategy we will display the numerical treatment of the $D \to K\pi\pi$ matrix equation, Eq. (4.49), explicitly. We first discuss the choice of integral points necessary to evaluate the discretized integrals of Eq. (4.49). Since s- and t-channel kinematics are identical and we have exploited this symmetry in the derivation of the final dispersive integrals, we have to choose the same s/t integration points. Thus we have one integration point set for the u-channel $\big(u_i,\, i \in \{0, \ldots, N_{\text{supp}}\}\big)$ and one for the s/t-channel $\big(s_i,\, i \in \{0, \ldots, N_{\text{supp}}\}\big)$. Strictly the upper limit of the dispersion integral is infinity. However, the integral saturates much earlier as higher energy contributions become quickly negligible. We choose an upper integration cutoff of $12\,\text{GeV}^2$. To test the impact of the cutoff, we vary the cutoff between $12\,\text{GeV}^2$ and $20\,\text{GeV}^2$. It turns out that these changes are negligible. Furthermore, the dispersive integrands inherit characteristic points, see Section 4.3.4, such as thresholds $\big(4M_\pi^2,\, (M_K + M_\pi)^2\big)$, scattering thresholds $\big(b_{s/t}$ and $b_u\big)$, pseudothresholds $\big(a_{s/t}$ and $a_u\big)$, and turning points of the angular average integration limits $\big(c_s,\, c_t,$ and $c_u\big)$, where we would like to have high numerical precision. The integration points are therefore distributed unevenly, see Fig 4.7, to have a higher accumulation of

points at these characteristic points. With the numerical method discussed below, we find that $N_{\text{supp}} = 1100$ is sufficient. For completeness we state the full matrix equation for the $D^+ \to \bar{K}\pi\pi^+$ decays. Rewriting the inhomogeneities given in Appendix C.3 into the matrix equation, analogously to Eq. (4.49), gives

$$\begin{pmatrix} \vec{A}_0^2 \\ \vec{A}_1^1 \\ \vec{A}_0^{1/2} \\ \vec{A}_0^{3/2} \\ \vec{A}_1^{1/2} \\ \vec{A}_2^{1/2} \end{pmatrix} = \begin{pmatrix} \mathbb{I} & 0 & -\frac{2}{\sqrt{3}}N_{su}^0 & \frac{2\sqrt{2}}{\sqrt{15}}R_{su}^0 & \frac{2}{\sqrt{3}}P_{su}^0 & 0 \\ 0 & \mathbb{I} & -2N_{su}^1 & -2\sqrt{10}R_{su}^1 & 2P_{su}^1 & 0 \\ -\frac{5}{2\sqrt{3}}M_{us}^0 & -\frac{1}{2}G_{us}^0 & \mathbb{I} - \frac{2}{3}N_{ts}^0 & \frac{\sqrt{10}}{3}\frac{2}{3}R_{su}^0 & -\frac{2}{3}P_{ts}^0 & 0 \\ \frac{\sqrt{5}}{2\sqrt{6}}M_{us}^0 & -\frac{\sqrt{5}}{2\sqrt{2}}G_{us}^0 & \frac{\sqrt{10}}{6}N_{ts}^0 & \mathbb{I} + \frac{2}{3}R_{su}^0 & \frac{\sqrt{10}}{6}P_{ts}^0 & 0 \\ -\frac{5\sqrt{3}}{2}M_{us}^1 & -\frac{3}{2}G_{us}^1 & -2N_{ts}^1 & \sqrt{10}R_{su}^1 & \mathbb{I} - 2P_{ts}^1 & 0 \\ \frac{\sqrt{15}}{2\sqrt{2}}M_{us}^1 & -\frac{3\sqrt{5}}{2\sqrt{2}}G_{us}^1 & \frac{\sqrt{10}}{2}N_{ts}^1 & 2R_{su}^1 & \frac{\sqrt{10}}{2}P_{ts}^1 & \mathbb{I} \end{pmatrix} \begin{pmatrix} \vec{\tilde{\mathcal{F}}}_0^2 \\ \vec{\tilde{\mathcal{F}}}_1^1 \\ \vec{\tilde{\mathcal{F}}}_0^{1/2} \\ \vec{\tilde{\mathcal{F}}}_0^{3/2} \\ \vec{\tilde{\mathcal{F}}}_1^{1/2} \\ \vec{\tilde{\mathcal{F}}}_2^{1/2} \end{pmatrix}, \tag{4.50}$$

where the vector components $\left(\vec{A}_L^I\right)_i$ and $\left(\vec{\tilde{\mathcal{F}}}_L^I\right)_i$ are given by $A_L^I(s_i)$ and $\tilde{\mathcal{F}}_L^I(s_i)$ respectively defined in Appendix C.3. The submatrices of size $N_{supp} \times N_{supp}$ are given by

$$\begin{aligned}
\left(M_{us}^m\right)_{ij} &= \int_{u_j}^{u_{j+1}} \frac{\mathrm{d}x}{\pi} \frac{\kappa_s^{2m+1}(s_i)\sin\delta_0^2(x)}{x^2|\Omega_0^2(x)|\kappa_u(x)} \left\langle u^2 \frac{P_m(z)\Omega_0^2(u)}{x-u} \right\rangle_{u_s}(s_i) \,, \\
\left(G_{us}^m\right)_{ij} &= \int_{u_j}^{u_{j+1}} \frac{\mathrm{d}x}{\pi} \frac{\kappa_s^{2m+1}(s_i)\sin\delta_1^1(x)}{x^2|\Omega_1^1(x)|\kappa_u^{2m+1}(x)} \left\langle u^2 \frac{P_m(z)\left(A_{s_i}z_s + D_{s_i}\right)\Omega_1^1(u)}{x-u} \right\rangle_{u_s}(s_i) \,, \\
\left(N_{su}^m\right)_{ij} &= \int_{s_j}^{s_{j+1}} \frac{\mathrm{d}x}{\pi} \frac{\kappa_u^{2m+1}(u_i)\sin\delta_0^{1/2}(x)}{x^4|\Omega_0^{1/2}(x)|\kappa_s^{2m+1}(x)} \left\langle s^4 \frac{P_m(z)\Omega_0^{1/2}(s)}{x-s} \right\rangle_{s_u}(u_i) \,, \\
\left(N_{ts}^m\right)_{ij} &= \int_{s_j}^{s_{j+1}} \frac{\mathrm{d}x}{\pi} \frac{\kappa_s^{2m+1}(s_i)\sin\delta_0^{1/2}(x)}{x^4|\Omega_0^{1/2}(x)|\kappa_s^{2m+1}(x)} \left\langle t^4 \frac{P_m(z)\Omega_0^{1/2}(t)}{x-t} \right\rangle_{t_s}(s_i) \,, \\
\left(P_{su}^m\right)_{ij} &= \int_{s_j}^{s_{j+1}} \frac{\mathrm{d}x}{\pi} \frac{\kappa_u^{2m+1}(u_i)\sin\delta_1^{1/2}(x)}{x|\Omega_1^{1/2}(x)|\kappa_s^{2m+1}(x)} \left\langle s \frac{P_m(z)\left(A_{u_i}z_u^2 - B_{u_i}z_u - C_{u_i}\right)\Omega_1^{1/2}(s)}{x-s} \right\rangle_{s_u}(u_i) \,, \\
\left(P_{ts}^m\right)_{ij} &= \int_{s_j}^{s_{j+1}} \frac{\mathrm{d}x}{\pi} \frac{\kappa_s^{2m+1}(s_i)\sin\delta_1^{1/2}(x)}{x|\Omega_1^{1/2}(x)|\kappa_s^{2m+1}(x)} \left\langle t \frac{P_m(z)\left(A_{s_i}^2 z_s^2 + B_{s_i}z_s + C_{s_i}\right)\Omega_1^{1/2}(t)}{x-t} \right\rangle_{t_s}(s_i) \,, \\
\left(R_{su}^m\right)_{ij} &= \int_{s_j}^{s_{j+1}} \frac{\mathrm{d}x}{\pi} \frac{\kappa_u^{2m+1}(u_i)\sin\delta_0^{3/2}(x)}{x^2|\Omega_0^{3/2}(x)|\kappa_s^{2m+1}(x)} \left\langle s^2 \frac{P_m(z)\Omega_0^{3/2}(s)}{x-s} \right\rangle_{s_u}(u_i) \,, \\
\left(R_{ts}^m\right)_{ij} &= \int_{s_j}^{s_{j+1}} \frac{\mathrm{d}x}{\pi} \frac{\kappa_s^{2m+1}(s_i)\sin\delta_0^{3/2}(x)}{x^2|\Omega_0^{3/2}(x)|\kappa_s^{2m+1}(x)} \left\langle t^2 \frac{P_m(z)\Omega_0^{3/2}(t)}{x-t} \right\rangle_{t_s}(s_i) \,,
\end{aligned} \tag{4.51}$$

with the Legendre polynomials $P_m(z)$ and $A_{s/u}$, $B_{s/u}$, $C_{s/u}$, and D_s defined in Appendix C.3. The subtraction-constant-dependent $\left(\vec{A}_L^I\right)_i$ are given by

$$\begin{aligned}
\left(\vec{A}_0^2\right)_i =& \frac{2}{\sqrt{3}}\Big\langle (c_2 + c_3 s + c_4 s^2 + c_5 s^3)\Omega_0^{1/2} + c_6(A_{u_i} z^2 + B_{u_i} z^3 + C_{u_i})\Omega_1^{1/2}\Big\rangle_{s_u}(u_i) \ , \\
\left(\vec{A}_1^1\right)_i =& 2\Big\langle (c_2 + c_3 s + c_4 s^2 + c_5 s^3) z\Omega_0^{1/2} + c_6(A_{u_i} z^3 + B_{u_i} z^2 + C_{u_i} z)\Omega_1^{1/2}\Big\rangle_{s_u}(u_i) \ , \\
\left(\vec{A}_0^{1/2}\right)_i =& \frac{2}{3}\Big\langle (c_2 + c_3 t + c_4 t^2 + c_5 t^3)\Omega_0^{1/2} + c_6(A_{s_i}^2 z^2 + B_{s_i} z + C_{s_i})\Omega_1^{1/2}\Big\rangle_{t_s}(s_i) \\
&+ \frac{1}{2}\Big\langle (A_{s_i} z + D_{s_i})(c_0 + c_1 u)\Omega_1^1\Big\rangle_{u_s}(s_i) \ , \\
\left(\vec{A}_0^{3/2}\right)_i =& -\frac{\sqrt{10}}{6}\Big\langle (c_2 + c_3 t + c_4 t^2 + c_5 t^3)\Omega_0^{1/2} + c_6(A_{s_i}^2 z^2 + B_{s_i} z + C_{s_i})\Omega_1^{1/2}\Big\rangle_{t_s}(s_i) \\
&- \frac{\sqrt{5}}{2\sqrt{2}}\Big\langle (A_{s_i} z + D_{s_i})(c_0 + c_1 u)\Omega_1^1\Big\rangle_{u_s}(s_i) \ , \\
\left(\vec{A}_1^{1/2}\right)_i =& 2\Big\langle (c_2 + c_3 t + c_4 t^2 + c_5 t^3) z\Omega_0^{1/2} + c_6(A_{s_i}^2 z^3 + B_{s_i} z^2 + C_{s_i} z)\Omega_1^{1/2}\Big\rangle_{t_s}(s_i) \\
&+ \frac{3}{2}\Big\langle (A_{s_i} z^2 + D_{s_i} z)(c_0 + c_1 u)\Omega_1^1\Big\rangle_{u_s}(s_i) \ , \\
\left(\vec{A}_2^{1/2}\right)_i =& 10\left\langle (c_2 + c_3 t + c_4 t^2 + c_5 t^3)\left(z^2 - \frac{\kappa_s^2(s_i)}{3}\right)\Omega_0^{1/2}\right\rangle_{t_s}(s_i) \\
&+ 10\left\langle (c_6\left(z^2 - \frac{\kappa_s^2(s_i)}{3}\right)(A_{s_i}^2 z^2 + B_{s_i} z + C_{s_i})\Omega_1^{1/2}\right\rangle_{t_s}(s_i) \\
&+ \frac{5}{2}\Big\langle (c_0 + c_1 u)\left(z^2 - \frac{\kappa_s^2(s_i)}{3}\right)(A_{s_i} z + D_{s_i})\Omega_1^1\Big\rangle_{u_s}(s_i) \ .
\end{aligned} \tag{4.52}$$

The numerical solution scheme we will follow is depicted in Fig. 4.8. For each of the seven subtraction constant configurations the A_L^I of Eq. (4.52) are straightforwardly evaluated. The angular integrals are evaluated following the prescription given in Section 4.3.4.

Calculating the matrix elements of Eq. (4.51) is more involved. The difficulty resides within the correct treatment of the Cauchy and pseudo singularities. The Cauchy singularities become relevant in the decay region as here the integration paths of the angular average overlap with the dispersive integration. Furthermore, we have to obtain an optimal balance between computation time and numerical accuracy.

First we need to specify how we calculate the discretized integrals. Routines like the standard Gauß-Legendre method which are commonly used for Cauchy kernels, see e.g. Refs. [94, 118–121], cannot be applied due to the more evolved singularity structure. What we will employ is a semi-analytic ansatz.

We combine all functions in the integrands that prevent an analytic calculation and linearly interpolate these in the intervals $[s_i, s_{i+1}]$. Since the combined functions are slowly

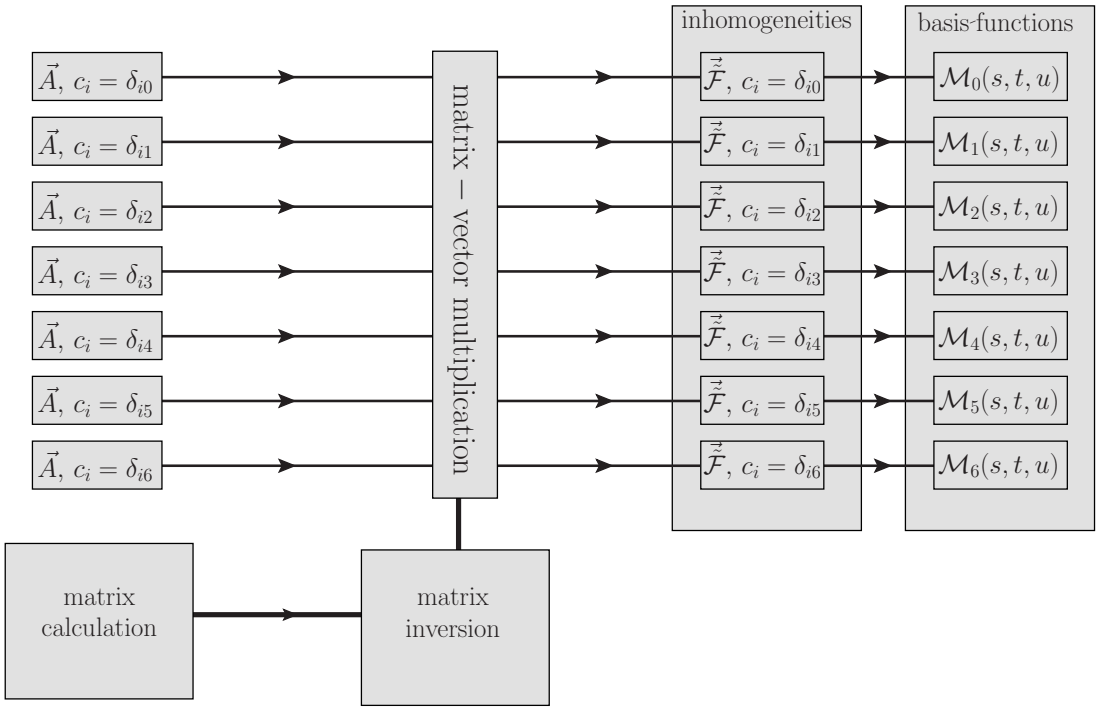

Figure 4.8: Sketch of the matrix equation solution strategy. The starting point is the calculation of the seven subtraction-constant-dependent $\vec{A}$. We set up the matrix given in Eq. (4.50), calculate the inverse and multiply the inverse matrix with the calculated $\vec{A}$ vectors and obtain the inhomogeneities. The basis functions are then obtained by calculating the dispersion integrals Eq. (4.44) in the corresponding subtraction constant configuration.

varying over the considered interval lengths this is legitimate. The emerging integrals are then calculated analytically. This procedure drastically improves the accuracy compared to simple integration routines. The treatment of the singular structures is then performed along the lines of hypersingular integrals.

To illustrate the determination of the matrix elements we will restrict to the s-channel case of Eq. (4.47)

$$\begin{aligned}
&\kappa_s^{2L+1}(s) \int_{s_{\text{th}}}^{\infty} \frac{\tilde{\mathcal{F}}(x)\sin\delta(x)}{x^n|\Omega(x)|\kappa_s^{2L+1}(x)} \left\langle t^n \frac{z^m \Omega(t)}{x-t} \right\rangle_{t_s} \mathrm{d}x \\
&= s\,\kappa_s^{2L-m}(s) \int_{s_{\text{th}}}^{\infty} \frac{\tilde{\mathcal{F}}(x)\sin\delta(x)}{x^n|\Omega(x)|\kappa_s^{2L+1}(x)} \int_{t_-(s)}^{t_+(s)} t^n \frac{\zeta^m(s,t)\Omega(t)}{x-t}\,\mathrm{d}t\,\mathrm{d}x\,,
\end{aligned} \tag{4.53}$$

with $\zeta(s,t) = \left(2ts - 3s_0 s + s^2 - \Delta\right)$ and $3s_0 = M_D^2 + M_K^2 + 2M_\pi^2$.

First we study the case $s > a_s = (M_D - M_\pi)^2$. The angular integral poses no problem as the two integral paths do not cross each other, see Fig. 4.6. We may simply use

$$s\,\kappa_s^{2L-m}(s)\int_{s_\mathrm{th}}^{\infty}\frac{\tilde{\mathcal{F}}(x)\sin\delta(x)}{x^n|\Omega(x)|\kappa_s^{2L+1}(x)}W(s,x)\,\mathrm{d}x\,,\quad W(s,x)\equiv\int_{t_-(s)}^{t_+(s)}t^n\frac{\zeta^m(s,t)\Omega(t)}{x-t}\,\mathrm{d}t\,, \tag{4.54}$$

where $W(s,x)$ can be determined numerically in a straightforward way. The discretized integral reads

$$\begin{aligned}\int_{s_\mathrm{th}}^{\infty}\frac{\tilde{\mathcal{F}}(x)\sin\delta(x)}{x^n|\Omega(x)|\kappa_s^{2L+1}(x)}W(s,x)\,\mathrm{d}x&=\sum_j\tilde{\mathcal{F}}(s_j)\int_{s_j}^{s_{j+1}}\frac{\tilde{\mathcal{F}}(x)\sin\delta(x)}{x^n|\Omega(x)|\kappa_s^{2L+1}(x)}W(s,x)\,\mathrm{d}x\\&=\begin{cases}\sum_j\tilde{\mathcal{F}}(s_j)\int_{s_j}^{s_{j+1}}\frac{c_0^j(s,b_s)+c_1^j(s,b_s)x}{\left(\lambda(x,M_K^2,M_\pi^2)(a_s-x)\right)^{L+1/2}}\,\mathrm{d}x\,, & s_j\le\frac{a_s+b_s}{2}\\ \sum_j\tilde{\mathcal{F}}(s_j)\int_{s_j}^{s_{j+1}}\frac{c_0^j(s,a_s)+c_1^j(s,a_s)x}{\left(\lambda(x,M_K^2,M_\pi^2)(b_s-x)\right)^{L+1/2}}\,\mathrm{d}x\,, & s_j>\frac{a_s+b_s}{2}\end{cases},\end{aligned} \tag{4.55}$$

where $c_0^j(s,v)+c_1^j(s,v)x$ is the linear interpolation of the function $W(s,x)\sin\delta(x)/(x^n|\Omega(x)|(v-x)^{L+1/2})$ in the interval $[s_j,s_{j+1}]$ for fixed s. Note that the resulting integrals can be performed analytically with the singularities moved into the upper complex plane to obtain the correct (physical) branch.

For the case $s < (M_D - M_\pi)^2$ the Cauchy kernel needs to be handled carefully as the integration paths meet. We rewrite

$$\begin{aligned}&\int_{s_\mathrm{th}}^{\infty}\tilde{\mathcal{F}}(x)\frac{\sin\delta(x)}{x^n|\Omega(x)|\kappa_s^{2L+1}(x)}\int_{t_-(t)}^{t_+(t)}t^n\frac{\zeta^m(s,t)\Omega(t)}{x-t}\,\mathrm{d}t\,\mathrm{d}x\\&=\int_{s_\mathrm{th}}^{\infty}\frac{\tilde{\mathcal{F}}(x)\sin\delta(x)}{x^n|\Omega(x)|\kappa_s^{2L+1}(x)}\int_{t_-(t)}^{t_+(t)}\zeta^m(s,t)\frac{t^n\Omega(t)-x^n\Omega(x)}{x-t}\,\mathrm{d}t\,\mathrm{d}x\\&\quad+\int_{s_\mathrm{th}}^{\infty}\int_{t_-(t)}^{t_+(t)}\frac{\tilde{\mathcal{F}}(x)e^{i\delta(x)}\sin\delta(x)}{\kappa_s(x)^{2L+1}(x-t)}\,\mathrm{d}t\,\mathrm{d}x\,.\end{aligned} \tag{4.56}$$

The first summand is treated analogously to Eq. (4.55). For the second summand we obtain

$$\begin{aligned}&\int_{s_\mathrm{th}}^{\infty}\int_{t_-(t)}^{t_+(t)}\frac{\tilde{\mathcal{F}}(x)e^{i\delta(x)}\sin\delta(x)}{\kappa_s^{2L+1}(x)(x-t)}\,\mathrm{d}t\,\mathrm{d}x\\&=\begin{cases}\sum_j\tilde{\mathcal{F}}(s_j)\int_{s_j}^{s_{j+1}}\int_{t_-(t)}^{t_+(t)}\frac{a_0^j(b_s)+a_1^j(b_s)x}{\left(\lambda(x,M_K^2,M_\pi^2)(a_s-x)\right)^{L+1/2}}\,\mathrm{d}t\,\mathrm{d}x\,, & s_j\le\frac{a_s+b_s}{2}\,,\\ \sum_j\tilde{\mathcal{F}}(s_j)\int_{s_j}^{s_{j+1}}\int_{t_-(t)}^{t_+(t)}\frac{a_0^j(a_s)+a_1^j(a_s)x}{\left(\lambda(x,M_K^2,M_\pi^2)(b_s-x)\right)^{L+1/2}}\,\mathrm{d}t\,\mathrm{d}x\,, & s_j>\frac{a_s+b_s}{2}\,,\end{cases}\end{aligned} \tag{4.57}$$

where now $a_0^j(v) + a_1^j(v)x$ is the linear interpolation of $e^{i\delta(x)} \sin\delta(x)/(v-x)^{L+1/2}$ in the interval $[s_j, s_{j+1}]$. Once the matrix is set up the equation is solved by inverting the matrix and multiplying consecutively with the seven $\vec{A}$ to obtain the inhomogeneities for each subtraction configuration.

To finally obtain the single-variable amplitudes $\mathcal{F}_L^I$ of each basis function, we have to perform the dispersion integral. We can either perform the dispersion integral similarly to the iteration scheme, explicitly outlined in Section 2.4, or follow the line employed for the matrix method, namely discretizing the integral and calculating the integrals semi-analytically. The second is straightforwardly read off from the above considerations

$$\begin{aligned}\mathcal{F}(s) &= \int_{s_{\text{th}}}^{\infty} \frac{\tilde{\mathcal{F}}(x)\sin\delta(x)}{x^n|\Omega(x)|\kappa_s^{2L+1}(x)(x-s)}\,\mathrm{d}x = \sum_j \tilde{\mathcal{F}}(s_j)\int_{s_j}^{s_{j+1}} \frac{\tilde{\mathcal{F}}(x)\sin\delta(x)}{x^n|\Omega(x)|\kappa_s^{2L+1}(x)(x-s)}\,\mathrm{d}x \\ &= \begin{cases} \sum_j \tilde{\mathcal{F}}(s_j)\int_{s_j}^{s_{j+1}} \frac{d_0^j(s,b_s)+d_1^j(s,b_s)x}{\left(\lambda(x,M_K^2,M_\pi^2)(a_s-x)\right)^{L+1/2}(x-s)}\,\mathrm{d}x\,, & s_j \le \frac{a_s+b_s}{2}\,, \\ \sum_j \tilde{\mathcal{F}}(s_j)\int_{s_j}^{s_{j+1}} \frac{d_0^j(s,a_s)+d_1^j(s,a_s)x}{\left(\lambda(x,M_K^2,M_\pi^2)(b_s-x)\right)^{L+1/2}(x-s)}\,\mathrm{d}x\,, & s_j > \frac{a_s+b_s}{2}\,, \end{cases}\end{aligned} \tag{4.58}$$

with $d_0^j(s,b_s) + d_1^j(s,b_s)x$ the linear interpolation of $\sin\delta(x)/(x^n|\Omega(x)|(v-x)^{L+1/2})$ in the interval $[s_j, s_{j+1}]$ for a fixed s.

4.6 Numerical results

Solving the coupled integral Eq. (4.44) with the algorithm presented in the previous section, we obtain the single-variable basis functions $(\mathcal{F}_L^I)_i$ depicted in Figs. 4.9 and 4.10. The vector resonances $K^*(892)$ (in $\mathcal{F}_1^{1/2}$) and $\rho(770)$ (in $\mathcal{F}_1^1$) as well as the πK D-wave resonance $K_2^*(1430)$ (in $\mathcal{F}_2^{1/2}$) are clearly visible. The $\mathcal{F}_0^{1/2}$ basis functions include the effects of the scalar states $K_0^*(800)$ and $K_0^*(1430)$, while the exotic $\mathcal{F}_0^2$ and $\mathcal{F}_0^{3/2}$ basis functions are free of resonances.

The error bands in Figs. 4.9 and 4.10 are determined by a conservative error estimate of the phase shifts: For the S-wave πK and $\pi\pi$ phases the error is assumed to rise linearly from zero at the threshold to $\pm 20°$ at 2 GeV. Beyond 2 GeV the error is fixed to $\pm 20°$. The πK isospin 1/2 P- and D-wave phase errors and $\pi\pi$ P-wave phase errors are similarly obtained, with the only difference that the linear rise of the error sets in after the $K^*(892)$, $K_2^*(1430)$, and $\rho(770)$ resonances, respectively. In the $\pi\pi$ P-wave case we additionally vary between the phase-shift data from Refs. [29–32].

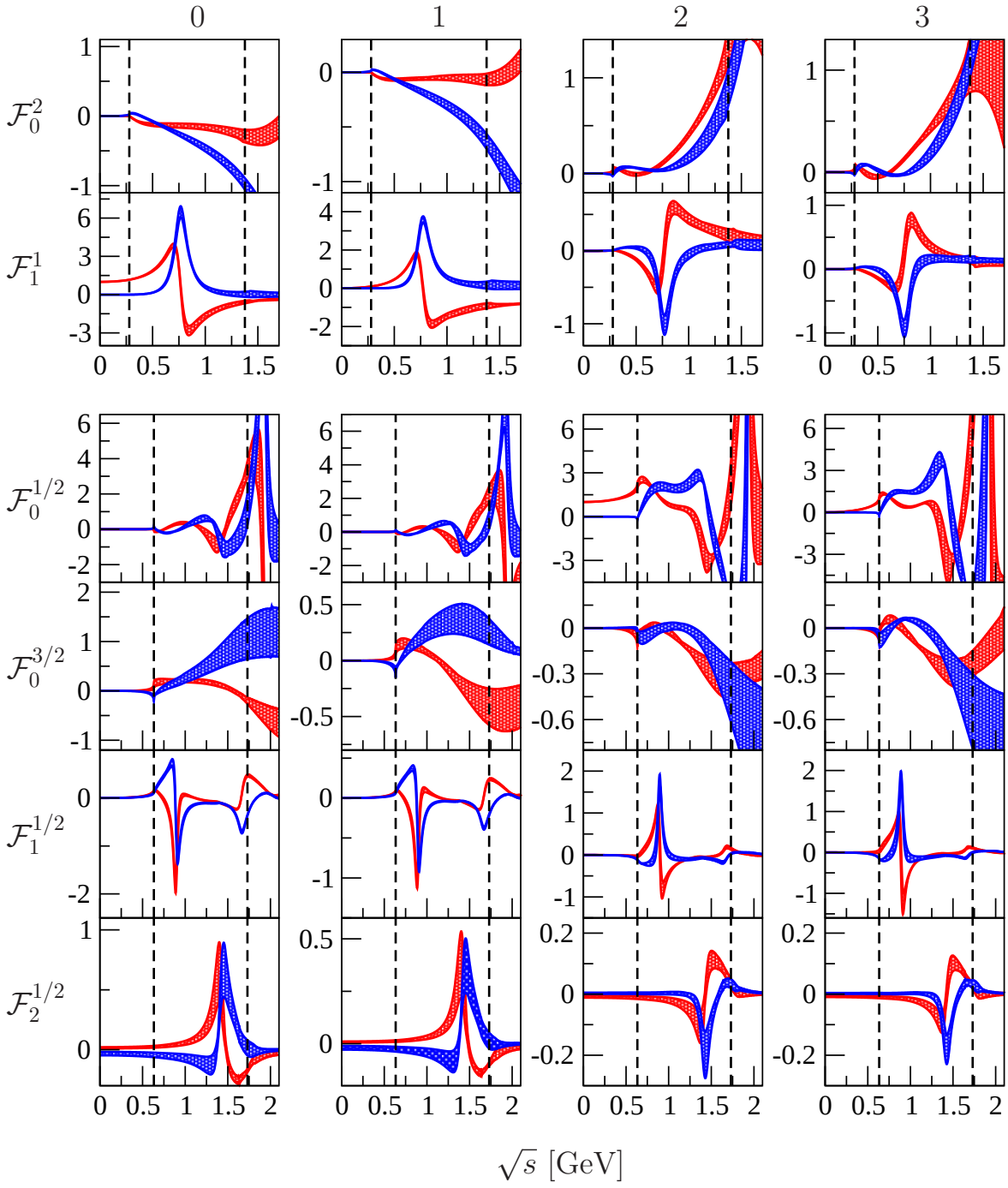

Figure 4.9: Real (red) and imaginary (blue) parts of the single-variable functions $(\mathcal{F}_L^I)_i$ for $i = 0, \ldots, 3$. The vertical dashed lines denote the kinematical limits of the decay region.

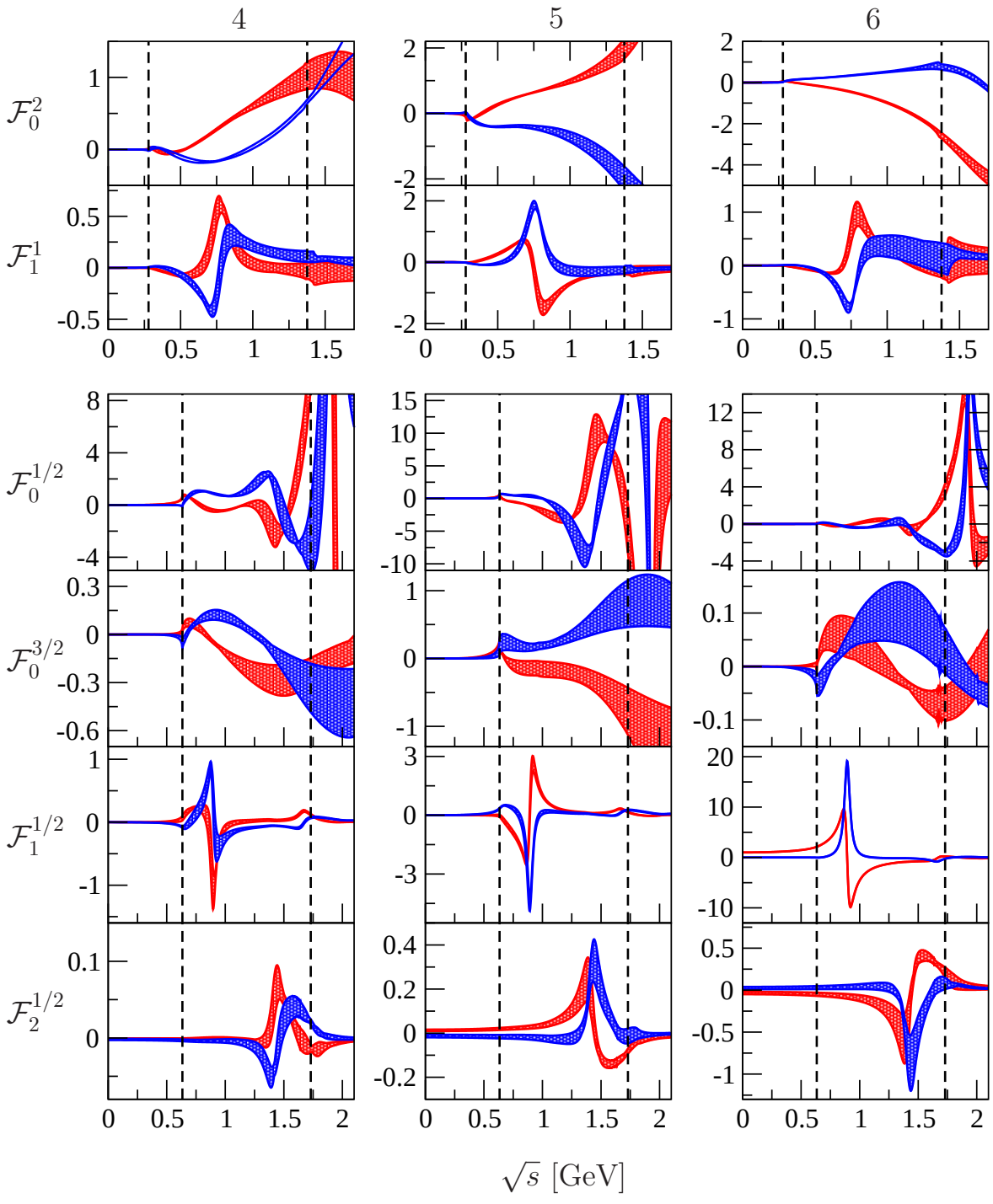

Figure 4.10: Real (red) and imaginary (blue) parts of the single-variable functions $(\mathcal{F}_L^I)_i$ for $i = 4, \ldots, 6$. The vertical dashed lines denote the kinematical limits of the decay region.

Chapter 5

Experimental comparison

In this chapter we will display the comparison of our theoretical decay amplitude to the experimental $D^+ \to K^-\pi^+\pi^+$ Dalitz plot data from the CLEO [97] and FOCUS [98] collaborations and the $D^+ \to \bar{K}^0\pi^-\pi^+$ Dalitz plot measured by BES III [100]. With the seven basis functions calculated, we will determine the subtraction constants with individual fits to the available three data sets and try to study the significance of crossed-channel rescattering effects in these decays as well as compare to other approaches. We conclude with combined fits to all data sets in order to probe the simultaneous treatment of the two isospin-related decay channels.

5.1 $D^+ \to K^-\pi^+\pi^+$ Dalitz plots

We begin with the comparison to the $D^+ \to K^-\pi^+\pi^+$ Dalitz plot data from the CLEO and FOCUS collaboration. As the decay is symmetric under the interchange of the two final-state pions, we can restrict the comparison to the region $s < t$ and mirror the $s > t$ half of the Dalitz plot into the $s < t$ region.

The experimental events are collected in equidistant bins of size $0.044\,\mathrm{GeV}^2 \times 0.044\,\mathrm{GeV}^2$. Bins which overlap with the phase space boundary are discarded, resulting in 493 bins over the considered fit region ($s < t < (M_K + M_{\eta'})^2$). The following event distribution function was used for the fit analogously to the experimental analyses

$$\mathcal{P}(s_i, t_i) = \int_{t_i-\delta}^{t_i+\delta} \int_{s_i-\delta}^{s_i+\delta} \Big[f_{\mathrm{sig}} \mathcal{N}_S |\mathcal{M}_{-++}(s,t,u)|^2 \epsilon(s,t) + (1 - f_{\mathrm{sig}}) \mathcal{N}_B B(s,t) \Big] \mathrm{d}s\, \mathrm{d}t\,, \quad (5.1)$$

with (s_i, t_i) being the center of the corresponding bin and 2δ the bin width, $\epsilon(s,t)$ the efficiency parametrization, $B(s,t)$ the background parametrization, $\mathcal{N}_{\mathrm{sig}}$ and $\mathcal{N}_B$ normalization constants such that the background and signal term are normalized to unity, and the signal fraction f_{sig}.

We minimize the following χ^2,

$$\chi^2 = \sum_{i=0}^{492} \frac{\left[\mathcal{N}\mathcal{P}(s_i,t_i) - (\#\text{events/bin})_i\right]^2}{(\#\text{events/bin})_i}\,, \tag{5.2}$$

where $\mathcal{N}$ is the number of events, the sum runs over the number of bins and the error on the binned data is assumed to be purely statistical. In addition to the full dispersive representation Eq. (4.44), we also fit a simplified decay amplitude to data, which is given by a sum of Omnès functions multiplied by polynomials:

$$\begin{aligned}\mathcal{M}_{-++}(s,t,u) = {}& c_0'\Omega_0^2(u) - \sqrt{\frac{2}{15}}c_1'\Omega_0^{3/2}(s) + \frac{1}{\sqrt{3}}\big(c_2' + c_3's + c_4's^2 + c_5's^3\big)\Omega_0^{1/2}(s) \\ & + \frac{c_6'}{\sqrt{3}}\big[s(t-u)-\Delta\big]\Omega_1^{1/2}(s) + \frac{c_7'}{2\sqrt{3}}\Big[3\big(s(t-u)-\Delta\big)^2 - \kappa_s^2(s)\Big]\Omega_2^{1/2}(s) \\ & + (t \leftrightarrow s)\,,\end{aligned} \tag{5.3}$$

where the c_i' are again complex fit constants. Equation (5.3) emulates a dispersively improved isobar model that neglects any crossed-channel rescattering effects. The number of polynomial fit constants is chosen to resemble the number of degrees of freedom in the full dispersive result Eq. (4.44) as far as possible; with certain caveats that preclude an immediate quantification of three-particle rescattering effects in the same straightforward way as performed for $\phi \to 3\pi$ decays in Ref. [34]. In Eq. (4.44), two subtraction constants c_0 and c_1 are contained in the $\pi\pi$ P-wave, which only contributes indirectly via the intermediate state $\bar{K}^0\pi^0\pi^+$ to the decay and thus does not show up in the pure Omnès amplitude Eq. (5.3). In addition, every Omnès function in Eq. (5.3) needs at least a normalization constant to adjust the strength of individual amplitudes, while some single-variable amplitudes do not have any subtraction constants. Finally, once the D-wave is included we have one additional complex fit parameter c_7' in the pure Omnès fits. For that reason we consider both Omnès and the full dispersive fits without (Omnès 1, full 1) and with D-wave (Omnès 2, full 2).

We have the freedom to fix one subtraction constant, as both the overall normalization and the overall phase are arbitrary and factorized out; we choose $c_2 = c_2' = 1$. This leaves 13 (15) real fit constants for the full / Omnès fits.

Following experimental custom, we will employ so-called fit fractions to characterize the relative importance of various single-variable functions. These are defined in the following way

$$\text{FF}_J^I = \frac{\int |P_J(x(s,t))\,\mathcal{F}_J^I(x(s,t))|^2\,\mathrm{d}s\,\mathrm{d}t}{\int |\mathcal{M}_{-++}(s,t,u)|^2\,\mathrm{d}s\,\mathrm{d}t}\,, \tag{5.4}$$

where the P_J denote the angular prefactors of the corresponding single-variable amplitudes in the total amplitude. The integration runs over the fitted Dalitz plot region. In general

these fit fractions are not unique due to the freedom of adding an element of the invariance group Eq. (C.41); the projections onto partial-wave amplitudes then will lead to different fit fractions.

5.1.1 CLEO data

The Dalitz plot measured by the CLEO collaboration [97] contains 140793 events. The efficiency and background parametrizations are given explicitly. We have refitted the parametrizations to the Monte Carlo and background samples and found agreement, exception for the threshold factors.[1] Our fit result to the CLEO Dalitz plot are summarized in Table 5.1, together with the fit fractions in Table 5.2. In the full dispersive fits (full fits 1/2), the resulting values for the subtraction constants in Table 5.1 have similar order of magnitude with the exception c_6, which is rather small. This can be understood by the large $\mathcal{F}_1^{1/2}$ single-variable amplitude in this particular basis function (see Fig. 4.10). Furthermore the phases of the $\mathcal{F}_1^1$ subtraction constants (c_0, c_1) nearly agree modulo π. The same holds for the $\mathcal{F}_0^{1/2}$ subtraction constants (c_2 to c_5) especially for the full fit 2. This suggests that with overall phases factorized, the subtraction constants for the $\mathcal{F}_1^1$ and likewise the $\mathcal{F}_0^{1/2}$ amplitude are almost real. The differences of the single-variable amplitude phases to the elastic phase shifts depicted in Fig. 5.3 are thus predominantly due to the dispersion integrals, i.e. the crossed-channel rescattering effects.

Including the D-wave improves the χ^2/d.o.f. slightly from 1.18 ± 0.03 to 1.10 ± 0.02. Note that in the full dispersive representation, no additional fit constants are introduced when the D-wave is added. The inclusion of the D-wave does not change the phases of most subtraction constants beyond their uncertainties, with the exception of c_6; the magnitudes, in contrast, change significantly for almost all subtractions. Considering the fit fractions in Table 5.2, we observe that the inclusion of the D-wave in the full fit 2 reduces the highly destructive interference between the two S-wave amplitudes in the πK channel. We wish to point out that also in Ref. [98], a large cancellation between the isospin 1/2 and isospin 3/2 S-wave components of -164% is seen, with individual fit fractions of $(207 \pm 24)\%$ and $(40 \pm 9)\%$, respectively, which show a comparable behavior to our full fit 1. Although the fit fraction of the D-wave itself is very small, it thus has a rather large impact on the S- and P-waves. A similar phenomenon is seen in Ref. [97] where the fit quality deteriorates considerably when removing the small D-wave. Although we do not fit the whole Dalitz plot, the fit fractions for the resonant single-variable amplitudes for $\mathcal{F}_0^{1/2}$, $\mathcal{F}_1^{1/2}$ and $\mathcal{F}_2^{1/2}$

[1] The threshold factors $T(x)$ used in there read [122]

$$T(x) = \begin{cases} \sin\left(\pi E_{\mathrm{th},x}|x - x_{\max}|\right), & \text{for } 0 < E_{\mathrm{th},x}|x - x_{\max}| < 1/2\,, \\ 1, & \text{for } E_{\mathrm{th},x}|x - x_{\max}| \geq 1/2\,. \end{cases}$$

	Full 1	Full 2		Omnès 1	Omnès 2
$\lvert c_0\rvert \times \mathrm{GeV}^2$	2.7 ± 0.8	1.2 ± 0.2	$\lvert c_0'\rvert$	0.9 ± 0.3	0.9 ± 0.7
$\lvert c_1\rvert \times \mathrm{GeV}^4$	3.8 ± 1.2	2.2 ± 0.5	$\lvert c_1'\rvert$	3.0 ± 1.5	4.0 ± 1.3
c_2	1 (fixed)	1 (fixed)	c_2'	1 (fixed)	1 (fixed)
$\lvert c_3\rvert \times \mathrm{GeV}^2$	2.8 ± 0.4	2.2 ± 0.1	$\lvert c_3'\rvert \times \mathrm{GeV}^2$	1.9 ± 0.2	2.0 ± 0.2
$\lvert c_4\rvert \times \mathrm{GeV}^4$	2.0 ± 0.5	1.4 ± 0.1	$\lvert c_4'\rvert \times \mathrm{GeV}^4$	0.9 ± 0.1	1.1 ± 0.1
$\lvert c_5\rvert \times \mathrm{GeV}^6$	0.7 ± 0.3	0.4 ± 0.1	$\lvert c_5'\rvert \times \mathrm{GeV}^6$	0.13 ± 0.3	0.19 ± 0.02
$\lvert c_6\rvert \times 10^2\mathrm{GeV}^4$	4 ± 3	6 ± 2	$\lvert c_6'\rvert \times \mathrm{GeV}^4$	0.11 ± 0.05	0.10 ± 0.03
			$\lvert c_7'\rvert \times 10^3\mathrm{GeV}^8$	—	6 ± 4
$\arg c_0$	0.1 ± 0.2	1.1 ± 0.3	$\arg c_0'$	0.2 ± 0.8	0.4 ± 0.4
$\arg c_1$	0.3 ± 0.2	1.2 ± 0.3	$\arg c_1'$	-0.8 ± 0.3	-0.4 ± 0.2
$\arg c_3$	-0.2 ± 0.1	0.0 ± 0.1	$\arg c_3'$	0.2 ± 0.2	0.3 ± 0.2
$\arg c_4$	-0.5 ± 0.1	0.0 ± 0.1	$\arg c_4'$	0.4 ± 0.2	0.2 ± 0.2
$\arg c_5$	-0.1 ± 0.1	0.1 ± 0.1	$\arg c_5'$	0.2 ± 0.4	0.0 ± 0.3
$\arg c_6$	-0.3 ± 1.2	-0.9 ± 0.2	$\arg c_6'$	0.0 ± 0.1	0.0 ± 0.3
			$\arg c_7'$	—	0.4 ± 0.3
χ^2/d.o.f.	1.18 ± 0.03	1.10 ± 0.02		1.30 ± 0.06	1.08 ± 0.02

Table 5.1: *Fit to CLEO data:* Numerical fit results for the subtraction constants c_i and c_i' and the corresponding χ^2/d.o.f.. Four fit scenarios are considered: the full dispersive fit, without D-wave (full 1) and with D-wave (full 2), and the Omnès fits of Eq. (5.3), without D-wave (Omnès 1) and with D-wave (Omnès 2). The errors on the parameters are evaluated by varying the basis functions within their error bands.

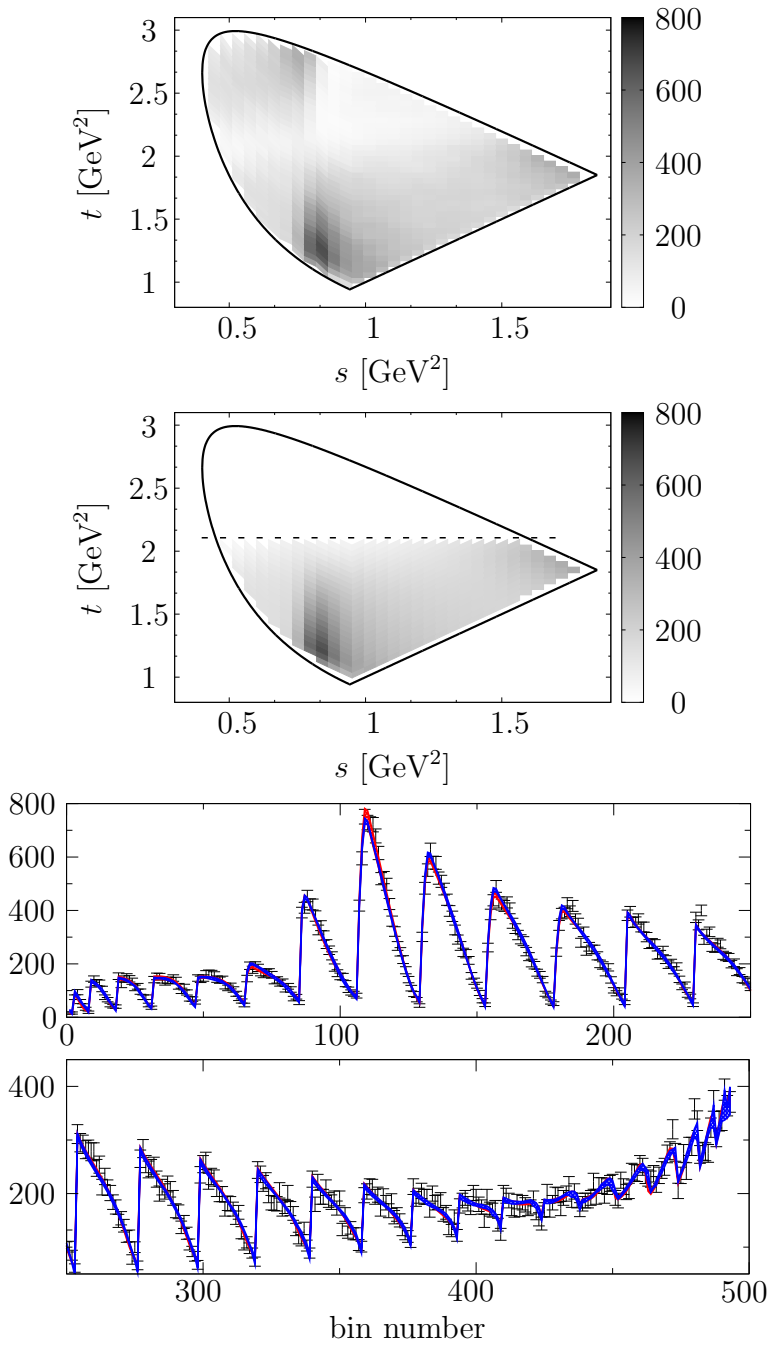

Figure 5.1: *From top to bottom:* The experimental data from CLEO [97] depicted in a binned Dalitz plot. Below that the theoretical Dalitz plot fitted to the data (fit 2). The dashed line denotes the $\eta' K$ threshold. The lowest plots show slices through the Dalitz plot. The red and blue curves correspond to the full fits 1 and 2, respectively.

Fit	FF_0^2	$2\times\mathrm{FF}_0^{1/2}$	$2\times\mathrm{FF}_1^{1/2}$	$2\times\mathrm{FF}_0^{3/2}$	$2\times\mathrm{FF}_2^{1/2}$
Full 1	$(37\pm23)\%$	$(190\pm60)\%$	$(11\pm3)\%$	$(65\pm35)\%$	—
Full 2	$(8\pm3)\%$	$(72\pm12)\%$	$(10\pm2)\%$	$(16\pm3)\%$	$(0.1\pm0.05)\%$
Omnès 1	$(48\pm16)\%$	$(178\pm22)\%$	$(7\pm1)\%$	$(395\pm35)\%$	—
Omnès 2	$(9.5\pm8)\%$	$(91\pm22)\%$	$(8\pm0.5)\%$	$(240\pm40)\%$	$(0.13\pm0.03)\%$

Table 5.2: *Fit fractions CLEO:* The resulting fit fractions of Eq. (5.4) for the different fit scenarios; the errors on the parameters are evaluated by varying the basis functions within their error bands. The fit fractions for the πK amplitudes are multiplied by two to account for the $s\leftrightarrow t$ symmetry.

agree well with the results from Refs. [97,98]. The $\mathcal{F}_0^2$ fit fraction corresponds to the isospin 2 $\pi\pi$ S-wave component of FF $\approx(9.8\ldots15.5)\%$ found in Ref. [97] within different fit models, and together with the fit fraction of $\mathcal{F}_0^{3/2}$ agrees with the non-resonant contribution found in Ref. [98] of FF $\approx(29.7\pm4.5)\%$.

Although the Omnès fits (Omnès 1, 2) yield overall similar χ^2 results, the strengths of the individual amplitudes shown in Table 5.2 are highly implausible and probably sufficient to reject this model. In particular the contribution of the non-resonant isospin 3/2 πK S-wave is vastly beyond all reasonable expectations, and cannot be justified. In contrast to the full fit, this situation is not ameliorated significantly by including the D-wave. We conclude that crossed-channel rescattering effects are essential to obtain sensible fit fractions.

The resulting Dalitz plot as well as a one-dimensional representation in terms of slices through it are displayed in Fig. 5.1. The bin numbering for the latter is organized in terms of t-slices for constant s, subsequently glued together with the next slice of higher s. We evaluate the event distribution function Eq. (5.1) over each bin and compare to experimental data. The rather small error band on the fit results suggests that the uncertainty in the basis functions is largely compensated by interference effects between the different single-variable amplitudes, as well as by corresponding variations in the fitted subtraction constants.

5.1.2 FOCUS

The FOCUS Dalitz plot data [98] includes 52460 $\pm$ 245 signal and 1897 $\pm$ 39 background events. With the resulting signal fraction of $\sim 96.5\%$ we perform the full and Omnès fits as above. Table 5.3 summarizes the fit results together with the fit fractions in Table 5.4. The overall picture is very similar to the CLEO fit results with a slightly bigger $\chi^2/\text{d.o.f.}\approx1.2$. The Omnès fits again result in nonphysical fit fractions (see Table 5.4), and from here on we

Fit constant	Full 1	Full 2		Omnès 1	Omnès 2
$\lvert c_0\rvert \times \mathrm{GeV}^2$	3.0 ± 0.8	0.6 ± 0.3	$\lvert c_0'\rvert$	0.4 ± 0.2	0.6 ± 0.3
$\lvert c_1\rvert \times \mathrm{GeV}^4$	3 ± 1	0.9 ± 0.3	$\lvert c_1'\rvert$	1.9 ± 0.8	2.2 ± 0.5
c_2	1 (fixed)	1 (fixed)	c_2'	1 (fixed)	1 (fixed)
$\lvert c_3\rvert \times \mathrm{GeV}^2$	2.8 ± 0.8	1.9 ± 0.1	$\lvert c_3'\rvert \times \mathrm{GeV}^2$	1.7 ± 0.2	1.8 ± 0.2
$\lvert c_4\rvert \times \mathrm{GeV}^4$	2.5 ± 0.6	1.1 ± 0.1	$\lvert c_4'\rvert \times \mathrm{GeV}^4$	0.9 ± 0.2	1.0 ± 0.2
$\lvert c_5\rvert \times \mathrm{GeV}^6$	0.4 ± 0.2	0.3 ± 0.1	$\lvert c_5'\rvert \times \mathrm{GeV}^6$	0.1 ± 0.2	0.3 ± 0.1
$\lvert c_6\rvert \times \mathrm{GeV}^4$	0.2 ± 0.1	0.0 ± 0.1	$\lvert c_6'\rvert \times \mathrm{GeV}^4$	0.1 ± 0.4	0.1 ± 0.1
			$\lvert c_7'\rvert \times 10^3\mathrm{GeV}^8$	—	7 ± 4
$\arg c_0$	0.5 ± 0.3	0.9 ± 0.3	$\arg c_0'$	0.7 ± 0.5	0 ± 1
$\arg c_1$	0.6 ± 0.4	1.1 ± 0.2	$\arg c_1'$	-1.1 ± 0.4	0.2 ± 0.3
$\arg c_3$	0.0 ± 0.2	0.0 ± 0.1	$\arg c_3'$	0.4 ± 0.2	0.2 ± 0.2
$\arg c_4$	-0.2 ± 0.3	0.0 ± 0.1	$\arg c_4'$	0.6 ± 0.2	0.2 ± 0.3
$\arg c_5$	0.2 ± 0.3	0.0 ± 0.1	$\arg c_5'$	0.8 ± 0.2	0.2 ± 0.3
$\arg c_6$	-0.6 ± 0.7	-1.0 ± 0.4	$\arg c_6'$	-0.7 ± 0.3	-0.9 ± 0.3
			$\arg c_7'$	—	-1.1 ± 0.5
χ^2/d.o.f.	1.20 ± 0.01	1.21 ± 0.02		1.25 ± 0.02	1.17 ± 0.01

Table 5.3: *Fit to FOCUS data:* Numerical fit results for the subtraction constants c_i and c_i' and the corresponding χ^2/d.o.f.. The same four fit scenarios as in Table 5.1 are considered. The errors on the parameters are evaluated by varying the basis functions within their error bands.

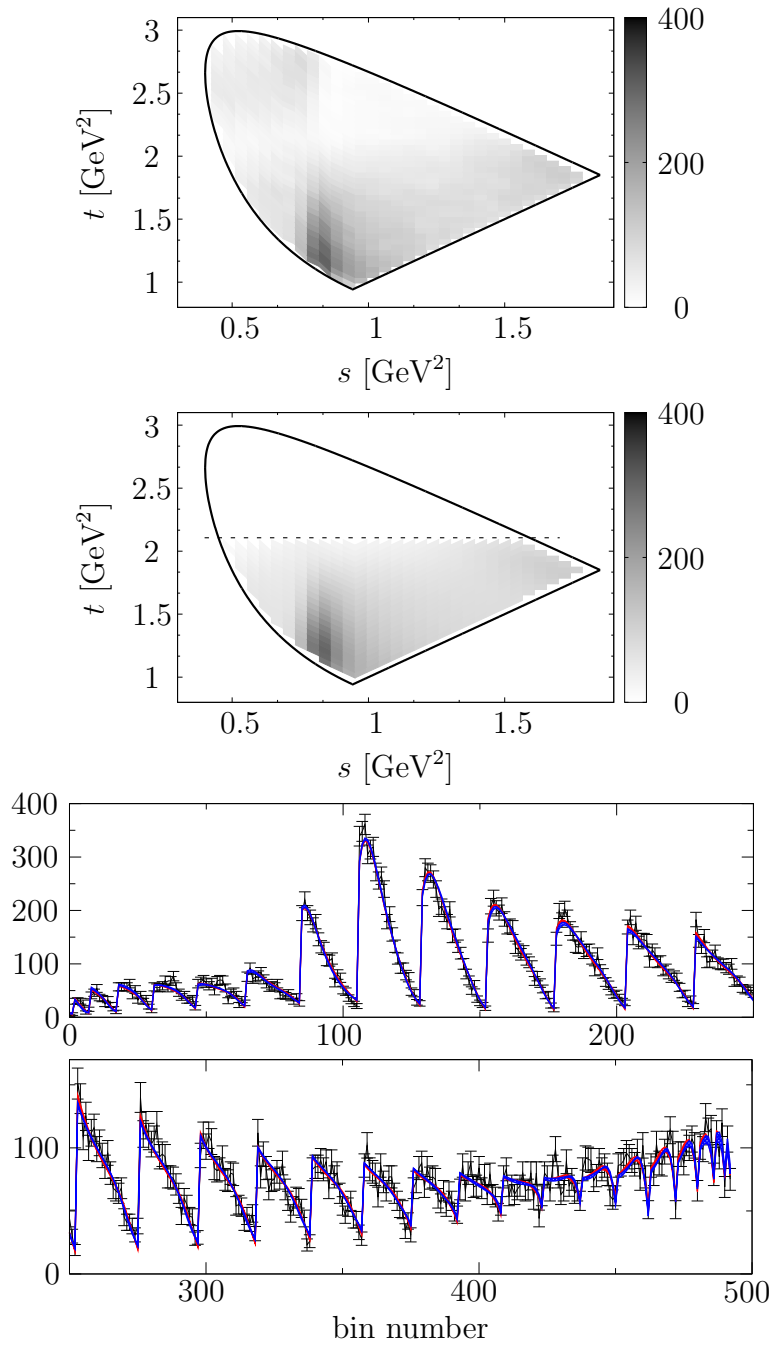

Figure 5.2: *From top to bottom:* The experimental data from FOCUS [98] depicted in a binned Dalitz plot. Below that the theoretical Dalitz plot fitted to the data (fit 2). The dashed line denotes the $\eta' K$ threshold. The lowest plots show slices through the Dalitz plot. The red and blue curves correspond to the full fits 1 and 2, respectively.

Fit	FF_0^2	$2 \times \mathrm{FF}_0^{1/2}$	$2 \times \mathrm{FF}_1^{1/2}$	$2 \times \mathrm{FF}_0^{3/2}$	$2 \times \mathrm{FF}_2^{1/2}$
Full 1	$(12 \pm 4)\%$	$(59 \pm 25)\%$	$(7.5 \pm 2.5)\%$	$(39 \pm 27)\%$	—
Full 2	$(5 \pm 3)\%$	$(67 \pm 10)\%$	$(12 \pm 1)\%$	$(8 \pm 6)\%$	$(0.17 \pm 0.07)\%$
Omnès 1	$(33 \pm 17)\%$	$(91 \pm 37)\%$	$(9 \pm 1)\%$	$(215 \pm 135)\%$	—
Omnès 2	$(89 \pm 42)\%$	$(20 \pm 12)\%$	$(11 \pm 1)\%$	$(180 \pm 60)\%$	$(0.4 \pm 0.05)\%$

Table 5.4: *Fit fractions FOCUS:* The resulting fit fractions of Eq. (5.4) for the different fit scenarios; the errors on the parameters are evaluated by varying the basis functions within their error bands. The fit fractions for the πK amplitudes are multiplied by two to account for the $s \leftrightarrow t$ symmetry.

will only compare the full fits of both experimental data sets. Starting with the fit without D-wave (full fit 1) we observe similar moduli of the subtraction constants compared to the CLEO results, however the phases do differ. The fit does not show the large destructive interference effects between the isospin 1/2 and isospin 3/2 S-wave that we find in the CLEO fit.

No improvement in the χ^2/d.o.f. is observed when we include the D-wave (full fit 2). However, the contribution from the non-resonant amplitudes, the isospin 2 and isospin 3/2 S-waves, are reduced (see Table 5.4). The fit fractions of the full fit 2 differ slightly from the CLEO fits; in particular the non-resonant S-waves contribute less in the FOCUS data.

In the full fit 2 the phases of the $\mathcal{F}_1^1$ subtraction constants persist to nearly agree modulo π; the same holds for $\mathcal{F}_0^{1/2}$ subtraction constants. It is reassuring that the overall picture of the phases of various subtraction constants is consistent in the full fit 2 results for both CLEO and FOCUS.

In Fig. 5.3, we compare moduli and phases of the resulting single-variable amplitudes as fitted to the two data sets; the phases are also compared to the input phase shifts used in the Omnès functions. The resulting phase motions largely agree in the two analyses within uncertainties, with the possible exception of some deviations in $\mathcal{F}_0^{1/2}$ in the region of the $K_0^*(800)$ resonance, where the phase extracted from the CLEO fit rises more quickly. There are significant deviations from the input phase shifts throughout: there is no naive realization of Watson's theorem in the presence of three-body rescattering effects, see e.g. recent discussions in Refs. [37,117]. This is also the explanation for the observed discrepancy of the πK $I = 1/2$ S-wave phase as extracted from these decays by the E791 [99] and FOCUS [102] collaborations, compared to the scattering phase-shift analyses [103]: while the phase shift rises to about 67°–97° at $\sqrt{s} = 1.3\,\mathrm{GeV}$ [115], the experimental analyses of D-decay data suggest an increase in the phase from threshold by about 133°–164° (read off

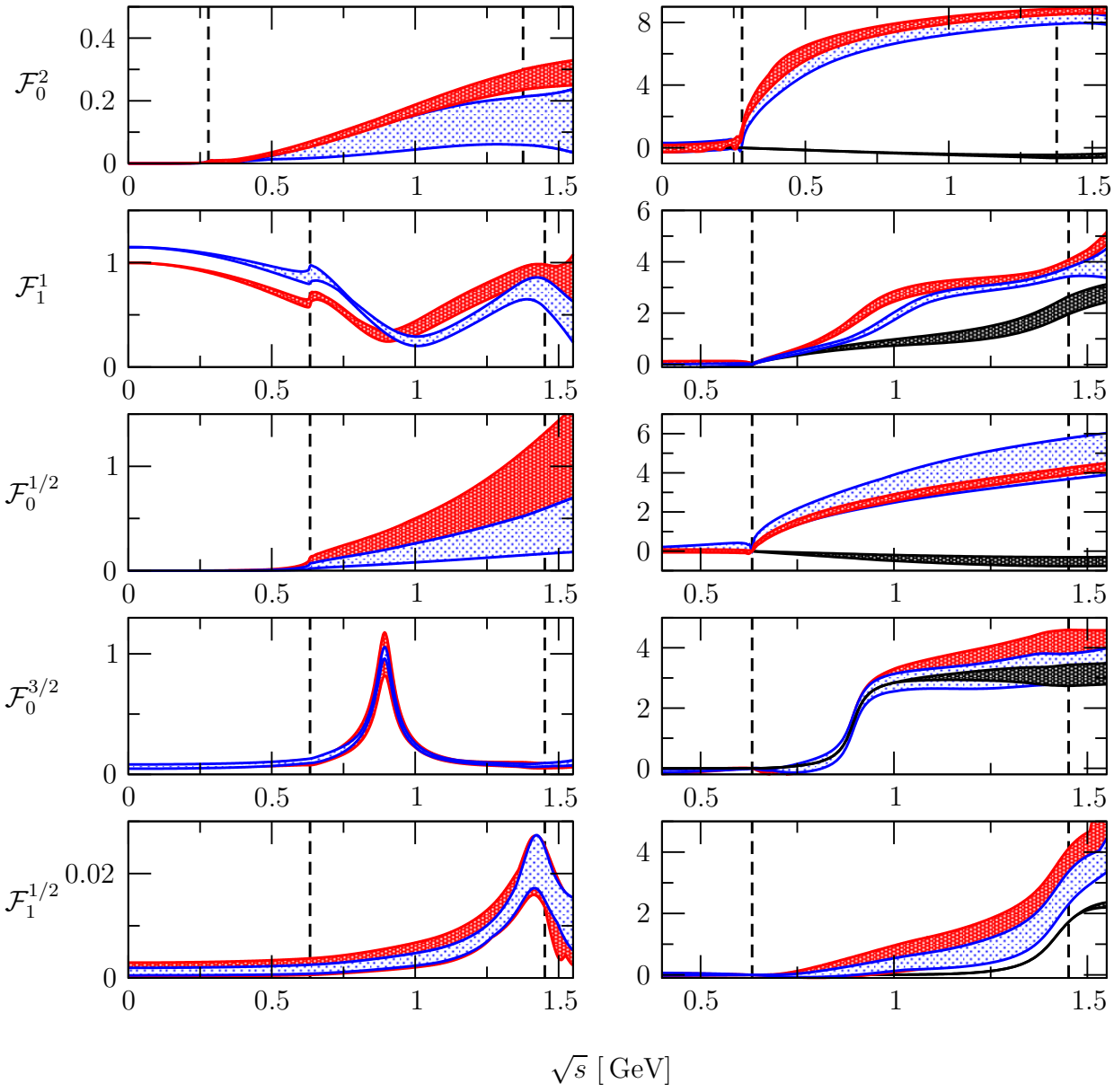

Figure 5.3: *Left column:* Absolute values of the single-variable amplitude in arbitrary units of full fit 2 (CLEO in red, FOCUS in blue). The overall normalization is chosen such that the absolute values in the $K^*(892)$ peak agree. *Right column:* Phases of the single-variable amplitudes (CLEO: red, FOCUS: blue) and input scattering phases (black) in radiant. The phases are fixed to zero at the two-particle ($\pi\pi$, πK) thresholds. The dotted lines visualize the fitted area; for the πK amplitudes from threshold to the $\eta' K$ threshold and the full phase space for the $\pi\pi$ amplitudes.

via Ref. [108]). Figure 5.3 shows that in the dispersive formalism, the phase at 1.3 GeV is about 182°–198° (CLEO) or 170°–183° (FOCUS)—even larger than found in Refs. [99,102]. We emphasize that these results are based on a formalism that uses the scattering phase shifts [115] as input: the deviations in the decay amplitude S-wave are due to complex phases induced by three-body rescattering effects.

In general, the corrections compared to input phase shifts are smallest for narrow resonances, in particular in the $I = 1/2$ πK P- and D-waves. The largest phase differences are observed in the non-resonant amplitudes, where the phases of $\mathcal{F}_0^2$ and $\mathcal{F}_0^{3/2}$ show a 2π rise due to zeros in imaginary or real parts close to threshold in individual basis functions. Note how these seemingly drastic differences are accompanied by very small absolute magnitudes of the amplitudes in question: in view of the aim to control the phase behavior of the complete, combined decay amplitude accurately, these specific deviations are still rather small.

Turning to the moduli of the single-variable amplitudes, the relative strength of the $K^*(892)$ resonance (in $\mathcal{F}_1^{1/2}$) compared with the $K_2^*(1430)$ (in $\mathcal{F}_2^{1/2}$) agrees between CLEO and FOCUS fits. However the dip in the $\mathcal{F}_0^{1/2}$ amplitude is shifted to higher energies in the FOCUS fit and slightly more pronounced. The moduli of the non-resonant amplitudes $\mathcal{F}_0^{3/2}$ and $\mathcal{F}_0^2$ turn out to be smaller in the FOCUS fit, which is also underlined by the fit fractions (compare Tables 5.2 and 5.4).

5.1.3 Combined fits

As a last step we want to perform combined fits including both data sets. Besides serving as a consistency check, the main motivation for a combined fit lies in the comparison to the adjacent $D^+ \to K_s^0\pi^0\pi^+$ Dalitz plot analysis. Given the rough agreement of both CLEO and FOCUS fits, with the exception of the modulus of the subtraction constant c_1 and the strengths of the non-resonant-amplitudes, see Fig. 5.3, there is little tension to be expected. We perform moreover the previously specified fit scenarios (full fits 1/2 and Omnès fits 1/2) and define the to be minimized χ^2_{combined} via the sum of the individual χ^2 values

$$\chi^2_{\text{combined}} \equiv \chi^2_{\text{CLEO}} + \chi^2_{\text{FOCUS}} \cdot \tag{5.5}$$

The fits yield consistent results with χ^2_{combined} values of 1.23 ± 0.02 (1.21 ± 0.02) for the full 1 (full 2) fit. Since the combined and individual fits are more or less redundant, we relegate the tables specifying the subtraction constant results as well as the fit fractions to the Appendix C.5. The resulting single-variable amplitudes are included in Fig. 5.6. In the individual fits we have restrained from showing the $\pi\pi$ P-wave amplitude since these fits do not constrain the P-wave amplitude well. However in Fig. 5.6 we will show all single-variable amplitudes in order to have a first hint on the viability of a combined treatment.

5.1.4 Comparison to other approaches

So far the only theoretical approach known to us that includes all relevant partial waves, three-particle rescattering effects, and the isospin coupled intermediate state $\bar{K}^0\pi^0\pi^+$ is Ref. [111]. The treatment is based on a unitary coupled-channel framework. The two-particle rescattering contributions are fixed by the πK and $\pi\pi$ scattering data, phases, and moduli. Three-body rescattering effects are generated by solving a Faddeev equation. In addition to the three-body rescattering a three-body potential, based on hidden local symmetry, is introduced modeling vector meson exchanges. The author studies the influence of individual rescattering contributions by considering different fit scenarios; crossed-channel rescattering effects and three-body potential turned off (isobar fit), three-body potential turned off (Z fit), and the full fit. An additional contact term breaking unitarity is allowed for, which in the full fit turns out to be negligible. The decay amplitude depends on 27 to 39 degrees of freedom depending on the considered fit model, which is more than twice the number of parameters included in our full fit.

To compare the fit fractions obtained in Ref. [111], we note that the isobar fit theoretically compares closest to our Omnès fits, while the Z fit does to our full fits. However the isobar fit has a large contribution from the unitarity-breaking contact term (considered as a "background" contribution) of 17.7%, such that a direct comparison is not sensible. Concerning the full and the Z fit, a large destructive interference between the isospin 1/2 and isospin 3/2 S-waves is seen, similar to our CLEO fit 1 configuration. The isospin 1/2 P-waves are of similar size, $\sim 15\%$ compared to our $10 - 14\%$, but the $\pi\pi$ S-wave contribution is smaller ($1.8 - 3.8\%$) than our contributions in either full fit 1 or CLEO full fit 2. It agrees only with the FOCUS full fit 2. — Concerning this comparison, we should stress once more that in contrast to Ref. [111], we do not fit the full Dalitz plot.

Unfortunately the improvement due to crossed-channel rescattering cannot be quantified in a simple way in Ref. [111] either. The improvement going from the isobar to the Z and then further to the full model can also be due to the introduction of further degrees of freedom; as discussed above, we encounter a similar problem in our analysis. However the background term, which gives an indication for missing physics, reduces dramatically once the crossed-channel rescattering effects and the coupled intermediate state $\bar{K}^0\pi^0\pi^+$ are included. This is a similar conclusion as drawn from the dispersive analysis of $\phi \to 3\pi$ Dalitz plots [34], which rendered phenomenological contact terms [123, 124] superfluous.

5.2 $D^+ \to \bar{K}^0\pi^0\pi^+$ Dalitz plot

In this section we compare our theoretical $D^+ \to \bar{K}^0\pi^0\pi^+$ decay amplitude to the Dalitz plot data of the $D^+ \to K^0_S\pi^0\pi^+$ decay measured by the BES III collaboration, see Ref. [100]. Strictly, the K^0_S is a mixture of the $\bar{K}^0$ and K^0 state and in principle the $D^+ \to K^0\pi^0\pi^+$

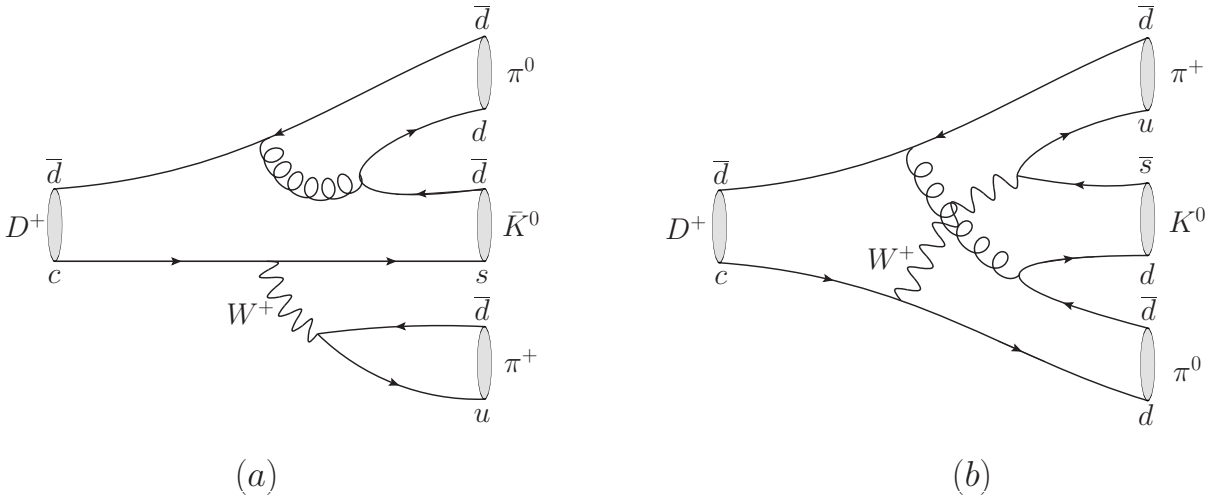

Figure 5.4: Quark line diagrams of the Cabibbo favored $D^+ \to \bar{K}^0\pi^0\pi^+$ decay (a) (from Fig. 4.2) and the doubly Cabibbo suppressed $D^+ \to K^0\pi^0\pi^+$ decay with $c \to d$ and $s \to u$ quark conversions (b).

decay should be considered as well. However the $D^+ \to K^0\pi^0\pi^+$ decay is doubly Cabibbo suppressed: We have a $c \to d$ and $s \to u$ quark transition, see Fig. 5.4 b), and the relative contribution to the Dalitz plot is crudely approximated by the ratio

$$\frac{|\mathcal{M}_{00+}(s,t,u)|^2}{|\mathcal{M}_{\bar{0}0+}(s,t,u)|^2} \sim \frac{|V_{cd}|^2|V_{su}|^2}{|V_{cs}|^2|V_{ud}|^2} \approx 0.3\% \,, \tag{5.6}$$

and therefore negligible, with the values of the Cabibbo matrix elements taken from Ref. [82].

The data[2] comprises of 166694 events in the Dalitz plot with a signal purity of about 85% provided in a binned $t \times u$ Dalitz plot with a bin size of $0.05\,\mathrm{GeV}^2 \times 0.05\,\mathrm{GeV}^2$. The binned data is already efficiency and background corrected and the event distribution function is, analogously to Eq. (5.1), given by

$$\mathcal{P}(t_i, u_i) = \int_{t_i-\delta}^{t_i+\delta} \int_{u_i-\delta}^{u_i+\delta} |\mathcal{M}_{\bar{0}0+}(s(t,u),t,u)|^2 \mathrm{d}u\,\mathrm{d}t \,, \tag{5.7}$$

with (t_i, u_i) being the center of the corresponding bin and $2\delta_x = 0.05\,\mathrm{GeV}^2$ the bin width.

We perform the fits analogously to the CLEO and FOCUS fits in Section 5.1 and restrict

[2]We are grateful to the BES III collaboration, in particular Li Haibo, Fu Chengdong and Andrzej Kupsc, for providing the data to us.

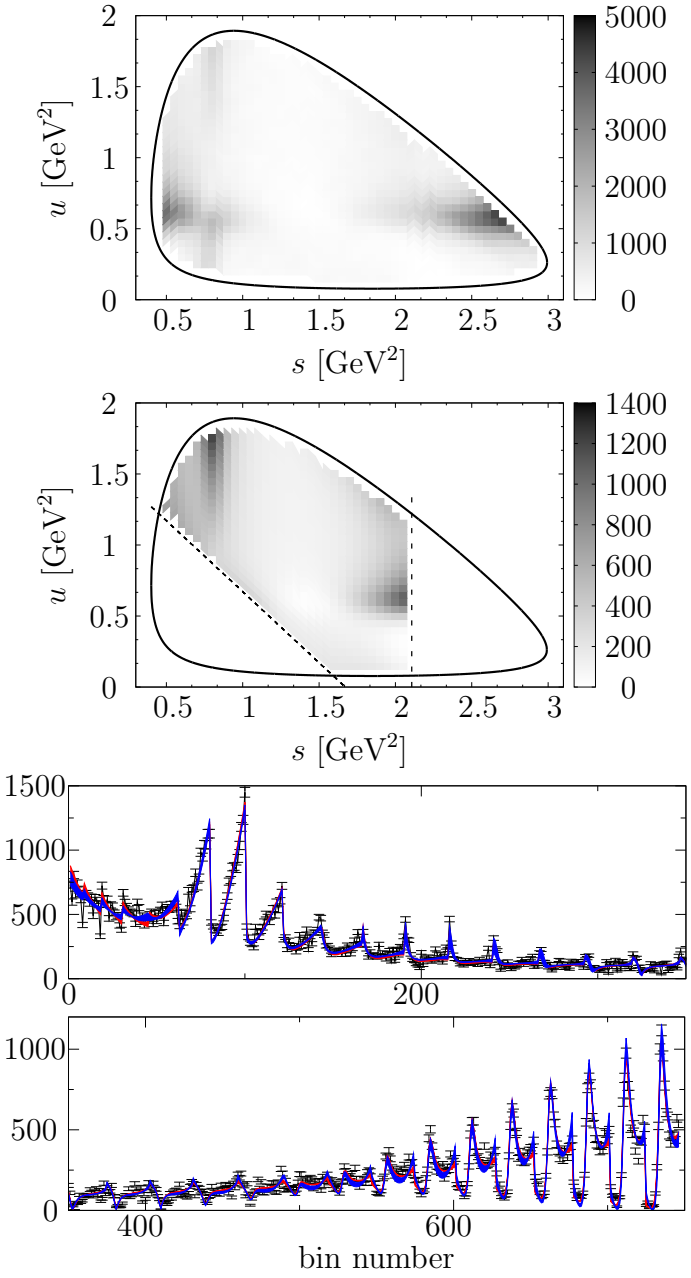

Figure 5.5: *From top to bottom:* The experimental data from BES III [100] is depicted in a binned Dalitz plot. Below that the theoretical Dalitz plot fitted to the data (fit 2) is shown. The dashed lines denote the restriction of the fits to the region $(s,t) < (M_{\eta'} + M_K)^2$. The lowest plots show slices through the Dalitz plot. The red and blue curves correspond to the full fits 1 and 2, respectively.

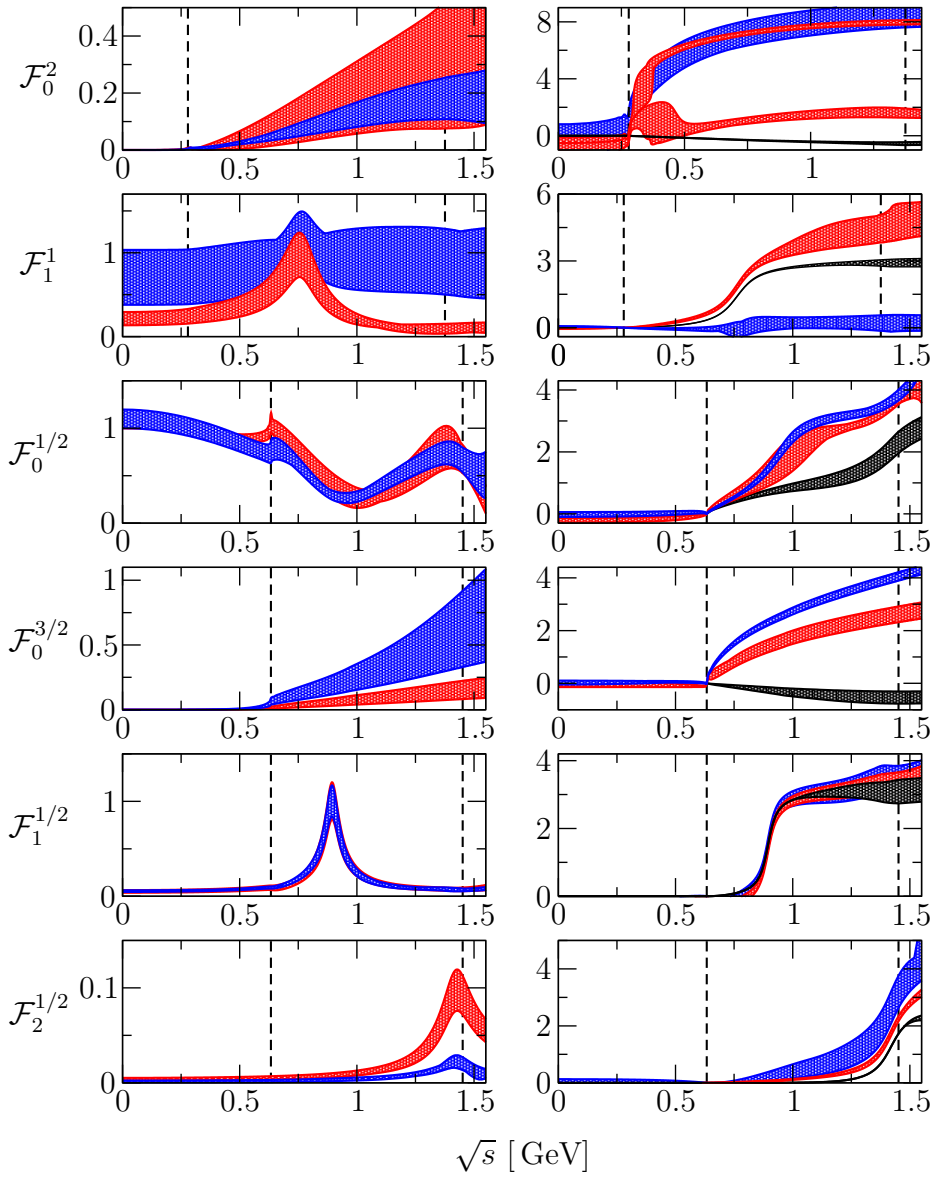

Figure 5.6: *Left column:* Absolute values of the single-variable amplitude in arbitrary units of full fit 2 (BES III in red, CLEO/FOCUS in blue). The overall normalization is chosen such that the absolute values in the $K^*(892)$ peak agrees with the ones in Fig. 5.3. *Right column:* Phases of the single-variable amplitudes (BES III in red, CLEO/FOCUS in blue) and input scattering phases (black) in radiant. The phases are fixed to zero at the two-particle ($\pi\pi$, πK) thresholds. Note that we obtain two separate solutions for the $\mathcal{F}_0^2$ phase. The dotted lines visualize the fitted area; for the πK amplitudes from threshold to the $\eta' K$ threshold and the full phase space for the $\pi\pi$ amplitudes.

	Full 1	Full 2		Full 1	Full 2
$\lvert c_0\rvert \times \mathrm{GeV}^2$	0.17 ± 0.01	0.21 ± 0.08	$\arg c_0$	0.4 ± 0.1	0.5 ± 0.2
$\lvert c_1\rvert \times \mathrm{GeV}^4$	0.26 ± 0.03	0.21 ± 0.09	$\arg c_1$	-0.5 ± 0.3	-0.2 ± 0.3
c_2	1 (fixed)	1 (fixed)	$\arg c_2$	0 (fixed)	0 (fixed)
$\lvert c_3\rvert \times \mathrm{GeV}^2$	1.8 ± 0.05	1.6 ± 0.1	$\arg c_3$	0.07 ± 0.02	0.05 ± 0.01
$\lvert c_4\rvert \times \mathrm{GeV}^4$	0.88 ± 0.08	0.7 ± 0.1	$\arg c_4$	0.03 ± 0.01	0 ± 0.05
$\lvert c_5\rvert \times \mathrm{GeV}^6$	0.2 ± 0.05	0.15 ± 0.05	$\arg c_5$	-0.12 ± 0.04	-0.14 ± 0.2
$\lvert c_6\rvert \times 10^2\mathrm{GeV}^4$	3 ± 6	5 ± 2	$\arg c_6$	-0.05 ± 0.02	-0.14 ± 0.5
χ^2/d.o.f.	1.27 ± 0.01	1.35 ± 0.07	—	—	—

Table 5.5: *Fit to BES III data:* Numerical fit results for the subtraction constants c_i and the corresponding χ^2/d.o.f.. Two fit scenarios are considered: the full dispersive fit, without D-wave (full 1) and with D-wave (full 2). The errors on the parameters are evaluated by varying the basis functions within their error bands.

the fit to the region $t, s < (M_{\eta'} + M_K)^2$ obtaining 746 bins. The χ^2 is given by

$$\chi^2 = \sum_{i=1}^{746} \frac{\left[\mathcal{N}\mathcal{P}(t_i, u_i) - (\#\text{corrected events/bin})_i\right]^2}{(\#\text{corrected events/bin})_i}\,, \tag{5.8}$$

where $\mathcal{N}$ is the overall normalization to the corrected data.

We refrain to perform a pure Omnès fit, since in this decay channel we have a major direct $\rho(770)$ resonance contribution and we would like to test the coupling of both $\bar{K}^0\pi^0\pi^+/K^-\pi^+\pi^+$ channels explicitly. Furthermore, every Omnès function needs at least one normalization constant in order to adjust its strength relative to the other Omnès functions. This would introduce an additional complex normalization constant to the set of constants c_i already given in Eq. (5.3) to accommodate for the additional $\pi\pi$ P-wave Omnès function. Consequently, a pure Omnès fit requires more complex fit constants than the full Khuri–Treiman fits and the information gained is therefore very limited. Instead we perform only the two full fit scenarios; without the πK D-wave $\mathcal{F}_2^{1/2}$ (full 1 fit) and including the D-wave (full 2 fit).

The corresponding fit results for the subtraction constants are summarized in Table 5.5 and the emanating fit fractions in Table 5.6. The fit fractions are defined analogously to Eq. (5.4), with the fit fractions of the same s- and t-channel single-variable amplitude

Fit	FF_0^2	FF_1^1	$\mathrm{FF}_0^{1/2}$	$\mathrm{FF}_1^{1/2}$	$\mathrm{FF}_0^{3/2}$	$\mathrm{FF}_2^{1/2}$
Full 1	$(5 \pm 2)\%$	$(21 \pm 5)\%$	$(39 \pm 5)\%$	$(9 \pm 0.5)\%$	$(6 \pm 2)\%$	—
Full 2	$(5 \pm 0.3)\%$	$(16 \pm 3)\%$	$(43 \pm 4)\%$	$(7 \pm 2)\%$	$(9 \pm 3)\%$	$(1.5 \pm 0.05)\%$

Table 5.6: *Fit fractions BES III:* The resulting fit fractions of Eq. (5.4) for the different fit scenarios; the errors on the parameters are evaluated by varying the basis functions within their error bands. The fit fractions of the πK amplitudes in the s- and t-channel are summed together.

combined. In Fig. 5.5 we display the experimental and the fitted theoretical Dalitz plot together with the affiliated slices through the Dalitz plot. The two fits show little difference in the subtraction constant values and fit fractions, opposed to our findings in the earlier $D^+ \to K^-\pi^+\pi^+$ analysis, where the D-wave has a sizable impact on the subtraction constants and fit fractions. Including the D-wave worsens the fit quality from $\chi^2/\text{d.o.f.} = 1.27 \pm 0.01$ (without D-wave) to $\chi^2/\text{d.o.f.} = 1.35 \pm 0.07$ (with D-wave). However, no region of particular disagreement is observed in the Dalitz plot. The modulus of the subtraction constants is significantly different to the ones extracted from the CLEO/FOCUS fits. It is therefore interesting to note that the phases of the subtraction constants attained in the BES III fit are comparable (modulo 2π) to the CLEO/FOCUS phases, with the exception of the phase of c_1: We note that c_1 is the linear $\pi\pi$ P-wave subtraction constant, which contributes only through intermediate states to the $D^+ \to K^-\pi^+\pi^+$ decay amplitude. The $\mathcal{F}_0^{1/2}$ subtraction constants mutually agree modulo π and can again be chosen nearly real with an overall phase factored out. This no longer holds for the $\mathcal{F}_1^1$ amplitude, although the tendency is also seen.

To compare the individual strengths of the $\mathcal{F}_L^I$ amplitudes between the BES III and the combined CLEO/FOCUS fits we again choose to normalize the decay amplitudes in such a way that the $\mathcal{F}_0^{1/2}$ amplitudes agree in the $K^*(892)$ peak. The arising single-variable amplitudes are shown in Fig. 5.6. Immediately we observe that we obtain two separated phase results for the $\pi\pi$ S-wave amplitude ($\mathcal{F}_0^2$). On closer inspection the effective difference is located in the low-energy region around 0.3 GeV. While one phase solution keeps rising, the other starts to decrease. Beyond 0.5 GeV both phases are separated by about 2π and therefore equivalent. Note that the monotonously rising phase is consistent with the CLEO/FOCUS combined fit. The modulus of $\mathcal{F}_0^2$ also agrees with the combined fit while the large error band stands out. Furthermore, we observe in three amplitudes ($\mathcal{F}_1^1$, $\mathcal{F}_2^{1/2}$, $\mathcal{F}_2^{3/2}$) major difference.

The $\mathcal{F}_1^1$ amplitude bears a clear ρ-meson peak, prominently also seen in the Dalitz plots

(see Fig 5.5). In comparison, the resulting combined CLEO/FOCUS fit $\mathcal{F}_1^1$ amplitude does not show the prominent ρ-meson, being weakly constrained by the $D^+ \to K^-\pi^+\pi^+$ Dalitz plot. In particular the phase emanating from the combined fit is more or less flat whereas the phase of the BES III fit shows a clear ρ resonance and is close to the input phase, though rising for higher energies.

Furthermore, the relative strengths of the $K^*(892)$ resonance (in $\mathcal{F}_1^{1/2}$) and the $K_2^*(1430)$ (in $\mathcal{F}_2^{1/2}$) do not agree. The BES III fit gives a much stronger $\mathcal{F}_2^{1/2}$ than the combined CLEO/FOCUS fit, however the phases mutually agree. In contrast, the phases of the $\mathcal{F}_0^{3/2}$ waves do not agree nor do their moduli. The BES III $\mathcal{F}_0^{3/2}$ amplitude is much smaller. We observe mutual agreement in the modulus and phases of the $\mathcal{F}_0^{1/2}$ amplitude. Also the $\mathcal{F}_1^{1/2}$ amplitudes which are matched in the $K^*(892)$ peak agree very nicely in modulus and phase.

Strictly, due to isospin symmetry, the CLEO, FOCUS, and BES III fits should result in the same values for the subtraction constants. Seeing that the BES III fit results clash with the combined CLEO/FOCUS results it is however doubtful that a combined fit will succeed. With the overall χ^2 given by the the sum of the individual χ^2,

$$\chi^2_{\text{combined}} = \chi^2_{\text{CLEO}} + \chi^2_{\text{FOCUS}} + \chi^2_{\text{BES}} \ , \tag{5.9}$$

we attempt to perform simultaneous fits of all data sets (CLEO, FOCUS and BES III) available to us. The fit gives χ^2_{combined} values of 1.7 ± 0.1 (2.5 ± 0.2) for the full fit 1 (fit 2). The inclusion of the πK D-wave in the combined fit considerably worsens the fit quality. This suggests that the heuristic inclusion of the πK D-wave, which is necessary to obtain sensible fit fractions in the individual CLEO fit, may be sufficient for the individual fits but not for a combined analysis.

5.3 Alternative D-wave model

In this section we will assess the origin of the bad fit qualities. Since the prime candidate is the πK D-wave we devise the following fit scenarios. We neglect the $\mathcal{F}_2^{1/2}$ single-variable amplitude throughout, similarly to the full 1 fit scenarios, but add the corresponding D-wave Omnès function multiplied by an additional subtraction constant c_7 and the corresponding Clebsch–Gordan coefficients. This provides a more flexible D-wave contribution,

$$\begin{aligned}
\mathcal{M}'_{-++}(s,t,u) =& \mathcal{M}_{-++}(s,t,u)|_{\mathcal{F}_2^{1/2}=0} + \frac{c_7}{2\sqrt{3}}\Big\{\big[3\big(t(s-u)-\Delta\big)^2 - \kappa_t^2(t)\big]\Omega_2^{1/2}(t) \\
&+ \big[3\big(s(t-u)-\Delta\big)^2 - \kappa_s^2(s)\big]\Omega_2^{1/2}(s)\Big\} \ , \\
\mathcal{M}'_{\bar{0}0+}(s,t,u) =& \mathcal{M}_{\bar{0}0+}(s,t,u)|_{\mathcal{F}_2^{1/2}=0} - \frac{c_7}{2\sqrt{6}}\big[3\big(t(s-u)-\Delta\big)^2 - \kappa_t^2(t)\big]\Omega_2^{1/2}(t) \ .
\end{aligned} \tag{5.10}$$

	BES III	CLEO/FOCUS	CLEO/FOCUS/BES
$\lvert c_0\rvert \times \mathrm{GeV}^2$	0.18 ± 0.02	1.2 ± 0.4	0.14 ± 0.03
$\lvert c_1\rvert \times \mathrm{GeV}^4$	0.18 ± 0.01	1.3 ± 0.4	0.16 ± 0.03
c_2	1 (fixed)	1 (fixed)	1 (fixed)
$\lvert c_3\rvert \times \mathrm{GeV}^2$	1.6 ± 0.1	1.6 ± 0.2	1.7 ± 0.1
$\lvert c_4\rvert \times \mathrm{GeV}^4$	0.7 ± 0.1	0.85 ± 0.15	0.8 ± 0.1
$\lvert c_5\rvert \times \mathrm{GeV}^6$	0.18 ± 0.02	0.19 ± 0.03	0.18 ± 0.01
$\lvert c_6\rvert \times 10^2\mathrm{GeV}^4$	3.3 ± 0.2	8 ± 2	3.6 ± 0.4
$\lvert c_7\rvert \times 10^3\mathrm{GeV}^8$	2.2 ± 0.1	3.5 ± 0.5	2.8 ± 0.2
$\arg c_0$	0.32 ± 0.08	-1.0 ± 0.4	0.4 ± 0.1
$\arg c_1$	-0.24 ± 0.07	-1.0 ± 0.4	-0.5 ± 0.4
$\arg c_3$	-0.08 ± 0.02	-0.09 ± 0.04	-0.11 ± 0.02
$\arg c_4$	-0.03 ± 0.01	0.15 ± 0.08	-0.08 ± 0.04
$\arg c_5$	-0.06 ± 0.02	-0.25 ± 0.15	-0.08 ± 0.04
$\arg c_6$	-0.6 ± 0.2	0.30 ± 0.10	-0.4 ± 0.5
$\arg c_7$	-0.6 ± 0.1	-0.25 ± 0.10	-0.8 ± 0.2
$\chi^2_{\mathrm{CLEO}}/\mathrm{d.o.f.}$	—	1.12 ± 0.01	1.17 ± 0.02
$\chi^2_{\mathrm{FOCUS}}/\mathrm{d.o.f.}$	—	1.25 ± 0.01	1.28 ± 0.01
$\chi^2_{\mathrm{BES}}/\mathrm{d.o.f.}$	1.08 ± 0.01	—	1.22 ± 0.02
$\chi^2_{\mathrm{Combined}}/\mathrm{d.o.f.}$	1.08 ± 0.01	1.17 ± 0.01	1.18 ± 0.02

Table 5.7: *Alternative D-wave fits:* Numerical fit results for the subtraction constants c_i and the corresponding individual and combined χ^2/d.o.f.. Three fit scenarios are considered: fit to the BES III data only (BES III), combined fit to CLEO and FOCUS data (CLEO/FOCUS), and combined fit to CLEO, FOCUS and BES III data (CLEO/FOCUS/BES). The errors on the parameters are evaluated by varying the basis functions within their error bands.

Individual fits	FF_0^2	FF_1^1	$\mathrm{FF}_0^{1/2}$	$\mathrm{FF}_1^{1/2}$	$\mathrm{FF}_0^{3/2}$	$\mathrm{FF}_2^{1/2}$
BES III	$(2 \pm 1)\%$	$(16 \pm 1)\%$	$(49 \pm 2)\%$	$(7 \pm 1)\%$	$(10 \pm 1)\%$	$(0.2 \pm 0.1)\%$
CLEO/FOCUS	$(11 \pm 2)\%$	—	$(24 \pm 6)\%$	$(9 \pm 1)\%$	$(6 \pm 3)\%$	$(0.2 \pm 0.1)\%$
CLEO/FOCUS/BES	FF_0^2	FF_1^1	$\mathrm{FF}_0^{1/2}$	$\mathrm{FF}_1^{1/2}$	$\mathrm{FF}_0^{3/2}$	$\mathrm{FF}_2^{1/2}$
BES III	$(1 \pm 0.5)\%$	$(21 \pm 3)\%$	$(41 \pm 3)\%$	$(8 \pm 1)\%$	$(7 \pm 1)\%$	$(0.3 \pm 0.1)\%$
CLEO/FOCUS	$(3 \pm 1)\%$	—	$(53 \pm 3)\%$	$(11 \pm 1)\%$	$(0.6 \pm 0.1)\%$	$(0.3 \pm 0.1)\%$

Table 5.8: *Alternative D-wave fit fractions:* The resulting fit fractions for the different fit scenarios: individual fits to the BES III data and the CLEO/FOCUS data, and a combined fit to all three data sets simultaneously (CLEO/FOCUS/BES). The errors on the parameters are evaluated by varying the basis functions within their error bands. The fit fractions of the πK amplitudes in the s- and t-channel are summed together.

These modified decay amplitudes are fitted to the Dalitz plot data sets. We consider the following three fit scenarios: fit to the BES III data alone (BES III), simultaneous fit to the CLEO and FOCUS data sets (CLEO/FOCUS), and a combined fit to the CLEO, FOCUS, and BES III data sets (CLEO/FOCUS/BES). The individual and combined fit results are summarized in Table 5.7 and the ensuing fit fractions in Table 5.8.

The BES III fit results for the subtraction constants turn out to be very similar to the full 1/2 BES III fits, see Table 5.5 for comparison. This is an anticipated result, since in the previous full 1/2 fit scenarios the inclusion of the D-wave did not change the subtraction constants substantially but led to a poorer χ^2 result. Similarly the fit fractions are alike, with the exception of the $\mathcal{F}_0^2$ and $\mathcal{F}_2^{1/2}$ single-variable amplitudes. The fit quality with the more flexible D-wave is improved to $\chi^2_{\mathrm{BES}}/\mathrm{d.o.f.} = 1.08 \pm 0.01$ compared to $\chi^2/\mathrm{d.o.f.} = 1.27 \pm 0.01$ ($\chi^2/\mathrm{d.o.f.} = 1.35 \pm 0.01$) for the full 1 (full 2) fit.

Considering the combined $D^+ \to K^-\pi^+\pi^+$ data sets from CLEO and FOCUS collaborations we observe that the subtraction constants differ severely from the previous combined fit results, see Table C.2. However, the fit quality differs marginally. It seems that the $D^+ \to K^-\pi^+\pi^+$ decay data does not constrain the values of the subtraction constants well. Furthermore, the subtraction constants c_2 up to c_5 do not agree modulo π. Thus the $\mathcal{F}_0^{1/2}$ subtraction constants cannot be chosen real relative to each other as we have seen previously. The fit fractions hint to large constructive interference effects, with a much smaller $\mathcal{F}_0^{1/2}$ fit fraction compared to the full 2 fit results given in Table C.1.

With all data sets combined in the CLEO/FOCUS/BES fit we obtain a combined

χ^2/d.o.f. $= 1.18 \pm 0.02$ which is hugely improved to the previous combined full 1/2 fits (χ^2/d.o.f. $= 1.7 \pm 0.1/2.5 \pm 0.2$). The χ^2 thus advocates that the discrepancy in the full 1/2 fits comes from the heuristically built-in D-wave. However, we note again that a thorough inclusion of the D-wave in the Khuri–Treiman formalism would necessitate further subtraction constants as discussed previously in Section 4.3.1.

The subtraction-constant results are very similar to the individual BES III fit values but the χ^2_{BES} worsens from 1.08 ± 0.01 to 1.22 ± 0.02. In contrast, we find that the obtained χ^2_{CLEO} and χ^2_{FOCUS} values are similar to the individual fit qualities although the subtraction constants are significantly different. This suggests that the $D^+ \to \bar{K}^0\pi^0\pi^+$ data constrains the subtraction constants much better than the $D^+ \to K^-\pi^+\pi^+$ decay data. The subtraction constants of the $\mathcal{F}_0^{1/2}$ single-variable amplitude can be chosen real relative to each other and thus the previously found relation is restored. The fit fractions for the $D^+ \to \bar{K}^0\pi^0\pi^+$ decay amplitude are very similar to the BES III fit while the large constructive interference effects seen in the CLEO/FOCUS fit do not show up as prominently in the $D^+ \to K^-\pi^+\pi^+$ fit fractions. Additionally, we observe that the fit fractions of the non-resonant waves $\mathcal{F}_0^2$ and $\mathcal{F}_0^{3/2}$ reduce compared to the individual BES III and CLEO/FOCUS fits.

5.4 Conclusion

In this part of the thesis we have analyzed the $D^+ \to K^-\pi^+\pi^+$ and $D^+ \to \bar{K}^0\pi^0\pi^+$ decays with a dispersive framework based on the Khuri–Treiman formalism that satisfies analyticity, unitarity, crossing symmetry, and includes crossed-channel rescattering among the three final-state particles.

We have simultaneously constructed the formalism for the decay $D^+ \to \bar{K}^0\pi^0\pi^+$, which is directly related to $D^+ \to K^-\pi^+\pi^+$ by charge exchange and can be constructed from different linear combinations of the same (isospin) amplitudes. The theoretical decay amplitudes depend on seven complex subtraction constants, one of which can be absorbed into an overall phase and normalization of the amplitudes. The remaining parameters are fitted to the experimental Dalitz plot data from the CLEO [97], FOCUS [98] and BES III [100] collaborations, restricting the kinematic region to below the $\eta' K$ threshold $\big((s,t) < (M_{\eta'} + M_K)^2\big)$, where the elastic approximation is assumed to work well.

In the case of the $D^+ \to K^-\pi^+\pi^+$ decays we have considered different fit scenarios with (full) and without (Omnès) crossed-channel rescattering effects, as well as with and without the πK isospin 1/2 D-wave. Although the Omnès fits give reasonable χ^2/d.o.f., we obtain large destructive interferences between single-variable amplitudes, which manifest themselves in unphysical fit fractions. The full fits result in good χ^2/d.o.f. around 1.1 for the CLEO data (1.2 for the FOCUS data), with sensible fit fractions throughout. Including the πK isospin 1/2 D-wave does not significantly improve the χ^2/d.o.f., however the fit fractions of the non-resonant waves are reduced, giving small interference effects between

the single-variable amplitudes. Furthermore the simultaneous fits to CLEO and FOCUS data provide consistent results.

Regarding the $D^+ \to \bar{K}^0\pi^0\pi^+$ decay amplitude we have confined ourselves to the full fit scenarios with and without the πK isospin 1/2 D-wave. The full fit results show good agreement with the data with a χ^2/d.o.f. of 1.27 ± 0.01 for the full 1 fit (without πK isospin 1/2 D-wave) and 1.35 ± 0.07 for the full 2 fit scenario, including the D-wave. In contrast to the CLEO/FOCUS fit results we obtain sensible fit fractions for both fit scenarios.

We have shown that we can describe the $D^+ \to K\pi\pi^+$ Dalitz plot data sets in the region where we deem elastic unitarity to hold approximately, solely relying on $\pi\pi$ and πK scattering phase-shift input and exploiting the constraints of dispersion theory.

Three-body rescattering effects suspend any strict relation between the phase of the decay partial waves and scattering phase shifts: we have shown that the significantly stronger rise of the πK S-wave phases, as observed in analyses of these D-meson decays [99, 102] in comparison to phase-shift data, can be understood at least qualitatively in the framework of Khuri–Treiman equations.

A simultaneous analysis of both Dalitz plots, $D^+ \to K^-\pi^+\pi^+$ and $D^+ \to \bar{K}^0\pi^0\pi^+$, shows disagreement with the χ^2_{combined} values of 1.7 ± 0.05 (2.5 ± 0.2) for the full fit 1 (fit 2) scenario. To investigate the discrepancy, we have devised a more flexible inclusion of the D-wave. We replace the single-variable D-wave amplitude with the corresponding D-wave Omnès function times an additional complex normalization fit constant. With these modified decay amplitudes we repeat the fits to the BES III data, combined CLEO/FOCUS data and the fit to all three data sets combined (CLEO, FOCUS, and BES III). The BES III and CLEO/FOCUS fits give χ^2/d.o.f. of 1.08 and 1.17 respectively, although the fit fractions show large constructive interference effects for the CLEO/FOCUS results.

The combined fit with this modified D-wave gives good fit results with a combined $\chi^2/\text{d.o.f.} = 1.18 \pm 0.02$ and sensible fit fractions. Furthermore the individual χ^2/d.o.f. amount to $\chi^2_{\text{CLEO}}/\text{d.o.f.} = 1.17$, $\chi^2_{\text{FOCUS}}/\text{d.o.f.} = 1.28$, and $\chi^2_{\text{BES}}/\text{d.o.f.} = 1.22$. We have thus traced the source of the disagreement to the more heuristically included πK D-wave. We have shown that we can consistently describe the combined $D^+ \to K^-\pi^+\pi^+$ and $D^+ \to \bar{K}^0\pi^0\pi^+$ data with an alternative D-wave in the region where the elastic approximation is approximately realized.

Overall we have shown that the Khuri–Treiman-type equations are a powerful tool to analyze three-particle decays also in the open-charm sector, but obstacles are still to be overcome. For example an analysis of the whole Dalitz plot region necessitates the inclusion of inelastic channels (most prominently $\eta'\pi$) in a coupled-channel framework. To do so more experimental input is required. Moreover the question on how to include higher partial waves consistently without loosing predictive power has to be addressed.

Summary and Outlook

In this thesis we have studied the three-body decays $V \to 3\pi$ with $V \in \{\omega, \phi, J/\psi, \dots\}$ and the isospin coupled $D^+ \to K^-\pi^+\pi^+/\bar{K}^0\pi^0\pi^+$ decays in the framework of Khuri–Treiman dispersion relations. Furthermore we investigated the $J/\psi \to \gamma^*\pi$ transition form factor dispersively. With the theoretically hard to understand $\omega \to \pi^0\mu^+\mu^-$ and $\phi \to \pi^0 e^+e^-$ experimental data at the high-energy end of the phase space, there is the hope that the larger phase space of the $J/\psi \to \gamma^*\pi$ transition form factor might help to resolve the puzzle. We predicted the differential decay rates as well as the branching ratios of $J/\psi \to \pi^0 e^+e^-/\pi^0\mu^+\mu^-$ where we used the prior obtained $J/\psi \to 3\pi$ amplitude to pin down the dominant $\pi\pi$ contribution to the spectral function.

The main aim of this thesis was to establish the dispersive framework for three-body decays with high decaying mass. While Khuri–Treiman equations are well established for lower decaying masses ($\lesssim 1$ GeV), the method has not been utilized in the higher mass region. However these higher mass decays have become important tests of the Standard Model and the search for new physics. A thorough understanding of the strong three-particle final-state interactions is thus required. The dispersion relations employed in this thesis provide an ideal tool for this endeavor [131]. Based on the fundamental properties of analyticity, unitarity, and crossing symmetry, they incorporate crossed-channel rescattering effects among the three-particles, which have been proven to be vital in low mass three-body decays [34].

On the basis of the $V \to 3\pi$ decays we have studied the dependence of the dispersion relations on the vector-meson mass. This system is particularly fruitful since the dispersive equations have a very simple form. We examined the dependence of crossed-channel rescattering effects on the vector-meson mass and found that in the very high mass limit the crossed-channel rescattering effects become negligible. Furthermore we have tested the stability of the commonly used iterative solution method and observed that for higher decaying masses and more subtractions the method fails.

We therefore devised a new solution strategy to solve the Khuri–Treiman equations and applied it to the Cabbibo favored and isospin related $D^+ \to K^-\pi^+\pi^+/\bar{K}^0\pi^0\pi^+$ decays. These provide an ideal test case for a first application in the open-charm sector since experimental data with good statistics is available and the relation of the two channels via

isospin symmetry allows for a simultaneous description with the same degrees of freedom. The obtained theoretical amplitudes have been fitted to $D^+ \to K^-\pi^+\pi^+$ data sets from the CLEO and FOCUS collaborations as well as $D^+ \to \bar{K}^0\pi^0\pi^+$ data provided by the BES III collaboration. We have performed a multitude of fit scenarios: fits to each data set alone, with/without crossed-channel rescattering effects, with and without D-wave as well as combined fits to all data sets. Summarizing, we observed that we can describe all data sets consistently in the region where the elastic approximation is assumed to be valid and we have seen that crossed-channel rescattering effects are essential to obtain sensible fit results. However to obtain consistent results for the combined fit to all data sets we had to introduce an alternative D-wave to the heuristically included Khuri-Treiman D-wave. Since a fully included D-wave would necessitate further subtractions and this fact is inherent for the Khuri–Treiman equations the consistent inclusion of higher partial waves without loosing predictive power remains a challenge. Additionally, to have a description of the full Dalitz plot region inelastic contributions need to be taken into account. A thorough inclusion would call for a coupled-channel approach, which necessitates further yet unavailable experimental input.

Overall, Khuri–Treiman-type equations provide an impressive device to analyze three-particle decays also for higher decaying masses. With the above challenges on the to-do list and the ultimate goal to study the CP violation and beyond the Standard Model relevant D- and B-meson decays, the dispersive approach can possibly profit from the progress in other non-perturbative QCD approaches. For example it has been seen in the past that the synergy between dispersion relations and effective field theories in the low-energy regime has been fruitful. The appearance of unknown subtraction constants is immanent in dispersion theory and thus limits the predictive power especially when high-order partial waves have to be considered. Therefore for lower mass three-body decays, e.g. $\eta \to 3\pi$ [45,46,91] and $\eta' \to \eta\pi\pi$ [58], chiral effective field theories were utilized to determine these subtractions constants. One can therefore hope that also for higher decaying masses the subtraction constants can be constrained by matching to effective theories, e.g. heavy-quark effective theory, to obtain a pure theoretical prediction. Recently, short-distance matchings to Khuri–Treiman-type equations have been performed, e.g. in Ref. [129] for the semileptonic $B \to \pi\pi\ell\bar{\nu}_\ell$ decays where the subtraction constants were matched to heavy-meson chiral perturbation theory or for the $\Upsilon(3S) \to \Upsilon(1s)\pi\pi$ decay in Ref. [130] where a chiral effective theory for heavy quarkonia was applied.

Where to go next? The natural next candidates the framework ought to be unleashed upon are the $D \to KK\pi/3\pi$ decays. These decays provide a prime opportunity to extend the approach to coupled-channel Khuri–Treiman equations, since we have a good theoretical knowledge and a strong dispersive description of the pion and kaon scalar isoscalar form factors, based on the coupled-channel Omnès framework, see Refs. [132,133] and references therein.

Appendix

Appendix A

Omnès functions and phase shifts

In this appendix we discuss the asymptotic behavior of the Omnès function with respect to the assumed asymptotic behavior of the phase-shift inputs. We display our numerical implementation and depict the resulting Omnès functions and the corresponding phase-shift inputs, taken from Refs. [29–32] ($\pi\pi$ phase shifts) and Ref. [115] (πK phase shifts).

A.1 Asymptotic behavior of the Omnès function

The Omnès function (Eq. (1.40)), evaluated on the right-hand cut, is given by

$$\Omega(s) = \exp\left[\frac{s}{\pi}\int_{s_{\text{th}}}^{\infty}\frac{\delta(s')}{s'(s'-s-i\epsilon)}\,\mathrm{d}s'\right]$$

Using Sokhotsky–Weierstrass we obtain for the exponent

$$\begin{aligned}\frac{s}{\pi}\int_{s_{\text{th}}}^{\infty}\frac{\delta(s')}{s'(s'-s-i\epsilon)}\,\mathrm{d}s' &= i\delta(s) + \frac{s}{\pi}\fint_{s_{\text{th}}}^{\infty}\frac{\delta(s')}{s'(s'-s)}\,\mathrm{d}s' \\ &= i\delta(s) + \frac{1}{\pi}\fint_{s_{\text{th}}}^{\infty}\left(\frac{1}{s'-s}-\frac{1}{s'}\right)\delta(s')\,\mathrm{d}s'\ ,\end{aligned}$$

where $\fint$ denotes the Cauchy principal value. Assuming that the phase is approximately constant ($= c\pi$) for $s \geq \Lambda_\Omega^2$ we have

$$= i\delta(s) + \frac{1}{\pi}\fint_{s_{\text{th}}}^{\Lambda_\Omega^2}\left(\frac{1}{s'-s}-\frac{1}{s'}\right)\delta(s')\,\mathrm{d}s' + c\fint_{\Lambda_\Omega^2}^{\infty}\left(\frac{1}{s'-s}-\frac{1}{s'}\right)\,\mathrm{d}s'\ .$$

Taking the $s \to \infty$ limit and applying Lebesgue's dominated convergence theorem to the second term we can interchange the integration with the limit and obtain

$$= c\pi i - \frac{1}{\pi}\fint_{s_{\text{th}}}^{\Lambda_\Omega^2}\frac{\delta(s')}{s'}\,\mathrm{d}s' + \lim_{s\to\infty} c\ln\left(\left|\frac{\Lambda_\Omega^2}{\Lambda_\Omega^2 - s}\right|\right)\ . \tag{A.1}$$

The asymptotic limit of the Omnès function thus yields

$$\lim_{s\to\infty}\Omega(s) = \exp\left[\underbrace{c\pi i - \frac{1}{\pi}\fint_{s_{\text{th}}}^{\Lambda_\Omega^2}\frac{\delta(s')}{s'}\,\mathrm{d}s'}_{=\text{constant}} + \lim_{s\to\infty}\left(c\,\ln\left(\left|\frac{\Lambda_\Omega^2}{\Lambda_\Omega^2 - s}\right|\right)\right)\right] . \tag{A.2}$$

The asymptotic behavior of the Omnès function expressed in terms of the assumed phase shift asymptotics is hence given by.

$$\lim_{s\to\infty}\Omega(s) \sim s^{-c} . \tag{A.3}$$

A.2 Numerical implementation

In the following we present the numerical evaluation of the Omnès function. Since the phase information is limited to the low-energy region we will match the phases from a certain energy $\sqrt{\Lambda}$ (the phase matching point) onwards to the assumed asymptotic behavior (integer multiplicands of π). The Omnès function is given as such by

$$\Omega_L^I(s) = \exp\left\{\frac{s}{\pi}\int_{s_{\text{th}}}^{\infty}\frac{\delta_L^I(x)}{x(x-s)}\,\mathrm{d}x\right\} = \exp\left\{\frac{s}{\pi}\int_{s_{\text{th}}}^{\Lambda}\frac{\delta_L^I(x)}{x(x-s)}\,\mathrm{d}x + \frac{s}{\pi}\int_{\Lambda}^{\infty}\frac{\delta_L^I(x)}{x(x-s)}\,\mathrm{d}x\right\} , \tag{A.4}$$

where the integral is split into a low-energy (below the matching point) and high-energy (above the matching point) part. Since we have explicit expressions for the continued phase shifts above the continuation point Λ the second integral in Eq. (A.4) can be calculated analytically. We define the high-energy integral by

$$C(s) \equiv \exp\left\{\frac{s}{\pi}\fint_{\Lambda}^{\infty}\frac{\delta_L^I(x)}{x(x-s)}\,\mathrm{d}x\right\} , \tag{A.5}$$

where $\fint$ denotes the Cauchy principal value and use the following two different phase continuation scenarios:

1. constant phase matching $\delta(s) = c\pi$ for $s > \Lambda$ with an arbitrary integer c

$$C(s) = \exp\left\{c\fint_{\Lambda}^{\infty}\frac{s}{x(x-s)}\,\mathrm{d}x\right\} = \left(\frac{\Lambda}{\Lambda - s}\right)^c ; \tag{A.6}$$

2. asymptotic continuation to a constant value $c\pi$ at infinity, with an arbitrary integer c: $\delta(s) = c\pi - A_L^I/(B_L^I - s)$ for $s > \Lambda$, where A_L^I, B_L^I are determined for each phase individually

$$C(s) = \exp\left\{\frac{s}{\pi}\fint_{\Lambda}^{\infty}\frac{c\pi - \frac{A_L^I}{B_L^I - x}}{x(x-s)}\,\mathrm{d}x\right\} = |\Lambda|^{-\frac{A_L^I}{B_L^I\pi}+c}\,|\Lambda - B_L^I|^{-\frac{A_L^I s}{B_L^I\pi(B_L^I - s)}}\,|\Lambda - s|^{-c+\frac{A_L^I}{\pi(B_L^I - s)}} . \tag{A.7}$$

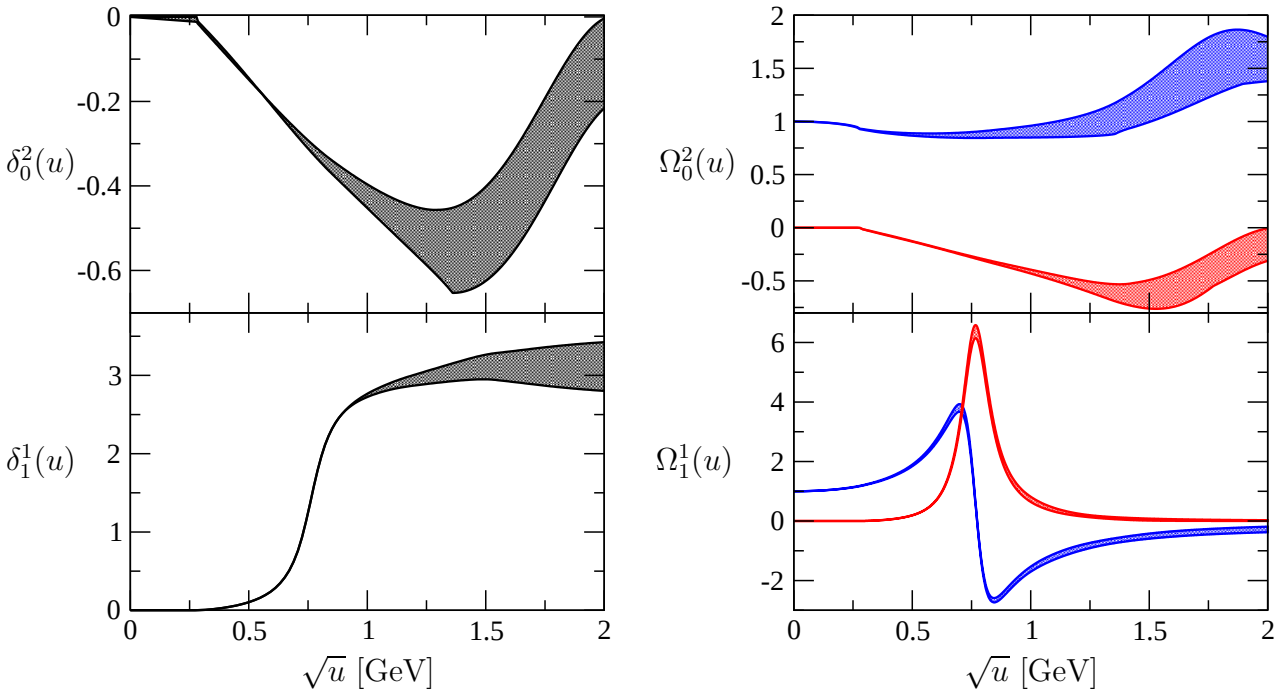

Figure A.1: *Left column:* The $\pi\pi$ phase-shift input δ_L^I from Refs. [29–32] with isospin I and angular momentum L are depicted. The errors are assumed to be $\pm 20°$ above 2 GeV. While for the S-wave we assume a generous linear rise of the error from threshold to 2 GeV for the P-wave we assume a linear rise of the error well after the $\rho(770)$ resonance. Below the $\rho(770)$ resonance the error is entirely given by the different phase-shift inputs. *Right column:* The real (blue) and imaginary (red) parts of the corresponding Omnès functions Ω_L^I with isospin I and angular momentum L are plotted. The error bands are entirely given by the phase-shift errors.

Unless the Omnès function is evaluated on the branch cut (infinitesimally above or below) the Cauchy kernel is well behaving and we have

$$\Omega_L^I(s) = \exp\left\{\frac{s}{\pi}\int_{s_{\text{th}}}^{\infty}\frac{\delta_L^I(x)}{x(x-s)}\,\mathrm{d}x\right\} = \exp\left\{\frac{s}{\pi}\int_{s_{\text{th}}}^{\Lambda}\frac{\delta_L^I(x)}{x(x-s)}\,\mathrm{d}x\right\}C(s) \tag{A.8}$$

The remaining integral can be numerically calculated without any further treatment. The variation of the phase matching point Λ is considered in the error estimation. On the branch cut we run into the Cauchy singularity and therefore treat this issue numerically as follows

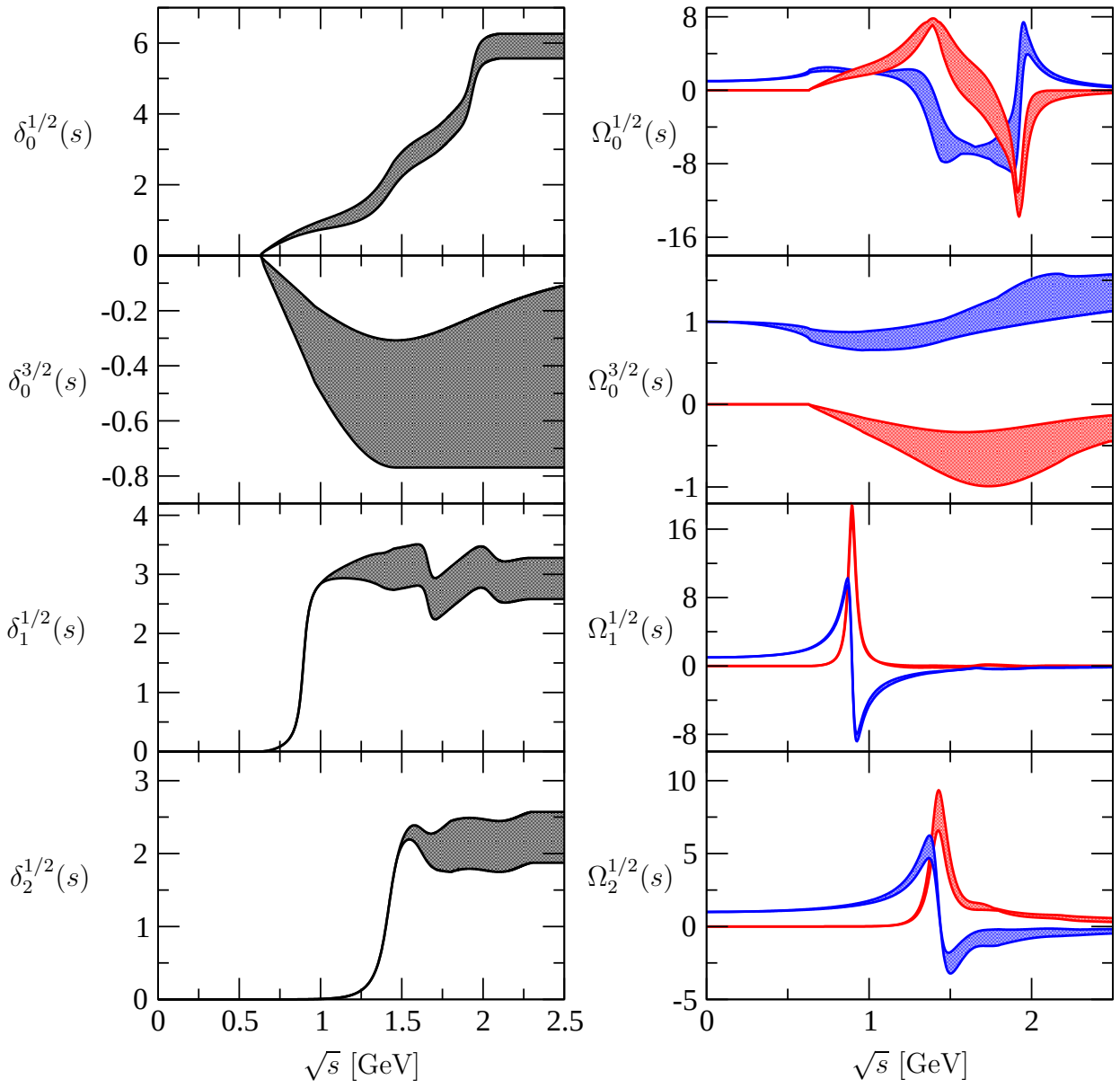

Figure A.2: *Left column:* The πK phase-shift input δ_L^I from Ref. [115] with isospin I and angular momentum L are depicted. The errors are assumed to be $\pm 20°$ above 2 GeV. For the S-waves the error is approximated by a linear rise from threshold to 2 GeV while for the P- and D-wave the linear rise starts after the prominant $K^*(892)$ and $K_2^*(1430)$ resonance respectively. *Right column:* The real (blue) and imaginary (red) parts of the corresponding Omnès functions Ω_L^I with isospin I and angular momentum L are plotted. The error bands are entirely given by the phase-shift errors.

$$\begin{aligned}\Omega_L^I(s\pm i\epsilon) &= \exp\left\{\frac{s}{\pi}\int_{s_{\rm th}}^{\infty}\frac{\delta_L^I(x)}{x(x-s\mp i\epsilon)}\,\mathrm{d}x\right\} = \exp\left\{\frac{s}{\pi}\fint_{s_{\rm th}}^{\Lambda}\frac{\delta_L^I(x)}{x(x-s)}\,\mathrm{d}x\pm i\delta(s)\right\}C(s)\\ &= \exp\left\{\frac{s}{\pi}\int_{s_{\rm th}}^{\Lambda}\frac{\delta_L^I(x)-\delta_L^I(s)}{x(x-s)}\,\mathrm{d}x+\frac{s}{\pi}\delta_L^I(s)\fint_{s_{\rm th}}^{\Lambda}\frac{1}{x(x-s)}\,\mathrm{d}x\pm i\delta(s)\right\}C(s)\\ &= \left|\frac{s_{\rm th}(s-\Lambda)}{\Lambda(s-s_{\rm th})}\right|^{\delta(s)/\pi}\exp\left\{\frac{s}{\pi}\fint_{s_{\rm th}}^{\Lambda}\frac{\delta_L^I(x)-\delta_L^I(s)}{x(x-s)}\,\mathrm{d}x\pm i\delta(s)\right\}C(s)\ .\end{aligned}\tag{A.9}$$

The integrand of the remaining integral is finite at the Cauchy singularity and can be evaluated numerically. The phase shifts are taken from Roy equation analyses of $\pi\pi$ scattering by the Bern [29–31] and the Madrid–Kraków [32] groups, as well as from the Roy–Steiner analysis of πK scattering by the Orsay group [115]. The phases and the corresponding Omnès functions are depicted in Figs. A.1-A.2.

Appendix B

Helicity formalism

We follow the agenda given in Section 2.2 and construct the orthonormal helicity basis with definite total angular momentum and z-component out of the plane wave helicity states. With the addition theorem for Wigner D-matrices we obtain, following Ref. [125]

$$\sum_{\mathcal{R}} D^{J\,*}_{L'M'}(\mathcal{R})\mathcal{R}|p;J,M;\lambda_1,\lambda_2\rangle = \sum_{\mathcal{R},L} D^{J\,*}_{L'M'}(\mathcal{R})D^{J'}_{LM}(\mathcal{R})|p;J,L;\lambda_1,\lambda_2\rangle$$
$$= \sum_{L} \frac{2}{2J+1}\delta_{JJ'}\delta_{MM'}\delta_{LL'}|p;J,L;\lambda_1,\lambda_2\rangle = \delta_{JJ'}\delta_{MM'}\frac{2}{2J+1}|p;J,L';\lambda_1,\lambda_2\rangle \ , \tag{B.1}$$

where $\mathcal{R}$ denotes an arbitrary rotation operator acting on the helicity state $|p;J,M;\lambda_1,\lambda_2\rangle$. We can therefore construct an orthonormal basis with definite total angular momentum J and z-component M from the plane waves $\psi_{p,\lambda_1,\lambda_2}$ via

$$|p;J,M;\lambda_1,\lambda_2\rangle = \frac{1}{2\pi}\left(\frac{2J+1}{4\pi}\right)^{\frac{1}{2}}\int D^{J}_{M\lambda}(\alpha,\beta,\gamma)^{\dagger}R_{\phi\Theta-\phi}\psi_{p,\lambda_1,\lambda_2}\mathrm{d}\omega$$
$$= \frac{1}{2\pi}\left(\frac{2J+1}{4\pi}\right)^{\frac{1}{2}}\int D^{J}_{M\lambda}(\alpha,\beta,\gamma)^{\dagger}|p,\Theta,\phi;\lambda_1,\lambda_2\rangle\mathrm{d}\omega \ , \tag{B.2}$$

with

$$\int \mathrm{d}\omega \equiv \int_0^{2\pi}\mathrm{d}\alpha\int_0^{\pi}\sin(\beta)\,\mathrm{d}\beta\int_0^{2\pi}\mathrm{d}\gamma \ . \tag{B.3}$$

We obtain for the transformation matrix between the two basis

$$\langle\Theta,\phi;\lambda_1',\lambda_2'|J,M;\lambda_1,\lambda_2\rangle = \delta_{\lambda_1\lambda_1'}\delta_{\lambda_2\lambda_2'}\left(\frac{2J+1}{4\pi}\right)^{\frac{1}{2}}D^{J\dagger}_{M\lambda}(\phi,\Theta,-\phi) \ . \tag{B.4}$$

In the case of $\Theta = 0$ we have

$$\langle J,M\lambda_a,\lambda_b|0,\phi,\lambda_a,\lambda_b\rangle = \left(\frac{2J+1}{4\pi}\right)^{\frac{1}{2}}D^{J}_{M\lambda}(\phi,0,-\phi) = \left(\frac{2J+1}{4\pi}\right)^{\frac{1}{2}}\delta_{M\lambda} \ . \tag{B.5}$$

Thus the basis transformed S-matrix elements read

$$\begin{aligned}
&\langle\Theta,\phi,\lambda_c,\lambda_d|S(s)|0,0,\lambda_a,\lambda_b\rangle \\
&= \sum_{JM}\langle\Theta,\phi,\lambda_c,\lambda_d|J,M,\lambda_c,\lambda_d\rangle\langle J,M,\lambda_c,\lambda_d|S(s)|J',M',\lambda_a,\lambda_b\rangle\langle J',M',\lambda_a,\lambda_b|0,0,\lambda_a,\lambda_b\rangle \\
&= \frac{1}{4\pi}\sum_{J,J'}\sqrt{2J+1}D^{\dagger}_{M\mu}(\phi,\theta,-\phi)\langle J,M,\lambda_c,\lambda_d|S(s)|J',M',\lambda_a,\lambda_b\rangle\sqrt{2J'+1}\delta_{M'\lambda} \\
&= \frac{1}{4\pi}\sum_{J}(2J+1)\langle\lambda_c,\lambda_d|S^J(s)|\lambda_a,\lambda_b\rangle D^{J\dagger}_{\lambda\mu}(\phi,\theta,-\phi)\ , \qquad \text{(B.6)}
\end{aligned}$$

where $\lambda=\lambda_a-\lambda_b$, $\mu=\lambda_c-\lambda_d$, and $S^J(s)$ denotes the S-matrix restricted to the subspace J where we used in addition the Wigner–Eckart theorem. From the Eq. (B.6) we infer the partial-wave decomposition for the decay amplitude

$$\mathcal{M}(s,\Theta_s)=\sum_J f_J(s)D^{J\dagger}_{\lambda\mu}(\phi,\theta,-\phi)\ , \qquad \text{(B.7)}$$

with $f_J(s)$ the partial wave of angular momentum J. Inserting these results into the cross section

$$\mathrm{d}\sigma(s,\Omega)=\frac{4\pi^2}{s}|\langle\Theta,\phi,\lambda_c,\lambda_d|T(s)|0,0,\lambda_a,\lambda_b\rangle|^2\mathrm{d}\Omega\ , \qquad \text{(B.8)}$$

we obtain

$$\sigma(s)=\int|f_{\lambda_c\lambda_d;\lambda_a\lambda_b}(s,\varphi,\Theta)|^2\,\mathrm{d}\Omega\ , \qquad \text{(B.9)}$$

with

$$f_{\lambda_c,\lambda_d;\lambda_a,\lambda_b}(s,\varphi,\Theta)=\frac{1}{\sqrt{s}}\sum_J\left(J+\frac{1}{2}\right)\langle\lambda_c,\lambda_d|T^J(s)|\lambda_a,\lambda_b\rangle e^{i(\lambda-\mu)\varphi}d^J_{\lambda\mu}(\Theta)\ . \qquad \text{(B.10)}$$

In the case of $V\pi\to\pi\pi$ we have $\lambda=\pm1,0$ and $\mu=0$. The zero helicity component does not contribute due to the vanishing phase space factor. It suffices to consider only the case $\lambda=1$, see Appendix V of Ref. [126]

$$d^J_{10}(\Theta)=-\frac{1}{\sqrt{J(J+1)}}\sin\Theta\,P'_J(\cos\Theta)\ . \qquad \text{(B.11)}$$

We obtain for the cross section

$$\sigma_{V\pi\to\pi\pi}(s)=\int\left|\frac{1}{2\sqrt{s}}\sum_J\frac{2J+1}{\sqrt{J(J+1)}}\langle0,0|T^J(s)|1,0\rangle P'_J(\cos\Theta)\right|^2\sin^2\Theta\,\mathrm{d}\Omega\ . \qquad \text{(B.12)}$$

The partial-wave expansion of the scalar amplitude $\mathcal{F}(s,t,u)$ can now be read off by comparing Eq. (B.12) to

$$\sigma = \frac{1}{64\pi^2 s}\frac{|\vec{k}_1'|_{out}}{|\vec{k}_1|_{in}}\int |\mathcal{M}(s,t,u)|^2 \,\mathrm{d}\Omega \;, \tag{B.13}$$

with

$$|\vec{k}_1'|_{out} = \frac{\lambda^{\frac{1}{2}}(s,m_1'^2,m_2'^2)}{2\sqrt{s}} \;, \quad |\vec{k}_1|_{in} = \frac{\lambda^{\frac{1}{2}}(s,m_1^2,m_2^2)}{2\sqrt{s}} \;.$$

We obtain for the cross section with $m_1' = m_2' = m_2 = M_\pi$ and $m_1 = M_V$

$$\sigma = \frac{1}{64\pi^2 s}\frac{\lambda^{\frac{1}{2}}(s,M_\pi^2,M_\pi^2)}{\lambda^{\frac{1}{2}}(s,M_V^2,M_\pi^2)}\int |\mathcal{M}(s,t,u)|^2 \,\mathrm{d}\Omega \;. \tag{B.14}$$

As we have three polarization states we have to divide by a factor 3 to obtain the unpolarized cross section. With $|\mathcal{M}(s,t,u)|^2$ from Eq. (2.7) we find

$$\sigma(s) = \frac{1}{3072\pi^2 s}(s-4m_\pi^2)^{\frac{3}{2}}\int |F(s,t,u)|^2 \sin\Theta^2 \mathrm{d}\Omega \;. \tag{B.15}$$

Comparing the Θ-dependent pieces of Eq. (B.12) and Eq. (B.15) we arrive at

$$\mathcal{F}(s,t,u) = \sum_J f_J(s) P_J'(\cos\Theta) \;. \tag{B.16}$$

Appendix C

Supplementary notes on $D^+ \to K\pi\pi^+$

In this appendix we specify the phase convention of charge conjugation for the pion and kaon states and complete the reconstruction of the $D^+ \to K\pi\pi^+$ decay amplitudes into single-variable amplitudes. We show the explicit construction of the inhomogeneities, the derivation of the invariance group, and the fit results of the combined analysis of CLEO and FOCUS data.

C.1 Phase conventions for isospin and charge conjugation

The phase convention we employ for the isospin and charge conjugation operator follows Ref. [127]. We adopt the Condon–Shortley phase convention from here on. Let U_C be the charge conjugation operator and I_3 the third component of the isospin operator. By definition we have

$$U_C I_3 U_C^{-1} = -I_3 \ . \tag{C.1}$$

To determine how the isospin eigenstates behave under charge conjugation we investigate the impact of U_C on the ladders operators $I_\pm$. The ladder operators of the charge conjugate particle multiplet are given by

$$I_\pm^C \equiv U_C I_\pm U_C^{-1} \ .$$

They must satisfy

$$\left[I_3^C, I_\pm^C\right] = \pm I_\pm^C \ , \tag{C.2}$$

with $I_3^C = U_C I_3 U_C^{-1}$. Combining Eq. (C.1) and Eq. (C.2) we obtain

$$\left[I_3, I_\pm^C\right] = \mp I_\pm^C \ . \tag{C.3}$$

Thus up to a phase we can identify $I_\pm^C$ with $I_\mp$ and choose the standard convention

$$I_\pm^C \equiv U_C I_\pm U_C^{-1} = -I_\mp \ . \tag{C.4}$$

We now define the kaon isospin wave functions by

$$|K^+\rangle = \left|\frac{1}{2},\frac{1}{2}\right\rangle, \quad |K^-\rangle = \left|\frac{1}{2},-\frac{1}{2}\right\rangle, \quad |\bar{K}^0\rangle = \left|\frac{1}{2},\frac{1}{2}\right\rangle, \quad |K^0\rangle = \left|\frac{1}{2},-\frac{1}{2}\right\rangle \ ,$$

where $|I, I_z\rangle$ denotes the eigenstate with isospin I and z-component I_z. Thus we obtain with Eq. (C.4)

$$I_+ U_C |K^+\rangle = -U_C I_- |K^+\rangle = -U_C |K^0\rangle \ . \tag{C.5}$$

Thus we can choose the charge conjugation phases in accordance with the Gell-Mann–Nishijima formula [128]

$$U_C|K^0\rangle = -|\bar{K}^0\rangle, \quad U_C|K^+\rangle = |K^-\rangle \ ,$$

With the pion isospin triplet defined as follows

$$|\pi^+\rangle = |1,1\rangle, \quad |\pi^0\rangle = |1,0\rangle, \quad |\pi^-\rangle = |1,-1\rangle,$$

we again deduce the phases of the pion triplet under charge conjugation

$$\begin{aligned} I_+ U_C|\pi^+\rangle &= -U_C I_-|\pi^+\rangle = -U_C|\pi^0\rangle \ , \\ I_- U_C|\pi^-\rangle &= -U_C I + -|\pi^-\rangle = -U_C|\pi^0\rangle \ . \end{aligned}$$

With the physical necessity $U_C|\pi^0\rangle = |\pi^0\rangle$ we have

$$U_C|\pi^+\rangle = -|\pi^-\rangle \ , \quad U_C|\pi^-\rangle = -|\pi^+\rangle \ .$$

C.2 Reconstruction theorem

We resume the study of the reconstruction theorem and discuss the inclusion of the πK D-wave as well as the reconstruction of the $D^+ \to \bar{K}^0\pi^0\pi^+$ decay amplitude.

C.2.1 Extension to the πK D-wave

In the following we discuss the inclusion of πK D-wave in the reconstruction theorem. We start out with the fixed-u dispersion relation of Eq. (4.8) extended to $L \leq 2$

$$\mathcal{M}_{-++}(s,t,u_0) = p_{n-1}(s,t,u_0) + \frac{t^n}{\pi}\int_{t_{\text{th}}}^{\infty} \frac{\operatorname{Im} f_0(t')}{t'^n(t'-t)}\mathrm{d}t'$$

$$+\frac{t^n}{\pi}\int_{t_{\rm th}}^{\infty}\frac{\big(t'(s'(t')-u_0)-\Delta\big)\mathrm{Im}\,f_1(t')}{\kappa_t(t')t'^n(t'-t)}\mathrm{d}t'$$
$$+\frac{t^n}{\pi}\int_{t_{\rm th}}^{\infty}\frac{\big(3\big(t'(s'(t')-u_0)-\Delta\big)^2-\kappa_t^2(t')\big)\mathrm{Im}\,f_2(t')}{\kappa_t^2(t')t'^n(t'-t)}\mathrm{d}t'+(t\leftrightarrow s)\ . \quad \text{(C.6)}$$

Following the derivation without D-wave in Section 4.3.1 we need to rewrite the dispersion integrals into general polynomial factors and a dispersion integral dependent on only one variable. We start with the additional D-wave piece

$$\frac{t^n}{\pi}\int_{t_{\rm th}}^{\infty}\frac{\big(3\big(t'(t-t'+s-u_0)-\Delta\big)^2-\kappa_t^2(t')\big)\mathrm{Im}\,f_2(t')}{\kappa_t^2(t')t'^n(t'-t)}\mathrm{d}t'$$
$$=\frac{t^n}{\pi}\int_{t_{\rm th}}^{\infty}\frac{3\big(t'^2(t-t')^2+t'^2(t-t')(s-u_0)+t'^2(s-u_0)^2\big)\mathrm{Im}\,f_2(t')}{\kappa_t^2(t')t'^n(t'-t)}\mathrm{d}t'$$
$$+\frac{t^n}{\pi}\int_{t_{\rm th}}^{\infty}\frac{\big(6(-t'(t-t')\Delta-t'(s-u_0)\Delta)+3\Delta^2-\kappa_t^2(t')\big)\mathrm{Im}\,f_2(t')}{\kappa_t^2(t')t'^n(t'-t)}\mathrm{d}t'\ . \quad \text{(C.7)}$$

In the following we separate the t-independent dispersive integrals which are absorbed in the overall subtraction polynomial. Furthermore we aim to retain a D-wave polynomial factor in front of the dispersion integral. For further convenience we define $\kappa_t^2(t)\equiv\sum_{i=0}^4 a_i t'^i$ and obtain

$$=\frac{t^n}{\pi}\int_{t_{\rm th}}^{\infty}\frac{3\big(t'^2(t-t')^2+t'^2(t-t')(s-u_0)+t'^2(s-u_0)^2\big)\mathrm{Im}\,f_2(t')}{\kappa_t^2(t')t'^n(t'-t)}\mathrm{d}t'$$
$$+\frac{t^n}{\pi}\int_{t_{\rm th}}^{\infty}\frac{\big(6(-t'(t-t')\Delta-t'(s-u_0)\Delta)+3\Delta^2-\kappa_t^2(t')\big)\mathrm{Im}\,f_2(t')}{\kappa_t^2(t')t'^n(t'-t)}\mathrm{d}t'$$
$$=\underbrace{-\frac{t^n}{\pi}\int_{t_{\rm th}}^{\infty}\frac{\big(3(t-t')+(s-u_0)\big)\mathrm{Im}\,f_2(t')}{\kappa_t^2(t')t'^{n-2}}\mathrm{d}t'}_{\mathcal{O}(t^{n+1})+\mathcal{O}(t^n(s-u_0))}$$
$$+3t^2(s-u_0)^2\frac{t^{n-2}}{\pi}\int_{t_{\rm th}}^{\infty}\frac{\mathrm{Im}\,f_2(t')}{\kappa_t^2(t')t'^{n-2}(t'-t)}\mathrm{d}t'-\underbrace{6\Delta\frac{t^n}{\pi}\int_{t_{\rm th}}^{\infty}\frac{\mathrm{Im}\,f_2(t')}{\kappa_t^2(t')t'^{n-1}}\mathrm{d}t'}_{\mathcal{O}(t^n)}$$
$$-6t(s-u_0)\Delta\frac{t^{n-2}}{\pi}\int_{t_{\rm th}}^{\infty}\frac{\mathrm{Im}\,f_2(t')}{\kappa_t^2(t')t'^{n-2}}\bigg(\frac{1}{t'-t}-\underbrace{\frac{1}{t'}}_{\mathcal{O}(t^{n-1}(s-u_0))}\bigg)\mathrm{d}t'$$
$$+3\Delta^2\frac{t^{n-2}}{\pi}\int_{t_{\rm th}}^{\infty}\frac{\mathrm{Im}\,f_2(t')}{\kappa_t^2(t')t'^{n-2}}\bigg(\frac{1}{t'-t}-\frac{1}{t'}\bigg)\mathrm{d}t'-\underbrace{3\Delta^2\frac{t^{n-1}}{\pi}\int_{t_{\rm th}}^{\infty}\frac{\mathrm{Im}\,f_2(t')}{\kappa_t^2(t')t'^n}\mathrm{d}t'}_{\mathcal{O}(t^{n-1})}$$

$$
\begin{aligned}
&- \frac{t^n}{\pi}\int_{t_{\rm th}}^{\infty} \frac{\left(\sum_{i=0}^{4} a_i t'^i\right)\mathrm{Im}\, f_2(t')}{\kappa_t^2(t')t'^n(t'-t)}\mathrm{d}t' \\
&= p_{n+1}(s,t,u_0) + 3\big(t(s-u_0)-\Delta\big)^2\frac{t^{n-2}}{\pi}\int_{t_{\rm th}}^{\infty}\frac{\mathrm{Im}\, f_2(t')}{\kappa_t^2(t')t'^{n-2}(t'-t)}\mathrm{d}t' \\
&- \left(\sum_{i=0}^{4} a_i t'^i\right)\frac{t^{n-2}}{\pi}\int_{t_{\rm th}}^{\infty}\frac{\mathrm{Im}\, f_2(t')}{\kappa_t^2(t')t'^{n-2}(t'-t)}\mathrm{d}t' \ ,
\end{aligned}
\tag{C.8}
$$

where in the last term we pulled out the a_i factors and subtracted each term accordingly. The additional polynomial terms are absorbed in $p_{n+1}(s,t,u_0)$. We thus get

$$
\begin{aligned}
&\frac{t^n}{\pi}\int_{t_{\rm th}}^{\infty}\frac{\big(3\big(t'(t-t'+s-u_0)-\Delta\big)^2-\kappa_t^2(t')\big)\mathrm{Im}\, f_2(t')}{\kappa_t^2(t')t'^n(t'-t)}\mathrm{d}t' \\
&= p_{n+1}(s,t,u_0) + \left[3\big(t(s-u_0)-\Delta\big)^2-\kappa_t^2(t)\right]\frac{t^{n-2}}{\pi}\int_{t_{\rm th}}^{\infty}\frac{\mathrm{Im}\, f_2(t')}{\kappa_t^2(t')t'^{n-2}(t'-t)}\mathrm{d}t' \ .
\end{aligned}
\tag{C.9}
$$

The S- and P-wave decomposition has already been performed in Section 4.3.1 and we therefore obtain

$$
\begin{aligned}
\mathcal{M}_{-++}(s,t,u_0) = p_{n+1}(s,t,u_0) &+ \frac{t^{n+1}}{\pi}\int_{t_{\rm th}}^{\infty}\frac{\mathrm{Im}\, f_0(t')}{t'^{n+1}(t'-t)}\mathrm{d}t' \\
&+ \big(t(s-u_0)-\Delta\big)\frac{t^{n-1}}{\pi}\int_{t_{\rm th}}^{\infty}\frac{\mathrm{Im}\, f_1(t')}{\kappa_t(t')t'^{n-1}(t'-t)}\mathrm{d}t' \\
&\left[3\big(t(s-u_0)-\Delta\big)^2-\kappa_t^2(t)\right]\frac{t^{n-2}}{\pi}\int_{t_{\rm th}}^{\infty}\frac{\mathrm{Im}\, f_2(t')}{\kappa_t^2(t')t'^{n-2}(t'-t)}\mathrm{d}t' + (t\leftrightarrow s) \ ,
\end{aligned}
\tag{C.10}
$$

Similarly the fixed-t dispersion relations reads

$$
\begin{aligned}
\mathcal{M}_{-++}(s,t_0,u) = p_{n+1}(s,t_0,u) &+ \frac{u^n}{\pi}\int_{u_{\rm th}}^{\infty}\frac{\mathrm{Im}\, h_0(u')}{u'^n(u'-u)}\mathrm{d}u' \\
&+ \frac{s^{n+2}}{\pi}\int_{s_{\rm th}}^{\infty}\frac{\mathrm{Im}\, f_0(s')}{s'^{n+2}(s'-s)}\mathrm{d}s' \\
&+ \big(s(t_0-u)-\Delta\big)\frac{s^{n-1}}{\pi}\int_{s_{\rm th}}^{\infty}\frac{\mathrm{Im}\, f_1(s')}{\kappa_s(s')s'^{n-1}(s'-s)}\mathrm{d}t' \\
&+ \left[3\big(s(t_0-u)-\Delta\big)^2-\kappa_s^2(s)\right]\frac{s^{n-2}}{\pi}\int_{s_{\rm th}}^{\infty}\frac{\mathrm{Im}\, f_2(s')}{\kappa_s^2(s')s'^{n-2}(s'-s)}\mathrm{d}s' \ .
\end{aligned}
\tag{C.11}
$$

Fixed-s and fixed-t dispersion relation are symmetric since $\mathcal{M}_{-++}(s,t,u) = \mathcal{M}_{-++}(t,s,u)$. Symmetrization of fixed-u, -t and -s dispersion relations yields

$$\begin{aligned}\mathcal{M}_{-++}(s,t,u) = p_{n+1}(s,t,u) &+ \frac{u^n}{\pi}\int_{u_{\text{th}}}^{\infty}\frac{\operatorname{Im} h_0(u')}{u'^{n+2}(u'-u)}\mathrm{d}u' \\ &+ \left\{\frac{s^{n+1}}{\pi}\int_{s_{\text{th}}}^{\infty}\frac{\operatorname{Im} f_0(s')}{s'^{n+1}(s'-s)}\mathrm{d}s'\right. \\ &+ \big(s(t-u)-\Delta\big)\frac{s^{n-1}}{\pi}\int_{s_{\text{th}}}^{\infty}\frac{\operatorname{Im} f_1(s')}{\kappa_s(s')s'^{n-1}(s'-s)}\mathrm{d}s' \\ &+ \left.\left[3\big(s(t-u)-\Delta\big)^2-\kappa_s^2(s)\right]\frac{s^{n-2}}{\pi}\int_{s_{\text{th}}}^{\infty}\frac{\operatorname{Im} f_2(s')}{\kappa_s^2(s')s'^{n-2}(s'-s)}\mathrm{d}s' + (t\leftrightarrow s)\right\}, \end{aligned} \tag{C.12}$$

and with the isospin decomposition given in Eq. (4.16) and the phase convention given in Appendix C.1

$$\begin{aligned}\mathcal{M}_{-++}(s,t,u) = p_{n+1}(s,t,u) &+ \frac{u^n}{\pi}\int_{u_{\text{th}}}^{\infty}\frac{\operatorname{Im} h_0^2(u')}{u'^{n+2}(u'-u)}\mathrm{d}u' \\ &+ \left\{\frac{1}{\sqrt{3}}\frac{s^{n+1}}{\pi}\int_{s_{\text{th}}}^{\infty}\frac{\operatorname{Im} f_0^{1/2}(s')}{s'^{n+1}(s'-s)}\mathrm{d}s' - \sqrt{\frac{2}{15}}\frac{s^{n+1}}{\pi}\int_{s_{\text{th}}}^{\infty}\frac{\operatorname{Im} f_0^{3/2}(s')}{s'^{n+1}(s'-s)}\mathrm{d}s'\right. \\ &+ \frac{1}{\sqrt{3}}\big(s(t-u)-\Delta\big)\frac{s^{n-1}}{\pi}\int_{s_{\text{th}}}^{\infty}\frac{\operatorname{Im} f_1^{1/2}(s')}{\kappa_s(s')s'^{n-1}(s'-s)}\mathrm{d}s' \\ &- \sqrt{\frac{2}{15}}\big(s(t-u)-\Delta\big)\frac{s^{n-1}}{\pi}\int_{s_{\text{th}}}^{\infty}\frac{\operatorname{Im} f_1^{3/2}(s')}{\kappa_s(s')s'^{n-1}(s'-s)}\mathrm{d}s' \\ &- \sqrt{\frac{2}{15}}\left[3\big(s(t-u)-\Delta\big)^2-\kappa_s^2(s)\right]\frac{s^{n-2}}{\pi}\int_{s_{\text{th}}}^{\infty}\frac{\operatorname{Im} f_2^{3/2}(s')}{\kappa_s^2(s')s'^{n-2}(s'-s)}\mathrm{d}s' \\ &+ \frac{1}{\sqrt{3}}\left[3\big(s(t-u)-\Delta\big)^2-\kappa_s^2(s)\right]\frac{s^{n-2}}{\pi}\int_{s_{\text{th}}}^{\infty}\frac{\operatorname{Im} f_2^{1/2}(s')}{\kappa_s^2(s')s'^{n-2}(s'-s)}\mathrm{d}s' \\ &+ \left.(t\leftrightarrow s)\right\}. \end{aligned} \tag{C.13}$$

Generally, in the s- and t-channel the order of subtraction for the next higher angular momentum single-variable amplitudes reduces by 1 while the order of subtraction for the u-channel single-variable amplitudes stays the same. This originates from the cosines of the scattering angles given in Eq. (4.2). In our particular case the πK S-waves is oversubtracted and therefore an exception of the above rule.

To obtain a non-zero D-wave the number of subtractions has to be at least $n = 2$, see Eq. (C.13). The most general order 3 polynomial with explicit $s \leftrightarrow t$ symmetry reads

$$\begin{aligned} p_3(s,t,u) =& a_0 + a_1(s+t) + a_2(s^2+t^2) + a_3(s^3+t^3) + b_1\big(s(t-u) + t(s-u)\big) \\ &+ b_2\big(s^2(t-u) + t^2(s-u)\big) \ . \end{aligned} \tag{C.14}$$

The a_i can be interpreted as πK S-wave subtraction constants if we subtract the S-wave one time further. Similarly b_1 and b_2 can be seen as parts of the P-wave subtraction constants (tuned by a_i) of order zero and one respectively. But again we have to subtract one time further. Finally we obtain

$$\begin{aligned} \mathcal{M}_{-++}(s,t,u) = \mathcal{F}_0^2(u) + \Bigg\{ & \frac{1}{\sqrt{3}}\mathcal{F}_0^{1/2}(s) - \sqrt{\frac{2}{15}}\mathcal{F}_0^{3/2}(s) \\ & + \big[s(t-u) - \Delta\big]\left(\frac{1}{\sqrt{3}}\mathcal{F}_1^{1/2}(s) - \sqrt{\frac{2}{15}}\mathcal{F}_1^{3/2}(s)\right) \\ & + \frac{1}{2}\big[3\big(s(t-u)-\Delta\big)^2 - \kappa_s^2(s)\big]\left(\frac{1}{\sqrt{3}}\mathcal{F}_2^{1/2}(s) - \sqrt{\frac{2}{15}}\mathcal{F}_2^{3/2}(s)\right) + (s \leftrightarrow t)\Bigg\} , \end{aligned} \tag{C.15}$$

with the single-variable amplitudes given by

$$\begin{aligned} \mathcal{F}_0^0(u) &\equiv \frac{u^2}{\pi}\int_{u_{th}}^{\infty} \frac{\operatorname{Im} h_0^0(u')}{u'^2(u'-u)}\mathrm{d}u' \ , \\ \mathcal{F}_0^{1/2}(s) &\equiv d_0 + d_1 s + d_2 s^2 + d_3 s^3 + \frac{s^4}{\pi}\int_{s_{\rm th}}^{\infty} \frac{\operatorname{Im}{}^{1/2} f_0(s')}{s'^4(s'-s)}\mathrm{d}s' \ , \\ \mathcal{F}_0^{3/2}(s) &\equiv \frac{s^4}{\pi}\int_{s_{\rm th}}^{\infty} \frac{\operatorname{Im} f_0^{3/2}(s')}{s'^4(s'-s)}\mathrm{d}s' \ , \\ \mathcal{F}_1^{1/2}(s) &\equiv d_4 + d_5 s + \frac{s^2}{\pi}\int_{s_{\rm th}}^{\infty} \frac{\operatorname{Im} f_1^{1/2}(s')}{\kappa_s(s')s'^2(s'-s)}\mathrm{d}s' \ , \\ \mathcal{F}_1^{3/2}(s) &\equiv \frac{s^2}{\pi}\int_{s_{\rm th}}^{\infty} \frac{\operatorname{Im} f_1^{3/2}(s')}{\kappa_s(s')s'^2(s'-s)}\mathrm{d}s' \ , \\ \mathcal{F}_2^{1/2}(s) &\equiv \frac{1}{\pi}\int_{s_{\rm th}}^{\infty} \frac{\operatorname{Im} f_2^{1/2}(s')}{\kappa_s^2(s')(s'-s)}\mathrm{d}s' \ , \\ \mathcal{F}_2^{3/2}(s) &\equiv \frac{1}{\pi}\int_{s_{\rm th}}^{\infty} \frac{\operatorname{Im} f_2^{3/2}(s')}{\kappa_s^2(s')(s'-s)}\mathrm{d}s' \ . \end{aligned} \tag{C.16}$$

As it turns out, there is a big issue with this decomposition concerning the convergence of the integrals. Due to the characteristic D-wave prefactors of the $\mathcal{F}_2^I$ amplitudes the D-waves violate the assumed high-energy behavior, motivated by the Froissart bound. This

has a serious impact on the whole coupled integral system. Since the D-wave contributes also to the imaginary parts of all other single-variable amplitudes via crossed-channel effects the dispersion integrals of these can become divergent. Thus we need to introduce further subtractions to ensure the convergence of the dispersive integrals. However these single-variable amplitudes equally violate the assumed high-energy behavior and we obtain additional unknown subtraction constants, which have to fitted to experimental data or determined from theoretical considerations.

C.2.2 $D^+ \to \bar{K}^0\pi^0\pi^+$ reconstruction theorem

We start out with the fixed-u dispersion relation

$$\begin{aligned}\mathcal{M}_{\bar{0}0+}(s,t,u_0) =& p_{n-1}(s,t,u_0) + \frac{t^n}{\pi}\int_{t_{\text{th}}}^{\infty}\frac{\operatorname{Im}\mathcal{M}_{\bar{0}0+}(s'(t'),t',u_0)}{t'^n(t'-t)}\mathrm{d}t' \\ &+ \frac{s^n}{\pi}\int_{s_{\text{th}}}^{\infty}\frac{\operatorname{Im}\mathcal{M}_{\bar{0}0+}(s',t'(s'),u_0)}{s'^n(s'-s)}\mathrm{d}s' \ ,\end{aligned} \tag{C.17}$$

where $p_{n-1}(s,t,u)$ denotes a polynomial of order $n-1$ in s, t and u_0. The following partial-wave decomposition of the s- and t-channel amplitudes read

$$\mathcal{M}_{\bar{0}0+}(s(t),t,u_0) = \sum_L f_L(t)P_L(z_t), \qquad \mathcal{M}_{\bar{0}0+}(s,t(s),u_0) = \sum_L g_L(s)P_L(z_s) \ . \tag{C.18}$$

Inserting the partial-wave decomposition Eq. (C.18) into Eq. (C.17) we find

$$\begin{aligned}\mathcal{M}_{\bar{0}0+}(s,t,u_0) = p_{n-1}(s,t,u_0) &+ \frac{t^n}{\pi}\int_{t_{\text{th}}}^{\infty}\frac{\operatorname{Im}f_0(t')}{t'^n(t'-t)}\mathrm{d}t' + \frac{s^n}{\pi}\int_{s_{\text{th}}}^{\infty}\frac{\operatorname{Im}g_0(s')}{s'^n(s'-s)}\mathrm{d}s' \\ &+ \frac{t^n}{\pi}\int_{t_{\text{th}}}^{\infty}\frac{\big(t'(s'(t')-u_0)-\Delta\big)\operatorname{Im}f_1(t')}{\kappa_t(t')t'^n(t'-t)}\mathrm{d}t' \\ &+ \frac{s^n}{\pi}\int_{s_{\text{th}}}^{\infty}\frac{\big(s'(t'(s')-u_0)-\Delta\big)\operatorname{Im}g_1(t')}{\kappa_s(s')s'^n(s'-s)}\mathrm{d}s' \ .\end{aligned} \tag{C.19}$$

Analogously to what has been done in Section 4.3.1 we obtain

$$\begin{aligned}\mathcal{M}_{\bar{0}0+}(s,t,u_0) = p_n(s,t,u_0) &+ \frac{t^{n+1}}{\pi}\int_{t_{\text{th}}}^{\infty}\frac{\operatorname{Im}f_0(t')}{t'^{n+1}(t'-t)}\mathrm{d}t' + \frac{s^{n+1}}{\pi}\int_{s_{\text{th}}}^{\infty}\frac{\operatorname{Im}g_0(s')}{s'^{n+1}(s'-s)}\mathrm{d}s' \\ &+ \big(t(s-u_0)-\Delta\big)\frac{t^{n-1}}{\pi}\int_{t_{\text{th}}}^{\infty}\frac{\operatorname{Im}f_1(t')}{\kappa_t(t')t'^{n-1}(t'-t)}\mathrm{d}t' \\ &+ \big(s(t-u_0)-\Delta\big)\frac{s^{n-1}}{\pi}\int_{s_{\text{th}}}^{\infty}\frac{\operatorname{Im}g_1(s')}{\kappa_s(s')s'^{n-1}(s'-s)}\mathrm{d}s'\end{aligned} \tag{C.20}$$

Similarly for fixed-t dispersion relations we obtain

$$\begin{aligned}\mathcal{M}_{\bar{0}0+}(s,t,u_0) =& p_{n-1}(s,t_0,u) + \frac{u^n}{\pi}\int_{u_{\rm th}}^{\infty}\frac{\operatorname{Im}\mathcal{M}_{-++}(s'(u'),t_0,u')}{u'^n(u'-u)}\mathrm{d}t' \\ &+ \frac{s^n}{\pi}\int_{s_{\rm th}}^{\infty}\frac{\operatorname{Im}\mathcal{M}_{-++}(s',t_0,u'(s'))}{s'^n(s'-s)}\mathrm{d}s' \ . \end{aligned} \tag{C.21}$$

With the partial-wave decompositions

$$\mathcal{M}_{\bar{0}0+}(s(u),t_0,u) = \sum_L h_L(u)P_L(z_u), \qquad \mathcal{M}_{\bar{0}0+}(s,t_0,u(s)) = \sum_L g_L(s)P_L(z_s) \ , \tag{C.22}$$

we find with $t_0 - s'(t') = t_0 - s + u - u'$

$$\begin{aligned}\mathcal{M}_{\bar{0}0+}(s,t_0,u) =& \, p_n(s,t_0,u) + \frac{u^n}{\pi}\int_{u_{\rm th}}^{\infty}\frac{\operatorname{Im}h_0(u')}{u'^n(u'-u)}\mathrm{d}u' + (t_0-s)\frac{u^n}{\pi}\int_{u_{\rm th}}^{\infty}\frac{\operatorname{Im}h_1(u')}{u'^n(u'-u)}\mathrm{d}u' \\ &+ \frac{s^{n+1}}{\pi}\int_{s_{\rm th}}^{\infty}\frac{\operatorname{Im}g_0(s')}{s'^{n+1}(s'-s)}\mathrm{d}s' \\ &+ \big(s(t_0-u)-\Delta\big)\frac{s^{n-1}}{\pi}\int_{s_{\rm th}}^{\infty}\frac{\operatorname{Im}g_1(s')}{\kappa_s(s')s'^{n-1}(s'-s)}\mathrm{d}s' \ . \end{aligned} \tag{C.23}$$

The fixed-s dispersion relation is given by

$$\begin{aligned}\mathcal{M}_{\bar{0}0+}(s_0,t,u) =& \, p_n(s_0,t,u) + \frac{u^n}{\pi}\int_{u_{\rm th}}^{\infty}\frac{\operatorname{Im}h_0(u')}{u'^n(u'-u)}\mathrm{d}u' + (t-s_0)\frac{u^n}{\pi}\int_{u_{\rm th}}^{\infty}\frac{\operatorname{Im}h_1(u')}{u'^n(u'-u)}\mathrm{d}u' \\ &+ \frac{t^{n+1}}{\pi}\int_{t_{\rm th}}^{\infty}\frac{\operatorname{Im}g_0(t')}{t'^{n+1}(t'-t)}\mathrm{d}t' \\ &+ \big(t(s_0-u)-\Delta\big)\frac{t^{n-1}}{\pi}\int_{t_{\rm th}}^{\infty}\frac{\operatorname{Im}g_1(t')}{\kappa_t(t')t'^{n-1}(t'-t)}\mathrm{d}t' \ . \end{aligned} \tag{C.24}$$

Symmetrization of fixed u, t and s dispersion relations yields

$$\begin{aligned}\mathcal{M}_{\bar{0}0+}(s,t,u) =& \, p_n(s,t,u) + \frac{u^n}{\pi}\int_{u_{\rm th}}^{\infty}\frac{\operatorname{Im}h_0^2(u')}{u'^n(u'-u)}\mathrm{d}u' + (t-s)\frac{u^n}{\pi}\int_{u_{\rm th}}^{\infty}\frac{\operatorname{Im}h_1^1(u')}{u'^n(u'-u)}\mathrm{d}u' \\ &+ \frac{s^{n+1}}{\pi}\int_{s_{\rm th}}^{\infty}\frac{\operatorname{Im}g_0(s')}{s'^{n+1}(s'-s)}\mathrm{d}s' + \frac{t^{n+1}}{\pi}\int_{t_{\rm th}}^{\infty}\frac{\operatorname{Im}f_0(t')}{t'^{n+1}(t'-t)}\mathrm{d}t' \\ &+ \big(s(t-u)-\Delta\big)\frac{s^{n-1}}{\pi}\int_{s_{\rm th}}^{\infty}\frac{\operatorname{Im}f_1(s')}{\kappa_s(s')s'^{n-1}(s'-s)}\mathrm{d}s' \\ &+ \big(t(s-u)-\Delta\big)\frac{t^{n}}{\pi}\int_{t_{\rm th}}^{\infty}\frac{\operatorname{Im}f_1(t')}{\kappa_t(t')t'^{n}(t'-t)}\mathrm{d}t' \ . \end{aligned} \tag{C.25}$$

With the isospin decomposition of Eq. (4.16) and the phase conventions given in Appendix C.1 we finally obtain

$$\begin{aligned}
\mathcal{M}_{\bar{0}0+}(s,t,u) = p_n(s,t,u) &- \frac{1}{2\sqrt{2}}\frac{u^n}{\pi}\int_{u_{\text{th}}}^{\infty}\frac{\operatorname{Im} h_0^2(u')}{u'^n(u'-u)}\mathrm{d}u' \\
&+ \frac{\sqrt{3}}{2\sqrt{2}}(t-s)\frac{u^n}{\pi}\int_{u_{\text{th}}}^{\infty}\frac{\operatorname{Im} h_1^1(u')}{u'^n(u'-u)}\mathrm{d}u' + \sqrt{\frac{3}{5}}\frac{s^{n+1}}{\pi}\int_{s_{\text{th}}}^{\infty}\frac{\operatorname{Im} f_0^{3/2}(s')}{s'^{n+1}(s'-s)}\mathrm{d}s' \\
&+ \sqrt{\frac{3}{5}}\big(s(t-u)-\Delta\big)\frac{s^{n-1}}{\pi}\int_{s_{\text{th}}}^{\infty}\frac{\operatorname{Im} f_1^{3/2}(s')}{\kappa_s(s')s'^{n-1}(s'-s)}\mathrm{d}s' \\
&\frac{1}{\sqrt{6}} + \frac{t^{n+1}}{\pi}\int_{t_{\text{th}}}^{\infty}\frac{\operatorname{Im} f_0^{1/2}(t')}{t'^{n+1}(t'-t)}\mathrm{d}t' + \frac{2}{\sqrt{15}}\frac{t^{n+1}}{\pi}\int_{t_{\text{th}}}^{\infty}\frac{\operatorname{Im} f_0^{3/2}(t')}{t'^{n+1}(t'-t)}\mathrm{d}t' \\
&+ \frac{1}{\sqrt{6}}\big(t(s-u)-\Delta\big)\frac{t^n}{\pi}\int_{t_{\text{th}}}^{\infty}\frac{\operatorname{Im} f_1^{1/2}(t')}{\kappa_t(t')t'^n(t'-t)}\mathrm{d}t' \\
&+ \frac{2}{\sqrt{15}}\big(t(s-u)-\Delta\big)\frac{t^n}{\pi}\int_{t_{\text{th}}}^{\infty}\frac{\operatorname{Im} f_1^{3/2}(t')}{\kappa_t(t')t'^n(t'-t)}\mathrm{d}t' \ , \qquad \text{(C.26)}
\end{aligned}$$

where the s- and t-channel partial-wave amplitudes have been re-expressed by

$$g_L(s) \equiv \sqrt{\frac{3}{5}}f_L^{3/2}(s) \ , \quad f_L(t) \equiv \frac{1}{\sqrt{6}}f_L^{1/2}(t) + \frac{2}{\sqrt{15}}f_L^{3/2}(t) \ . \qquad \text{(C.27)}$$

Considering $n = 2$ in accordance with the assumed asymptotic behavior, based on the Froissart bound, one general, but not the only general, order two polynomial with the condition $3s_0 = s + t + u$ reads

$$p_n(s,t,u) = a_0 + a_1 t + a_2 t^2 + b_1(t-s) + b_2 u(t-s) + c_2 s(t-u) \ . \qquad \text{(C.28)}$$

We can interpret the constants a_i as isospin 1/2 πK S-wave subtraction constants, b_1 and b_2 as subtraction constants of the isospin 1 $\pi\pi$ P-wave and c_2 as πK isospin 1/2 S-wave subtraction constant tuned by a_0, thus giving the same single-variable amplitudes as in Eq. (4.20). Note that assigning the subtraction constants to certain single-variable amplitudes is not unique and different choices are equivalent. The inclusion of πK D-wave amplitudes works analogously to the discussion above in Appendix C.2.1.

C.3 Inhomogeneities

In this appendix we determine the inhomogeneities from Eq. (4.31). To demonstrate the procedure we will perform the calculation explicitly in the case of $f_L^{I=1/2}(s)$,

$$f_L^{1/2}(s) = \sqrt{3}\mathcal{M}_{-++}^{1/2,L}(s) = \kappa_s^L(s)\big(\mathcal{F}_L^{1/2}(s) + \hat{\mathcal{F}}_L^{1/2}(s)\big) \, . \qquad \text{(C.29)}$$

We start with the projection of the decay amplitude $\mathcal{M}_{-++}$, Eq. (4.22), onto isospin eigenstates in the s-channel. We introduce the following crossing matrices:

$$M_s^I \equiv \sum_{I'} X_{st}^{II'} M_t^{I'}\,, \qquad M_t^I \equiv \sum_{I'} X_{tu}^{II'} M_u^{I'} \tag{C.30}$$

and so on, where M_x^I is the isospin I eigenstate in the x-channel and $X_{xy}^{II'}$ the crossing matrix for the transition from channel y to x, where I and I' are the matrix component indices. We obtain the following explicit forms:

$$X_{st} = \frac{1}{3}\begin{pmatrix} 2 & -\sqrt{10} \\ -\sqrt{\frac{5}{2}} & -2 \end{pmatrix} = X_{ts}\,, \qquad X_{us} = \frac{1}{3}\begin{pmatrix} 1 & \sqrt{10} \\ \sqrt{3} & -\sqrt{\frac{6}{5}} \end{pmatrix}. \tag{C.31}$$

The t-channel and u-channel single-variable amplitudes can be split, with the aid of the crossing matrices, into $I_s = 1/2$ and $I_s = 3/2$ contributions,

$$\begin{aligned} \frac{\mathcal{F}_L^{1/2}(t)}{\sqrt{3}} - \sqrt{\frac{2}{15}}\mathcal{F}_L^{3/2}(t) &= \underbrace{\frac{2}{3\sqrt{3}}\left(\mathcal{F}_L^{1/2}(t) - \sqrt{\frac{5}{2}}\mathcal{F}_L^{3/2}(t)\right)}_{I_s=1/2} \underbrace{+\frac{1}{3\sqrt{30}}\big(\sqrt{10}\mathcal{F}_L^{1/2}(t) + 4\mathcal{F}_L^{3/2}(t)\big)}_{I_s=3/2}, \\ \mathcal{F}_0^2(u) &= \underbrace{\frac{1}{6}\big(\sqrt{3}(t-s)\mathcal{F}_1^1(u) + 5\mathcal{F}_0^2(u)\big)}_{I_s=1/2} \underbrace{-\frac{1}{6}\big(\sqrt{3}(t-s)\mathcal{F}_1^1(u) - \mathcal{F}_0^2(u)\big)}_{I_s=3/2}, \end{aligned} \tag{C.32}$$

with $L \in \{0,1\}$. Retaining the $I = 1/2$ pieces only, we have

$$\begin{aligned} \mathcal{M}_{-++}^{I_s=1/2}(s,t,u) = {} & \frac{1}{\sqrt{3}}\mathcal{F}_0^{1/2}(s) + \frac{2}{3\sqrt{3}}\Big(\mathcal{F}_0^{1/2}(t) - \sqrt{\frac{5}{2}}\mathcal{F}_0^{3/2}(t)\Big) + \frac{1}{\sqrt{3}}\big[s(t-u) - \Delta\big]\mathcal{F}_1^{1/2}(s) \\ & + \frac{2}{3\sqrt{3}}\big[t(s-u) - \Delta\big]\Big(\mathcal{F}_1^{1/2}(t) - \sqrt{\frac{5}{2}}\mathcal{F}_1^{3/2}(t)\Big) \\ & + \frac{1}{6}\big(\sqrt{3}(t-s)\mathcal{F}_1^1(u) + 5\mathcal{F}_0^2(u)\big)\,. \end{aligned} \tag{C.33}$$

Since there is no isospin 1 component in the u-channel amplitudes of $\mathcal{M}_{-++}$, the projections onto this specific component yield zero and therefore provide an additional cross-check. Similarly no $I_s = 1/2$ component should appear in $\mathcal{M}_{\bar{0}0+}$. We are left with the angular momentum projection defined generally by, see Eq. (4.32),

$$\langle z^n \mathcal{M}\rangle_{x_y}(y) \equiv \frac{1}{2}\int_{-1}^{1} \mathrm{d}z_y\, z_y^n \mathcal{M}(x(y,z_y))\,. \tag{C.34}$$

We immediately obtain

$$\langle z^n f\rangle_{u_s} = \langle z^n f\rangle_{u_t}\,,\ \ \langle z^n f\rangle_{t_s} = \langle z^n f\rangle_{s_t}\,,\ \text{and}\ \ \langle z^n f\rangle_{t_u} = (-1)^n \langle z^n f\rangle_{s_u}\,. \tag{C.35}$$

The angular average integration is straightforwardly performed in the scattering region. The continuation to the decay region, where the naive integration would cross the right-hand cut, has been discussed extensively before [34, 40]. We now perform the partial-wave projection

$$\mathcal{M}^{I_s=1/2,L}_{-++}(s,t,u) \equiv \frac{2L+1}{2}\int_{-1}^{1} \mathrm{d}z_s P_L(z_s)\mathcal{M}^{I_s=1/2}_{-++}\big(s,t(s,z_s),u(s,z_s)\big)\,, \tag{C.36}$$

with the Legendre polynomials $P_L(z_s)$ and angular momentum L. For the S-wave we obtain

$$\begin{aligned}\sqrt{3}\mathcal{M}^{1/2,0}_{-++}(s) = \frac{5\sqrt{3}}{6}\left\langle \mathcal{F}_0^2\right\rangle_{u_s} + \frac{1}{2}\left\langle \big(A_s z + D_s\big)\,\mathcal{F}_1^1\right\rangle_{u_s} + \mathcal{F}_0^{1/2}(s) + \frac{1}{3}\Bigg[\left\langle 2\mathcal{F}_0^{1/2} - \sqrt{10}\mathcal{F}_0^{3/2}\right\rangle_{t_s}\\ + \left\langle \big(A_s^2 z^2 + B_s z + C_s\big)\big(2\mathcal{F}_1^{1/2} - \sqrt{10}\mathcal{F}_1^{3/2}\big)\right\rangle_{t_s}\Bigg]\,,\end{aligned} \tag{C.37}$$

where

$$\begin{aligned} A_x &= \frac{\kappa_x(x)}{2x}\,, & B_x &= \frac{\kappa_x(x)(x^2+\Delta)}{2x^2}\,,\\ C_x &= \frac{(x^2-\Delta)^2 - x^2(\Sigma_0-2x)^2}{4x^2}\,, & D_x &= -\frac{3x^2-\Delta-x\Sigma_0}{2x}\,, \end{aligned} \tag{C.38}$$

with $\Sigma_0 = M_D^2 + M_K^2 + 2M_\pi^2$, $x \in \{s,t\}$. Thus from Eq. (C.37), the inhomogeneity can be immediately read off from the relation $\sqrt{3}\mathcal{M}^{1/2,0}_{-++}(s) = \mathcal{F}_0^{1/2}(s) + \hat{\mathcal{F}}_0^{1/2}(s)$. The full set of inhomogeneities is given in terms of the angular averages

$$\begin{aligned}\hat{\mathcal{F}}_0^2(u) =& \frac{2}{\sqrt{3}}\Bigg[\left\langle \mathcal{F}_0^{1/2} - \sqrt{\frac{2}{5}}\mathcal{F}_0^{3/2}\right\rangle_{s_u}\\ &- \left\langle \big(A_u z^2 - B_u z - C_u\big) z^2\left(\mathcal{F}_1^{1/2} - \sqrt{\frac{2}{5}}\mathcal{F}_1^{3/2}\right)\right\rangle_{s_u}\Bigg]\,,\\ \hat{\mathcal{F}}_1^1(u) =& \frac{2}{\kappa_u(u)}\Bigg[\left\langle z\big(\mathcal{F}_0^{1/2} + \sqrt{10}\mathcal{F}_0^{3/2}\big)\right\rangle_{s_u}\\ &- \left\langle \big(A_u z^3 - B_u z^2 - C_u z\big)\big(\mathcal{F}_1^{1/2} + \sqrt{10}\mathcal{F}_1^{3/2}\big)\right\rangle_{s_u}\Bigg]\,,\\ \hat{\mathcal{F}}_0^{1/2}(s) =& \frac{5\sqrt{3}}{6}\left\langle \mathcal{F}_0^2\right\rangle_{u_s} + \frac{1}{2}\left\langle \big(A_s z + D_s\big)\,\mathcal{F}_1^1\right\rangle_{u_s}\end{aligned}$$

$$
\begin{aligned}
&+\frac{1}{3}\Big[\Big\langle 2\mathcal{F}_0^{1/2}-\sqrt{10}\mathcal{F}_0^{3/2}\Big\rangle_{t_s}+\Big\langle\big(A_s^2z^2+B_sz+C_s\big)\big(2\mathcal{F}_1^{1/2}-\sqrt{10}\mathcal{F}_1^{3/2}\big)\Big\rangle_{t_s}\Big]\,,\\
\hat{\mathcal{F}}_1^{1/2}(s)=&\frac{1}{\kappa_s(s)}\Big[\frac{5\sqrt{3}}{2}\big\langle z\mathcal{F}_0^2\big\rangle_{u_s}+\frac{3}{2}\big\langle\big(A_sz^2+D_sz\big)\,\mathcal{F}_1^1\big\rangle_{u_s}\\
&+\Big\langle 2z\mathcal{F}_0^{1/2}-\sqrt{10}z\mathcal{F}_0^{3/2}\Big\rangle_{t_s}+\Big\langle\big(A_s^2z^3+B_sz^2+C_2z\big)\big(2\mathcal{F}_1^{1/2}-\sqrt{10}\mathcal{F}_1^{3/2}\big)\Big\rangle_{t_s}\Big]\,,\\
\hat{\mathcal{F}}_0^{3/2}(s)=&-\frac{\sqrt{5}}{2\sqrt{6}}\big\langle\mathcal{F}_0^2\big\rangle_{u_s}+\frac{\sqrt{5}}{2\sqrt{2}}\big\langle\big(A_sz+D_s\big)\,\mathcal{F}_1^1\big\rangle_{u_s}\\
&-\frac{1}{6}\Big[\Big\langle\sqrt{10}\mathcal{F}_0^{1/2}+4\mathcal{F}_0^{3/2}\Big\rangle_{t_s}+\Big\langle\big(A_s^2z^2+B_sz+C_s\big)\big(\sqrt{10}\mathcal{F}_1^{1/2}+4\mathcal{F}_1^{3/2}\big)\Big\rangle_{t_s}\Big]\,.\\
\hat{\mathcal{F}}_2^{1/2}(s)=&\frac{1}{\kappa_s^2(s)}\Big[\frac{25}{2\sqrt{3}}\big\langle(3z^2-1)\,\mathcal{F}_0^2\big\rangle_{u_s}+\frac{5}{2}\big\langle\big(A_sz+D_s\big)\big(3z^2-1\big)\,\mathcal{F}_1^1\big\rangle_{u_s}\\
&+\frac{10}{3}\Big\langle(3z^2-1)\,\mathcal{F}_0^{1/2}\Big\rangle_{t_s}-\frac{15\sqrt{10}}{3}\Big\langle(3z^2-1)\,\mathcal{F}_0^{3/2}\Big\rangle_{t_s}\\
&+\frac{10}{3}\Big\langle\big(A_s^2z^2+B_sz+C_s\big)(3z^2-1)\,\mathcal{F}_1^{1/2}\Big\rangle_{t_s}\Big]\,,
\end{aligned}
\tag{C.39}
$$

where in addition to Eq. (C.38) we have used

$$
A_u=\frac{1}{4}\kappa_u(u)^2\,,\qquad B_u=\frac{1}{2}u\kappa_u(u)\,,\qquad C_u=\frac{\big(\Sigma_0-2u\big)^2-u^2}{4}-\Delta\,. \tag{C.40}
$$

C.4 Invariance group matching

In this appendix, we study the polynomial ambiguities in the decomposition of the total decay amplitudes Eq. (4.22) into single-variable functions, dubbed "invariance group". We wish to determine the polynomial at most linear in the Mandelstam variables that can be added to the different single-variable amplitudes, leaving the total decay amplitudes Eq. (4.22) invariant. For this purpose, we make use of the relation $s+t+u=3s_0=M_D^2+M_K^2+2M_\pi^2$. It is easy to check that adding the following terms to the various S-waves as well as the $\pi\pi$ P-wave:

$$
\begin{aligned}
&\mathcal{F}_0^{2^{\rm inv}}(u)=a_0+b_0u\,,\quad \mathcal{F}_1^{1^{\rm inv}}(u)=-\frac{5}{\sqrt{3}}b_0+2d_0\,,\\
&\mathcal{F}_0^{1/2^{\rm inv}}(s)=c_0+d_0s\,,\quad \mathcal{F}_0^{3/2^{\rm inv}}(s)=\frac{\sqrt{5}}{2\sqrt{2}}\Big(\sqrt{3}\big[a_0+b_0(3s_0-2s)\big]+2(c_0+d_0s)\Big)\,,
\end{aligned}
\tag{C.41}
$$

leaves both $\mathcal{M}_{-++}(s,t,u)$ and $\mathcal{M}_{\bar{0}0+}(s,t,u)$ unchanged. The most general full decay amplitudes are therefore obtained by

$$
\mathcal{F}_L^{I^{\rm new}}(s)=\mathcal{F}_L^I(s)+\mathcal{F}_L^{I^{\rm inv}}(s)\,, \tag{C.42}
$$

which, according to Eq. (C.41), has a four-parameter gauge freedom built in.

Following Ref. [116], we rewrite the polynomial representations of $\mathcal{F}_L^{I\,\mathrm{inv}}(s)$ Eq. (C.41) into the Omnès representation $\mathcal{F}_{L\Omega}^{I\,\mathrm{inv}}(s)$ in order to match to Eq. (4.30):

$$\mathcal{F}_{L\Omega}^{I\,\mathrm{inv}}(s) \equiv \Omega_L^I(s)\left\{\pi_L^I(s) + \frac{s^n}{\pi}\int_{s_\mathrm{th}}^\infty \frac{\mathrm{d}x}{x^n}\,\frac{\sin\delta_L^I(x)\hat{\mathcal{F}}_L^{I\,\mathrm{inv}}}{|\Omega_L^I(x)|(x-s)}\right\}, \tag{C.43}$$

with the subtraction polynomials $\pi_L^I(s)$. As the invariance polynomials $\mathcal{F}_L^{I\,\mathrm{inv}}(s)$ do not have discontinuities, it immediately follows that $\hat{\mathcal{F}}_L^{I\,\mathrm{inv}}(s) = -\mathcal{F}_L^{I\,\mathrm{inv}}(s)$, which is also confirmed by a straightforward calculation. We determine the subtraction polynomials by equating the polynomial and Omnès representations of the invariance group. We obtain

$$\pi_L^I(s) = \frac{\mathcal{F}_L^{I\,\mathrm{inv}}(s)}{\Omega_L^I} + \frac{s^n}{\pi}\int_{s_\mathrm{th}}^\infty \frac{\mathrm{d}x}{x^n}\,\frac{\sin\delta_L^I(x)\mathcal{F}_L^{I\,\mathrm{inv}}}{|\Omega_L^I(x)|(x-s)}\,. \tag{C.44}$$

The next step is to rewrite the inverse Omnès function into a dispersion relation. Its discontinuity is given by

$$\mathrm{disc}\frac{1}{\Omega_L^I(s)} = -2i\frac{\sin\delta_L^I(x)}{|\Omega_L^I(x)|}\,, \tag{C.45}$$

which thus yields

$$\frac{1}{\Omega_L^I(s)} = P_{L\Omega}^I(s) - \frac{s^n}{\pi}\int_{s_\mathrm{th}}^\infty \frac{\mathrm{d}x}{x^n}\,\frac{\sin\delta_L^I(x)}{|\Omega_L^I(x)|(x-s)}\,, \tag{C.46}$$

with the subtraction polynomial $P_{L\Omega}^I(s) = 1 + \sum_{i=1}^{n-1}(\omega_L^I)_i s^i$. The subtraction constants $(\omega_L^I)_i$ are given by the following sum rules, provided that the dispersion integrals converge:

$$(\omega_L^I)_i = -\frac{1}{\pi}\int_{s_\mathrm{th}}^\infty \frac{\mathrm{d}x}{x^{i+1}}\frac{\sin\delta_L^I(x)}{|\Omega_L^I(x)|}\,. \tag{C.47}$$

Therefore Eq. (C.44) yields

$$\pi_L^I(s) = P_{L\Omega}^I(s)\mathcal{F}_L^{I\,\mathrm{inv}}(s) + \frac{s^n}{\pi}\int_{s_\mathrm{th}}^\infty \frac{\mathrm{d}x}{x^n}\,\frac{\sin\delta_L^I(x)\big(\mathcal{F}_L^{I\,\mathrm{inv}}(x) - \mathcal{F}_L^{I\,\mathrm{inv}}(s)\big)}{|\Omega_L^I(x)|(x-s)}\,. \tag{C.48}$$

As an example we will study the single-variable amplitude $\mathcal{F}_0^2$ with $\mathcal{F}_0^{2\,\mathrm{inv}}(s) = a_0 + b_0 s$. We obtain

$$\pi_0^2(s) = a_0 + \Big[b_0 + a_0(\omega_0^2)_1\Big]s + \left((\omega_0^2)_1 - \frac{1}{\pi}\int_{s_\mathrm{th}}^\infty \frac{\mathrm{d}x}{x^2}\,\frac{\sin\delta_L^I(x)}{|\Omega_L^I(x)|}\right) b_0 s^2\,. \tag{C.49}$$

Using the sum rule value for $(\omega_0^2)_1$ we find

$$\pi_0^2(s) = a_0 + \Big[b_0 + a_0(\omega_0^2)_1\Big]s\,. \tag{C.50}$$

Fit	FF_0^2	$2 \times \mathrm{FF}_0^{1/2}$	$2 \times \mathrm{FF}_1^{1/2}$	$2 \times \mathrm{FF}_0^{3/2}$	$2 \times \mathrm{FF}_2^{1/2}$
Full 1	$(28 \pm 8)\%$	$(240 \pm 120)\%$	$(22 \pm 4)\%$	$(80 \pm 50)\%$	—
Full 2	$(7 \pm 4)\%$	$(69 \pm 13)\%$	$(10 \pm 2)\%$	$(11 \pm 5)\%$	$(0.1 \pm 0.05)\%$
Omnès 1	$(70 \pm 40)\%$	$(260 \pm 80)\%$	$(7 \pm 1)\%$	$(490 \pm 190)\%$	—
Omnès 2	$(60 \pm 30)\%$	$(220 \pm 120)\%$	$(9 \pm 1)\%$	$(360 \pm 140)\%$	$(0.3 \pm 0.1)\%$

Table C.1: *Fit fractions of the combined CLEO/FOCUS fits:* The resulting fit fractions of Eq. (5.4) are given for the different fit scenarios; the errors on the parameters are evaluated by varying the basis functions within their error bands.

The other subtraction polynomials are obtained in an analogous way and read

$$\begin{aligned}
\pi_0^2(s) &= a_0 + (b_0 + a_0(\omega_0^2)_1)s\,, \qquad \pi_1^1(s) = -\frac{5}{\sqrt{3}}b_0 + 2d_0\,, \\
\pi_0^{1/2}(s) &= c_0 + \Big[d_0 + (\omega_0^{1/2})_1\Big]s + \Big[d_0(\omega_0^{1/2})_1 + c_0(\omega_0^{1/2})_2\Big]s^2 + \Big[d_0(\omega_0^{1/2})_2 + c_0(\omega_0^{1/2})_3\Big]s^3 \\
\pi_0^{3/2}(s) &= \frac{\sqrt{5}}{2\sqrt{2}}\Big\{\sqrt{3}(a_0 + 3b_0 s_0) + 2c_0 \\
&\qquad + \Big[(\omega_0^{3/2})_1\Big(\sqrt{3}(a_0 + 3b_0 s_0) + 2c_0\Big) - 2\Big(\sqrt{3}b_0 - d_0\Big)\Big]s\Big\}\,,
\end{aligned} \tag{C.51}$$

with no contributions to the πK P- and D-waves. Polynomial terms with higher order than the subtraction polynomials of the corresponding amplitudes (see Section 4.3.5) have been omitted.

As we have argued above that a choice of the constants a_0, …, d_0 corresponds to a mere "gauge" choice and is unobservable, we can decide to fix them by requiring the (linear) subtraction polynomials in the non-resonant S-waves ($I = 2$ $\pi\pi$ and $I = 3/2$ πK) to vanish. Equation (C.51) proves that this is feasible: we can eliminate all subtraction constants in $\mathcal{F}_0^2$ by the appropriate choice of a_0 and b_0, and all constants in $\mathcal{F}_0^{3/2}$ by adjusting c_0 and d_0. The result is the system Eq. (4.44) in the main text, which is thus free of ambiguities.

C.5 Combined CLEO/FOCUS fits

In Tables C.1 and C.2 we show the fit results from the combined fits to CLEO and FOCUS data performed in Section 5.1.3.

	Full 1	Full 2		Omnès 1	Omnès 2
$\lvert c_0\rvert \times \mathrm{GeV}^2$	2.4 ± 1.0	0.8 ± 0.2	$\lvert c_0'\rvert$	0.6 ± 0.3	0.5 ± 0.2
$\lvert c_1\rvert \times \mathrm{GeV}^4$	3.4 ± 0.8	1.6 ± 0.3	$\lvert c_1'\rvert$	2.8 ± 1.5	2.9 ± 0.4
c_2	1 (fixed)	1 (fixed)	c_2'	1 (fixed)	1 (fixed)
$\lvert c_3\rvert \times \mathrm{GeV}^2$	2.7 ± 0.4	2.1 ± 0.1	$\lvert c_3'\rvert \times \mathrm{GeV}^2$	1.8 ± 0.2	2.0 ± 0.1
$\lvert c_4\rvert \times \mathrm{GeV}^4$	2.0 ± 0.5	1.25 ± 0.15	$\lvert c_4'\rvert \times \mathrm{GeV}^4$	0.9 ± 0.1	1.1 ± 0.1
$\lvert c_5\rvert \times \mathrm{GeV}^6$	0.45 ± 0.06	0.30 ± 0.05	$\lvert c_5'\rvert \times \mathrm{GeV}^6$	0.14 ± 0.03	0.19 ± 0.02
$\lvert c_6\rvert \times 10^2\mathrm{GeV}^4$	7.0 ± 0.3	1.5 ± 0.5	$\lvert c_6'\rvert \times 10^2\mathrm{GeV}^4$	8 ± 3	6 ± 1
			$\lvert c_7'\rvert \times 10^3\mathrm{GeV}^8$	—	3.0 ± 1.5
$\arg c_0$	0.2 ± 0.3	1.1 ± 0.4	$\arg c_0'$	-0.7 ± 0.5	0.6 ± 0.3
$\arg c_1$	0.4 ± 0.3	1.3 ± 0.4	$\arg c_1'$	-0.8 ± 0.3	-0.4 ± 0.2
$\arg c_3$	-0.2 ± 0.2	-0.1 ± 0.1	$\arg c_3'$	0.3 ± 0.2	0.1 ± 0.1
$\arg c_4$	-0.3 ± 0.2	-0.1 ± 0.2	$\arg c_4'$	0.5 ± 0.2	0.3 ± 0.1
$\arg c_5$	0.0 ± 0.3	0.0 ± 0.1	$\arg c_5'$	0.4 ± 0.4	0.1 ± 0.3
$\arg c_6$	-1.4 ± 1.1	-0.7 ± 0.5	$\arg c_6'$	-0.3 ± 0.2	-0.2 ± 0.1
			$\arg c_7'$	—	2.6 ± 0.2
$\chi^2_{\mathrm{CLEO}}/\mathrm{d.o.f.}$	1.19 ± 0.02	1.15 ± 0.02		1.27 ± 0.04	1.12 ± 0.02
$\chi^2_{\mathrm{FOCUS}}/\mathrm{d.o.f.}$	1.31 ± 0.02	1.30 ± 0.02		1.33 ± 0.03	1.26 ± 0.01
$\chi^2_{\mathrm{combined}}/\mathrm{d.o.f.}$	1.23 ± 0.02	1.21 ± 0.02		1.3 ± 0.02	1.17 ± 0.02

Table C.2: *Combined fit to the CLEO and FOCUS Dalitz plots:* Numerical fit results for the subtraction constants c_i and the corresponding χ^2/d.o.f.. Two fit scenarios are considered: the full dispersive fit, without D-wave (full 1) and with D-wave (full 2). The errors on the parameters are evaluated by varying the basis functions within their error bands.

Bibliography

[1] H. Fritzsch, M. Gell-Mann and H. Leutwyler, Phys. Lett. B **47**, 365 (1973).

[2] S. L. Glashow, Nucl. Phys. **22**, 579 (1961).

[3] S. Weinberg, Phys. Rev. Lett. **19**, 1264 (1967).

[4] A. Salam, Conf. Proc. C **680519**, 367 (1968).

[5] G. Aad *et al.* [ATLAS Collaboration], Phys. Lett. B **716**, 1 (2012), [arXiv:1207.7214].

[6] S. Chatrchyan *et al.* [CMS Collaboration], Phys. Lett. B **716**, 30 (2012), [arXiv:1207.7235].

[7] C. Hanhart, [arXiv:1512.02190].

[8] S. Bethke, G. Dissertori and G. Salam, Quantum Chromodynamics in: K. A. Olive *et al.* [Particle Data Group Collaboration], Chin. Phys. C **38**, 090001 (2014).

[9] H. D. Politzer, Phys. Rev. Lett. **30**, 1346 (1973).

[10] D. J. Gross and F. Wilczek, Phys. Rev. Lett. **30**, 1343 (1973).

[11] S. Weinberg, Physica A **96**, 327 (1979).

[12] B. Kubis, [hep-ph/0703274].

[13] S. Scherer, Adv. Nucl. Phys. **27**, 277 (2003), [hep-ph/0210398].

[14] R. J. Eden, P. V Landshoff, D. I. Olive and J. C. Polkinghorne, The Analytic S-Matrix, Cambridge University Press, (2002).

[15] H. Lehmann, K. Symanzik, and W. Zimmerman, Nuovo Cimento 1, 205 (1955)

[16] D. Olive, Nuovo Cim. **26** 73 (1962).

[17] M. Bando, T. Kugo, S. Uehara, K. Yamawaki and T. Yanagida, Phys. Rev. Lett. **54**, 1215 (1985).

[18] M. Bando, T. Kugo and K. Yamawaki, Phys. Rept. **164**, 217 (1988).

[19] M. Benayoun, H. B. O'Connell and A. G. Williams, Phys. Rev. D **59**, 074020 (1999), [hep-ph/9807537].

[20] M. Benayoun, P. David, L. DelBuono and F. Jegerlehner, Eur. Phys. J. C **72**, 1848 (2012), [arXiv:1106.1315].

[21] M. F. M. Lutz and S. Leupold, Nucl. Phys. A **813**, 96 (2008), [arXiv:0801.3821].

[22] N. I. Muskhelishvili, Singular integral equations, P. Noordhoff, (1953).

[23] R. Omnes, Nuovo Cim. **8**, 316 (1958).

[24] J. Gasser and U.-G. Meißner, Nucl. Phys. B **357**, 90 (1991).

[25] F. K. Guo, C. Hanhart, F. J. Llanes-Estrada and U.-G. Meißner, Phys. Lett. B **678** 90 (2009), [arXiv:0812.3270].

[26] J. F. De Troconiz and F. J. Yndurain, Phys. Rev. D **65**, 093001 (2002), [hep-ph/0106025].

[27] C. Hanhart, Phys. Lett. B **715**, 170 (2012), [arXiv:1203.6839].

[28] K. M. Watson, Phys. Rev. **95** 228 (1954).

[29] B. Ananthanarayan, G. Colangelo, J. Gasser and H. Leutwyler, Phys. Rept. **353** 207 (2001), [hep-ph/0005297].

[30] I. Caprini, G. Colangelo and H. Leutwyler, Eur. Phys. J. C **72** 1860 (2012), [arXiv:1111.7160].

[31] I. Caprini, G. Colangelo and H. Leutwyler, in preparation.

[32] R. García-Martín, R. Kamiński, J. R. Peláez, J. Ruiz de Elvira and F. J. Ynduráin, Phys. Rev. D **83** 074004 (2011), [arXiv:1102.2183].

[33] F. Niecknig, Diplomarbeit, Universität Bonn (2011)

[34] F. Niecknig, B. Kubis and S. P. Schneider, Eur. Phys. J. C **72**, 2014 (2012), [arXiv:1203.2501].

[35] G. Colangelo, M. Hoferichter, M. Procura and P. Stoffer, JHEP **1509**, 074 (2015), [arXiv:1506.01386].

[36] G. Colangelo, M. Hoferichter, B. Kubis, M. Procura and P. Stoffer, Phys. Lett. B **738**, 6 (2014) [arXiv:1408.2517].

[37] S. P. Schneider, B. Kubis and F. Niecknig, Phys. Rev. D **86**, 054013 (2012), [arXiv:1206.3098].

[38] M. Hoferichter, B. Kubis, S. Leupold, F. Niecknig and S. P. Schneider, Eur. Phys. J. C **74**, 3180 (2014), [arXiv:1410.4691].

[39] N. N. Khuri and S. B. Treiman, Phys. Rev. **119** 1115 (1960).

[40] J. B. Bronzan and C. Kacser, Phys. Rev. **132** 2703 (1963).

[41] I. J. R. Aitchison, Phys. Rev. **137** B1070 (1965).

[42] I. J. R. Aitchison and R. Pasquier Phys. Rev. **152** 1274 (1966).

[43] R. Pasquier and J. Y. Pasquier, Phys. Rev. **170** 1294 (1968).

[44] R. Pasquier and J. Y. Pasquier, Phys. Rev. **177** 2482 (1969).

[45] A. V. Anisovich and H. Leutwyler, Phys. Lett. B **375** 335 (1996), [hep-ph/9601237].

[46] J. Kambor, C. Wiesendanger and D. Wyler, Nucl. Phys. B **465** 215 (1996), [hep-ph/9509374].

[47] J. M. Charap and E. Leader, Annals Phys. **105** 39 (1977).

[48] M. Ablikim *et al.* [BESIII Collaboration], Phys. Lett. B **710**, 594 (2012), [arXiv:1202.2048].

[49] E. Witten, Nucl. Phys. B **223**, 422 (1983).

[50] M. Jacob and G. C. Wick, Annals Phys. **7**, 404 (1959), [Annals Phys. **281**, 774 (2000)].

[51] T. Hannah, Nucl. Phys. B **593** 577 (2001), [hep-ph/0102213].

[52] J. Stern, H. Sazdjian and N. H. Fuchs, Phys. Rev. D **47** 3814 (1993), [hep-ph/9301244].

[53] M. Knecht, B. Moussallam, J. Stern and N. H. Fuchs, Nucl. Phys. B **457**, 513 (1995), [hep-ph/9507319].

[54] B. Ananthanarayan and P. Büttiker, Eur. Phys. J. C **19** 517 (2001), [hep-ph/0012023].

[55] M. Zdráhal and J. Novotný, Phys. Rev. D **78**, 116016 (2008), [arXiv:0806.4529].

[56] P. Stoffer, [arXiv:1412.5171].

[57] M. Froissart, Phys. Rev. **123** 1053 (1961).

[58] S. P. Schneider, PhD thesis, University of Bonn (2013), [http://hss.ulb.uni-bonn.de/2013/3126/3126.htm].

[59] H. R. Kutt, Numer. Math. **24**, 205-210 (1975).

[60] N. I. Ioakimidis, Z. Angew. Math. Mech. **63**, 572-574 (1983).

[61] G. Monegato, J. Comput. Appl. Math. **50**, 9-31 (1994).

[62] S. Descotes-Genon and B. Moussallam, Eur. Phys. J. C **74** 2946 (2014), [arXiv:1404.0251].

[63] B. Kubis and F. Niecknig, Phys. Rev. D **91**, no. 3, 036004 (2015), [arXiv:1412.5385].

[64] C. Hanhart, A. Kupść, U.-G. Meißner, F. Stollenwerk and A. Wirzba, Eur. Phys. J. C **73**, 2668 (2013), [arXiv:1307.5654].

[65] A. Anastasi *et al.* [KLOE-2 Collaboration], [arXiv:1601.06565].

[66] L. G. Landsberg, Phys. Rept. **128**, 301 (1985).

[67] R. Arnaldi *et al.* [NA60 Collaboration], Phys. Lett. B **677**, 260 (2009), [arXiv:0902.2547].

[68] G. Usai [NA60 Collaboration], Nucl. Phys. A **855**, 189 (2011).

[69] A. Anastasi *et al.* [KLOE-2 Collaboration], [arXiv:1601.06565].

[70] B. Ananthanarayan, I. Caprini and B. Kubis, Eur. Phys. J. C **74**, 3209 (2014), [arXiv:1410.6276].

[71] M. Ablikim *et al.* [BESIII Collaboration], Phys. Rev. D **89**, 092008 (2014), [arXiv:1403.7042].

[72] J. Fu, H.-B. Li, X. Qin and M.-Z. Yang, Mod. Phys. Lett. A **27**, 1250223 (2012), [arXiv:1111.4055].

[73] Y.-H. Chen, Z.-H. Guo and B.-S. Zou, Phys. Rev. D **91**, 014010 (2015), [arXiv:1411.1159].

[74] S. P. Schneider, B. Kubis and F. Niecknig, Phys. Rev. D **86**, 054013 (2012), [arXiv:1206.3098].

[75] B. Kubis and R. Schmidt, Eur. Phys. J. C **70**, 219 (2010), [arXiv:1007.1887].

[76] G. Köpp, Phys. Rev. D **10**, 932 (1974).

[77] A. P. Szczepaniak and M. R. Pennington, Phys. Lett. B **737**, 283 (2014), [arXiv:1403.5782].

[78] P. Guo, R. Mitchell and A. P. Szczepaniak, Phys. Rev. D **82**, 094002 (2010), [arXiv:1006.4371].

[79] I. V. Danilkin, C. Fernández-Ramírez, P. Guo, V. Mathieu, D. Schott, M. Shi and A. P. Szczepaniak, [arXiv:1409.7708].

[80] R. García-Martín, R. Kamiński, J. R. Peláez, J. Ruiz de Elvira and F. J. Ynduráin, Phys. Rev. D **83**, 074004 (2011), [arXiv:1102.2183].

[81] I. Caprini, G. Colangelo and H. Leutwyler, Eur. Phys. J. C **72**, 1860 (2012), [arXiv:1111.7160]; in preparation.

[82] K. A. Olive *et al.* [Particle Data Group Collaboration], Chin. Phys. C **38**, 090001 (2014).

[83] R. Escribano, Eur. Phys. J. C **65**, 467 (2010), [arXiv:0807.4201].

[84] Q. Zhao, Phys. Lett. B **697**, 52 (2011), [arXiv:1012.1165].

[85] F.-K. Guo, C. Hanhart and U.-G. Meißner, Phys. Rev. Lett. **103**, 082003 (2009), [Erratum-ibid. **104**, 109901 (2010)], [arXiv:0907.0521].

[86] F. Niecknig and B. Kubis, JHEP **1510** 142 (2015), [arXiv:1509.03188].

[87] M. Battaglieri *et al.*, Acta Phys. Polon. B **46** 257 (2015), [arXiv:1412.6393].

[88] I. I. Bigi and A. I. Sanda, *CP violation* (2nd ed.), Camb. Monogr. Part. Phys. Nucl. Phys. Cosmol. **28** (2009) 1.

[89] S. Gardner and U.-G. Meißner, Phys. Rev. D **65** 094004 (2002), [hep-ph/0112281].

[90] J. T. Daub, C. Hanhart and B. Kubis, JHEP **1602**, 009 (2016), [arXiv:1508.06841].

[91] S. Lanz, PoS CD **12** 007 (2013), [arXiv:1301.7282].

[92] P. Guo, I. V. Danilkin, D. Schott, C. Fernndez-Ramrez, V. Mathieu and A. P. Szczepaniak, Phys. Rev. D **92**, no. 5, 054016 (2015), [arXiv:1505.01715].

[93] I. V. Danilkin, C. Fernndez-Ramrez, P. Guo, V. Mathieu, D. Schott, M. Shi and A. P. Szczepaniak, Phys. Rev. D **91**, no. 9, 094029 (2015), [arXiv:1409.7708].

[94] M. Jamin, J. A. Oller and A. Pich, Nucl. Phys. B **622** 279 (2002), [hep-ph/0110193].

[95] L. Edera and M. R. Pennington, Phys. Lett. B **623** 55 (2005), [hep-ph/0506117].

[96] B. Moussallam, Eur. Phys. J. C **53** 401 (2008), [arXiv:0710.0548].

[97] G. Bonvicini *et al.* [CLEO Collaboration], Phys. Rev. D **78** 052001 (2008), [arXiv:0802.4214].

[98] J. M. Link *et al.* [FOCUS Collaboration], Phys. Lett. B **653** 1 (2007), [arXiv:0705.2248].

[99] E. M. Aitala *et al.* [E791 Collaboration], Phys. Rev. D **73** 032004 (2006), [Phys. Rev. D **74** 059901 (2006)], [hep-ex/0507099].

[100] M. Ablikim *et al.* [BESIII Collaboration], Phys. Rev. D **89**, no. 5, 052001 (2014), [arXiv:1401.3083].

[101] S. Descotes-Genon and B. Moussallam, Eur. Phys. J. C **48** 553 (2006), [hep-ph/0607133].

[102] J. M. Link *et al.* [FOCUS Collaboration], Phys. Lett. B **681** 14 (2009), [arXiv:0905.4846].

[103] D. Aston *et al.*, Nucl. Phys. B **296** 493 (1988).

[104] J. A. Oller, Phys. Rev. D **71** 054030 (2005), [hep-ph/0411105].

[105] D. R. Boito and R. Escribano, Phys. Rev. D **80** 054007 (2009), [arXiv:0907.0189].

[106] B. El-Bennich, A. Furman, R. Kamiński, L. Leśniak and B. Loiseau, Phys. Rev. D **74** 114009 (2006), [hep-ph/0608205].

[107] B. El-Bennich, A. Furman, R. Kamiński, L. Leśniak, B. Loiseau and B. Moussallam, Phys. Rev. D **79** 094005 (2009), [Phys. Rev. D **83** 039903 (2011)], [arXiv:0902.3645].

[108] P. C. Magalhães *et al.*, Phys. Rev. D **84** 094001 (2011), [arXiv:1105.5120].

[109] P. C. Magalhães and M. R. Robilotta, Phys. Rev. D **92**, no. 9, 094005 (2015), [arXiv:1504.06346].

[110] K. S. F. F. Guimarães, O. Lourenço, W. de Paula, T. Frederico and A. C. dos Reis, JHEP **1408** 135 (2014), [arXiv:1404.3797].

[111] S. X. Nakamura, Phys. Rev. D **93**, no. 1, 014005 (2016), [arXiv:1504.02557].

[112] R. E. Cutkosky, J. Math. Phys. **1** 429 (1960).

[113] J. Gasser, B. Kubis and A. Rusetsky, Nucl. Phys. B **850** 96 (2011), [arXiv:1103.4273].

[114] P. Guo, [arXiv:1506.00042].

[115] P. Büttiker, S. Descotes-Genon and B. Moussallam, Eur. Phys. J. C **33** 409 (2004), [hep-ph/0310283]; B. Moussallam, private communication.

[116] H. Leutwyler, private communication.

[117] P. Guo, I. V. Danilkin and A. P. Szczepaniak, [arXiv:1409.8652].

[118] M. Hoferichter, C. Ditsche, B. Kubis and U.-G. Meißner, JHEP **1206** 063 (2012), [arXiv:1204.6251].

[119] J. F. Donoghue, J. Gasser and H. Leutwyler, Nucl. Phys. B **343** 341 (1990).

[120] B. Moussallam, Eur. Phys. J. C **14** 111 (2000), [arXiv:9909292].

[121] S. Descotes-Genon, Ph.D. Thesis, Université de Paris-Sud, France (2000).

[122] M. Dubrovin, private communication.

[123] A. Aloisio *et al.* [KLOE Collaboration], Phys. Lett. B **561** 55 (2003), [Phys. Lett. B **609** 449 (2005)], [hep-ex/0303016].

[124] R. R. Akhmetshin *et al.*, Phys. Lett. B **642** 203 (2006).

[125] E. P. Wigner, *Group Theory and its application to the quantum mechanics of atomic spectra*, Academic Press (1959).

[126] D. M. Brink and G. R. Satchler, *Angular Momentum*, Oxford University Press (1968).

[127] W. M. Gibson and B. R. Pollard, *Symmetry Principles in Elementary Particle Physics*, ISBN-9780521299640.

[128] M. Gell-Mann, Phys. Rev. **92** 833 (1953).
T. Nakano and K. Nishijima, Prog. Theor. Phys. **10** 581 (1953).

[129] X. W. Kang, B. Kubis, C. Hanhart and U.-G. Meißner, Phys. Rev. D **89**, 053015 (2014), [arXiv:1312.1193].

[130] Y. H. Chen, J. T. Daub, F. K. Guo, B. Kubis, U.-G. Meißner and B. S. Zou, Phys. Rev. D **93**, no. 3, 034030 (2016), [arXiv:1512.03583].

[131] B. Kubis, [arXiv:1108.5866].

[132] J. T. Daub, H. K. Dreiner, C. Hanhart, B. Kubis and U. G. Meissner, JHEP **1301**, 179 (2013) [arXiv:1212.4408].

[133] J. T. Daub, C. Hanhart and B. Kubis, JHEP **1602**, 009 (2016) [arXiv:1508.06841].

Acknowledgements

A PhD thesis is not possible without the support of many people and I therefore want to express my deep gratitude to everyone who supported me over the last years.

To begin with, I would like to thank my supervisor Professor Dr. Bastian Kubis. He has given me as much support as I could have hoped for well beyond the usual. Throughout my thesis he always lend a sympathetic ear to me and his patience and support helped me to overcome the unavoidable low-points. I am grateful for his encouragement to participate in various conferences and meetings and for providing the opportunity to do so. The deeply shared admiration for my "major numerical problem" and his encouraging wink: "Da muss jemand dran arbeiten" has been much appreciated.

Secondly I give my gratitude to Prof. Dr. Christoph Hanhart for numerous fruitful discussions, his great support during conferences, and his willingness to answer any question I confronted him with.

I owe thanks to the whole working group for the weekly group meetings and discussions, especially to my long time collaborator Dr. Sebastian Schneider for the successful and rewarding teamwork. Additionally, I want to thank Prof. Dr. Simon Eidelman, Dr. Martin Hoferichter, Prof. Dr. Andrzej Kupść, Prof. Dr. Mike Pennington, Dr. Peter Stoffer, Felix Stollenwerk, and many others for useful discussions at various occasions.

A very special thanks goes out to my office mates Shahin Bour, Johanna Daub, Nico Klein, and Deborah Rönchen for the pleasant time with amusing and heated discussions about politics and other affairs as well as the moral support and homely atmosphere required to work late hours.

I am grateful to Matthias Frink and Mark Lenkewitz for numerous activities besides the academic world, discussions, and the drink and snack supplies from their office whenever needed. Furthermore I thank all the participants of the HISKP Wednesday 5 o'clock football event. It has always been fun. I thank the "Friday Tibetans group" consisting of Peter Klassen, Erik Altenbach, and Felix Bleckmann for the excellent Friday lunch meetings and of course the unsurpassed cuisine of the Tibeter Imbiss needs to be mentioned.

I also thank Johanna Daub, Bai Long, Peter Stoffer, and Erik Wilbring for the regular Tichu & Co. evenings. And in particular Erik and Johanna for the nice trip around China.

I owe my best friends Felix and Sonja special thanks for simply everything we have

done together in the last years, Skiing holidays, trips together, our running and triathlon "project", and all the time they have gifted me.

And finally and most importantly to my parents for the best education and love a child can dream of, to my sister for the deep friendship and love, and to Johanna for the wonderful time spent together and the time to come with "Zwergi".